# Development of Integrated Superconducting Balanced Mixers for THz Focal Plane Arrays

Inaugural-Dissertation

zur

Erlangung des Doktorgrades

der Mathematisch-Naturwissenschaftlichen Fakultät

der Universität zu Köln

Vorgelegt von

Sina Fathi

aus Teheran, Iran

Köln, 2019

Berichterstatter:

Prof. Dr. Jürgen Stutzki
Prof. Dr. Andreas Zilges

Tag der mündlichen Prüfung: 22.02.2019

# Abstract

This thesis work covers the development of integrated superconducting balanced mixers for heterodyne (resolution$> 10^7$) THz focal plane arrays. The aim was to develop on chip integrated balanced superconductor-insulator-superconductor (SIS) mixers at 800-1100 GHz and in addition at the Intermediate Frequency (IF) 4-12 GHz integrated 180° IF hybrids both for the CHAI (CCAT Heterodyne Array Instrument) receiver for the Cerro Chajnantor Atacama Telescope (CCAT) observatory. A planar 180°hybrid-ring coupler, two separate slotline antennas, two separate slotline to CPW transitions to employ for the 800-1100 GHz balanced SIS mixer, based on NbTiN circuitry, were designed and all were integrated on one 6 $\mu$m silicon substrate.
At the IF side of the integrated balanced mixers, two different configurations of superconducting integrated 180° IF hybrids were designed to combine the two generated IF outputs at either $\Sigma$ or $\Delta$ port depending on the choice of the input port of the hybrid. These 4-12 GHz IF hybrid coupler designs were based on planar lumped elements to miniaturize the size to about $0.5 \times 2.2\ \mu m^2$. The designs were simulated for 500 $\mu$m and 9 $\mu$m silicon substrates. The latter is studied in order to integrate it at a later stage with the RF part of the mixer on one substrate. The lithography mask and subsequently the micro-fabrication of the IF hybrids were made. The measurement of the Nb based IF hybrid on a 500 $\mu$m silicon with Vector Network Analyzer (VNA) in liquid helium is reported. The measured results are analyzed and compared to the IF hybrid with the implemented superconducting Nb in the simulation.
These developments and designs will be available and applicable for future receivers of the CCAT-prime observatory. Because the original envisioned CCAT-observatory project was discontinued due to the lack of funding, it was decided that my 800-1100 GHz designs would not be further developed into working mixers for the time being and that other projects would get priority.
My work continued with the the development of integrated 1.9 THz balanced Hot Electron Bolometer (HEB) mixers. This development is relevant for 1.9 THz focal plane array receivers for the airborne Stratospheric Observatory for the Far Infrared

(SOFIA), for which the mixers are developed in our group. The LO power consumption of the array presently limits its usable RF bandwidth. This power consumption could be reduced by a factor of 5 by using integrated balanced mixers. The mixers are based on superconducting NbN HEBs and Au is applied as normal metal to wire the mixers. The development contained design, micro-nanofabrication, DC and cryogenic-high frequency measurements. All designed planar elements consisted of an 1 octave broadband 180°RF hybrid-ring coupler, two slotline tapered antennas, two slotline to CPW transitions, two or four 120Ω HEB bridges, two low pass filters (LPFs) and two DC/IF blocking capacitors integrated on one 3 $\mu$m silicon substrate and simulated using CST suite. A further integrated 1.9 THz HEB mixer was designed to support the two separate IF outputs at one side of a 3 $\mu$m silicon substrate with employing a CPW-CPW crossover.

The micro-nanofabrication of the 1.9 THz balanced mixers was done in house using E-beam and photo-lithography techniques. Almost all DC measured devices contained HEB bridges that were sufficiently similar in normal state resistance and transition temperature. The average resistance of the devices, in the one available wafer for measurements, was about 17% too low. The transition temperature of the devices was around 7.9 K, in comparison to 8.5 K for our state of the art single pixel mixers. The two machined 1.9 THz balanced waveguide blocks for testing of the devices were machined in the institute's in house workshop. I have tested the transmission of the blocks, and thereby the workmanship, with a THz time Domain Spectrometer, showed about 2.4 dB of loss per mm waveguide length at room temperature, for a split block waveguide made of the oxygen free copper tellurium alloy (CuTe).

The cryogenic RF measurements showed a very similar LO-power coupling to both mixers in the balanced device, from both input ports of the mixer. By using an in house built Quantum Cascade Laser (QCL) LO as a local oscillator and a severely attenuated Virginia Diode multiplier chain (VDI) LO as a signal source I have shown proper balanced mixer behavior, thereby validating the design. Signal suppression up to 38 dB was shown by inverting the bias voltages on one of the mixers in the balanced device, which added a 180° phase change to the IF of one of the mixers.

# Zusammenfassung

Diese Arbeit befasst sich mit der Entwicklung von integrierten, supraleitenden, balancierten, heterodynen Mischern für THz Fokalebenenanordnung mit Auflösungen über $10^7$. Ziel war der Entwurf eines integrierten, balancierenden Supraleiter-Isolator-Supraleiter-Mischer (SIS) und eines integrierten 180 ZF-Hybriden Koppler für das CCAT Heterodyne Array Instrument, CHAI am Cerro Chajnantor Atacama Telescope (CCAT) Observatorium.
Der symmetrische SIS-Mischer soll von 800 bis 1100 GHz betrieben werden. Sein Entwurf für den HF-Teil beinhaltet einen planaren 180°-Hybridringkoppler, zwei separate Slot Line-Antennen, zwei separate Slot Line zu CPW-Übergänge auf Basis von NbTiN-Schaltungen. Diese Bauelemente werden gemeinsam auf einem 6 $\mu$m dicken Siliziumsubstrat integriert.
Für den ZF-Teil des Mischers wurden zwei verschiedene Konfigurationen eines supraleitenden, integrierten 180° IF-Hybridkopplers entwickelt. Mit ihnen lassen sich die beiden erzeugten ZF-Ausgänge je nach Wahl des Eingangsports des Hybride-Kopplers entweder am a- oder b-Port kombinieren. Um die Größe der IF-Hybridkoppler auf $0.5 \times 2.2\ \mu m^2$ zu minimieren, basieren diese auf planaren, konzentrierten Schaltkreiselemente.
Die Entwürfe für den ZF-Teil wurden für 500 $\mu$m und 9 $\mu$m Siliziumsubstrate simuliert. Das letztere wurde untersucht, um es zu einem späteren Zeitpunkt direkt mit dem HF-Teil des Mischers auf einem Substrat zu fabrizieren. Nach Herstellung der Lithographie Maske und anschließender Mikrofertigung, wurde der Nb-basierte ZF-Hybrid auf einem 500 $\mu$m Siliziumsubstrat mit dem Vector Network Analyzer in flüssigem Helium getestet.
Die Messergebnisse wurden analysiert und mit der Simulation des ZF-Hybridkopplers mit implementierten supraleitenden Nb verglichen. Diese Entwicklungen und Designs können für zukünftige Empfänger des CCAT-Prime-Observatoriums verwendet werden. Da das ursprünglich geplante CCAT-Beobachtungsprojekt mangels finanzieller Mittel eingestellt wurde, konnten keine weiteren Untersuchungen oder Weiterentwick-

lungen bezüglich des 800-1100 GHz-Designs erfolgen.
Neuer Schwerpunkt meiner Arbeit wurde die Entwicklung von integrierten 1,9 THz symmetrischen Hot Electron Bolometer (HEB) Mischern. Diese ist relevant für den 1,9 THz Focal-Plane-Array-Empfänger, der auf dem Flugzeug Stratospheric Observatory for the Far Infrared (SOFIA) eingesetzt wird. Für den Betrieb des Empfängers wird ein lokaler Oszillator (LO) benötigt. Die LO-Leistungsaufnahme des Empfängers begrenzt derzeit seine nutzbare HF-Bandbreite. Der benötigte Leistungsverbrauch könnte durch den Einsatz von integrierten balancierenden Mischern um den Faktor fünf reduziert werden. Die Mischer basieren auf supraleitenden Niobnitrit (NbN) Hot Electron Bolometern. Die Verdrahtung der Mischer besteht aus Gold. Die Entwicklung umfasste Design, Mikro-Nanofabrikation, DC und kryogenische Hochfrequenzmessungen. Alle entworfenen, planaren Elemente bestehen aus einem ein-Oktaven breitbandigen 180° HF Hybrid-Ringkoppler, zwei Slot Line-Antennen, zwei Slot Line zu CPW-Übergängen, zwei oder vier 120Ω HEB-Brücken, zwei Tiefpass-Filters (LPFs) und zwei DC/ZF-Sperrkondensatoren, die auf einem 3 $\mu$m langem Siliziumsubstrat integriert wurden. Sie wurden mit Hilfe der kommerziellen Software CST-Suite simuliert.
Zusätzlich wurde ein weiterer integrierter 1,9 THz HEB-Mischer entwickelt, um die beiden separaten ZF-Ausgänge auf einer Seite des 3 $\mu$m langen Siliziumsubstrats unter Verwendung einer CPW-CPW-Weiche zu vereinen. Die Mikro-Nanofertigung der 1,9 THz symmetrischen Mischer erfolgte im unserem Institut unter Verwendung von Elektronenstrahl- und Fotolithographie-Techniken.
Fast alle HEB-Brücken besitzen während DC Messungen überwiegend ähnliche Widerstände im normalleitenden Zustand und Übergangstemperaturen. Der mittlere Widerstand in einen verfügbaren Wafer für die Messungen, war etwa 17% zu niedrig und die Übergangstemperatur lag bei 7,9 K, welcher im Vergleich bei unseren hochmodernen Einpixel-Mischern 8,5 K beträgt.
Die beiden bearbeiteten 1,9 THz symmetrischen Hohlleiterblöcke zum Testen der Mischer wurden in der feinmechanischen Werkstatt unseres Instituts hergestellt.
Ich habe die Transmission der Blöcke mit einem THz Time Domain Spektrometer gemessen und gezeigt, dass pro mm Hohlleiterlänge bei einen geteilten Wellenleiterblock aus der sauerstofffreien Kupfer-Telluriumlegierung (CuTe) ca. 2,4 dB Verlust bei Raumtemperatur vorliegt. Bei den kryogenen HF-Messungen zeigte sich eine sehr ähnliche LO-Leistungskopplung für beide Mischer in der balancierten Vorrichtung, von beiden Eingangsports. Durch die Verwendung eines hausintern entwickelten Quantenkaskadenlasers (QCL) als LO und einer stark abgeschwächten Virginia Diode Multiplikator-Kette (VDI) als Signalquelle habe ich ein balanciertes Mischerverhalten

nachgewiesen und damit das Design validiert. Die Signalunterdrückung bis zu 38 dB wurde durch Umkehrung der Vorspannung an einem der Mischer in der balancierenden Vorrichtung gezeigt, die eine 180° Phasenänderung auf die ZF eines der Mischer hinzufügt.

# Contents

**1 Introduction** **1**
1.1 Astronomical motivations . . . . . 1
1.2 Earth atmosphere and observatories . . . . . 3
1.3 Heterodyne focal plane array receivers . . . . . 5
1.4 Sensitive THz detectors . . . . . 7
1.5 Thesis outlook . . . . . 9

**2 Physics of the Hot Electron Bolometer (HEB) and cryogenic THz material properties** **11**
2.1 Bolometers . . . . . 11
2.2 Superconducting Hot Electron Bolometers . . . . . 13
2.2.1 HEB bridge . . . . . 13
2.3 HEBs as mixing elements . . . . . 15
2.4 Receiver sensitivity . . . . . 19
2.5 Material selection for THz circuits . . . . . 21
2.5.1 Normal metals, Gold . . . . . 21
2.5.2 Superconductors, NbTiN . . . . . 24

**3 Design of THz balanced mixers fully integrated on-chip** **29**
3.1 Balanced mixers . . . . . 29
3.2 RF circuitry fully on chip . . . . . 31
3.2.1 Integrated balanced mixers based on 90° and 180° RF hybrids . 31
3.2.2 A THz 180° hybrid-ring coupler . . . . . 34
3.3 Planar tapered antennas . . . . . 42
3.3.1 Slotline to CPW transitions . . . . . 45
3.4 Integration of hybrid-ring coupler with transition and antenna on silicon at 800-1100 GHz . . . . . 46
3.5 Non-crossover 1.9 THz Integrated Balanced HEB (IB-HEB) mixers . . 52

3.5.1 DC/IF blocking capacitors . . . 56
3.5.2 CPW based Low Pass Filter (LPF) . . . 57
3.5.3 Integration of the IF blocking capacitor and the RF-LPF with a HEB bridge . . . 59
3.5.4 Non-crossover integrated 1.9 THz balanced HEB with 2 HEBs . 61
3.5.5 Non-crossover integrated 1.9 THz balanced mixers with 4 HEBs 63
3.6 Crossover integrated 1.9 THz balanced HEBs . . . 66
3.7 IF circuitry . . . 74
3.7.1 IF Circuitry for the non-crossover RF circuit . . . 74
3.7.2 IF circuitry for the crossover RF circuit . . . 77

**4 Fabrication of the 1.9 THz 180° integrated balanced HEB mixers 81**
4.1 Design of a lithography mask . . . 81
4.2 Device micro-nanofabrication . . . 83
4.3 1.9 THz waveguide balanced mixer blocks . . . 87

**5 Terahertz Time Domain Spectroscopy (TTDS) to study machined waveguide blocks 91**
5.1 Introduction . . . 91
5.2 Direct TTDS measurements . . . 93
5.3 90° angle TTDS measurements . . . 95

**6 Measurements of the fabricated 1.9 THz balanced HEB mixers 99**
6.1 DC characterizations . . . 99
6.2 Heterodyne measurements . . . 108
6.2.1 IF LNA noise measurements . . . 114
6.3 Balanced response characterization . . . 115

**7 Integrated superconducting IF circuitry for THz mixers 121**
7.1 A 180° lumped element IF hybrids . . . 122
7.1.1 Design of an integrated superconducting 4-12 GHz 180° IF hybrid 125
7.1.2 Fabrication of the 180° IF hybrid device . . . 136
7.2 Test fixture block . . . 139
7.2.1 Measurement of the 180° IF hybrid device . . . 140

**8 Summary and conclusion 145**

**Bibliography 151**

# Chapter 1

# Introduction

## 1.1 Astronomical motivations

The life cycle of the interstellar medium (ISM) plays an important role in understanding how a star forms and a galaxy evolves. The ISM, besides its influence on the formation of new stars, is also affected by the feedback of recently formed stars [1]. In general, astronomers rely on the observations of spectral lines which are emitted by molecules and atoms to study the physical conditions of the ISM and the molecular clouds that will end up forming stars. Up to now, over 100 interstellar molecules have been identified from the simplest diatomic species to long chains like [1]Cyanopolyyne $HC_{11}N$ [2]. As an example of the study of the ISM properties via spectral line observations, we can consider the case of high-mass stars. Massive stars (with masses above 10 solar masses) emit ultraviolet photons that interact with their surroundings ionizing, dissociating and heating the nearby interstellar gas [3]. These interactions produce the so-called photon-dominated regions (PDR's) where the physical conditions of the surrounding ISM are dominated by the UV radiation emitted from these stars. In PDR's a number of spectral lines from ions, atoms and small molecules dominate the spectrum at infrared and (sub)millieter wavelengths [4].
Understanding the properties of the ISM and the molecular clouds where most stars form through spectral line observations, requires to characterize how the energy is absorbed and radiated back. Molecular clouds cool themselves by radiating energy via dust grains and via spectral line transitions of molecules and atoms. At the densities of the molecular clouds, the abundant $H_I$, $H_2$ and helium particles can collide with the molecules, atoms and dust grains to excite internal degrees of freedom. These

[1]http://www.astro.uni-koeln.de/cdms

excitations decay by emitting photons at different energies producing line radiation. As an example, one of the most dominant cooling molecules is CO. After collision of CO with abundant hydrogen and helium, the relaxation of the excited CO molecule results in the emission of a photon in the infrared and (sub)millimeter regimes. Line radiation between low-energy rotational levels of CO occur at frequencies of a few GHz, e.g. the J:(1-0) transition happens at 2.6 mm (115 GHz). In the heated gas nearby young massive stars (e.g. PDR's), the high energy levels of CO can get populated with gas kinetic temperatures of 4000 K. At the high temperatures, higher rotational CO transitions occur, e.g. the CO J:(7-6) emits at 806.7 GHz [5].

Another source of cooling are the atomic fine structure transitions. Some of the most important coolants in the submillimeter and far-infrared regimes are the fine structure lines of [OI], [CI] and [CII]. The square brackets denote forbidden transitions [2]. The atomic oxygen in its neutral form OI exists in large regions of the ISM. Emission from $^3P_1$ to $^3P_2$ levels of [OI] is at 63.18 $\mu$m (4.7 THz) and from $^3P_0$ to $^3P_1$ is at 146 $\mu$m (2.05 THz). Carbon which has an elemental abundance comparable to oxygen also has fine-structure cooling. In [CI] the transition from $^3P_1$ to $^3P_0$ is at 609 $\mu$m (492 GHz) and $^3P_2$ to $^3P_1$ is at 370 $\mu$m (810.8 GHz). The atomic carbon is ionized by ultraviolet radiation which results in $C^+$, which is observed in the transition of [CII]. The $C^+$ ion has only one p-electron of which the ground state is split into two quantized levels with spin-orbit interaction. The excitations to the upper fine-structure lines occur mostly due to the interactions with the hydrogen atoms. For [CII] the emitted fine structure line from highest energy level of P, $^2P_{3/2}$ to $^2P_{1/2}$ is at 158 $\mu$m (1.898 THz).

In addition to molecules and atoms, dust is another important component of the ISM that contributes to the cooling and heating processes. Dust radiation is commonly observed as a continuum radiation at infrared and (sub)millimeter wavelengths [2], [6].

In summary, characterizing the physical processes that regulate the ISM, requires an understanding of the heating and cooling mechanisms that can be investigated by observing a number of spectral line transitions. In particular, those of the main cooling agents like atomic oxygen and carbon, and their ionized species, which are among the most abundant species in the Universe. Most of the cooling fine-structure lines occur in the far-infrared and submillimeter regimes. Therefore, instrumentation covering this range of the electromagnetic spectrum is necessary to observe and characterize the main processes that dominate the properties of the ISM.

[2]Based on electric-dipole selection rules in quantum mechanics all downward transitions are forbidden and that is possible only for slower magnetic dipole interactions.

## 1.2 Earth atmosphere and observatories

The water vapor molecules of earth's atmosphere absorb most of the incoming radiations at the THz frequency range. There are different approaches to overcome the atmospheric transmission like building ground based observatories at high altitudes, use airborne or space satellite observatories. Despite the complexity, the Herschel observatory with on board the heterodyne instrument for the far-infrared (HIFI) receiver has been launched into space in 2009 which it was one of the examples of space satellite observatories. HIFI consisted of a set of 7 heterodyne receivers covering 480-1250 GHz (SIS mixers) and 1410-1910 GHz (HEB mixers). Because it was a space project, the telescope had limited collecting area with a 3.5 m diameter antenna [7]. In addition, it had a life time limitation because of using liquid helium as a cooling agent. In 2013 Herschel ran out of liquid helium.

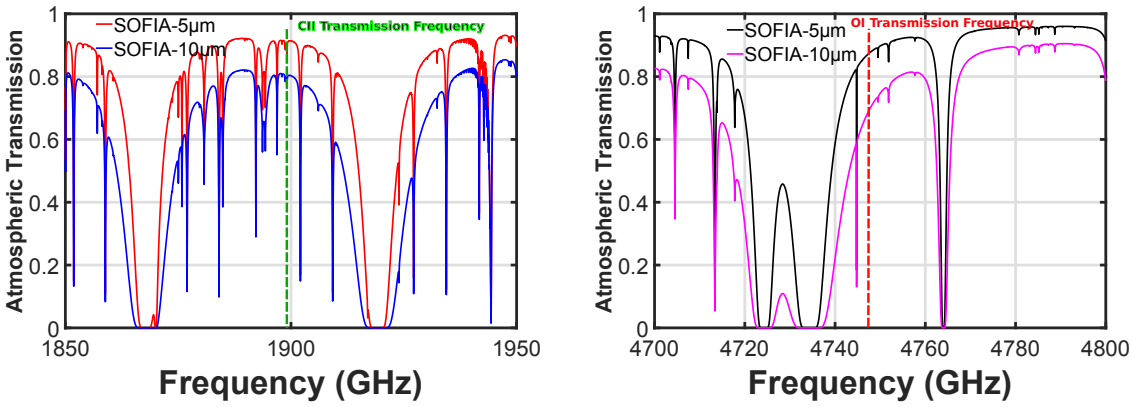


Figure 1.1: The SOFIA atmospheric transmission calculated for two different PWV (Precipitable Water Vapor) conditions [8], Left: Around 1.9 THz where the green line indicates [CII] transmission frequency, Right: Around 4.7 THz where the red line indicates [OI] transmission frequency.

The Stratospheric Observatory for Infrared Astronomy (SOFIA) is the only operational airborne observatory in the THz regime. This is an 80/20 joint project of the National Aeronautics and Space Administration (NASA) and the Deutsche Zentrum für Luft- und Raumfahrt (DLR). In figure 1.1, the atmospheric transmission for the SOFIA airborne observatory at 1.9 THz and 4.7 THz is depicted where any ground base observatory is almost blind. The German REceiver for Astronomy at THz frequencies (GREAT) was the first version of the heterodyne receiver on the board. It had a single pixel HEB detectors covering frequency windows between 1250-2700 GHz. It is upgraded to the focal plane array receivers (upGREAT) with two channels of single

ended Hot Electron Bolometer (HEB) mixers working at 1.9-2.5 THz with 14 pixels (low frequency array, LFA), 4.745 THz with 7 pixels (high frequency array, HFA).
As an example for a ground based observatory, Atacama Large Millimeter/submillimeter Array (ALMA) must be mentioned. It is located at the 5000 meter high Chajnantor Plateau in Chile. However, the telescope and other facilities can only operate at the shortest wavelengths at air conditions with very low water vapor. Another example of the high altitude telescopes is NANTEN 2 which operates in a collaboration between institutes in Germany (Kölner Observatorium für Submillimeter Astronomie (KOSMA), Universität zu Köln, Argelander-Institut Universität Bonn), Japan (Nagoya and Osaka University), South Korea (Seoul National University), Switzerland(ETH Zürich), University of New South Wales (UNSW), and Chile (Universidad de Chile). Since 2004 it has one of the very few heterodyne array receivers SMART (Sub-millimeter Array Receiver for two frequencies) located in Pampa La Bola in northern Chile at 4900 meter close to APEX and ALMA with 8 pixels in 450-490 GHz and in 800-880 GHz bands.

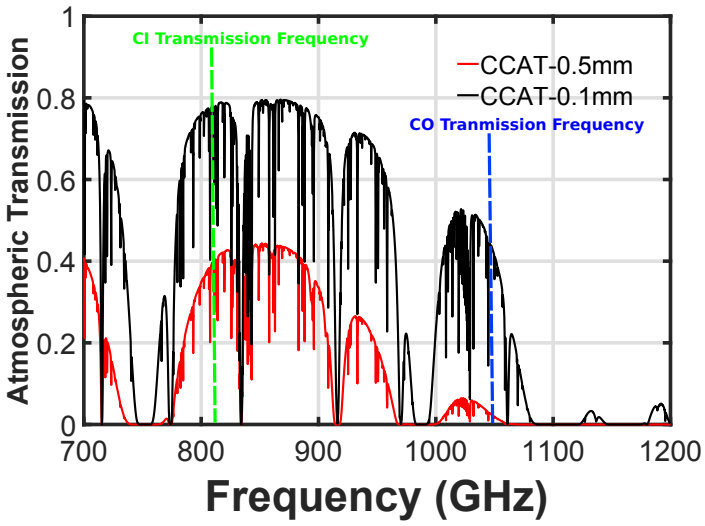


Figure 1.2: Calculated atmosphere transmission for the CCAT observatory site under the two different PWV (Precipitable Water Vapor) conditions as 0.5 mm (typical weather) and 0.1 mm (good weather) [8]. The green and blue lines indicate [CI] and [CO] transmission frequencies, respectively.

The CCAT-prime will be a new observatory located at 600 meters higher than Chajnantor Plateau, at 5600 m. It lies above the atmospheric layer with water vapors which absorbs most of the millimeter and submillimeter radiations, see figure 1.2. This will be a 6 meter off-axis submillimeter telescope, called CCAT-p, which is the path finder

for a future 25 meter telescope comparable to the previously planned CCAT telescope. CCAT-p brings the possibility to do large scale mapping of the atomic fine structure lines in the sub-millimeter wavelengths and lower THz frequencies, e.g. [CI]-lines as well as the mid-j CO lines. Cologne will build a heterodyne focal plane array receiver named CHAI (CCAT-p Heterodyne Array Instrument). It will have a 2×64 pixel heterodyne receiver at the 460 GHz and 800 GHz bands. CCAT-p, thanks to observation of [CI] will be an important complement to the observation of ionized carbon [CII] by the SOFIA observatory.

## 1.3 Heterodyne focal plane array receivers

Observations at the THz frequencies could be done by direct (low to mid-resolution) detectors or heterodyne spectrometers (high resolution, $R > 10^7$), respectively. Here $R = \nu/\Delta\nu$ is the resolving power of an observed spectrum. High resolution spectroscopy is required to resolve the profile of the observed spectral lines, and study the kinematics of the gas in extended, resolved source in great detail [9]. For this type of spectrometer, coherent receivers using heterodyne technique are used. In figure 1.3 the heterodyne measurement technique is depicted. Incoming radiation (RF signal) is received by a telescope and coupled to the receiver using Gaussian optics. Then it is combined with a relatively stronger monochromatic radiation (LO signal), with a slightly different frequency, by an optical beam combiner. There are two approaches to combine. A diplexer has the advantage of transmitting almost the total LO signal and the total RF signal, whereas a beam splitter with RF signal transmission A, has an LO reflection (which is the part of the LO signal that is used) of (1-A) if the beamsplitter is lossless. So striving for e.g. a transmission of 90% immediately means a LO-reflection of 10%. The remaining 90% of the LO power will not be used. Unfortunately a diplexer is considerably more complex to build and operate.
Signals are combined, in a highly non-linear element (mixer) and generates a signal in the gigahertz frequency range (IF signal), because in that frequency range low noise amplifiers and sensitive spectrometers are commercially available. Subsequently, the IF signal is amplified by a cryogenic low noise amplifier (LNA) and is ready for the IF spectroscopy outside the dewar. In the heterodyne technique the information of amplitude and phase is preserved. The sensitivity of the heterodyne based receivers is expressed in noise temperature. In theory the minimum achievable (double side band) noise temperature in the heterodyne system can not be lower than the quantum value of $(h\nu/\mathrm{k}_B)$ which for 1.9 THz is about 91.2 K. The $h$, $\mathrm{k}_B$ terms stand for Planck and

Boltzmann constants, respectively. Depending on the frequency of operation and the mixing element used, the best noise temperatures of present heterodyne receivers vary between 3-10 times higher the quantum noise limit. For example the average value of the noise temperature in the single ended HEB based mixers of upGREAT is about 1000 K [10]. Generally, the reason for high resolution of the heterodyne receivers is that the spectroscopy is done after the down conversion by the IF backend which multiplies the resolution (R) with a factor $f_{Signal}/f_{IF}$. As an example for a 1.9 THz heterodyne receiver with and IF band center frequency of 2 GHz, this factor is about 950. If one includes also a spectrum channel-count 64 K [11], resolution of $10^6$ is easily achievable.

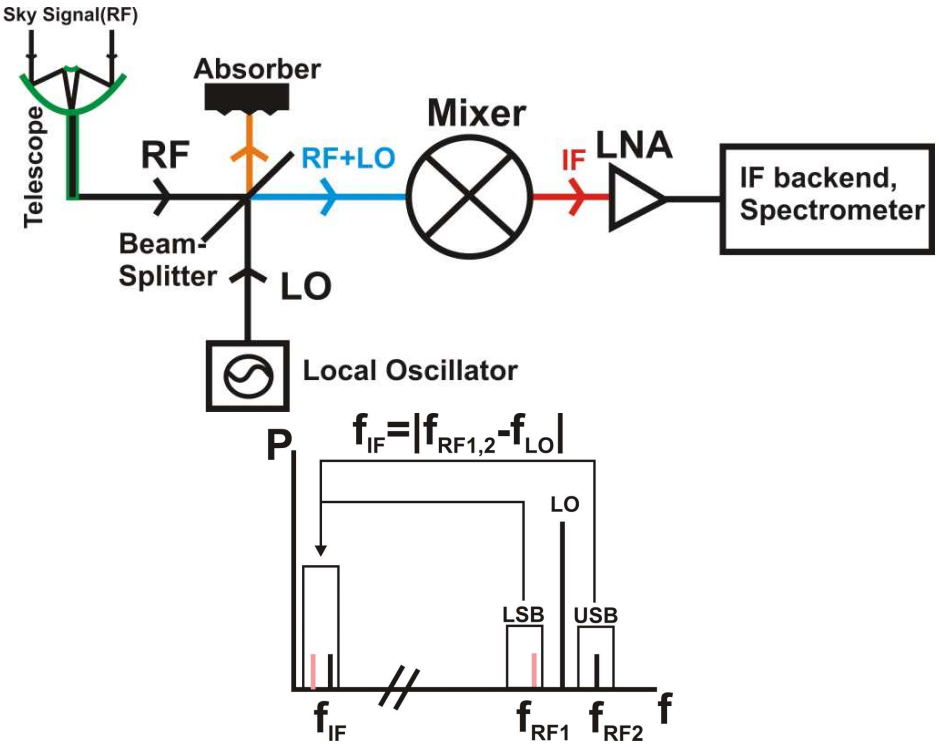


Figure 1.3: The top shows the schematic view of a double side band heterodyne receiver with a single ended mixer and a beam splitter as RF and LO signal-combiner. There is also an absorber to receive the transmitted LO and reflected RF signals. The bottom image shows the down conversion scheme. The upper (USB) and lower (LSB) side bands of the RF signal are multiplied with the strong LO signal in the middle of them to the intermediate frequency (IF).

Multi-pixel arrays of heterodyne mixers are a solution for large scale mapping of extended sources. This is achieved by using focal plane array receivers which need less observation time for achieving a given sensitivity. The observation time to obtain a certain sensitivity is proportionally related to the square of the receiver temperature

and inverse of the number of feeds in a multi-beam system, provided that the pixels in a multi-beam system a noise temperature as similar as possible to a single pixel system [12]. The first supra-THz heterodyne array receiver (upGREAT) is built for the SOFIA observatory with resolution above $10^7$ [13] [9]. upGREAT is presently the only existing operational focal plane array receiver for the 1.9 and 4.7 THz frequency channels based on waveguide mixers with feedhorn antennas. The sky and LO signals are coupled to the two 7 pixel HEB mixers with beam splitter wire grids or Mylar foils. In order to be able to have more pixels by using the total LO power without reducing the IF bandwidth, I have worked on the development of 1.9 THz balanced HEB mixers. In a balanced configuration the LO and RF input ports are separated inside the mixer, so there is no need for any beam splitter or diplexer. This configuration simplifies making focal plane arrays especially for many pixels at lower (CCAT-p) or higher (new upGREAT) frequencies.

## 1.4 Sensitive THz detectors

Up to 700 GHz the Superconducting Insulator Superconductor (SIS) mixers are the most sensitive heterodyne detectors, with a sensitivity close to the quantum noise limit of $h\nu/\mathrm{k}_B$ [14], [15]. A SIS junction is a sandwich of two superconductors with a very thin ~1 nm insulating layer between them. Charge carriers both Cooper pairs and quasiparticles can tunnel through the barrier. A typical junction size is about $1\mu\mathrm{m}^2$. The most commonly used SIS mixers are based on $\mathrm{Nb/Al_3O_2/Nb}$ junctions. The $T_C$ of Nb is about 9.2 K which gives the gap frequency around 700 GHz. In theory, as can be understood from the semiconductor model of the superconductor [16], the gap voltage of the SIS junction is proportional to the sum of the gap parameters of the superconductors of its electrodes, $V_{gap} = (\Delta_1 + \Delta_2)/e$, which is around 2.7 mV for a SIS with 2 Nb electrodes. Since the SIS junction can be used as heterodyne mixer to 2 times the frequency given by $f_{gap} = 2(e/h)V_{gap}$, a Nb based junction can be used as a mixer to about 1.4 THz.

The performance of a superconducting material is related to frequency as is expressed in the gap frequency ($f_{gap}$) of the material. The $f_{gap}$ is related to critical temperature ($T_C$) of a superconductor with $f_{gap} = 3.5T_C\mathrm{k}_B/h$, according to the BCS [17] theory. At the gap frequency the energy of the incident photons is large enough to break the Cooper pairs in the superconductor. This energy equals $hf_{gap} = 2\Delta/e$, with $\Delta$ the superconducting gap parameter of the superconductor. Accordingly for frequencies higher than $f_{gap}$ the material looses its superconductive properties and becomes

dissipative as is expressed in the frequency-dependent surface impedance of superconducting thin film, see Section 2.5.

In practice, SIS mixers can only reach the quantum noise limit if the efficiency of photon coupling to the tunnel junction is high enough. Therefore, there is a need of proper antennas (coupling the signal on the mixer device) and also impedance matching of the combination of junction capacitance with inductive tuning circuit to compensate the parallel-plate capacitance of junction to the rest of mixer circuitry. However, at high frequencies making such a tuning circuit is challenging. It is due to the inverse relation of capacitance impedance with frequency ($Z_C = 1/j\omega C$) and the loss of superconductors used for tuning inductors that increases drastically with frequency, once above the gap. One approach to push the operation frequency of the SIS mixers is to increase the gap frequency of a superconductor to detect signals with higher energies (higher frequencies) [18]. This can be achieved by adding higher $T_C$ superconductors like NbTiN with $T_C$ about 14 K instead of Nb transmission lines. If Nb junction electrodes are used, NbTiN tuning needs to be implemented with the use of an Au relaxation layer to prevent heating due to Andreev reflection [19].

For frequencies above 1 THz, the superconducting Hot Electron Bolometers (HEBs) are attractive candidates for sensitive THz detectors. Their sensitivity is independent of the radiation frequency for a wide frequency range [20], above the gap frequency of the HEB. A HEB consists of a superconducting thin films about 5 nm thick, with a reduced $T_C$. In such a film, conduction electrons build a 2D electron gas that has a thermal response time in the GHz range. This is fast enough to apply them as a mixer with a GHz IF bandwidth. HEB mixers have some advantages over SIS mixers most notably they are not limited to a maximum frequency by the energy gap of the superconductors (NbTiN, NbN), they require a relatively low LO power 20-1000 nW that does not increase with frequency and they have no need for an external magnetic field to suppress Cooper pairs tunneling. The RF circuit is simplified because the RF impedance is frequency independent and resistive for $f_s > 2 \triangle (T)/h$ and the thermal response of HEB is too slow to follow the RF so in contrast to e.g. SIS mixers, no harmonics of LO and RF will have to be taken into account [21]. However, compared to SIS mixers HEB based mixers suffer from a narrower IF bandwidth limited to e.g. 0.5-3.5 GHz for a NbN HEB on a Si substrate. This value for SIS based mixers exceeds to more than 18 GHz (even though IF components like LNAs, IF wilkinson/180°hybrid for balanced mixers cannot always cover the whole band). Recently, [22] has shown the significant IF bandwidth improve up to 7 GHz without noticeable change in receiver noise. This has been achieved by employing GaN buffer layer to a NbN HEB bridge

and applied to the 1.3 THz balanced waveguide mixer. The recent $MgB_2$ HEB is a promising candidate for future THz mixers with high IF bandwidth, high sensitivity and high operation temperature. For example in [23], the measured 1.6 THz $MgB_2$ HEB shows a noise temperature of about 1600 K at 20 K operating temperature with about 11 GHz IF noise bandwidth. Up to now, this kind of detectors need much more LO power to get pumped than the present upGREAT mixers.

## 1.5 Thesis outlook

This thesis covers the physics of Hot Electron Bolometers (HEBs) and using them as mixing elements in Chapter 2. The receiver sensitivity is also described. At the end of this chapter, I have calculated the surface impedance versus frequency for the normal metal Au and the superconducting NbTiN at cryogenic temperatures and high frequencies. Chapter 3 contains the motivation for making balanced integrated THz mixers with emphasizing the development of 800-1100 GHz integrated 180°hybrid-ring coupler. The complete design of 1.9 THz balanced HEB mixers integrated on 3 $\mu$m thick silicon substrates is described in details. In Chapter 4, the fabrication of the 1.9 THz balanced HEB mixers and the waveguide balanced blocks are reported. I have studied the manufactured balanced blocks along existing upGREAT 1.9 THz horns with using the Terahertz Time Domain Spectroscopy (TTDS) which is reported in Chapter 5. The DC characterization of the fabricated 1.9 THz balanced HEBs in addition to the heterodyne RF balanced measurements can be found in Chapter 6. The development of superconducting IF circuitry for the THz mixers is presented also in Chapter 7. The thesis is concluded in the Chapter 8 with emphasizing challenges and future works.

# Chapter 2

# Physics of the Hot Electron Bolometer (HEB) and cryogenic THz material properties

In this chapter, the physics behind the Hot Electron Bolometers (HEB) which are employed as mixing devices in the development of my balanced 1.9 THz mixers is discussed. Additionally, the material selection for wiring the THz mixers and implementing the calculated surface impedances of the 200 nm thick Au and 350 nm thick superconducting NbTiN at the cryogenic-high frequency situation is reported.

## 2.1 Bolometers

In general a bolometer is a thermal power detector consisting of an absorbing element with the heat capacity $C$, to convert the incident radiation into an increased temperature, a heat sink at temperature $T_S$ and a thermal conductance $G$ to connect the absorbing element to the heat sink [24], see figure 2.1. If incident radiation with power $P$ hits the absorber with the temperature $T_B$, it increases with the time rate of $dT_B/dt = P/C$. The $T_B$ reaches to the limiting value $T_B = T_S + P/G$ with the thermal constant $\tau = C/G$. At the non-presence of the incident radiation, $T_B$ relaxes back to $T_S$ with the same $\tau$. These thermal detectors give a response to periodic signals at a frequency of $w \approx 1/\tau$.
Bolometers use an electrical resistance as thermometer for measuring the temperature of the radiation absorber. For a high sensitivity and a large RF bandwidth the absorber should have a low heat capacity and a large absorptivity over the wide frequency

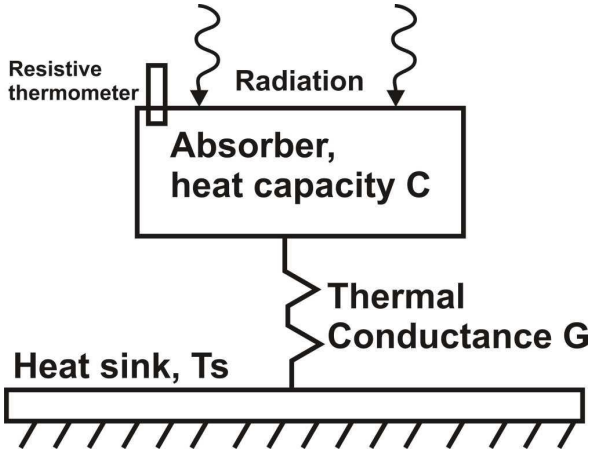


Figure 2.1: Schematic of a thermal detector when incoming radiation are incident on the absorber.

range. In addition, the heat sink substrate should have a low heat capacity and a large thermal conductivity. The linked thermometer to either the absorber or the substrate also has a low heat capacity, low electrical noise and its electrical resistance is a steep function of temperature. The thermal link has a low heat capacity and proper thermal conductance. The change in voltage drop per watt of the absorbed signal power is called bolometer's responsivity which should take into account the influence of the electro-thermal feedback [24]

$$S_A = IR\alpha/G_e(1 + iw_S\tau_e), [V/W] \tag{2.1}$$

where $I$ is the biased constant current for the resistive thermometer $R$, $\alpha$ [$K^{-1}$] is characterization parameter for the thermometer $\alpha = R^{-1}(dR/dT)$ at $T = T_0$ [K] (temperature of the bolometer before absorbing a radiation), and the effective heat conductance $G_e = G - I^2R\alpha$ ($I^2R\alpha$ the electro-thermal feedback) which for superconducting bolometers is $G_e > G$ with a positive value of $\alpha$. The measured time constant is $\tau_e = C/G_e$, and the frequency response of the bolometer is determined by $1/\tau_e$. Bolometric detectors for infrared and submillimeter applications are operated at and below liquid helium temperature to obtain very high intrinsic sensitivity. An example is the Transition Edge Sensor (TES) which consists in essence of a superconducting strip of material. The temperature dependence of the resistance of a superconducting film is very steep in the transition from the normal state to the superconducting state and can provide very sensitive thermometers with a small volume. For instance, bolometers using TES are among the most sensitive THz detectors [25].

## 2.2 Superconducting Hot Electron Bolometers

Hot Electron Bolometers (HEBs) belong to the type of square law detectors which give a response to the incident power as a voltage (current) output proportional to the square of the signal amplitude. They can be used as direct detectors or down-converting mixers for the heterodyne systems. Above some relaxation frequency $1/\tau$, the reponsivity of such bolometers decreases, and this is the upper limit of the IF band of the bolometer that is used as a mixer. The responsivity varies depending on the device physics of the bolometer. Like TES, hot electron bolometers also consist of a strip of superconducting material, but contrary to TES this strip of material is also very thin, significantly thinner than the superconducting penetration depth. A state of the art NbN HEB has a thickness of about 5 nm.

### 2.2.1 HEB bridge

The HEB device consists of an about few nanometer thin film superconductor on a substrate and two contact pads as terminals. It is also called a HEB bridge. The term of HEB bridge's length $L_{heb}$ is the distance between two contact pads which is a few hundred nanometers and the width of a HEB bridge $W_{heb}$ is the distance between two edges of a contact pad perpendicular to the length of a HEB which is of the order of a few micrometers. In figure 2.2, the scanning electron microscopy (SEM) image of a HEB bridge with $L_{heb} \sim 200$ nm and $W_{heb} \sim 3$ $\mu$m HEB bridge with a thickness of 4.5-5 nm superconductor NbN thin film on a silicon substrate and two Au contact pads as terminals is depicted.

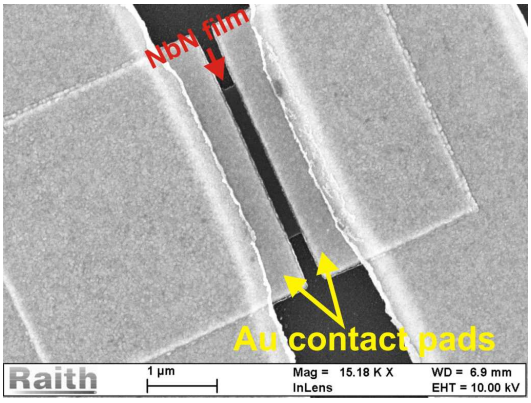


Figure 2.2: Scanning Electron Microscopy (SEM) image of a NbN HEB.

There are two DC measurable curves to characterize a superconducting HEB bridge which are the R-T and the DC-IV curves. The transition temperature $T_c$ and the

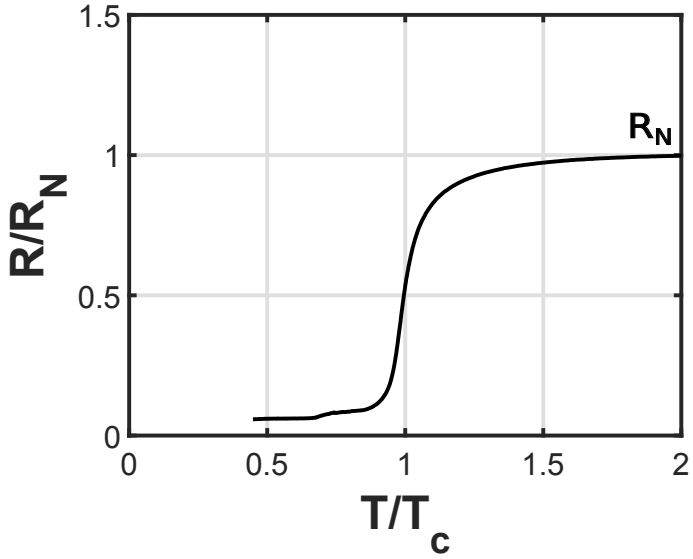


Figure 2.3: R-T normalized to the $R_N$ and $T_c$.

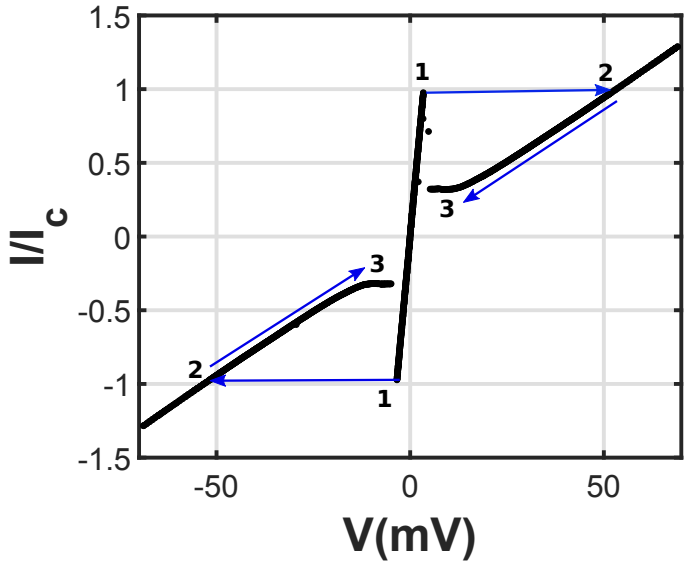


Figure 2.4: DC-IV curve of a HEB bridge without applied radiation. It is normalized at the Y-axis to the current at the critical voltage ($I_c$). Bias supply used in the current mode.

resistance at 20 K $R_N$ are two important parameters which can be achieved from a R-T curve. Higher $T_c$ usually indicates a better film quality and hitting the right $R_N$ is important for the design purpose. As an example, a measured R-T response of a HEB is depicted in figure 2.3, $R_N$ is noted on the plot. From a DC-IV curve one can obtain also $R_N$ and the current $I_c$ at the critical voltage [26]. In [10] it is shown that in one

fabricated batch of HEB devices, a device with a lower current at the critical voltage needs less LO pump power, which is very important especially at THz frequencies where there is a lack of strong LO's to pump a many pixels focal plane array.
As an example, a measured DC-IV curve is depicted in figure 2.4. One can clearly identify two hysteresis features in the curve [26]. The supercurrent flows in the region 1. With increasing the DC current, the current source supplies enough energy to destroy superconductivity (Normal state) $1 \rightarrow 2$. With reducing the current again, the HEB bridge does not recover the superconductivity and stays in the normal state $2 \rightarrow 3$, causing hysteresis. This continues until the trapping current $I_t$ where the the superconductivity is energetically favorable. The same behavior happens at the opposite bias polarity. The hysteresis will be vanished when enough radiation power (LO) maintains a HEB device in a steady normal state [5]. The 1.9 THz is clearly above the gap frequency of the NbN HEB bridge material ($T_c \sim$9 K) and the absorbed radiation break Cooper pairs. The value of $\tau_e$ prohibits RF currents at THz frequencies and the radiation will just change the resistance of the bolometer. The present state of the theory attributes the change of the resistance to a thermal process (heating) [26].

## 2.3 HEBs as mixing elements

The thermodynamic system of a superconducting film on a dielectric can be studied in four coexisting subsystems as cooper pairs, quasiparticles, phonons in the film and phonons in the substrate. A non-equilibrium situation happens when any of these subsystems do not follow the equilibrium distribution function with the same temperature as the other sub-systems. In order to describe the non- equilibrium behavior, solutions to the integral kinetic equations for the space-and time-dependence distribution functions are needed.
The 2-T hot electron model is used generally in case of non-equilibrium superconductors maintained at temperature close to the $Tc$ which the quasiparticles and phonons are defined by thermal, normal-state distribution functions with their own effective temperatures, $Te$ (electron temperature) and $Tp$ (phonon temperature). These temperatures are assumed in a way that each subsystem has a rapid thermalization mechanism. In figure 2.5 the thermalization scheme of the main steps for the hot electron model in depicted. It shows the energy exchange between sub-systems. $\tau_{ep}$ is the electron energy relaxation time via electron-phonon interaction and $\tau_{es}$ is the time of phonon escape into the substrate. $\tau_{ee}$ is the interaction time between the electrons

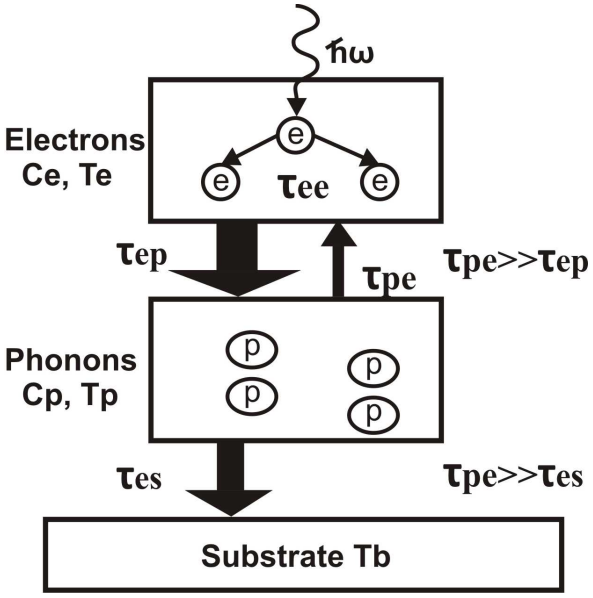


Figure 2.5: Thermalization scheme of the 2-T hot electron model.

which is much shorter than the $\tau_{ep}$ and the $\tau_{es}$. $C_e$ and $C_p$ are the electron and phonon specific heats, respectively. $\tau_{pe}$ is the phonon-electron energy relaxation time. The energy-flow balance is in equilibrium under the condition of

$$\tau_{pe} = \tau_{ep}(C_p/C_e). \tag{2.2}$$

The electron specific heat below $T_C$ shows an exponential temperature dependence which even for small temperature deviations from equilibrium leads to nonlinear equations. However, these equations are simplified at the temperature in the vicinity of $T_C$ where the superconducting energy gap is strongly suppressed. Additionally, the concentration of Cooper pairs is very small, and unpaired electrons are regarded as normal electrons with the ordinary Fermi distribution function. In the normal state, there is a much weaker temperature dependency of the specific heat of electrons, so $C_e$ the electron heat capacity is taken as a constant. Therefore, the general linear equations of the hot electron effect in superconductors can be written as

$$\frac{dT_e}{dt} = -\frac{T_e - T_p}{\tau_{ep}} + \frac{1}{C_e}W(t), \tag{2.3}$$

$$\frac{dT_p}{dt} = \frac{C_e}{C_p}\frac{T_e - T_p}{\tau_{ep}} - \frac{T_p - T_0}{\tau_{es}}, \tag{2.4}$$

where W(t) is the absorbed power by the electron subsystem per unit volume and $T_0$ is the substrate temperature [27]. There are two kinds of energy relaxation mechanisms in HEB devices, relaxation via phonons in the HEB and ultimately via the phonons in the substrate and relaxation via diffusion through the contacts. NbN and NbTiN HEBs have a slow diffusion rate compare to Nb or Al HEBs and the phonon cooling is predominant [28]. The most common phonon-cooled mixers are based on NbN thin films [27]. As an example of the recent phonon-cooled HEBs, NbN based HEBs on silicon substrates are employed as mixing elements in the upGREAT's LFA and HFA focal plane arrays for the SOFIA observatory [10]. The intrinsic IF bandwidth of the mixer is determined by the combination of $\tau_{ep}$ and $\tau_{es}$. The IF bandwidth for the phonon-cooled HEBs can be increased with employing a substrate material with a better match (lattice matched) to the superconducting film, like using MgO bufffer layer on the silicon substrate for the NbN HEB mixers [29]. This would increase $G_e$. Another approach is to decrease the thickness of the bolometer, which influences $C_e$ and $\tau_{ep}$. This has been observed e.g. in [10]. However, NbN thinner than 2.5 nm gets in-homogeneous and loses its superconductivity [30]. The IF bandwidth and the noise temperature of the phonon-cooled HEBs increase with the bias current. Therefore, in order to get an optimum of low noise temperature and a high IF bandwidth, one needs to find the bias regime that results in a compromise between IF bandwidht and noise temperature.

As already mentioned, the noise temperature of the HEB mixers does not increase by increasing the frequency only due to the quantum noise limit [20]. Up to now, there is no any complete theory which can explain the mixing in the HEB mixers [26]. Several approaches by the standard-model [31] [32], the broken-line transition model [33], hot spot-model [34] [35] by several groups have been studied. There is a large discrepancy between experimentally measured noise performance and the much lower noise that is predicted theoretically. The proposed equivalent HEB circuit to describe the mixing process can be shown as figure 2.6. The HEB device is DC biased by the $I_{dc}$ and RF biased by the pumping LO power $P_{LO}$ at $\omega_{LO}$. The amount of absorbed DC and RF power determine the temperature of the HEB and consequently the DC resistance of the device. When a weak RF signal at a frequency $\omega_s$ hit the bolometer, it interferes with the $P_{LO}$. This causes a modulation at the $\omega_{IF}$ of the HEB temperature $\Delta\Theta$. Consequently, it also modulates the HEB resistance $\Delta R$ which becomes proportional to the $\sqrt{P_{LO}P_S}cos(\omega_{IF}t)$. Because the HEB is DC biased with $I_{DC}$, therefore, the DC voltage over the bolometer with $\Delta R$ drives an IF current proportional to the

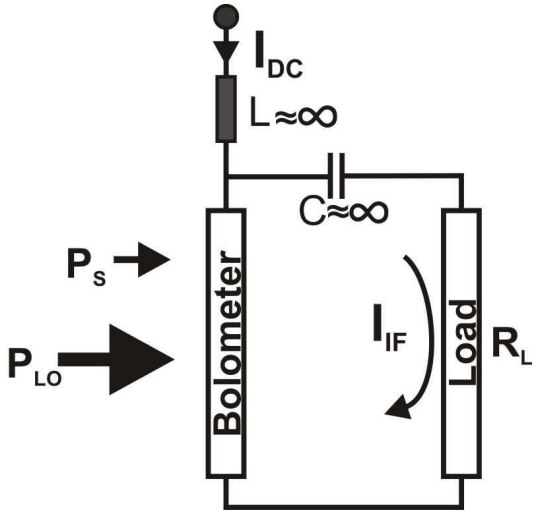


Figure 2.6: Equivalent circuit of a HEB mixer.

$\sqrt{P_{LO}P_S}cos(\omega_{IF}t)$ through the load resistance $R_L$. Since this generated current also has to pass the bolometer, therefore, it contributes to the modulation of the power absorption (electrothermal feedback). In the standard (lumped element) model of the HEB mixers, the conversion gain is proportionally related to the $dR/d\Theta$ (steepness of resistance versus temperature at $T_c$, the critical temperature) where $\Theta$ is the electron temperature ($\approx T_c$), and $G_e$, the thermal conductance between the electrons and the substrate as [32]

$$\text{Conversion gain} \propto (\frac{dR}{d\Theta}^2)\frac{1}{G_e^2}. \tag{2.5}$$

Also the IF bandwidth is

$$\text{IF bandwidth} \propto G_e. \tag{2.6}$$

The noise contribution from the bolometer referred to the mixer input (the output noise divided by the conversion gain) becomes

$$\text{Fluctuation noise} \propto \Theta^2 G_e, \tag{2.7}$$

$$\text{Johnson noise} \propto \frac{\Theta^2 G_e}{dR/d\Theta^2}, \tag{2.8}$$

where fluctuation noise (the main noise mechanism) is because of the existing fundamental fluctuations in the temperature of the bolometer medium. The Johnson noise is the intrinsic thermal noise of the electrons in the bolometer. From the above equations, can be seen that in order to have lower noise, $dR/d\Theta$ should be as large as possible, and $G_e$ and $\Theta$ small. A smaller $G_e$ however, limits the IF bandwidth. Never-

theless, the nature of HEB detectors is complicated and the entities described are not constants, for instance $dR/d\Theta$ depends on bias conditions, temperature, device geometry, and $G_e$ is a complicated function of the temperature and other device details [28]. In addition, the superconducting nature of the HEB, especially the mechanism that creates and changes resistance in a superconductor has not been taken into account in this theoretical description [26].

## 2.4 Receiver sensitivity

The receiver's sensitivity refers to the ability of detecting radiation with the lowest noise contributions. Therefore, the added noise and conversion efficiency of the mixer are important characteristics of a heterodyne receiver. In heterodyne based receivers, the noise temperature ($T_N$) is used to express the system's added noise. Noise powers ($P_N$) are typically expressed in terms of noise temperature $P_N = k_B T_N B$(bandwidth) for radio-astronomy and microwave instrumentation because in this frequency range the (linear) Rayleigh-Jeans limit of the Planck blackbody power spectrum [36] can (approximately) be used. Fundamentally [37] a coherent (meaning detecting amplitude and phase) receiver adds at least one quantum of noise at the input frequency, leading to a minimum noise temperature of $h\nu/k_B$. Generally, the equivalent input noise temperature $T_N$ of a mixer is the measured output power when a 0 K matched load is connected to the input of the mixer divided by the mixer gain. Because there is no achievable 0 K source, therefore the Y-factor method using 2 matched inputs with a significant diffference in temperature is utilized [38]. In practice this factor can be measured by recording the measured power at hot load to the power at cold load

$$Y = \frac{P_{hot}}{P_{cold}} = \frac{(T_{hot} + T_N)GB}{(T_{cold} + T_N)GB}, \tag{2.9}$$

where $T_{hot}$ is about 295 K (ambient temperature) and $T_{cold}$ is about 77 K (liquid Nitrogen temperature).
Subsequently, the equivalent noise temperature $T_N$ relates to the Y-factor as

$$T_N = \frac{T_{hot} - YT_{cold}}{Y - 1}. \tag{2.10}$$

There are also several elements in the chain of a receiver which add noise to the

total receiver noise. The noise budget calculation of the receiver consisting of several cascading elements is given as

$$T_{Receiver} = T_{N1} + \frac{T_{N2}}{G_1} + \frac{T_{N3}}{G_1 G_2} + ..., \tag{2.11}$$

where the $G_n$ and $T_{Nn}$ are the gain and equivalent input noise temperature of the element number n ($n = 1, 2, ...$), respectively [38].
For receivers at THz frequencies the use of the Rayleigh-Jeans approximation introduces a significant error that increases with frequency. The power spectral density (power per unit bandwidth) is not linearly proportional to the physical temperature of the radiation source anymore. In addition, the quantum noise becomes important with increasing frequency, where the ratio $h/k_B$ is equal to 0.048 K per GHz, so at 4.2 K, the $h\nu/k_B$ = 173 K at 1.9 THz. At THz frequencies, instead of using hte Rayleigh-jeans limit, an effective noise temperature instead of physical temperature is introduced [39]. There are two approaches to calculate the effective noise temperature for a thermal source at THz frequencies, one is to use the Planck formula and the other using the Callen and Welton [40] formula

$$T_{Planck} = T[\frac{\frac{h\nu}{k_B T}}{e^{h\nu/k_B T} - 1}], \tag{2.12}$$

$$T_{C\&W} = T[\frac{\frac{h\nu}{k_B T}}{e^{h\nu/k_B T} - 1}] + \frac{h\nu}{2k_B}, \tag{2.13}$$

where $T$ is the physical temperature. The Callen and Welton formula has an extra term $h\nu/2k_B$ compared to the Planck's. Consequently, the Eq.2.10, should be re-written to new equations using the Planck or Callen and Welton temperatures

$$T_{N,Planck/C\&W} = \frac{T_{hot,Planck/C\&W} - YT_{cold,Planck/C\&W}}{Y - 1}. \tag{2.14}$$

The effect of using the Callen and Welton equivalent temperature for the input loads is that in the measured mixer noise temperature the quantum noise is subtracted from the result.

## 2.5 Material selection for THz circuits

An accurate estimate of the propagation constant in the wiring and circuitry of sensitive THz detectors is very important for the design. Dissipation should be avoided whenever possible, and accurate knowledge of the propagation velocity and the characteristic impedance are necessary for a transmission line design. The detectors work at high frequencies and at cryogenic temperatures, and thus the metal thin films used to built up the circuits are in a very specific corner of their parameter space. The conductivity $\sigma$ increases at cryogenic temperatures in metals, so the skin depth decreases. This type of a behavior in metals, is described by the complex surface impedance. It is the absorption and reflection response to the high frequency electromagnetic waves at the surface of conductors. The surface impedance is a quantity that contains information about the penetration of fields into an infinite conducting slab of thickness d. It is important to calculate the surface impedance of the material of choice and implement it into the design to obtain more realistic simulation results. This is done in CST suite [41] by making a tabulated surface impedance which is a table consisting of real and imaginary calculated values of the surface impedance against frequency in the relevant frequency range. After generating the table, CST suite fits the imaginary and real parts of the complex surface impedance to a function of frequency that is subsequently used in the simulations.
Below the gap frequency a superconductor acts like a lossless metal, however the Cooper pairs add an imaginary part to the surface impedance. Above the gap frequency, superconductors are getting lossy and act like normal conductors.
First I talk about the anomalous resistivity in normal metals at the cryogenic-high frequency situation and approximate the surface impedance for the gold which is used in the 1.9 THz balanced HEB mixers. After that, it will cover the calculations for the superconducting NbTiN which is going to be used in the 800-1100 GHz balanced SIS mixers.

### 2.5.1 Normal metals, Gold

For normal metals which in my design case, Gold as a conductor for transmission lines, it is taken into account the effects of finite film thickness and electron mean free path. Calculations for Gold estimate the attenuation, dispersion and characteristic impedance of the striplines as a function of frequency and dielectric thickness. Both radiation and dielectric losses become relatively less important in comparison to conductor losses when the dielectric thickness is reduced. So it is investigated for the

imperfect conductors, lossless dielectric and neglecting radiations.
A normal conductor depending on its operation frequency and temperature can be in three different situations as normal skin effect, anomalous skin effect and extreme anomalous skin effect. Therefore, first, it is important to find out that our conductor with thickness of d stays in which situation. After that, the surface impedance based on that situation is going to be calculated. In [42], it is shown that the normal metal like Copper goes to be in the anomalous limit at lower frequencies at cryogenic temperature compared to Copper at 295 K.
The surface impedance for a sinusoidal electric field $E_x(z,\omega)e^{i\omega t}$ and current density $J_x(z,\omega)e^{i\omega t}$ taking the surfaces of the conductor at the planes $z = 0$ and $z = d$ is defined by

$$Z_s(\omega) = \frac{E_x(0,\omega)}{\int_0^d dz J_x(z,\omega)}, \tag{2.15}$$

with the boundary condition that the magnetic field be zero at $z = d$ as it is a case for stripline with $w >> s$. The real and imaginary parts of $Z_{surface}$ are called surface resistance (contributes to loss) and reactance (contributes to inductance), respectively. The surface impedance for a conductor is evaluated simply by the local equation for the dependence of current density J on the electric field E

$$J = \sigma E, \tag{2.16}$$

where $\sigma$ is the complex conductivity. This local equation is taken into account because the mean free path l for normal electrons is short in comparison to all other dimensions. The surface impedance then can be written [42] by combining the Eq.2.16 and Maxwell's equations

$$Z_s = (i\omega\mu_0/\sigma)^{1/2} coth[(i\omega\mu_0\sigma)^{1/2} d]. \tag{2.17}$$

So in principle, when knowing the DC conductivity and the frequency, the surface impedance is known. For a normal metal the conductivity is a real constant which can be measured in DC. Then the mean free path l is derived from the Drude electron conductivity

$$\sigma = \frac{ne^2}{mv_f} l, \tag{2.18}$$

where n is the number density of electrons, e the electron charge, m is the mass of electron and $v_f$ is the Fermi velocity of electrons in the conductor. In the derivation of the Eq.2.17, it is seen that for the case of infinite conductor thickness, the field amplitudes decay exponentially with the distance into the conductor. The characteristic

decay length for the normal conductor is the classical skin depth

$$\delta_c = (\omega\mu_0\sigma/2)^{-1/2}. \tag{2.19}$$

As can be seen the $\delta_c$ decreases with increasing frequency and increasing conductivity, whereas l increases for increasing conductivity. Above a certain frequency $\delta_c < l$, and this frequency is lower for higher conductivity. At this frequency the local relation between E and J (Eq.2.16) is no longer valid because the E-field changes significantly over the length of a mean free path. At such high frequencies the skin effect is called to be anomalous.

At 4.2 K, this anomalous situation happens even at lower frequencies because the mean free path of the electrons increases with the increasisng conductivity of the normal conductor at lower temperatures. The relation between J and E is changed to the non-local form [43]

$$J(r) = \frac{3\sigma}{4\pi l}\int d^3\rho\rho(\rho.E(r+\rho))\rho^{-4}e^{-\rho/l}, \tag{2.20}$$

with the assumption that the relaxation time $\tau$ is small compared to the inverse frequency, $\omega\tau << 1$. In this case, the calculation of the surface impedance requires an extra boundary condition taking into account the scattering of electrons from the conductor surface. There have been included two simple limits, diffuse scattering and specular reflection. The former one provides better agreement with the experiment shown in [43]. Therefore, only the diffuse scattering is taken into account in the present calculations

$$\begin{aligned} \frac{d^2E_x}{dz^2} &= i\alpha l^{-3}\int_0^d dz^{'}E_x(z^{'})K((z^{'}-z)/l), \\ K(u) &= \int_0^\infty dr[\frac{1}{r}-\frac{1}{r^3}]e^{-|u|\Theta}, \end{aligned} \tag{2.21}$$

where $\alpha = 3/2l^2/\delta_c^2$ [42]. This equation is solved in the limit of infinite d and for a case of extereme anamolous limit $\alpha >> 1$ by Reuter and Sondheimer [44]

$$Z_s = \frac{1}{3^{1/2}\pi^{1/3}}(1+\sqrt{3}i)\frac{\alpha^{2/3}}{\sigma l}. \tag{2.22}$$

Now, it is possible to classify the type of 200 nm thick Au which is used for wiring the 1.9 THz balanced HEB mixer. The conductivity $\sigma$ is measured in DC and at 4.2 K for a 200 nm Au, which is about $7.7\times10^7\ 1/m\Omega$. The density number of electrons

$n$ $5.9 \times 10^{28}$ $1/m^3$ and the Fermi velocity $v_f$ $1.4 \times 10^6$ $m/s$ are taken from literature for bulk Gold [45]. The electron mass is $9.11 \times 10^{-31}$ Kg. The ratio of $\sigma/l$ for each material is a constant value from Eq. 2.18, therefore the calculated value of l is about 65 nm. The calculated normal skin effect of the 200 nm Au at 1.9 THz using Eq.2.19 is about 29 nm. Therefore, the mean free path is about 2.4 times larger than the normal skin depth which is not the local limit ($l < \delta_c$) but also not the extreme anomalous limit $\alpha >> 1$. This case is called the anomalous limit. For the 50 nm Au also stays in the anomalous limit since the thickness of the conductor and the mean free path are still higher than the normal skin depth. As it is clear that the desired Au is in the anomalous limit therefore Eq.2.21 is used for calculating the surface impedance. In [42] and [46] the numerical solution of Eq.2.21 and calculation of the surface impedance based on Eq.2.15 are reported. Here, with using the reported solutions, the complex surface impedance of the 200 nm Au is calculated over the frequency and plotted in figure 2.7. The plot also shows the fit from CST suite to enable to implement the data into the simulations.

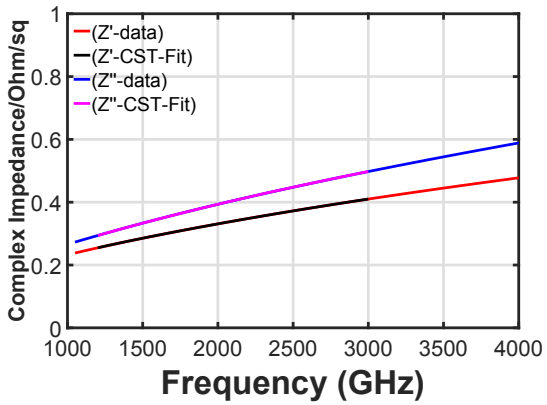


Figure 2.7: Complex impedance over the frequency of the 200 nm Au with the fitting from CST suite. $z^{'}$ and $z^{"}$ stand for the real and imaginary parts of the surface impedance, respectively.

### 2.5.2 Superconductors, NbTiN

The RF surface impedance of a superconductor is influenced by the inertia of the Cooper pairs in the superconductor. The surface reactance results from the incomplete shielding of RF field which allows the superconductor to store RF energy inside of its surface. The decay depth for the electric field in a superconductor at frequencies lower

than energy gap frequency ($2\Delta/\hbar$), is the London penetration depth

$$\lambda_L = (\hbar coth(\Delta/2kT)/\pi\mu_0\Delta\sigma_n)^2, \tag{2.23}$$

which is frequency independent in contrast to the normal skin effect$\delta_c$.
NbTiN is chosen in my design work for wiring the 800-1100 GHz balanced Nb/AlOx/Nb SIS mixers because of its higher frequency gap than for example Nb (700 GHz). Below the energy gap frequency of NbTiN ($\sim$1100 GHz), the surface resistance of the superconductor is orders of magnitude lower than that of a normal metal like Au resulting in a much lower loss. However, the imaginary part of the surface impedance at frequencies the gap frequency increases with $\omega$ like an inductance. Above the energy gap, a superconductor behaves like a normal conductor with a conductivity of $\sigma_n$.
For superconductors Mattis-Bardeen is applied to calculate the complex conductivity which includes the effects caused by the energy gap. Mattis-Bardeen has derived a realistic result of the complex conductivity [47]. In [47] the extreme anomalous limit (penetration of the field is small compared with the coherence length), is used to simplify the complex integral giving $\sigma(\omega)$. A coherence length [43] is

$$\frac{1}{\xi} = \frac{1}{\xi_0} + \frac{1}{l}, \tag{2.24}$$

where $\xi_0$ is the intrinsic coherence length, describing the interaction of paired electrons, and l is the mean free path of unpaired electrons. A complex conductivity for the superconductor state is introduced as $\sigma = \sigma_1 - i\sigma_2$. $\sigma_1$ and $\sigma_2$ are described [47], [48] as

$$\frac{\sigma_1}{\sigma_N} = \frac{2}{\hbar\omega}\int_{\varepsilon_0}^{\infty}[f(E) - f(E+\hbar\omega)]g(E)dE + \frac{1}{\hbar\omega}\int_{\varepsilon_0-\hbar\omega}^{-\varepsilon_0}[1-2f(E+\hbar\omega)]g(E)dE, \tag{2.25}$$

$$\frac{\sigma_2}{\sigma_N} = \frac{1}{\hbar\omega}\int_{\varepsilon_0-\hbar\omega,-\varepsilon_0}^{\varepsilon_0}\frac{[1-2f(E+\hbar\omega)](E^2+\varepsilon_0^2+\hbar\omega E)}{(\varepsilon_0^2-E^2)^{1/2}[(E+\hbar\omega)^2-\varepsilon_0^2]^{1/2}}, \tag{2.26}$$

where $\Delta = \Delta(T)$ is the energy gap parameter, $f(E) = [1+exp(E/kT)]^{-1}$ is the Fermi-Dirac distribution function and $\sigma_N$ is the normal-state conductivity at the critical temperature. In the case of $\sigma_1$, the first integral represents conduction by the thermally excited normal electrons and the second integral refers to the generation of quasi particles by high frequency fields (it is zero for $\hbar\omega < 2\Delta$). The $\sigma_2$ describes the

response of the Cooper pairs. The lower limit in the integral of the $\sigma_2$ becomes $-\Delta$ when $\hbar\omega > 2\Delta$.

Our NbTiN layers however are not in the extreme anomalous limit. The penetration depth calculated from Eq.2.23 is of the order of 300 nm for the normal resistivity $\sigma_n$ of $9 \times 10^5$ $(1/\Omega.\text{m})$ and the $T_c = 14.5$ K that have been measured at DC, assuming that NbTiN behaves like a BCS [16] superconductor. We have not measured the mean free path of our layers, but literature values for layers with comparable reistivity and $T_c$, fabricated in a similar way and on a similar substrate (Si) [49] report a mean free path the order of 5 nm. Consequently $l \ll \lambda_L$, and the NbTiN layer is in the local limit. In addition, with a mean free path of this order, the coherence length is also changed and we take the equation proposed by Pippard Eq.2.24 to determine the coherence length in the NbTiN film, resulting in $\xi \gg \lambda_L$. As remarked by Barends [50] under these conditions the integral in Mattis-Bardeen paper [47] can also be approximated, giving the same equations for $\sigma(\omega)$. Subsequently, the surface impedance is calculated using Eq.2.17 by a comlpex conductivity $\sigma(\omega)$.

The surface impedance versus the frequency is imported as a tabulated impedance as a function of frequency into CST studio where the software fits the imported data for both real and imaginary parts with a lowest possible error. This is shown in figure 2.8, left plot. It is clearly seen that the resistance of the NbTiN $z^{'}$ increases and being like normal resistance at about 1083 GHz (the frequency gap of the NbTiN). The imaginary part $z^{"}$ also increases with increasing the frequency. For the example, the influence of the 350 nm superconducting NbTiN on a circuit (ring-hybrid coupler) is depicted in figure 2.8. This shows a clear drop of the transmission at the frequency where the resistance drastically increases. The simulated S-parameters show how the transmission from ports 1 and 4 to parts 2 and 3 drops at about the frequency of increasing resistance (1080 GHz).

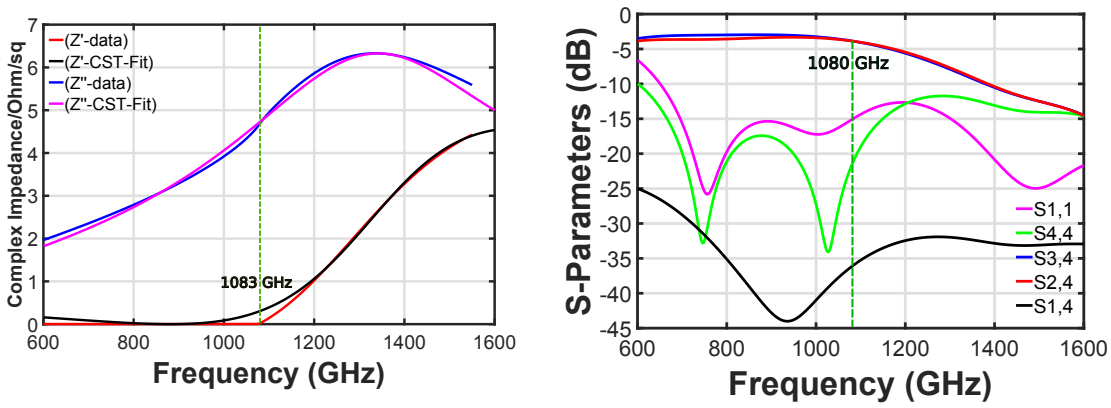


Figure 2.8: Implemented NbTiN material in CST simulations, Left: Fitting the tabulated impedance of NbTiN. The red and blue curves are the real and imaginary parts of calculated impedance. At 1080 GHz the resistance drastically increases. Right: S-parameters of the designed hybrid-ring coupler showing that the transmission drastically drop at the gap frequency of NbTiN.

# Chapter 3

# Design of THz balanced mixers fully integrated on-chip

This chapter reports the designs of integrated THz balanced mixers. First, it covers the motivation of having RF circuitry fully on one substrate. After that, the idea behind choosing a 180 degree hybrid-ring coupler is presented. The design towards developing 800-1100 GHz integrated balanced SIS mixers is reported. The design skills acquired during this first project, I have implemented in the design of integrated 1.9 THz balanced HEB mixers. Additionally, the design of IF circuitry to combine the IF signals of the 1.9 THz balanced output is presented.

## 3.1 Balanced mixers

A balanced mixer has advantages over a single ended type of mixer. Separation of the input ports of the RF and LO signals is one of the main advantages. Consequently, there is no need for a beamsplitter or diplexer for combining the two incoming RF and LO signals, as is the case for a single ended mixer. RF and LO are combined in the RF-hybrid preceeding the mixers. This eases the complexity of building focal plane array receivers. Especially for focal plane arrays with a large number of pixels, an inteferometric optical diplexer, which would combine LO and RF with 100% efficiency, is technically not feasible. A solution using beamsplitters is a possibility, but has the disadvantage of using only a small ($<$10% usually) fraction of the available LO power. Even though there exist some high power (about few milliwatt) quantum cascade lasers at THz frequencies, of which one could afford to throw away 90% of the power, the reported quantum cascade lasers are not broadly tunable (few GHz). In addition, if

one would find a way to make arrays with even more pixels, the problem of the LO power will come up again. In a balanced configuration, two mixers are implemented for one array pixel. Therefore, there is need of two times the pump power per pixel compared to a single ended mixer. However, since LO and RF are combined inside the mixer pixel, and consequently the full available LO power can be incident on the mixer, in general one has about 50% more LO power available, compared to a beamsplitter coupled array of single ended mixers. Balanced mixers also suppress any possible LO noise and spurious signals contribution to the receiver noise, which is an advantage if synthesizer driven solid state LO's are used [51], [52], [53]. In figure 3.1, the schematic of a balanced mixer is depicted. There are two antennas for coupling the incoming RF and LO signals to the chip. The transition part in my design is a crucial element, because of the difference between the transmission line type of the planar waveguide antenna (slotline) and the rest of RF circuitry (coplanar waveguide line (CPW)). The transitions are followed by a 90°/ 180° RF hybrid, which is a 4-port coupler having 2 input and 2 output ports. The two input signals of the hybrid are equally divided between the two output ports with either a 0° or 90°/ 180°. Practical hybrids differ from ideal by signals phase-and amplitude-loss and voltage standing wave ratio (VSWR) [51]. There are two IF/DC blocks implemented in my design to prohibit any DC bias current or down converted IF signal transmission directly between two mixers. The mixers generate IF from incoming RF and LO signals. For radio astronomy, sensitive cryogenic mixers are used, like superconductor-insulator-superconductor (SIS) tunnel junctions, or superconducting hot electron bolometers (HEB). The DC-IV curve of such elements (SIS or HEB) is anti-symmetric, with the same magnitude of conversion and noise for opposite (positive and negative) bias voltages. Therefore by choosing the DC bias of the two mixers that together form a balanced mixer, with opposite bias polarity, one can introduce an additional 180° phase shift to the IF signal of the mixer. Two Low Pass Filters (LPF) are placed at the output of the mixers to avoid any unwanted RF signals at the IF outputs. At the IF side, either a 180° IF hybrid coupler or an IF Wilkinson power combiner can be used. In figure 3.1 the situation with the two mixers biased with the same polarity is shown. Consequently, the IF signal can be measured at the delta port (180° phase difference) of the IF hybrid. At the sigma port (0° phase difference) of the IF hyrbid coupler, the LO noise can be measured. This is expressed mathematically in detail in Subsection 3.2.1. For my measurements in Chapter 6, I have used an external non-integrated warm IF hyrbid coupler. In Chapter 7, the development of a superconducting integrated 180° IF coupler is introduced.

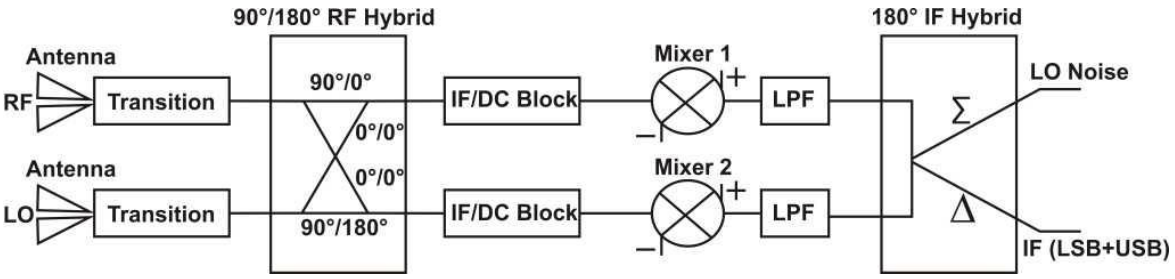


Figure 3.1: Schematic of a balanced mixer using a 90°/ 180° RF hybrid coupler. The IF output port one can choose depending on the bias polarity of the mixing elements. Using an IF Wilkinson coupler instead of an IF hybrid supplies a broadband IF bandwidth, but as a 3 port device can only supply-either LO the noise or the LSB+USB at the output.

## 3.2 RF circuitry fully on chip

To our knowledge the only SIS or HEB THz balanced mixer with its RF circuitry fully integrated on one chip is reported in [52]. This is a balanced SIS mixer with an integrated 90° RF hybrid. There are 2 reported designs in these [54], [53] on balanced HEB mixers at 1.4 THz and 2.7 THz, respectively. However, the 90° RF hybrid is not integrated but is a micro-machined waveguide coupler, fabricated using photolithographic techniques. After the waveguide coupler, two split signals are guided to two separate single ended HEB mixers mounted on the waveguides. One important advantage of a micro-fabricated integrated RF hybrid instead of a micro-machined waveguide is the reproducibility of the hybrid coupler with similar dimensions. This is crucial when building many pixels for a focal plane array receiver. The nano/micro-fabrication has less tolerance, compared to machining RF coupler waveguides. It also reduces the large amount of time needed for fabricating several balanced mixers. In addition assembly tolerances of the chip into the waveguide block do not influence the balance between the 2 mixers if they are on one chip. Additionally, it is really difficult to machine any kind of THz 180° ring shape coupler. To our knowledge there is no report about trying to machine such a structure.

### 3.2.1 Integrated balanced mixers based on 90° and 180° RF hybrids

There are two kinds of balance mixer configurations based on 90° or 180° RF hybrids. In this thesis work, I have designed THz balanced mixers integrated with a planar 180° RF hybrid on one chip. The 180° based balanced mixers have a better and more

broadband LO/RF isolation than mixers based on 90° hybrids, due to the properties of these hybrids. The 180° hybrid also better isolates the two mixers from each other, when they are not totally similar due to the possible fabrication tolerances [51]. I have employed an uniplanar CPW-slotline based 180° hybrid-ring coupler which needs a lower number of microbridges compared to the planar 90° branch line coupler in [52], for details see Subsection 3.2.2. This leads to lower fabrication complexity. An advantage of a 90° hybrid coupler however is that the two IF outputs of the balanced mixer stay at one side of the substrate channel, while in the non-crossover balanced mixer in Subsection 3.5.4 the two IF outputs are in opposite substrate channels. I have solved this with introducing a CPW-CPW crossover between the input RF and one of the IF outputs which in Section 3.6 is described in details.
In the following, I calculate the down converted IF signal in a balanced mixer with the 180° RF hybrid. Two HEBs are chosen as mixing elements. First, all circuit elements are assumed to be ideal (no phase or amplitude imbalance in RF hybrid coupler, no difference in DC characteristics between two HEBs). The calculations are done when two HEBs are oppositely biased, see figure 3.2. Here the $D^2$ and $C^2$ are power direct and coupled normalized transmissions. In an ideal hybrid coupler $D^2, C^2 = 0.5$ and $D^2 + C^2 = 1$ which means energy is conserved (no amplitude loss in the coupler).

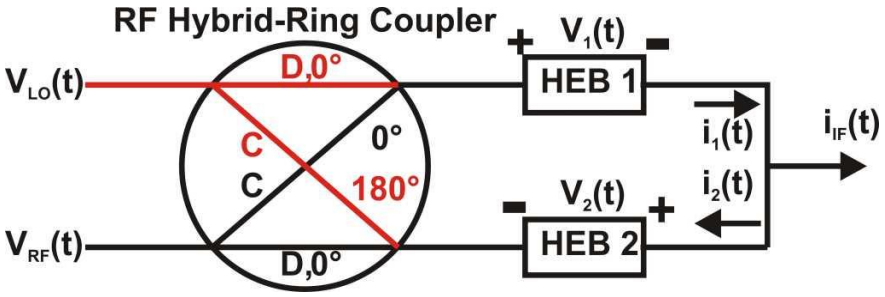


Figure 3.2: Schematic of a balanced mixer for calculations.

Defining voltages of RF and LO as

$$V_{RF}(t) = V_{RF} cos(w_{RF} t + \varphi), \tag{3.1}$$

$$V_{LO}(t) = V_{LO} cos w_{LO} t. \tag{3.2}$$

Therefore the total ac voltages incident on mixer 1 and mixer 2 are

$$v_1(t) = C V_{RF} cos(w_{RF} t + \varphi) + D V_{LO} cos w_{LO} t, \tag{3.3}$$

$$\begin{aligned} v_2(t) &= DV_{RF}cos(w_{RF}t + \varphi) + CV_{LO}cos(w_{LO}t \pm \pi) \\ &= DV_{RF}cos(w_{RF}t + \varphi) - CV_{LO}cosw_{LO}t, \end{aligned} \tag{3.4}$$

where the minus sign is added by a $\pm\pi$ phase shift in the 180° RF hybrid-ring coupler. Now it is assumed that the two mixing elements are two similar HEB mixers with similar gain. HEBs are square law type of mixers. That means they square the total RF voltage incident on the mixer. Two HEBs do not produce higher order mixing terms in contrast to Schottky mixers or SIS mixers [51].
The current at the IF summation node, if the mixers have an opposite DC bias, is

$$\begin{aligned} i_{IF}(t) &= i_1(t) - i_2(t) \\ &= av_1(t)^2 - bv_2(t)^2. \end{aligned} \tag{3.5}$$

Substituting Eq.3.3 and Eq.3.4 into Eq.3.5 gives, assuming the two HEB mixers are equal $a \equiv b$,

$$\begin{aligned} i_{IF}(t) &= b(CV_{RF}cos(w_{RF}t + \varphi) + DV_{LO}cosw_{LO}t)^2 \\ &\quad - b(DV_{RF}cos(w_{RF}t + \varphi) - CV_{LO}cosw_{LO}t)^2 \\ &= 4bV_{RF}V_{LO}(cos(w_{RF}t + \varphi)cosw_{LO}t) \\ &= 2bV_{RF}V_{LO}(cos((w_{RF} + w_{LO})t + \varphi) + cos((w_{RF} - w_{LO})t) + \varphi). \end{aligned} \tag{3.6}$$

The sum term of RF and LO frequencies cannot exist in an HEB mixer, because it is dissipated ( the HEB cannot "follow" high frequency signals). So, the subtract term is the only existing term at the output of an ideal balanced HEB mixer. For simplicity of the following calculations, the $\varphi$ term is not taken to account.
In a case of biasing two HEBs with the same polarity

$$\begin{aligned} i_{IF}(t) &= i_1(t) + i_2(t) \\ &= bv_1(t)^2 + bv_2(t)^2 \\ &= 2b(V_{RF}^2cos^2w_{RF}t + V_{LO}^2cos^2w_{LO}t). \end{aligned} \tag{3.7}$$

These two terms with RF and LO frequencies squared again cause only heating of the mixer and therefore, no IF current is at the output. This can be changed by adding the IF's of the two mixers via a 180° IF hybrid instead of directly as shown in figure 3.2. In that case the IF signal will be present at the Delta port output of the hybrid.

Perfect amplitude modulated (AM) LO noise is fully rejected in an ideal balanced mixer. In reality, the rejection of LO noise is limited by the balance of the RF hybrid and the conversion loss (gain smaller than one) match between two mixing elements and LO to RF isolation.
Considering an AM noise signal superimposed into the LO signal

$$V'_{LO}(t) = (V_{LO} + V_n(t))cosw_{LO}t. \tag{3.8}$$

Therefore, the ac voltages over mixers 1 and 2 in figure 3.2 are

$$v_1(t) = CV_{RF}cosw_{RF}t + DV_{LO}cosw_{LO}t + DV_n(t)cosw_{LO}t \tag{3.9}$$

$$v_2(t) = DV_{RF}cosw_{RF}t - CV_{LO}cosw_{LO}t - CV_n(t)cosw_{LO}t, \tag{3.10}$$

substituting these new voltages in Eq.3.5 gives

$$\begin{aligned} i_{IF}(t) = {} & 2bV_{RF}V_{LO}(cos(w_{RF} + w_{LO})t + cos(w_{RF} - w_{LO})t) \\ & + 2bV_{RF}V_n(cos(w_{RF} + w_{LO})t + cos(w_{RF} - w_{LO})t). \end{aligned} \tag{3.11}$$

Because of $V_{RF}V_n << V_{RF}V_{LO}$, consequently the second term with AM LO noise at the IF output is almost zero.

### 3.2.2 A THz 180° hybrid-ring coupler

Here, the total RF circuit designs of THz balanced mixers are based on CPW transmission lines. The only not CPW based element is the planar antenna. The design of slotline tapered antenna is explained in Section 3.3 and Section 3.5 for 800 GHz and 1.9 THz, respectively. CPW lines show advantages like much easier shunt or series mounting of lumped (active and passive) components, not needed drilling holes through the substrate for access to ground and less complex in transmission to slotline (no need for double-side transition like microstrip-slotline). Their performance is comparable or even better than microstripline for guiding the signal, concerning dispersion and losses [55]. They are applied regularly in designing of high frequency circuits. An advantage over for example microstrip lines is using high resistive silicon as a lossless dielectric and results in less complex with only few bridges over the lines. Additionally, they

need thinner substrate (important for avoiding waveguide unwanted modes) and much less wide lines with the same impedance value (easier to integrate).
180° hybrid couplers are indispensibale components in balanced mixers. The hybrid-ring coupler is a well known and commonly used 180° hybrid. The hybrid-ring coupler in microstrip technology is the basic type of its kind applied in many printed microwave circuits. However, it supports only 20-25% bandwidth. This number has been improved in [56] [57] but each of those designs suffers from complex construction. The CPW-slotline hybrid-ring coupler technology can extend the bandwidth with a simpler design and an uniplanar structure. Uniplanar structure microwave integrated circuit does not need to use the back side of the substrate. Consequently there is no need for via holes for ground connections. In figure 3.3, the ring coupler is a $(3\lambda/2)$ conventional CPW-slotline coupler. It consists of three quarter-wavelengths, one phase delay slotline $(3\lambda/4)$ and four CPW to slotline T-junctions. The 180° phase difference achieved by an electrical length difference between $(3\lambda/4)$ and $(\lambda/4)$ which is frequency dependent due to dispersion. The measured coupler shows about 0.19 octave bandwidth with ± 0.3 dB power dividing balance and over 20 dB isolation between ports 1 and 4 and 1.2 dB insertion loss (in the measurements they have bonded over CPWs) [58]. An uniplanar reverse-phase CPW hybrid-ring coupler is introduced in [59]. It consists of a 180° reverse-phase CPW-slotline back to back balun. It improves amplitude and phase imbalance over about one octave broad bandwidth in comparison to conventional hybrid-ring couplers because of the existing frequency independent 180° phase change [59], see figure 3.3. The size of the hybrid-ring is half that of the conventional type. The impedance of the feed lines are chosen as 50 Ω. The characteristic impedance of the inner circle CPW and slotline is then 70.7 Ω,

$$Z_S = \sqrt{2}.Z_{CPW}, \tag{3.12}$$

where $Z_S$ and $Z_{CPW}$ are the impedance of the inner circle slotline and CPW feed line, respectively. The radius of the ring is

$$2\Pi r = \lambda. \tag{3.13}$$

First we discuss the broadband response of the CPW-slotline transition and next the generation of a zero or 180° phase difference with back-to-back baluns. CPW and

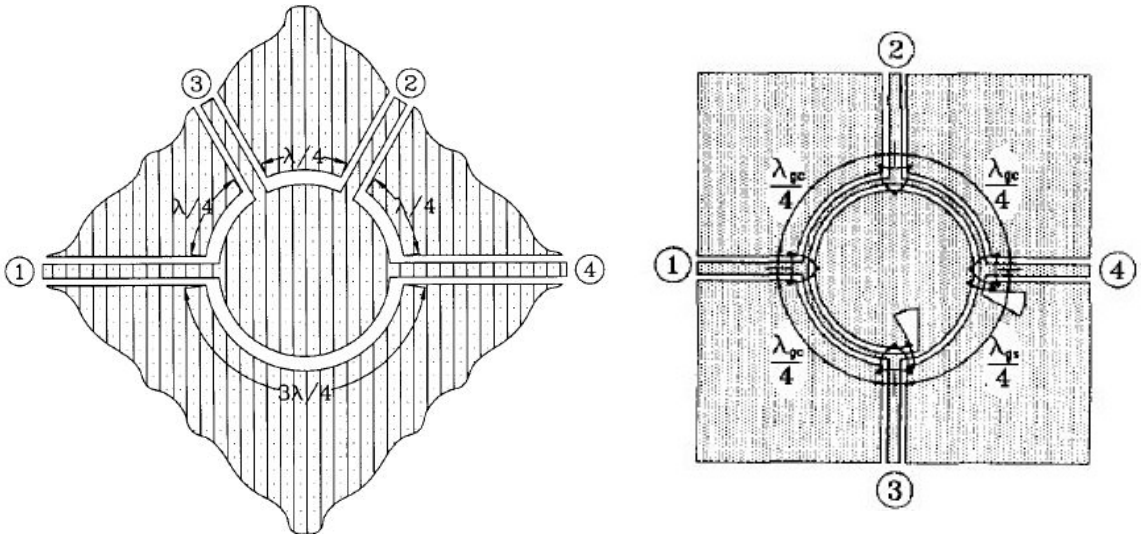


Figure 3.3: 180°hybrid-ring coupler, Left: Uniplanar conventional CPW-slotline[58], Right: Uniplanar CPW reverse-phase with a 180° reverse-phase CPW-slotline back-to-back balun [59].

slotline are types of transmission lines that are extensively used in high frequency integrated circuits. They provide easy ground connections, easy series and shunt device mounting and simple (uniplanar) fabrication processes. Therefore, for using both of them in the high frequency circuits, there is a need of broad band transitions between CPW and slotlines. In [58], different types of transitions systematically based on experimental investigations have been reported. This consists of a combination of open/short CPW to a uniform/nonuniform slotline short stub.

A broadband and easily fabricated type of transition is shown in figure 3.4. It consists of a CPW short and radial stub (non-uniform slotline short slot). The center of the CPW line is connected to one side of slotline which results in the CPW short. The slotline radial stub is a broadband open. This gives a broadband CPW-slotline transition. Almost the entire CPW excited power transfers to the slotline [60]. Additionally this transition type forms a 90° bend in the transmission structure. As a result, this makes the layout flexible. About 2.3 octaves bandwidth at 1.1-5.7 GHz is reported of such transitions.

Next, to demonstrate the concept of 0° and 180° reverse-phase back-to-back baluns, see figures 3.5 and 3.6. They consist of one CPW-slotline tee junction and two CPW-slotline transitions. When the signal is on the CPW line with 4 $\mu$m width and 4 $\mu$m gap equal to about 50 $\Omega$ on a 9 $\mu$m silicon substrate, it transmits with CPW mode as noted in figure 3.5 with arrows. The signal equally is divided to two signals for

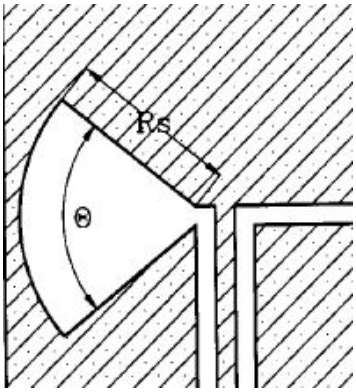


Figure 3.4: A broadband CPW-slotline transition with shorted CPW and a slotline radial stub as a broadband open. The $R_S$ and $\Theta$ are stub's length and angle, respectively.

example with about 0.5 dB and 185$^{\circ}$ differences in amplitude and phase at 900 GHz at ports 1 and 2, respectively. These responses are depicted in figure 3.6. Two slotlines with a gap of 2 $\mu$m are applied as the key elements for the signal division. The CPW mode is converted to the slotline mode with a help of a micro bridge. This bridge is applied to confine the CPW mode on the coplanar line and also to ground the unwanted slotline mode of the launched signal. By choosing the similar or different gap of the two CPW outputs (see figure3.5), one can decide between having a zero or 180$^{\circ}$ phase difference. Two CPW-slotline transitions with open slotline radial stub and short CPW increase the bandwith and improve the matching of the transition. The thickness of the silicon substrate and perfect conductor (PEC) as a top electrode are 9 $\mu$m and 400 nm, respectively. A PEC background and waveguide ports [41] are implemented for 3D electromagnetic simulations of which the results are depicted in figure 3.6.

After re-designing several types of hybrid-ring couplers to our desired THz frequencies, I ended up to base my design on the coupler introduced in [61], a new wide-band and reduced-size uniplanar hybrid-ring coupler. This $4\lambda/5$ type of design is 20% smaller than $\lambda$ hybrid-ring coupler in figure 3.3-Right. This design has four CPW feed lines, three in-phase CPW-sotline T-junctions and one out-of-phase CPW-slotline tee junction. This out-of-phase T-junction introduces 180° phase difference and is a frequency independent(broad band). This T-junction is a different type of CPW-slotline tee junctions than the one explained in figure 3.5. The difference is, that here the CPW feedline first sees two split CPWs of $\lambda/10$ length and after that two CPW-slotline transitions which end up in two slotlines, also of $\lambda/10$ length. Therefore the ring consists of more slotlines than CPWs which it makes especially at high frequencies easier to

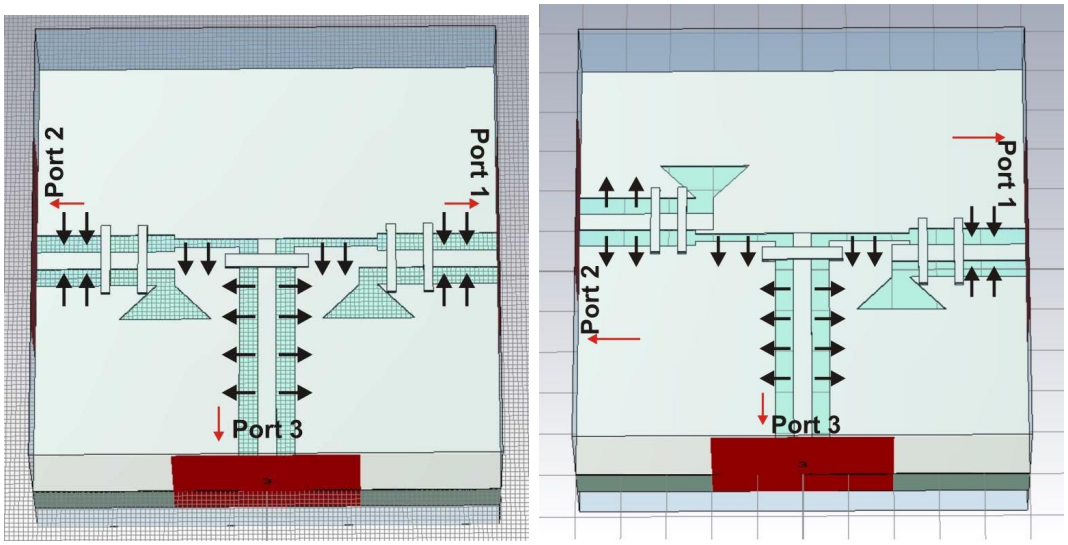


Figure 3.5: E-field distribution (noted as arrows) for the reverse-phase CPW-slotline T-junction, Left: 0° phase phase difference Right: 180° phase difference between two equally divided output signals.

fabricate due to less necessary micro-bridges. The impedance of the CPW feed lines is 50 Ω. Θ, the electric length of a quarter of the slotline ring circumference is [61]

$$Z_S = Z_C = Z_{C0}\sqrt{1 - cot\Theta^2}. \tag{3.14}$$

The minimum Θ is 45° (i.e. $\lambda/8$). However the simulations indicated that for the wide-band operation Θ needs to be 72° (i.e. $\lambda/5$). Therefore from Eq.3.14, characteristic impedances are $Z_S = Z_C = 66.9\ \Omega$ [61]. I have re-designed this uniplanar $0.8\lambda$ hybrid-ring coupler on a 6 $\mu$m silicon substrate ($\varepsilon_r = 11.9$) to cover the band of 800-1100 GHz. The final optimum design of this coupler is depicted in figure 3.7. Additionally, the E-field distributions for 0° and 180° phase differences are shown. The four CPW feed lines with center line width ($W_{CPW} = 3$) $\mu$m and gap ($G_{CPW} = 2.5$) $\mu$m have about 50 Ω impedance. When the port 4 is excited, signal in CPW mode transmits. Each slot of the CPW gets connected to a separate slotline with a gap $G_S$ of 2 $\mu$m and an impedance of about 62 Ω. The 3 dB split signals transmit in slotline mode. After passing the length of $\lambda/5 = 126$ $\mu$m from Eq.3.15, each of them reach a CPW 50 Ω line towards the ports 2 and 3,

$$\frac{\lambda}{\lambda_0} = \sqrt{\frac{2}{\varepsilon_r + 1}}. \tag{3.15}$$

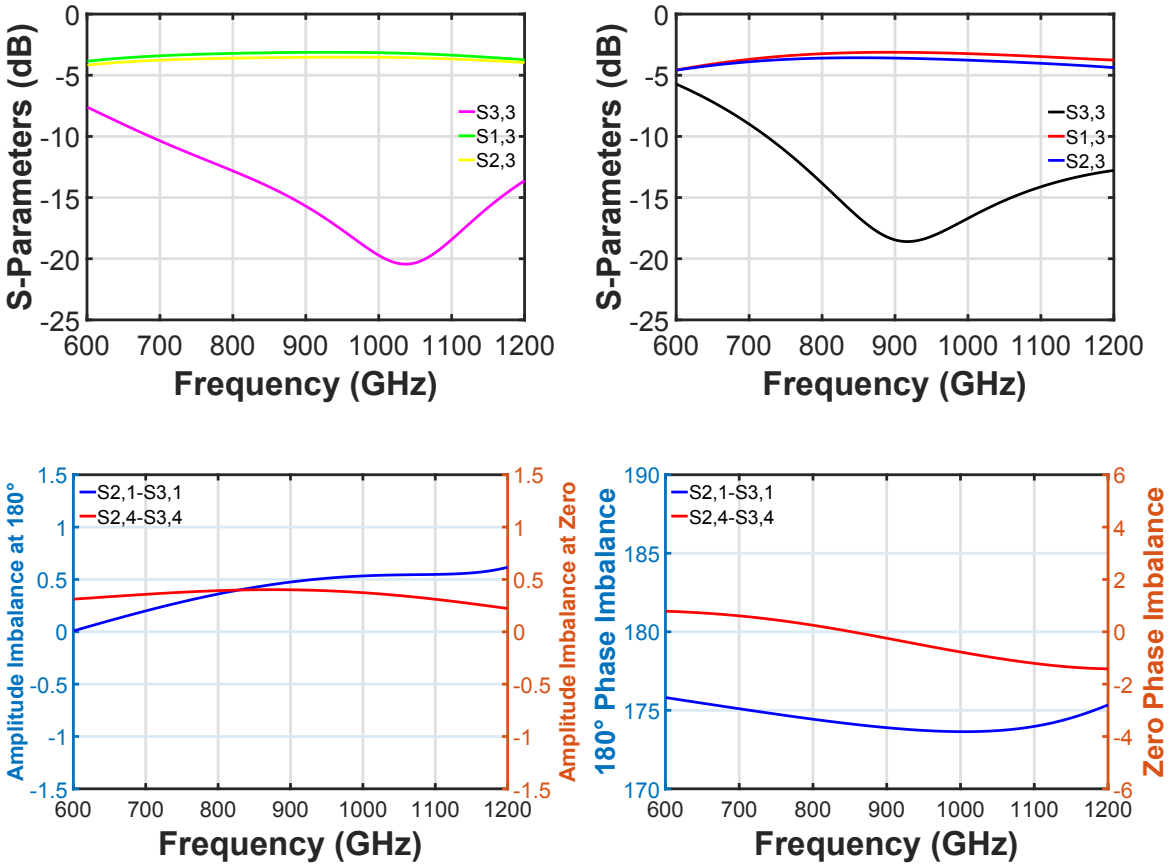


Figure 3.6: S-parameters of a mode converter+phase shifter, Left: Zero phase Right: 180° phase differences between two equally output signals. Amplitude is in dB and phase in degrees.

There are three micro-bridges with 400 $\mu$m SiO2 as a dielectric at this side to prevent the coupled slotline mode to propagate in the CPW lines. In an ideal chase, the ports 2 and 3 receive 3 dB split signals with zero phase imbalance. When port 1 is excited, the signal transmits with CPW mode. It reached to the first part of the out-of-phase T-junction which is a CPW T-junction. The optimum impedance of two inner circle CPWs is about 62 $\Omega$ with width of $W_C = 1.5$ $\mu$m and gap $G_C = 2$ $\mu$m. The second part of the T-junction are two shorted CPWs with $\lambda/10$ length and open slotline radial stub with optimum 9 $\mu$m length and 25° angle. Two opposite slots of two CPWs are connected to two separate 62 $\Omega$ slotlines with again $\lambda/10$ length. After that, they meet two CPW feed lines towards ports 2 and 3. Consequently, in an ideal situation, 3 dB split signals with 180° phase difference reach at ports 2 and 3. Ports 1 and 4 must be isolated from each other. This happens when port 4 is excited, two signals

with 180° phase difference meet and cancel each other at the CPW towards port 1. The same thing happens when port 1 is excited. Two signals with slotline mode and 180° phase difference meet and cancel each other at the CPW line towards port 4. The S-parameters in figure 3.8 show 1 octave broad band response from 700-1400 GHz with a 1000 GHz center frequency. There is a high isolation between ports 1 and 4 of about -45 dB at the mid of the band. S1,1 and S4,4 are lower than -10 dB over the bandwidth. The amplitude and phase imbalance between ports 2 and 3 when port 1 is excited, (S2,1-S3,1) is about 0.5 dB and ±2° in the band, respectively. The amplitude and phase imbalance between ports 2 and 3 when port 4 is excited (S2,4-S3,4) are about ±0.4 and ±2° in the band, respectively.

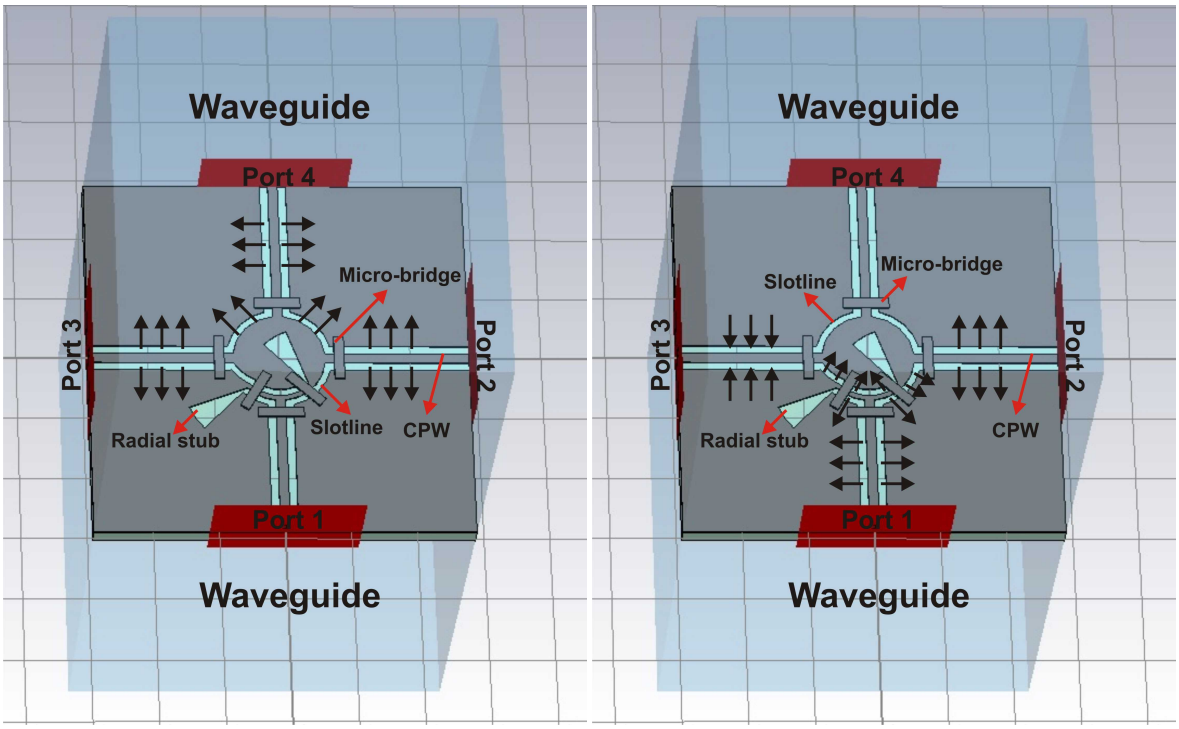


Figure 3.7: A 800-1100 GHz hybrid-ring coupler with arrows showing the mode of transmitted signal, Left: When port 4 is excited. The signal gets equally divided between ports 2 and 3 with 0° phase difference. Right: When port 1 is excited. The signal gets equally divided between ports 2 and 3 with 180° phase difference. The waveguide dimension is 230×116 $\mu m^2$. Two radial stubs with a length of 19 $\mu$m. The micro-bridges are with 400 nm tick SiO2. Silicon substrate has a thickness of 6 $\mu$m. Ports are the waveguide type.

In reality, the ideal case is to replace the PEC in simulations with a loss free superconducting material for wiring the mixers, see Section 2.5. The gap frequency of superconducting NbTiN is about 1.1 THz for the material quality that I choose for the

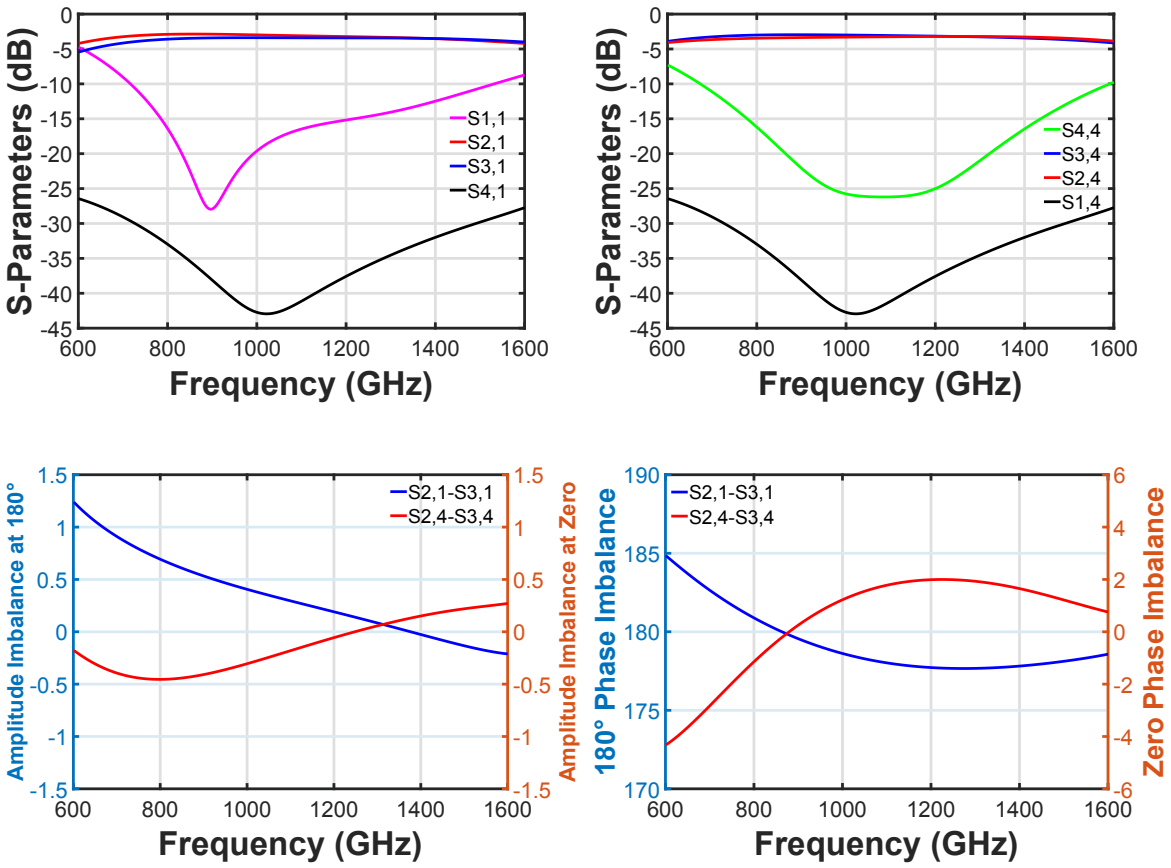


Figure 3.8: S-parameters of simulated 800-1100 GHz hybrid-ring coupler: Top-Left: port 1 is excited, Top-Right: Port 4 is excited, Bottom-Left: Amplitude imbalance in dB between ports 2 and 3 when port 1 (blue) and port 4 (red) are excited, Bottom-Right: Phase imbalance in degrees between ports 2 and 3 when port 1 (blue) and port 4 (red) are excited

simulation. The surface impedance of NbTiN, calculated from its DC properties (see Subsection 2.5.2) is implemented into CST as a table, as function of frequency. This table is than fitted by a mathematical function in CST ( see figure 2.8) for the quality of the fit and this function is used in the simulation. The result of the simulation is shown in figure 2.8. It can be seen in figure 3.9 that the transmission above the gap frequency of the NbTiN degrades rapidly due to the losses in the material.

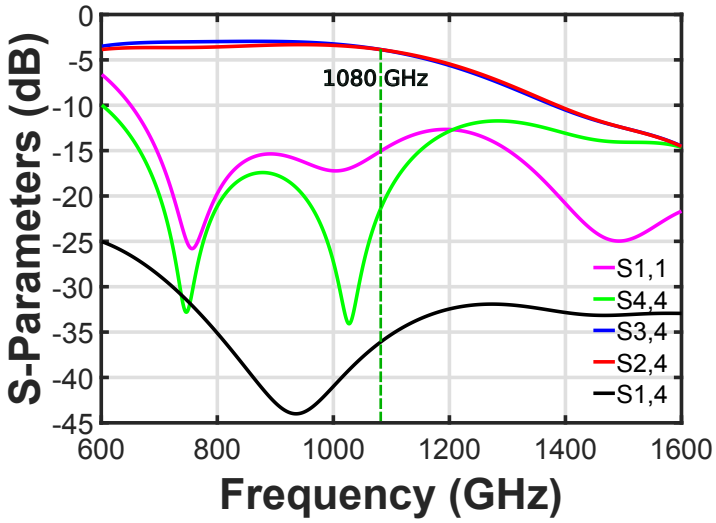


Figure 3.9: S-parameters of the simulated 800-1100 GHz hybrid-ring coupler where the superconducting NbTiN is implemented instead of PEC for the bottom and top metal layers.

## 3.3 Planar tapered antennas

In the following section, the transition from rectangular waveguide to a CPW based mixer circuit is discussed. It is divided in two parts. The first is the transition of a signal from a waveguide to the circuit with an E-plane slotline planar antenna. The second part is a CPW-slotline transition to change the slotline mode to the CPW mode, see Subsection 3.3.1. A tapered slotline antenna (TSA) has a planar geometry which makes it easier to integrate it in a planar circuit on the same substrate with planar detector devices like SIS tunnel junctions or HEB bolometers. Its performance depends on the geometry of antenna and the permittivity and thickness of the substrate. It introduces a broad bandwidth with a symmetrical field pattern. This type of antenna is in a good match to the TE10 mode of rectangular waveguide [62], [63]. At 802 GHz a broken linearity tapered slotline antenna (BLTSA) was used on a 1.7 $\mu$m thick dielectric layer of $SiO_2/Si_3N_4$. It consists of a taper with three linear sections [63]. [64] studied the tapered slotline antenna with an integrated CPW-slotline transition on a 31-mil duroid substrate with a 2.2 dieceltric constant at center frequency of 10 GHz. In [52] the functionality of a planar slotline tapered antenna integrated on a 6 $\mu$m silicon with the 350-500 GHz balanced SIS mixers is proven. The antenna in both studies is an E-field TSA. In figure 3.10, the 800-1100 GHz TSA on a 6 $\mu$m thick silicon substrate is shown. A small length of the silicon substrate is extended into the waveguide for improving the matching between the TSA and the waveguide TE10

mode [55]. The optimum length of this extension is about 8.5 $\mu$m. The TSA has three sections with four opening widths. The taper at the end reaches to a slotline with 3.5 $\mu$m width. This is close to the value of one of the gaps of the CPW feed lines in figure 3.7 that are 2.5 $\mu$m wide. The antenna is placed in the center of a waveguide with lateral dimension of $230\times116$ $\mu m^2$. There is a 6 $\mu$m gap between edge of silicon substrate and metal wall of waveguide at both sides of antenna. The antenna is grounded to the waveguide wall, being in the simulation the PEC surrounding of the structure with two beamleads. Its simulated frequency response shows that the planar antenna is a broadband covering both 800 GHz and 1100 GHz, see figure 3.10. This design is modified to be applied for balanced and single ended THz mixers. I made use of a different type of CPW-slotline transition described in Subsection 3.3.1. The reason for this is that the HEB bridge sits inside one of the CPW gaps and one of the HEB contacts is connected to the center line of the CPW. Therefore, if we want to DC bias the HEB and the center line of CPW-slotline transition shoudl not be shorted to ground like in [64], [52] and [65]. This is crucial for a single ended HEB mixer and better than introducing a DC/IF block capacitor. The new optimum design of TSA is shown in figure 3.11 with its simulated frequency response. The length of this design is shorted in compared to the design in figure 3.10 up to the 8 $\mu$m width of taper. This is the width of total CPW feed line (width of two slots+center line of a CPW). Therefore the length of antenna is shorten at the point where the width is 8 $\mu$m. The S-parameters result shows that this shorted design works better at higher frequencies and is wide band enough to cover both 800 GHz and 1100 GHz.

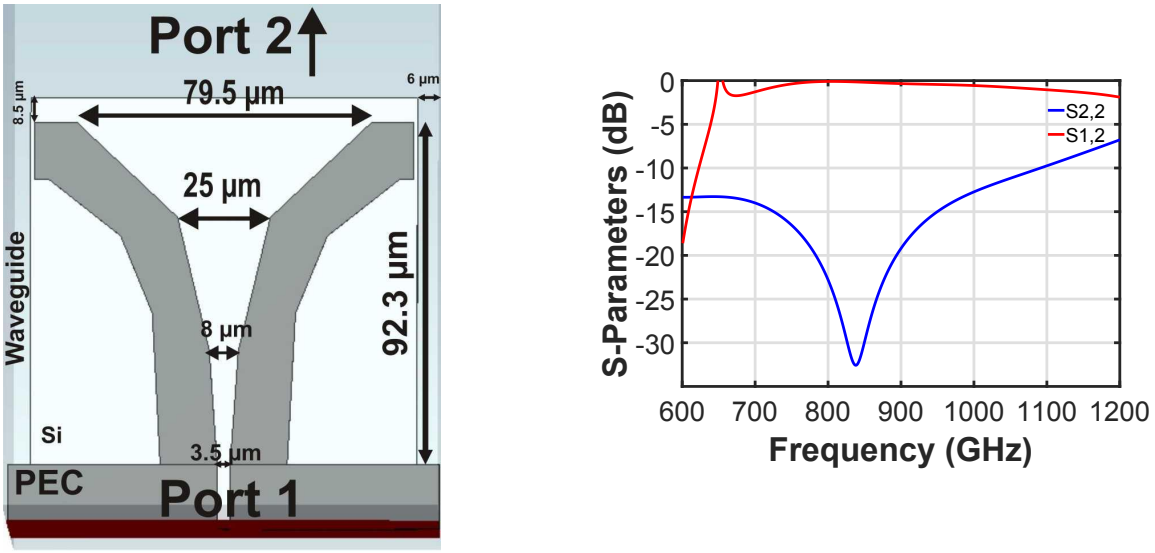


Figure 3.10: A broadband planar tapered slotline antenna (TSA), Left: The antenna with PEC on a 6 $\mu$m silicon substrate in the center of waveguide with lateral dimension of 230×116 $\mu$m$^2$. The silicon is about 8.5 $\mu$m is extended into the waveguide and about 6 $\mu$m away from the waveguide walls. Right: The simulated S-parameters when waveguide port number 2 is excited. The red curve shows about -0.3 dB transmission (S1,2) at 900 GHz. The blue curve shows the reflection at port 2 (S2,2) with -20 dB at 900 GHz. The design is broad band and covers both 800 GHz and 1100 GHz bands.

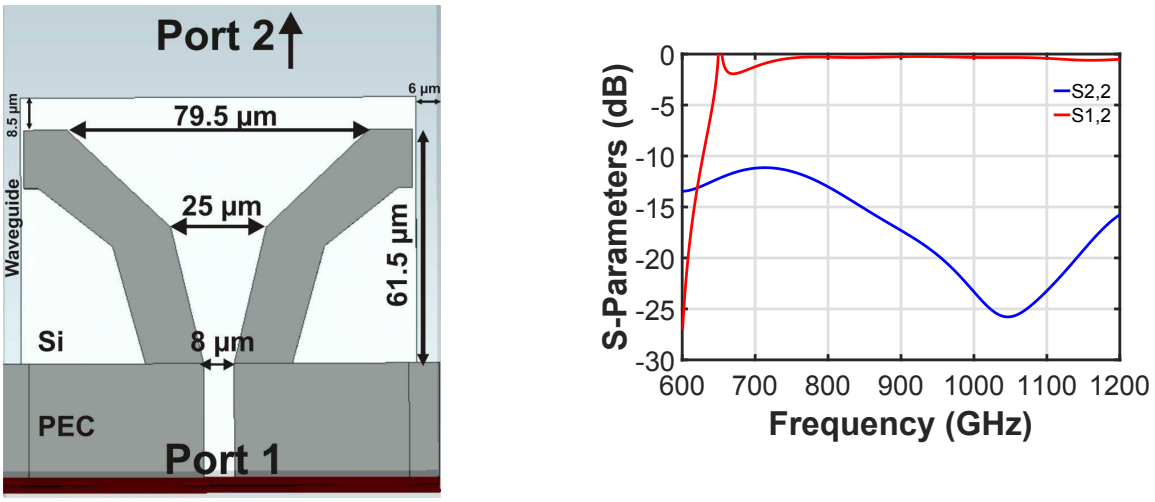


Figure 3.11: A shorted TSA match to the 8 $\mu$m slotline wide, Left: The antenna Right: The simulated S-parameters when waveguide port number 2 is excited. The red curve shows about -0.25 dB transmission (S1,2) at 900 GHz. The blue curve shows the reflection at port 2 (S2,2) with -17 dB at 900 GHz. Its broadband design covers both 800 GHz and 1100 GHz bands.

### 3.3.1 Slotline to CPW transitions

The signal coming from the antenna is in a slotline mode but the rest of the design is based on transmission lines carrying a CPW mode. Therefore there is a need of a transition to convert the slotline mode to the CPW mode. The transition has three parts, a uniform CPW, phase shifter and slotline. Several CPW-slotline transitions are reported in [64], [52] and [65]. They have proposed transitions based on short circuit CPW. As mentioned in the antenna section, we are interested in a transition design with the open circuit type of CPW-slotline transition. In [66], this type of transition is demostrated on a RT/Duroid 6010 with relative permitivity of 10.2 at 13 GHz. The final design of a CPW-slotline with open CPW with 900 GHz center frequency is depicted in figure 3.12 with its E-field distribution. Additionaly, its frequency response shows the covering of both 800 GHz and 1100 GHz bands. The transmission from port 2 to port 1 (S1,2) at 900 GHz is about -0.24 dB. The reflection at port 2 (S2,2) is about -15 dB at 900 GHz. The width of slotline is 8 $\mu$m and CPW has a center width of 3 $\mu$m and 2.5 $\mu$m gap. The extra $\lambda/2$ slotline is a phase shifter to convert the modes. The optimum width is chosen to be same as gap width of CPW (2.5 $\mu$m). The initial value is calculated by Eq.3.15 and the optimum length is 68 $\mu$m. The optimum length of strip inside the slotline is 2.5 $\mu$m. The mode conversion occurs due to different length that the wave propagates in the two slots. The two ground planes are kept at the same potential by using a microbridge with 400 nm SiO2 as a dielectric. This prevents propagation of the unwanted slotline mode on the CPW side. The efficiency of the transmission between the slotline and the CPW is centered at the desired band center frequency. At other frequencies this value reduces but the roll off is slow (mixture of both two modes). According to [66] the modes bouncing back and forth between the bridge, where the slotline mode is reflected, and the slotline to broaden the bandwidth. This back and forth bouncing increases the efficiency of transmission too. In [67], they have shown experimentally for the first time the suppression of coupled slotline mode on CPW with using air-bridge.

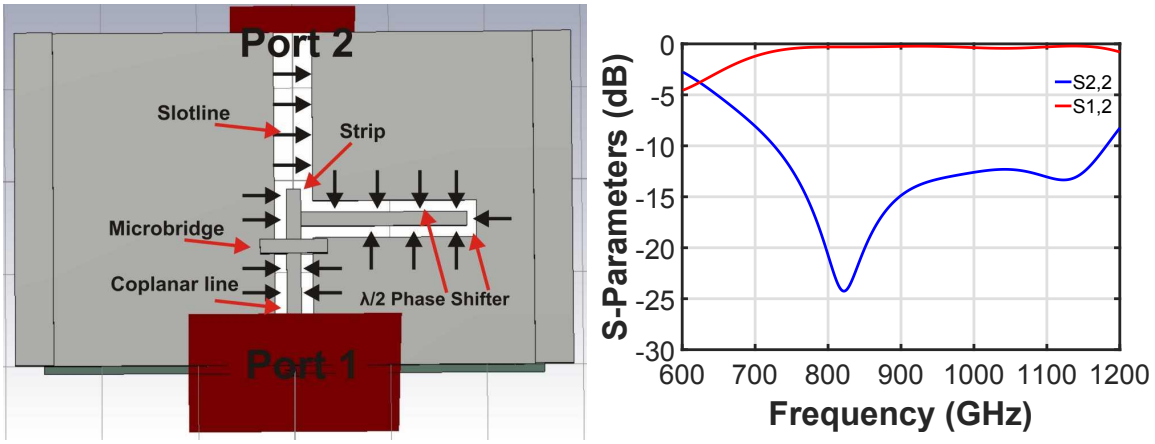


Figure 3.12: A 800-1100 GHz slotline to CPW mode transition, Left: Design with a $\frac{\lambda}{2}$ (68 $\mu$m) extra slot length and (2.5 $\mu$m) extra center line of CPW inside the 8 $\mu$m slotline towards the antenna Right: Simulated results of the transition with S2,2 as a reflection at 8 $\mu$m slotline and S1,2 transition from the port 2 with slotline to the port 1 with CPW line.

## 3.4 Integration of hybrid-ring coupler with transition and antenna on silicon at 800-1100 GHz

At first, the designed antenna in Section 3.3 is integrated with the transition in Subsection 3.3.1 on one 6 $\mu$m thick silicon substrate. In addition, these two circuit elements must be matched. The optimum length of slot for matching between the antenna and the transition is about 74 $\mu$m. This is the line where the coupled slotline mode propagates. In figure 3.13 the final design of combination of antenna with the transition is shown. It is simulated in a waveguide with dimension of 230×116 $\mu m^2$. The reflection at port 2 (S2,2) and transmission from port 2 to 1 (S1,2) for different length of the slotline between TSA and CPW-slotline transition is also depicted. It is obvious that the blue curve (S2,2, L74) for reflection at port 2 and red curve (S1,2, L74) for transmission have the best performance. It performs with -13 dB reflection and -0.26 dB transmission at 900 GHz. It is broadband and covers 800 and 1100 GHz bands.
The next step in designing the balanced mixer is the integration of two of these antennas with the hybrid-ring coupler from figure 3.7. To predict the response of the integration quickly and reliably before drawing in 3D, the design studio feature of CST suite is applied. The simulated S-parameters of each circuit element are used to calculate the total scattering parameters. In principle, it shows how well the circuit elements are matched together. This is depicted in figure 3.14 where the circuit el-

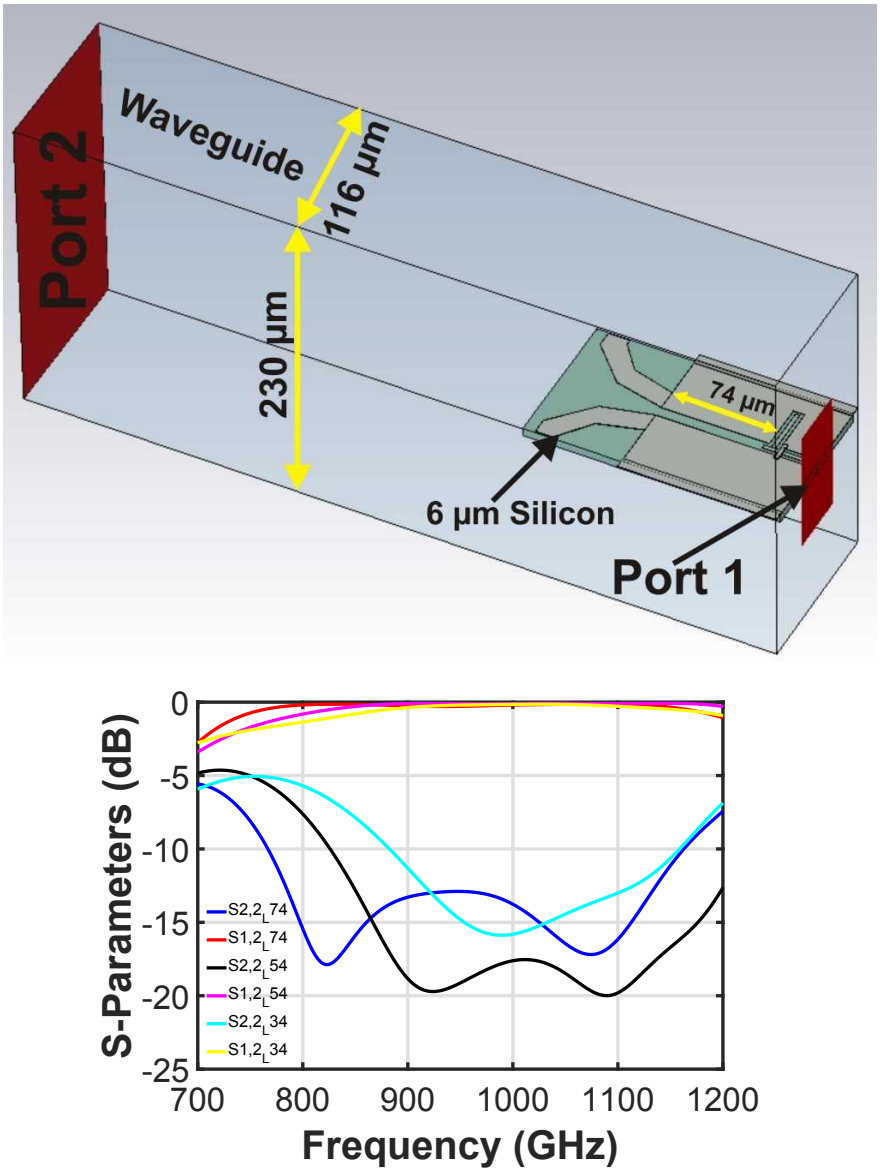


Figure 3.13: An integration of the tapered slotline antenna with a CPW-slotline transition with PEC on a 6 $\mu$m thick silicon substrate. The waveguide dimension is 230×116 $\mu m^2$. The signal at port 2 is excited and the S2,2 shows the reflection and S1,2 the transmission from port 2 to 1. The slotline with a length of 74 $\mu$m is introduced for optimum matching between the antenna and transition. It covers both 800 and 1100 GHz bands.

ements are as S-parameters blocks. Additionally, ports 1 to 4 are added to run the simulation same as waveguide ports in 3D during simulating the hybrid-ring coupler. It is possible to define impedance of the ports to any values. Nevertheless, the 50 Ω is given which is close to the value of the 3D waveguide ports. This figure also shows the S-parameters when the port 1 and 4 are excited. The isolation between ports 1 and

4 is a about -40 dB at 900 GHz. The reflection S1,1 and S4,4 are pretty much lower than -10 dB however they barely can cover the 800 GHz frequency. Nevertheless, we are satisfied with these preliminary results and now is the step to draw all elements in 3D environment, simulate and fine tune the matching.

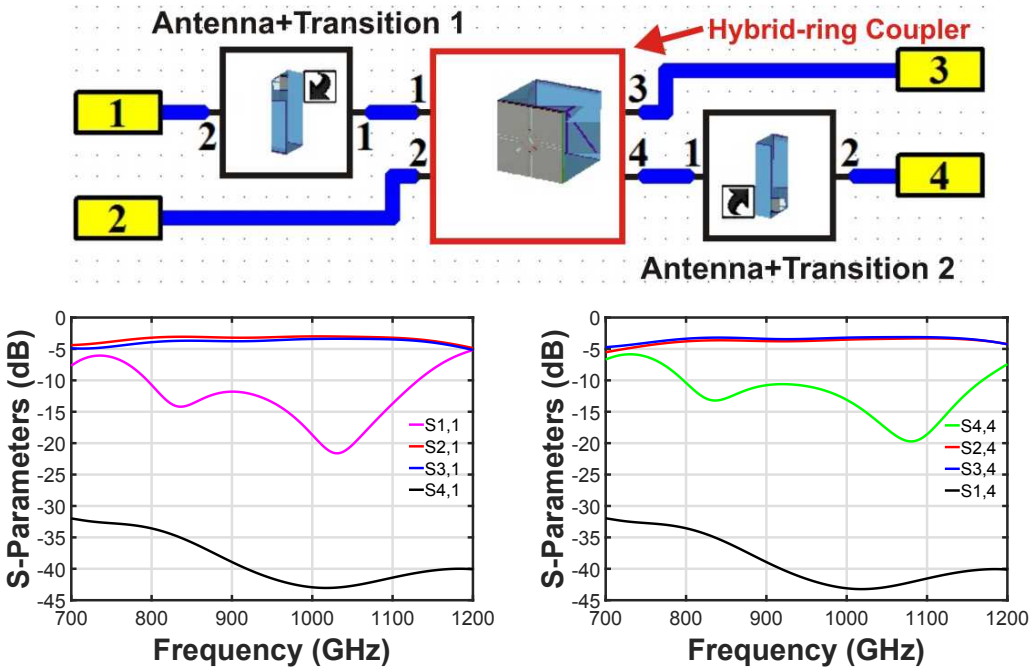


Figure 3.14: S-parameters building blocks consisting of hybrid-ring coupler and two tapered slotline antennas with CPW to slotline transitions in the design studio environment of CST suite. The simulations show high isolation (black curve) about -40 dB at 900 GHz between ports 1 and 4. Reflections at ports 1 (magenta curve) and 4 (cyan curve) cover the desired band however S4,4 is shifted more to the higher frequency than S1,1.

In the CST microwave studio (3D environment) the two optimum antennas with transitions are integrated with the hybrid-ring coupler at ports 1 and 4. Ports 2 and 3 are matched to about 50 Ω using the waveguide ports, see figure 3.15. The very first step is trying to obtain the optimum matching between the antennas+transitions to the hybrid-ring coupler. This is achieved by changing the length of L1 and L2 CPW lines. The S-parameters in figure 3.15 show the frequency response of the integration with an optimum $L1 = L2 = 50$ $\mu$m. These values are obtained after several runs of simulations with changing the L1, L2 and the length of the slotline radial stubs. The new length of the radial stubs is 16 $\mu$m which is important for the port 1 response (shorter length shifting the band to higher frequency and better matching at the mid of the band). As it is shown the response at port 4 (at the 0° side of the hybrid-ring coupler)

covers 800 and 1100 GHz bands but still suffers at the mid of the band. However, the reflection at port 1 (S1,1 at the 180° side of hybrid-ring coupler) only shifts over the band by changing the L1. This is not sufficient as the S1,1 does not cover two desired frequencies properly and its reflection is about -8 dB at 900 GHz.

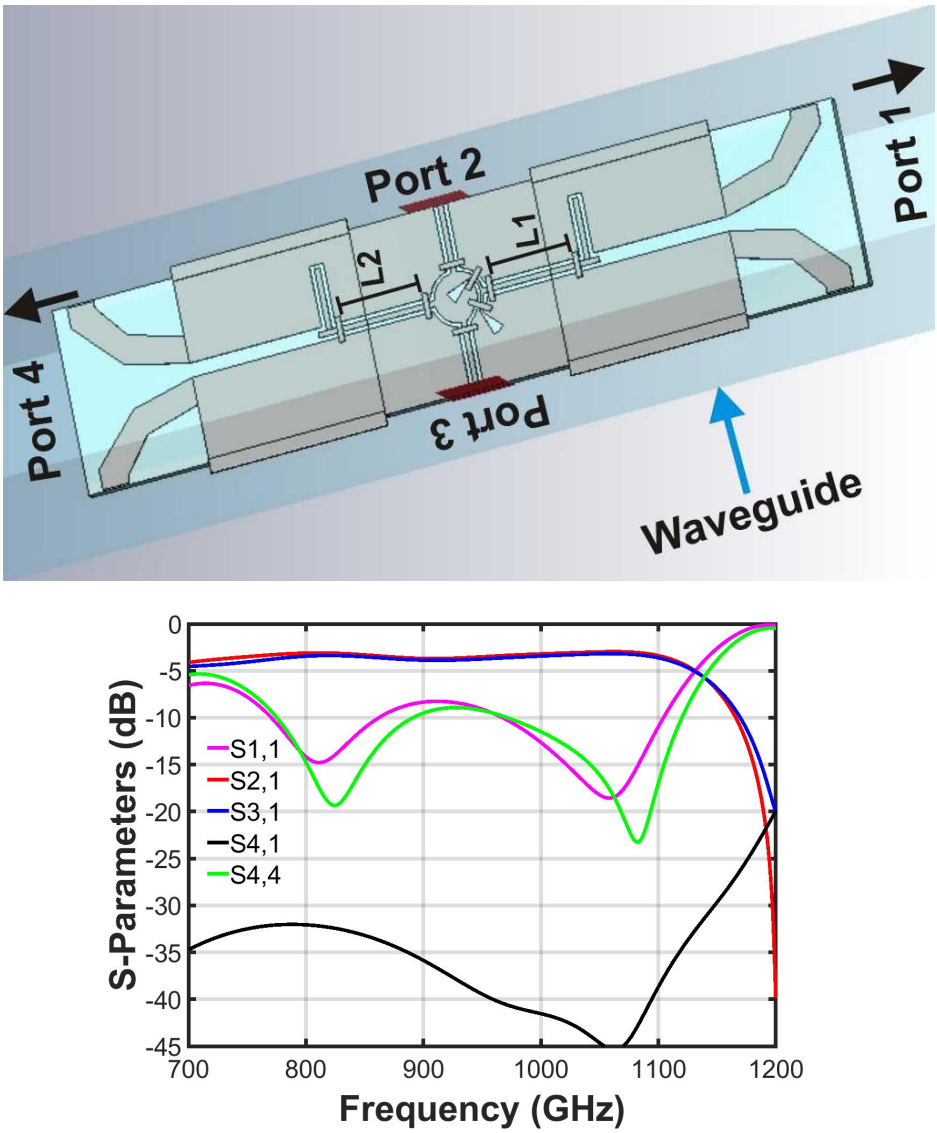


Figure 3.15: Two antennas and transitions integrated with the hybrid-ring coupler in 3D CST microwave studio. They are on a 6 $\mu$m thick silicon substrate. The waveguide dimension is 230×116 $\mu m^2$. There are L1 (50 $\mu$m) and L2 (50 $\mu$m)CPW matching lines. The S-parameters show about -45 dB isolation between ports 1 and 4. S1,1 and S4,4 cover the band from 800 GHz to 1100 GHz. The -3 dB split (S2,1 and S3,1) is better at the low and high side of the band.

One should notice that to have a broadband design with all elements covering 800 GHz and 1100 GHz is quite challenging. However, it avoids having two separate mixers with

800 GHz and 1100 GHz center frequencies. It remains to be seen if it is in practice possible to keep the tolerances , e.g. in block fabrication and assembly low enough to realise the bandwidth. I have improved the total design with adding a matching element at the side of port 1. This is done by introducing an extra micro-bridge to the L1 line. In general, this makes the L1 line to be as a T matching network type with new bridge as a capacitor to GND and two inductors with L3 and L1-L3 lengths. The final design and its frequency response are depicted in figures 3.16 and 3.17 , respectively. The bandwidth tunes by changing the location of this added bridge. The optimum values for L3 and L1-L3 are 37.5 $\mu$m and 12.5 $\mu$m where the new L1 is the same as before 50 $\mu$m. The new L2 is 55 $\mu$m. The length of slotline radial stub is 16 $\mu$m. The S-parameters show that both S1,1 and S4,4 cover 800 GHz and 1100 GHz with lower than -10 dB at 900 GHz. The solation between ports 1 and 4 is about -35 dB at 900 GHz. This number is at least 2 times improved compared to the reported isolation value (-15 dB at the mid of band) in [5] with using 90° RF branch line coupler. In addition, 0.25 dB amplitude imbalance between ports 2 and 3 when port 1 is excited in the whole band. This value is about -0.25 dB when port 4 is excited. There are at about zero phase imbalance at the mid of bandwidth between ports 2 and 3 when ports 1 and 4 are excited.

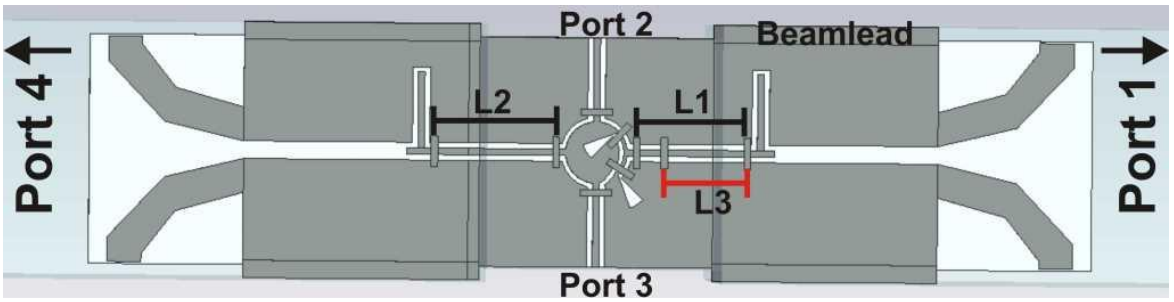


Figure 3.16: An integration of the hybrid-ring coupler with two TSAs+CPW-slotline transitions embedding a micro-bridge over the L1 line at the side of port 1. This is placed in the center of recangular waveguide with lateral dimension of 230×116 $\mu$m$^2$. There are beamleads to keep the GND connection to the waveguide wall with PEC surrounding.

The next step is to implement superconducting NbTiN material instead of PEC. The subsequent step would then have been to integrate the SIS mixer junctions to the ports 2 and 3 in figure 3.16. There need also two low pass filters (LPF), two DC/IF blocks and a impedance network to match the junctions to the hybrid-ring coupler. However, this project did not proceed anymore. This project was stopped due to the cut off the CCAT project budget from USA side and the high workload due to the development

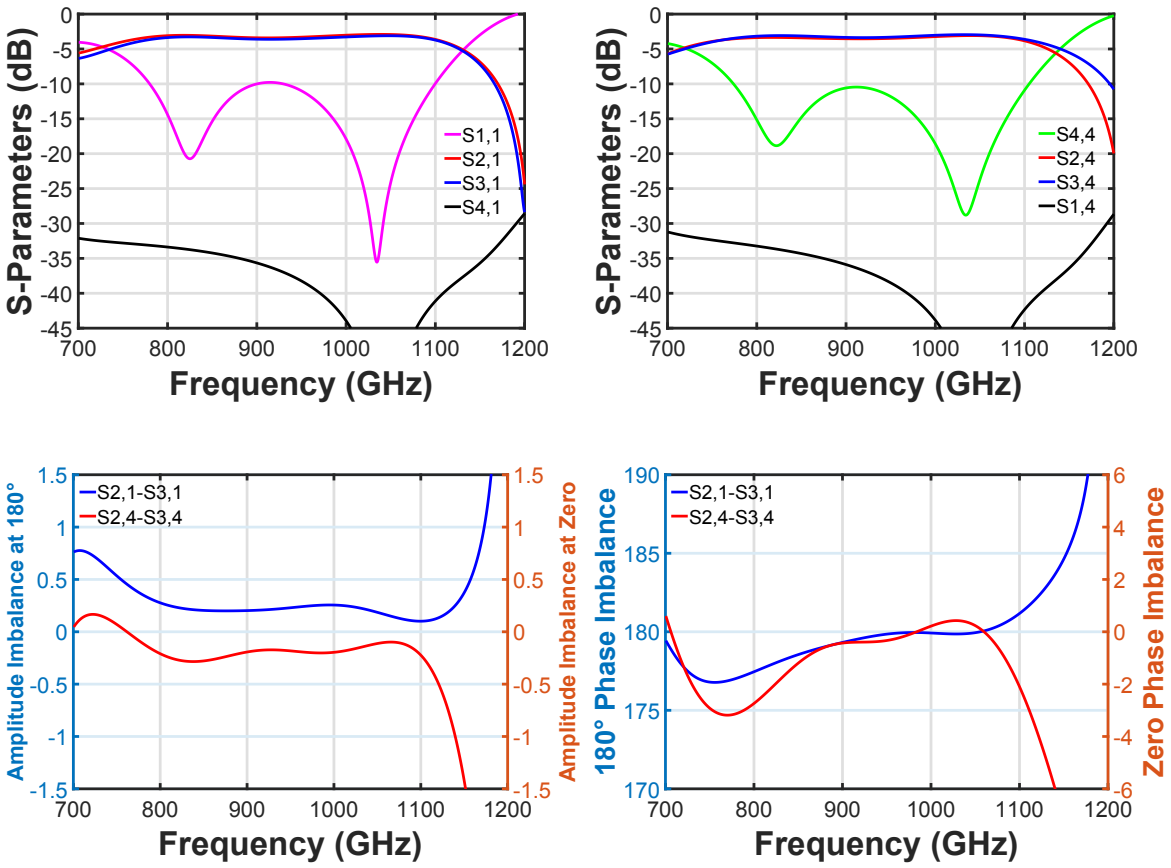


Figure 3.17: Simulated results of the final integration of hybrid-ring coupler with TSAs+CPW-slotline transitions embedding a micro-bridge over the L1 line at side of port 1. S-parameters, amplitude and phase imbalanced when ports 1 and 4 are excited.

for upGREAT [10], especially concerning the device and mixer block fabrications. It would not have been possible to fabricate the designed devices or the blocks. At that time, because of the LO power and tunability issues in the upGREAT receiver for SOFIA [10], my work was redirected towards the development of 1.9 THz balanced HEB mixers. The new 1.9 THz balanced HEB design approach builds on the gained knowledge from designing 800-1100 GHz balanced SIS mixers.

## 3.5 Non-crossover 1.9 THz Integrated Balanced HEB (IB-HEB) mixers

This section focuses on the design of 1.9 THz balanced HEB mixers with an integrated RF 180° hybrid-ring coupler. Because of the fact that with increasing frequency the size of circuit scales down, therefore the new circuit elements have smaller dimensions compared to the 800-1100 GHz balanced SIS mixers in Sections 3.2.2-3.4. Consequently, one needs to design more carefully and take into account all possible fabrication and assembly tolerances. Unlike the design in Section 3.4, here we do not need to cover two frequencies at the edge of lower and higher bands. The goal of this mixer is to detect the observational line at 1.9 THz, so there is no need for really broad band designs as the existing LO's like a QCL and a multiplier chain from VDI do not have more than few tens of GHz tunability.

It starts with designing of a 1.9 THz hybrid-ring coupler. At this frequency the radius of a ring is reduced to 9.7 $\mu$m length. The silicon substrate is chosen to be 3 $\mu$m thick. This thickness does not scale exactly from 6 to 3 $\mu$m as frequency increases from 800 GHz to 1.9 THz, but there were some 3 $\mu$m SOI wafers available in our micro-fabrication laboratory. The waveguide dimension is $100\times50$ $\mu m^2$, determined by the existing upGREAT LFA horns, which has about 1.5 THz cut off frequency.

Because it is not possible to scale the lower frequency design with one factor up to 1.9 THz, there is need for a detailed re-design. As we discussed earlier, the superconducting material candidate for THz frequency devices is NbTiN. But as we have shown in figure 3.9, the resistance of this material increases drastically at above 1.1 THz. Since we presently do not have a superconducting material with a higher gap frequency at our disposal, like e.g. $MgB_2$ [23], we use Au as a normal metal to wire our mixers. In order to implement this into our simulations, we have calculated surface impedance of Au in the anomalous limit, see Subsection 2.5.1. The tabulated surface impedance of a 200 nm Au is implemented into the simulations as top and bottom metal electrodes of the design. The optimum length and angle of the slotline radial stubs are 9.5 $\mu$m and 35°, respectively. The final design of a 1.9 THz hybrid-ring coupler is depicted in figure 3.18. This design shows how small the size of the ring is at 1.9 THz, and that the center radial stub is almost as large as the size of the total ring. The three micro-bridges at the 180° reverse-phase T-junction are very close to each other which might cause some difficulties in device fabrication. Because of the limited space the 2 micro-bridges close to the radial stubs are only 1 $\mu$m wide. The other bridges are 2 $\mu$m wide, as was used at 800 GHz. We expect that by using E-beam lithography for

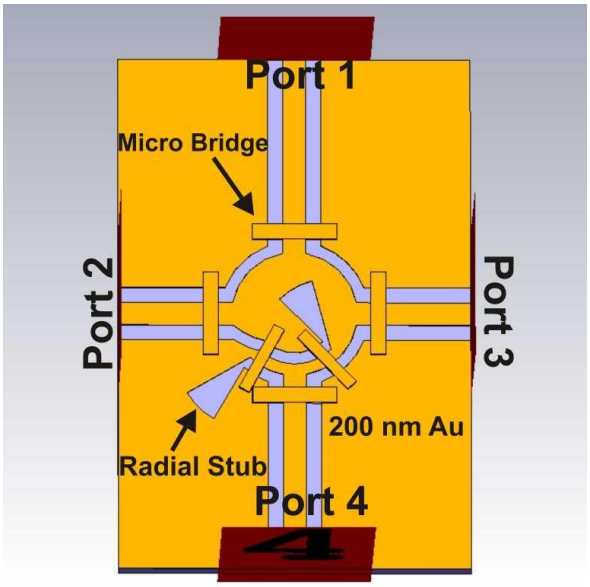


Figure 3.18: 1.9 THz hybrid-ring coupler with a 200 nm thick Au. It is a uniplanar coupler on a 3 $\mu$m silicon substrate.

fabrication, with a tolerance of 0.5 $\mu$m, still possible to fabricate.
The functional principle of the design is the same as mentioned earlier for 800-1100 GHz coupler in Subsection 3.2.2. The four CPW feed lines have width and gap of 3 $\mu$m and 2 $\mu$m which gives an impedance of about 50 $\Omega$. Ports 1 and 4 are connected to the 0° and 180° sides of the 1.9 THz hybrid-ring coupler. Here, Ports 2 and 3 are also 50 Ohm however later they will be connected to the two substrate channels with integrated HEB bridges. The two CPWs of the out-of-phase 180°T-junction have a size of 1.5 $\mu$m center line width and 1.5 $\mu$m gap width. This leads to a characteristic line impedance of about 58 $\Omega$. The two slots of the T-junction have a 1.5 $\mu$m slot width which is also about 58 $\Omega$. These impedance values are a bit lower than the values for 800-1100 GHz ring coupler due to the small size of the 1.9 THz coupler. There is 400 nm thick SiO2 under the micro-bridges. The complete design of the uniplanar 1.9 THz hybrid-ring coupler is depicted in figure 3.18. This is simulated in a frequency range of 1.2-2.6 THz and its S-parameters are shown in figure 3.19. The responses show that this ring coupler is a wide band with more than 1 octave bandwidth. At the center of band the isolation between ports 1 and 4 (S1,4) reaches to -50 dB. Reflections at the two excited ports 1 and 4 (S1,1 and S4,4 ) are about -20 dB at 1.9 THz. There are about $\pm$0.5 dB and -1 to +0.5 dB amplitude imbalances between ports 2 and 3 when ports 1 and 4 are excited, respectively. At 1.9 THz these imbalances reach to about -0.2 dB. The design shows a really good -3 dB power split to ports 2 and 3. There

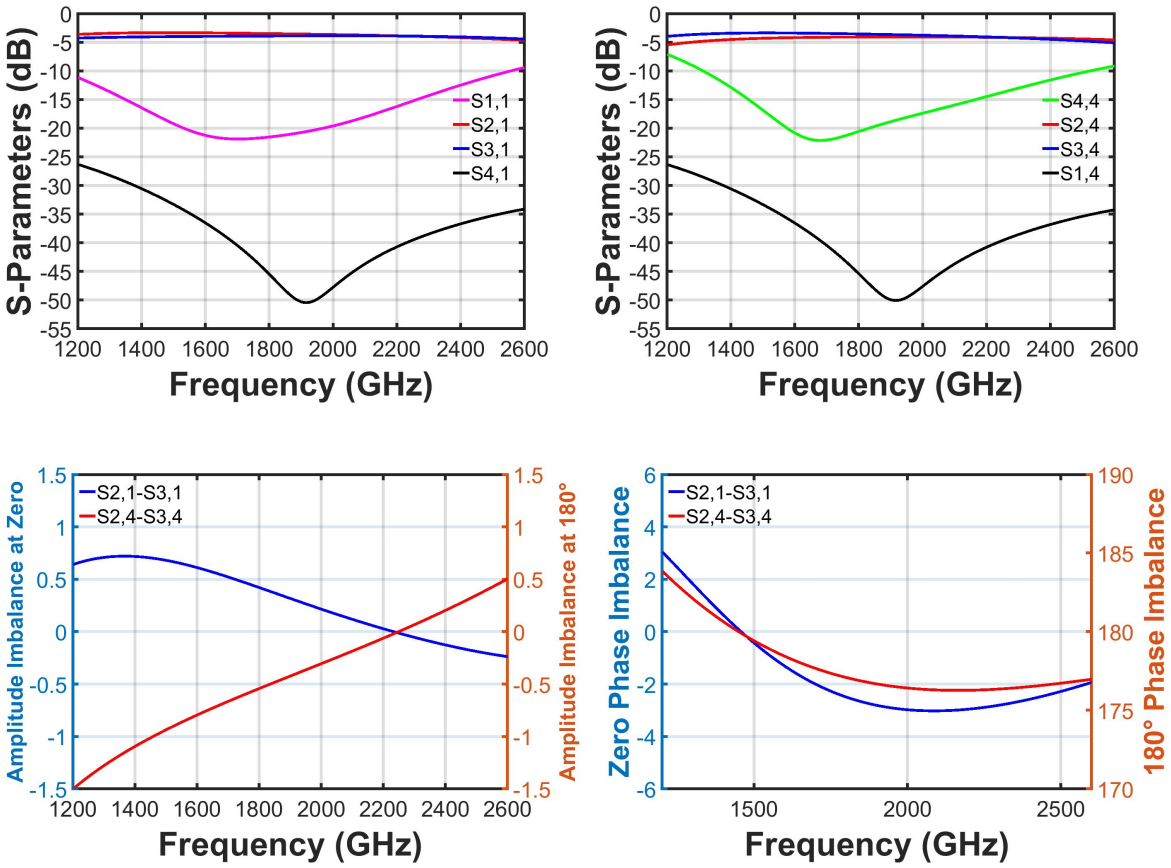


Figure 3.19: S-parameters of a planar 1.9 THz hybrid-ring hybrid coupler, Top-Left: when port 1 (0° side of the coupler) is excited. Top-Right: when port 4 (180° side of the coupler) is excited. Bottom-Left: the amplitude imbalance between ports 2 and 3 when ports 1 and 4 are excited. Bottom-Right: the phase imbalance between ports 2 and 3 when ports 1 and 4 are excited.

is about ±3° phase imbalance between ports 2 and 3 when port 1 is excited. This is about ±2° when port 4 is excited.

There is a need of a 1.9 THz planar E-field antenna to couple the incoming signal to the mixer chip. The design follows the principles of 800-1100 GHz slotline tapered antenna (TSA) reported in section 3.3. The new antenna design is shown in figure 3.20. It is integrated with a 1.9 THz CPW-slotline transition on a 3 $\mu$m silicon substrate. The design of the 1.9 THz CPW-slotline is based on the design of the transition at 800-1100 GHz from subsection 3.3.1. Port 1 is the waveguide port with free space impedance of 612 Ω. The waveguide dimension is 100×50 $\mu m^2$. It has about 1.5 THz cut off frequency. Port 2 is connected to the CPW line with a center line $W_C = 3$ $\mu$m and gap $G_C = 2$ $\mu$m impedance of about 50 Ω. As we already mentioned, at this

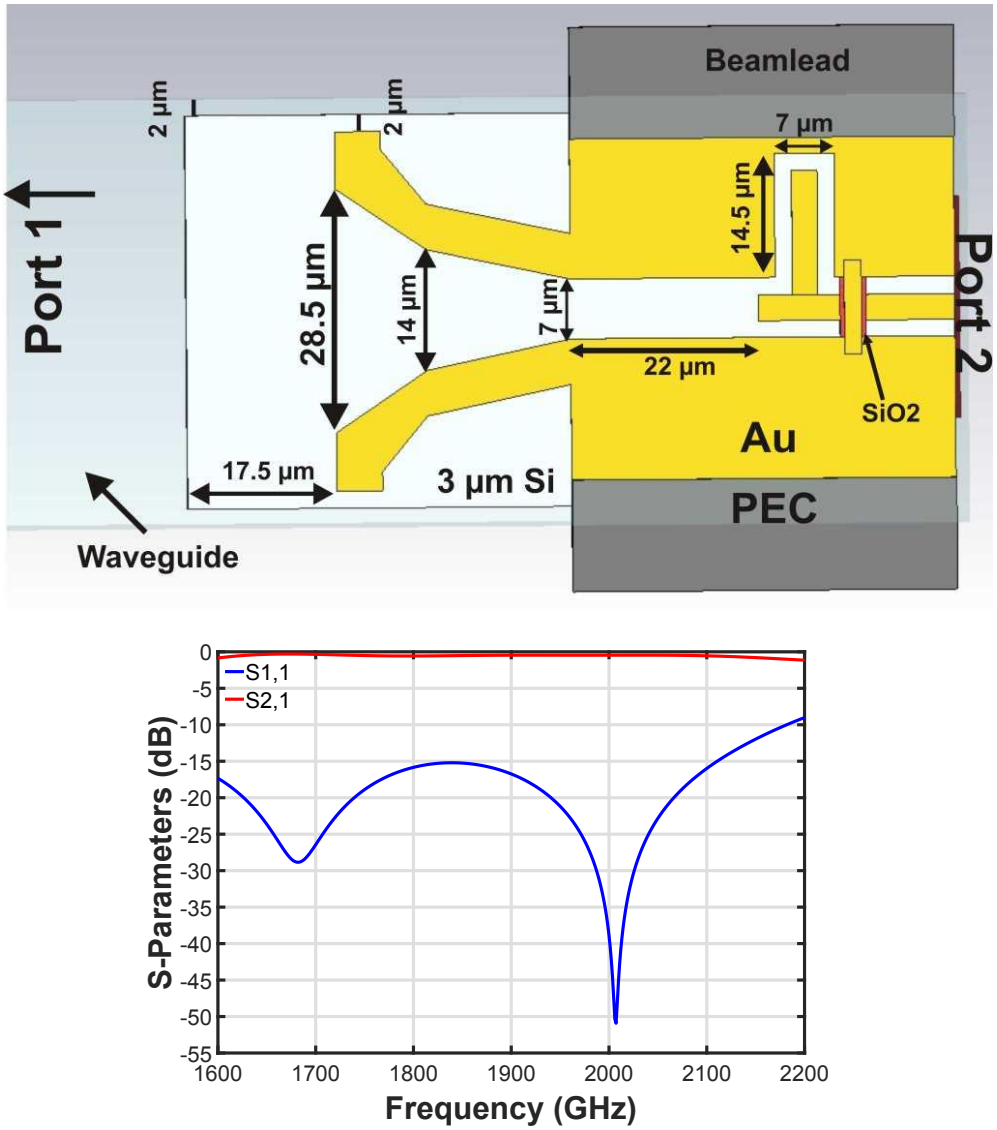


Figure 3.20: An integration of a 1.9 THz antenna with a CPW to slotline transition on a 3 $\mu$m silicon substrate. Simulated S-parameters are also plotted. S1,1 (blue curve) is the reflection of the incoming signal at port 1. S2,1 (red curve) is the transmission of the signal from port 1 to port 2.

frequency dimensions are critical. Therefore, tolerances must be carefully taken into account.

The silicon substrate is placed in the center of waveguide with a distance of 2 $\mu$m away from the waveguide walls. This is important to have enough tolerance for mounting the silicon membrane inside the waveguide. We have introduced about 2 $\mu$m gap between antenna tips to the silicon edges. This has been applied to accommodate possible fabrication tolerances. About 17.5 $\mu$m silicon is extended into waveguide to

enhance the coupling of the signal to the chip. The end of the TSA reaches to the slotline with a width of 7 $\mu$m. The coupled signal transmits the distance of 22 $\mu$m in slotline mode. This is the optimum distance for matching the 1.9 THz TSA to the CPW-slotline transition. After that, the signal splits between two slots. One of them transmits about $\frac{\lambda}{2}$= 2×14.5 $\mu$m longer path. Both reach to the CPW line with a 180° phase difference continue as a signal with the CPW mode. For more details about the working principle of this transition, see the Subsection 3.3.1. Two beam leads are added to our simulations for GND contacts. In the real case they are used also for bonding the device on to the machined waveguide block. The simulated results of this integration is depicted in figure 3.20. It shows a broadband response from 1.6-2.2 THz. The reason that we have not taken frequencies lower than 1.6 THz is because of being close to the cut-off frequency of the waveguide. This makes the simulations unstable and the results can not be trusted. The transmission from port 1 to port 2 (S2,1) is about -0.46 dB at 1.9 THz. The simulation with PEC instead of the Au has transmission about -0.13 dB. This means the implemented 200 Au as a metal layer in the integration has about 0.33 loss to the transmission between ports 1 and 2.

### 3.5.1 DC/IF blocking capacitors

RF and LO signals are mixed down to the IF frequency signal with the two HEB mixing elements integrated into ports 2 and 3 from the hybrid-ring coupler in figure 3.18. Also, the HEBs need to be DC biased for mixing. Therefore, the DC currents are blocked by integrating a DC/IF block before each of the HEBs. In addition, this DC/IF block reflects back the generated IF to the device output, for more details about the layout see Subsection 3.5.3. The final design of the blocking capacitor is depicted in figure 3.21. The center line of the CPW line is connected to two capacitors in series with 400 nm thick SiO2 as a dielectric. They are connected electrically at their top electrodes and are separated at the bottom electrodes with a 1.5 $\mu$m gap filled by SiO2. The bottom electrodes are 1 $\mu$m extended more to avoid any DC connection to the top electrodes due to any possible fabrication tolerances. Each parallel plate capacitor has a 7 $\mu$m length and 9 $\mu$m width for bottom and top electrodes and a 400 nm SiO2 with 3.75 relative dielectric constant. This gives the capacitance about 0.6 nF with calculating based on Eq.3.16.

$$C_{parallel-plate} = \frac{\varepsilon_r A}{d}. \tag{3.16}$$

There are two micro-bridges at the input and output of the blocking capacitors to permit only the transmission of the desirable mode of the CPW. These capacitors in series fully transmit the incoming signals at the desired RF frequencies but they are an open circuit for the generated IF frequencies and DC currents. The frequency response of the DC/IF block is depicted in figure 3.21. It shows a high transmission from port 1 to port 2 (S2,1) at RF frequencies higher than about 1600 GHz and at the lowest about -60 dB transmission at the DC and IF frequencies (the IF noise bandwidth of our HEB mixers is in the range of 0.5-3 GHz).

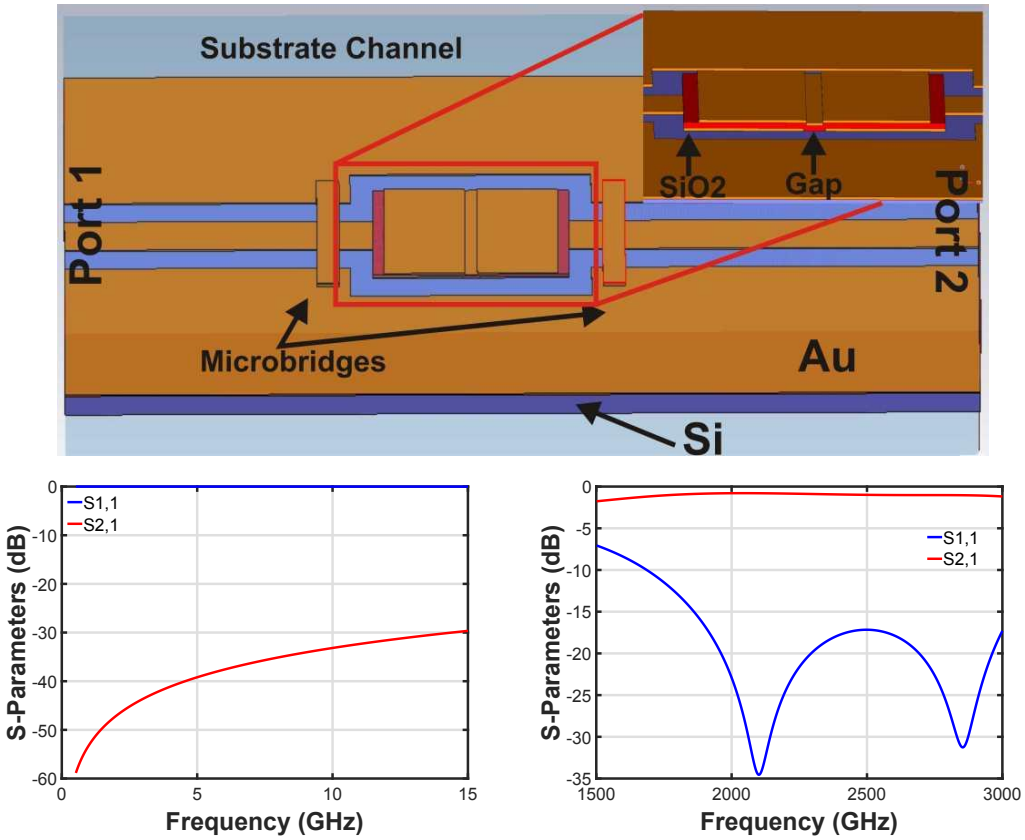


Figure 3.21: DC/IF block capacitors in series with a 200 nm thick Au as a metal layer and 400 nm thick SiO2 as a dielectric. Simulated S-parameters at the RF and IF frequencies when the port 1 is excited.

### 3.5.2 CPW based Low Pass Filter (LPF)

Low pass filter (LPF) is one of the key elements in single ended and balanced mixer circuits, see figure 3.1. The ideal LPF's reflect any RF signal to prevent it from leaking away, reducing the conversion of the mixer. In addition the filter transmits the IF and the DC signals. As my HEB mixer circuitry is CPW based therefore the aim is to

design a CPW-LPF. The final design is shown in figure 3.22. The LPF is a three stages filter consisting of a network of capacitors and inductors. There are three large capacitors paralleled to the CPW line and two inductors in series. The capacitance of these three parallel plate capacitors with 16 $\mu$m long and 7 $\mu$m wide and 400 nm thick SiO2 is C1=C2=C3=1.05 nF. One should notice that the top electrodes are extended to the GND. Therefore, the region gives the capacitance is where the top electrode has SiO2 and bottom electrode under it. Two CPW based inductors have optimum length of L1=L2=13 $\mu$m. There is a micro-bridge at the RF side (port 1) to maintain the wanted CPW mode. At the port 2 side is also a bridge at the IF circuitry shown in figure 3.37. The simulated S-parameters at IF and RF frequencies are depicted in figure 3.24. It shows totally transmitted (S2,1) at IF frequency and about -40 dB reflection of S2,1 at the desired RF frequency band.

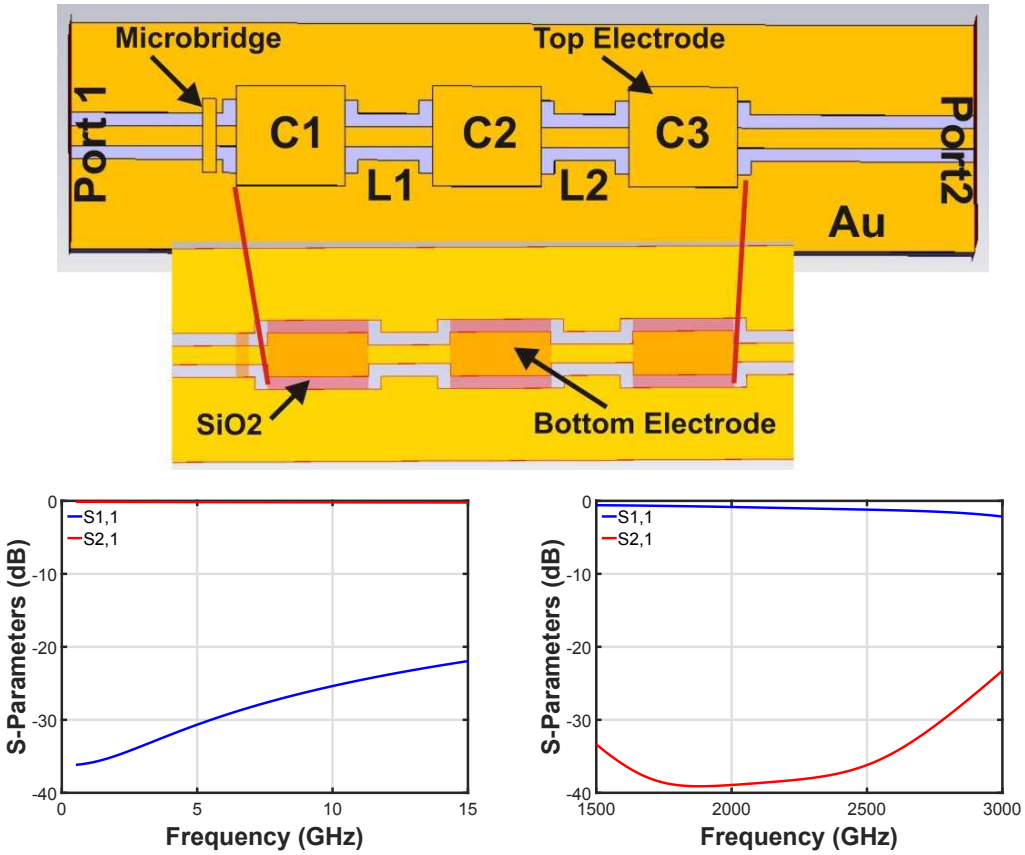


Figure 3.22: Three stages LPF consisting of three grounded capacitors (C1, C2, C3) to the CPW line and two CPW lines (L1, L2) acting as inductors. The simulated S-parameters at the IF and RF frequencies.

### 3.5.3 Integration of the IF blocking capacitor and the RF-LPF with a HEB bridge

Here, a HEB bridge is integrated with the DC/IF block from Subsection 3.5.1 and LPF from Subsection 3.5.2. In addition, the substrate is placed in a substrate channel which is a waveguide with lateral dimension of 20×34 $\mu$m$^2$. Here, HEB bridges are implemented in my designs as a discrete port with impedance of 120 Ω. This value is in principle the $R_N$, the normal state resistance of the HEB at 20 K. It is measured in the RT-curve of the HEB. The resistance is determined during fabrication by adjusting the aspect ratio of the HEB bridge. If the sheet resistance $R_sheet$ of the HEB material is (approximately) known, the impedance $Z_HEB$ is given by the aspect ration ($\frac{L_{HEB}}{W_{HEB}}$) times the sheet resistance

$$Z_{HEB} = \frac{L_{HEB} R_{Sheet}}{W_{HEB}}, \tag{3.17}$$

where $W_{HEB}$, $L_{HEB}$ and $R_{Sheet}$ are width of Au contacts, length between two Au contacts and sheet resistance of about 4.5 nm NbN film, see figure 3.23. $Z_{HEB}$ is the impedance of the HEB bridge. As an example $R_{Sheet}$ is about 1600 Ω/square which results in a 120 Ω impedance with the $W_{HEB}$ = 3 $\mu$m and $L_{HEB}$ = 200 nm. In my

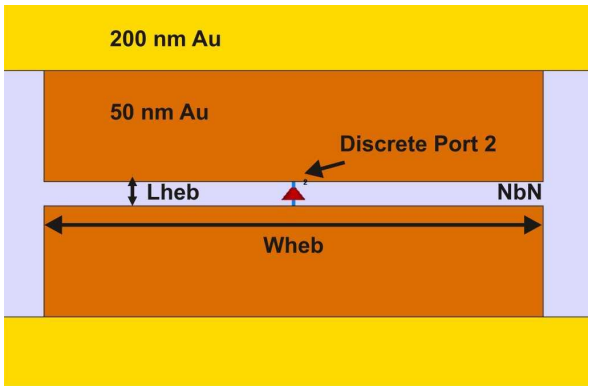


Figure 3.23: Zoom into the HEB bridge with Au contacts and superconducting NbN layer. The HEB bridge is simulated as the 120 Ω discrete port.

simulations, HEBs are replaced by 120 Ω discrete ports. The HEB bridge is located inside one of the slots of the CPW line. It is connected by 50 nm thick Au contact pads to the CPW center line and to the GND of the circuit. All of the elements are integrated on a 3 $\mu$m silicon substrate and simulated, see figure 3.24. It needs a careful design to match the combination of the blocking capacitor, HEB and LPF to the 50 Ω ports (port 2 and 3) of the ring coupler. I have done several rounds of simulations to find the relative optimum position of the DC/IF block, the HEB bridge

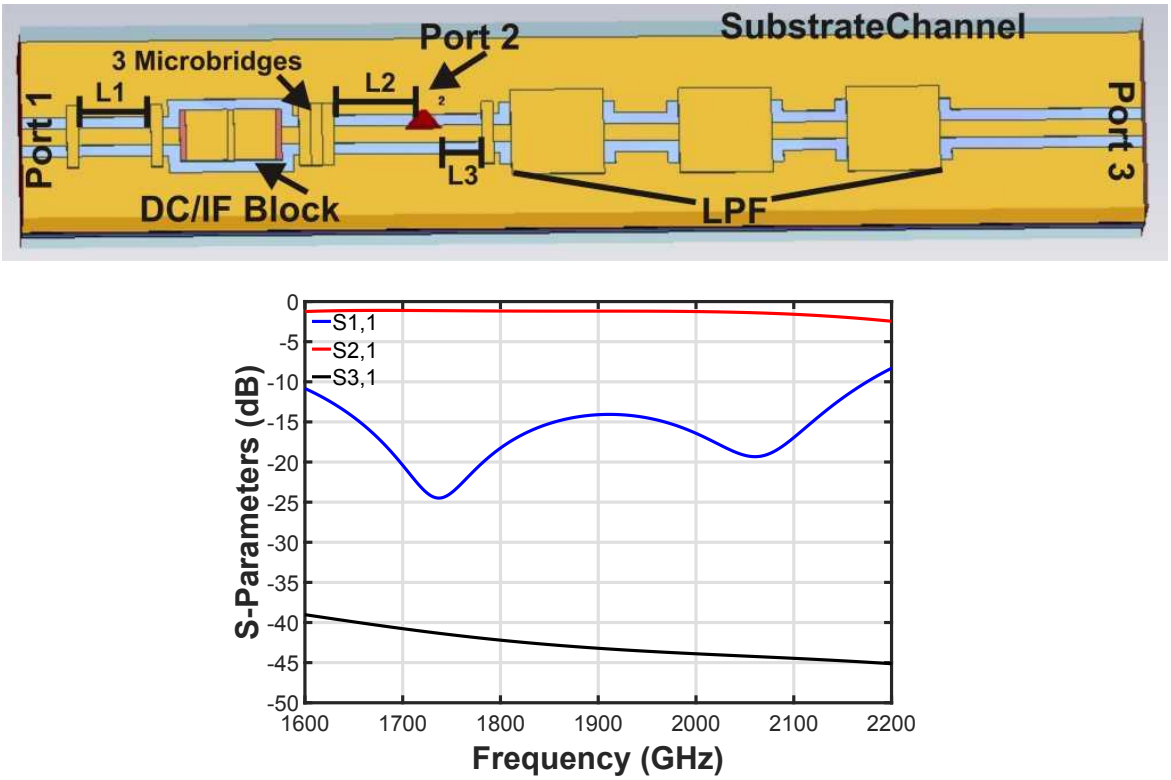


Figure 3.24: A HEB arm consisting of integration of the LPF, the DC/IF block and the HEB bridge. It is placed in the substrate channel with lateral dimension of 20×34 $\mu$m$^2$. The length of 20 $\mu$m is the height of the substrate and 34 $\mu$m is the width of channel. The frequency response is shown when the port 1 is excited. The blue curve as reflection at port 1, the red curve transmission from port 1 to the discrete port 2 and the black curve is the filtered RF signal from port 3.

and the LPF. Some extra micro-bridges are added as small capacitors to make a Pi-matching networks with inductors (CPW straight lines) between them. I have seen in my simulations that the 3 micro-bridges set is necessary to introduce more capacitance to for improving the S1,1 at the mid of the bandwidth, where $L1 = 12.5$ $\mu$m, $L2 = 13.5$ $\mu$m and $L3 = 8$ $\mu$m. As the HEB bridge is placed in one of the slots of CPW therefore it sees the RF incoming signal in two paths. Part of it travels over L2 and the rest travels over $L2+2\times L2$. Therefore, it is crucial to get the correct L2 and L3 in a way that these signals add up constructively at the HEB. The generated IF also travels in both directions. However at the IF frequency is not at all critical because L2 and L3 are very much smaller than the wavelength. The transmission loss from port 1 to the HEB is about 1.2 dB at the 1.9 THz. However when the implemented 200 nm Au is replaced by PEC is about 0.2 dB. Therefore, there is about 1 dB loss introduced by Au to the transmission of RF signal to the HEB.

### 3.5.4 Non-crossover integrated 1.9 THz balanced HEB with 2 HEBs

In this step, all designed RF elements of the mixer circuit are integrated on one 3 $\mu$m silicon substrate. A 200 nm thick sputtered Au is used for the bottom and top electrodes. The 400 nm thick SiO2 is applied as a dielectric layer. The optimum final design of a non-crossover 1.9 THz balanced HEB mixer with 2 HEBs is shown in figure 3.25. This design consists of one HEB per substrate channel. For the design with 2 HEB bridges per substrate channel, see Subsection 3.5.5. It is called non-crossover because the two IF outputs (ports 5 and 6) of this design are at the opposite side without an IF-RF crossover. For the crossover design type, see Section 3.6. The dimensions of the waveguide and the substrate channels are 100×50 $\mu m^2$ and 20×40 $\mu m^2$, respectively. There are about 2.5 $\mu$m Au thick beam leads for contact and registration of the device on the waveguide block. The cryogenic THz properties of Au implemented into CST as a tabulated surface impedance as a function of frequency. For use in the simulation these tables are fitted with a function inside CST suite, see Subsection 2.5.1. Ports 1 and 4 are for the incoming RF and LO signals. Ports 2 and 3 are discrete ports with 120 Ω, the normal state resistance of the HEB bridges, and ports 5 and 6 are the IF output ports of the mixer device. The RF input impedance of the HEB arms is approximately 50 Ω, matched to the ports 2 and 3. Also, there is need to avoid any additional loss in Au by a longer path length. Therefore, the ideal case is to integrate HEB arms as close as possible to the hybrid-ring coupler. However, in my simulations I have seen that when the substrate is inside the waveguide, some amount of the incoming RF signal jumps over the channel. This means the HEB arm acts as an extra antenna and catches some of the propagated RF signal in the waveguide. Consequently, the optimum 12 $\mu$m extra length is introduced between the substrate channels and the output ports of the hybrid-ring coupler towards ports 2 and 3. There is a need of an additional matching procedure. This is needed due to the new impedance which ports 2 and 3 of the hybrid-ring coupler see after adding the substrate channels and the additional CPW line. The matching is achieved by changing the CPW line distance (varying the inductance) between the micro-bridges at the slotline-CPW transitions and micro-bridges at the 0° and 180° sides of the hybrid-ring coupler. This distance at the both sides is equal to 5 $\mu$m. The complete 1.9 THz non-crossover balanced HEB mixer with two HEBs is simulated and its S-parameters are shown in figure 3.26. The isolation between the excited ports 1 and 4 (S1,4 or S4,1) is about -35 dB over the whole bandwidth from 1.6-2.1 THz. The

transmission to ports 2 and 3 when ports 1 and 4 are excited, show about -5.2 dB instead of -3 dB which mostly due to the loss of the implemented 200 nm Au. The reflections at ports 1 (S1,1) and 4 (S4,4) are about -15 dB at 1.9 THz. The excited signal at port 1 is filtered out (reflected back) before reaching to the IF ports 5 (S5,1) and 6 (S6,1) with about -45 dB. This value is also about -45 dB when port 4 is excited. There is a maximum $\pm 0.5$ dB amplitude imbalance between ports 2 and 3 when port 1 is excited. This value is even less when port 4 is excited. At 1.9 THz the amplitude imbalances reaches to about 0 dB. There are about $2^{\circ}$ phase imbalances between ports 2 and 3 when ports 1 and 4 are excited.

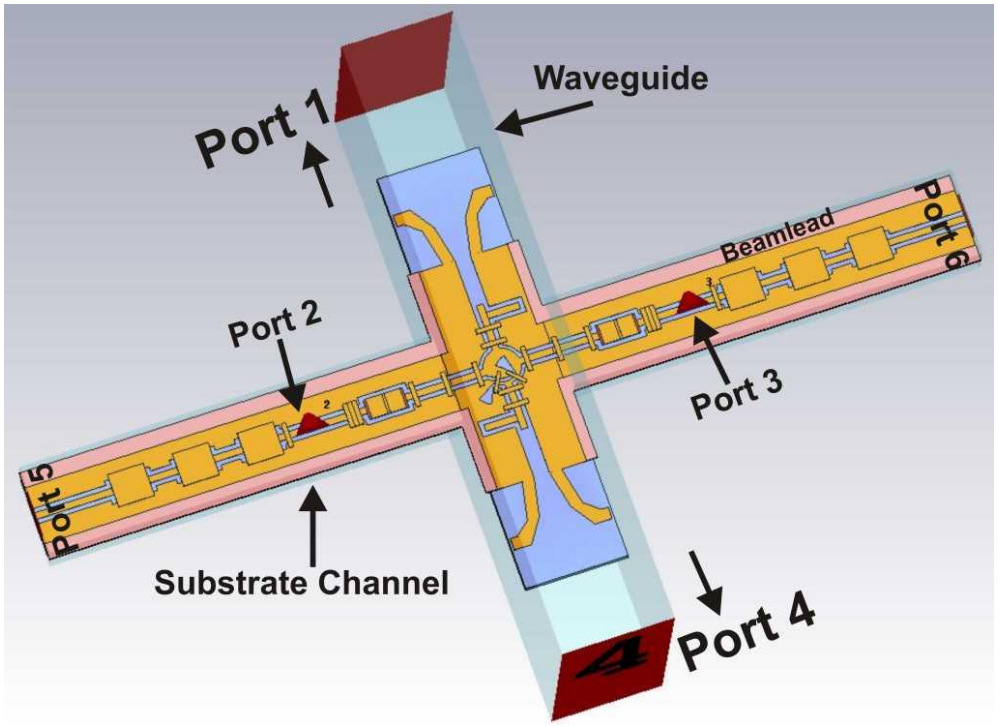


Figure 3.25: The complete on-chip RF circuitry of a 1.9 THz non-crossover balanced HEB with one HEB bridge per substrate channel. There are beam leads for GND connections (in pink). These are also used for registration when mounting the device inside of the waveguide and substrate channels. Ports 1 and 4 are waveguide ports for incoming signals. Two 120 $\Omega$ discrete ports 2 and 3 are implemented as HEB bridges. Ports 5 and 6 are two IF outputs of the mixer device.

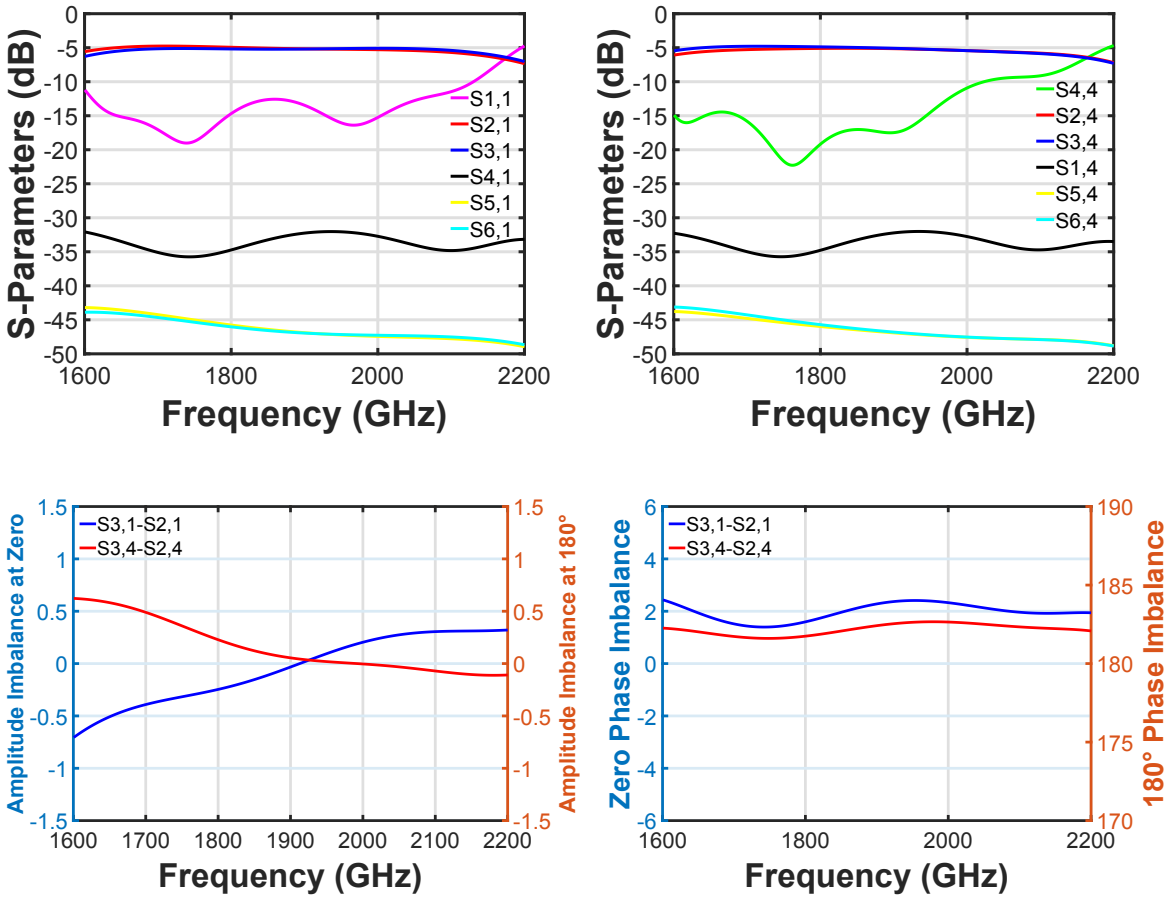


Figure 3.26: S-parameters of the complete on-chip 1.9 THz balanced HEB mixer with one HEB bridge per substrate channel, Top-Left: When port 1 at the 0° side of the hybrid-ring coupler is excited, Top-Right: When port 4 at the 180° side of the hybrid-ring hybrid coupler in excited, Bottom-Left: Amplitude imbalances in dB between ports 2 and 3 when a signal is excited at port 1 (S3,1-S2,1) and at port 4 (S3,4-S2,4), Bottom-Right: Phase imbalances in degrees between ports 2 and 3 when a signal is excited at ports 1 and 4.

### 3.5.5 Non-crossover integrated 1.9 THz balanced mixers with 4 HEBs

The design of the 1.9 THz non-crossover balanced HEB with one HEB bridge per substrate channel is presented in Subsection 3.5.4. The HEB bridge is placed in one of the slots of CPW lines, which causes an asymmetry. In order to keep all configurations symmetric, I have added a variation of the design with an additional HEB bridge parallel to the existing HEB bridge in the opposite slot of the CPW line. As with the situation of one HEB per substrate channel design, here the RF- and LO-signal travel

exactly the same length to reach to the two parallel HEBs. The reflected RF/LO signal from the LPF also sees the same distance of the CPW line to reach back to the two HEBs. In addition two generated IF signals by the two HEBs travel the same distance towards the output and reflecting back from the DC/IF block. This is an experimental configuration to check out if this configuration creates a more balanced situation. The total impedance of the two HEBs in parallel is chosen to be 90 Ω that is 180 Ω per HEB. This impedance value based on Eq.3.17 for $L_{HEB}$ is 200 nm, results in $W_{HEB} = 1.85$ $\mu$m. Considering the new impedance value and the configuration of the two HEB bridges placed in the two slots of the CPW line, the new HEB arm needs to be designed separately with the same principles as in Subsection 3.5.3. After that, by tuning the CPW length between the micro-bridges of the CPW-slotline transition and the hybrid-ring coupler at the side of ports 1 and 4. The optimum final design and simulated frequency response of the 1.9 THz balanced HEB mixer with two HEBs on each substrate channel is depicted in figure 3.27. The elements of the circuit are

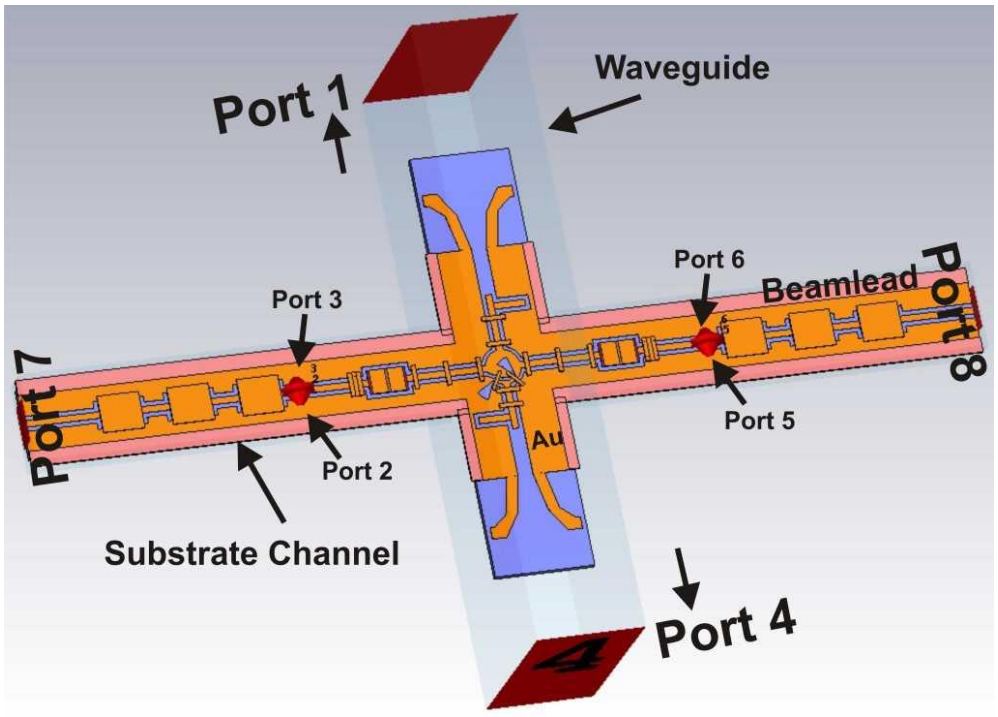


Figure 3.27: The complete integrated 1.9 THz 180° balanced HEB with 2 HEBs per substrate channel. Discrete ports 2, 3, 5 and 6 are as HEB bridges each with 180 Ω. The lateral dimension of the waveguide and substrate channels are 100×50 $\mu$m$^2$ and 20×34 $\mu$m$^2$, respectively.

integrated on a 3 $\mu$m silicon. The 200 nm Au is implemented for bottom and top electrodes and 2.5 $\mu$m thick Au for the beamleads. Ports 1 and 4 are for the RF and

LO incoming signals, respectively. The 180 Ω discrete ports 2, 3, 5 and 6 are as the HEB bridges. Ports 7 and 8 are as the IF outputs. The zoom into the right the HEB arm is also shown in figure 3.28. After several line length tuning, adding or removing micro-bridges and changing the position of HEB bridges the optimum achieved values are as the following $L_1 = 10$ $\mu$m, $L_2 = 5$ $\mu$m, $L_3 = L_4 = 13$ $\mu$m, $L_5 = 22$ $\mu$m and $L_6 = 4.6$ $\mu$m. Again, the two micro-bridges at the two slotline radial stubs have a width of 1 $\mu$m while all other micro-bridges are 2 $\mu$m wide with a 400 nm thick SiO2 as a dielectric. This design is added to the same lithography mask with the balanced mixer circuit mentioned in Subsection 3.5.4, for more details see Section 4.1.

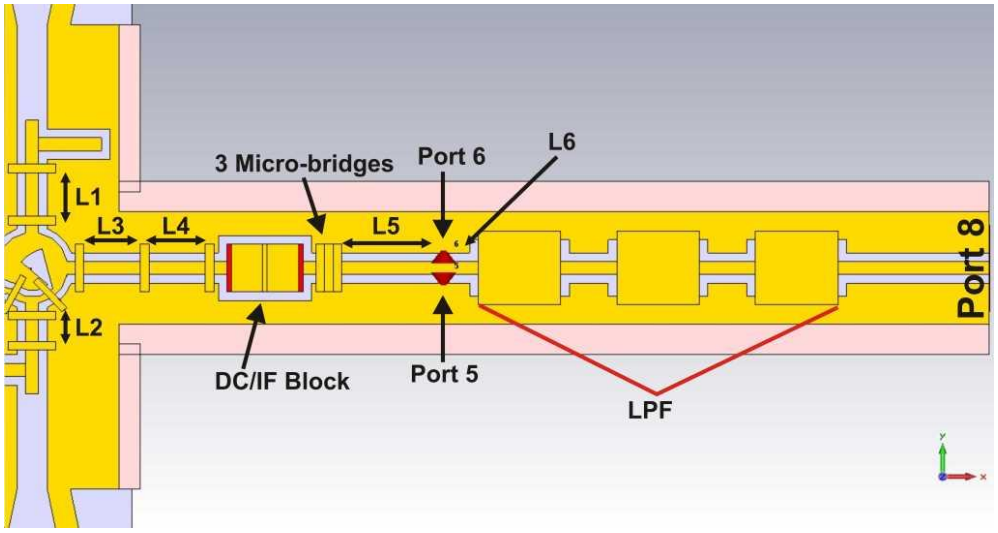


Figure 3.28: Zoom in view of the 1.9 THz integrated 180° balanced HEB with 2 HEBs per substrate channel.

The simulated S-parameters of the final design are depicted in figure 3.29. The transmission from port 1 or 4 to ports 2, 3, 5 and 6 instead of -6 dB per HEB bridge is about -8 dB at 1.9 THz due to the loss in implemented 200 nm Au. The isolation between ports 1 and 4 (S1,4) or (S4,1) is about -35 dB in the whole band. The amplitude imbalance between ports 2, 3 and 5, 6 when port 1 (0° side) is excited is about 0 at the 1.9 THz and $\pm 0.4dB$ at the edges of the bandwidth. The phase imbalance is about -2.5° in almost entire band. The amplitude imbalance between ports 2, 3 and 5, 6 when port 4 (180° side) is excited is about -0.1 dB at 1.9 THz, about 0 dB at the high side of the bandwidth and -0.5 dB at the lowest side of the bandwidth. For phase imbalance the value is 2.5°. The RF signals of the excited ports 1 and 4 are filtered out from IF-ports 7 and 8 by about -50 dB.

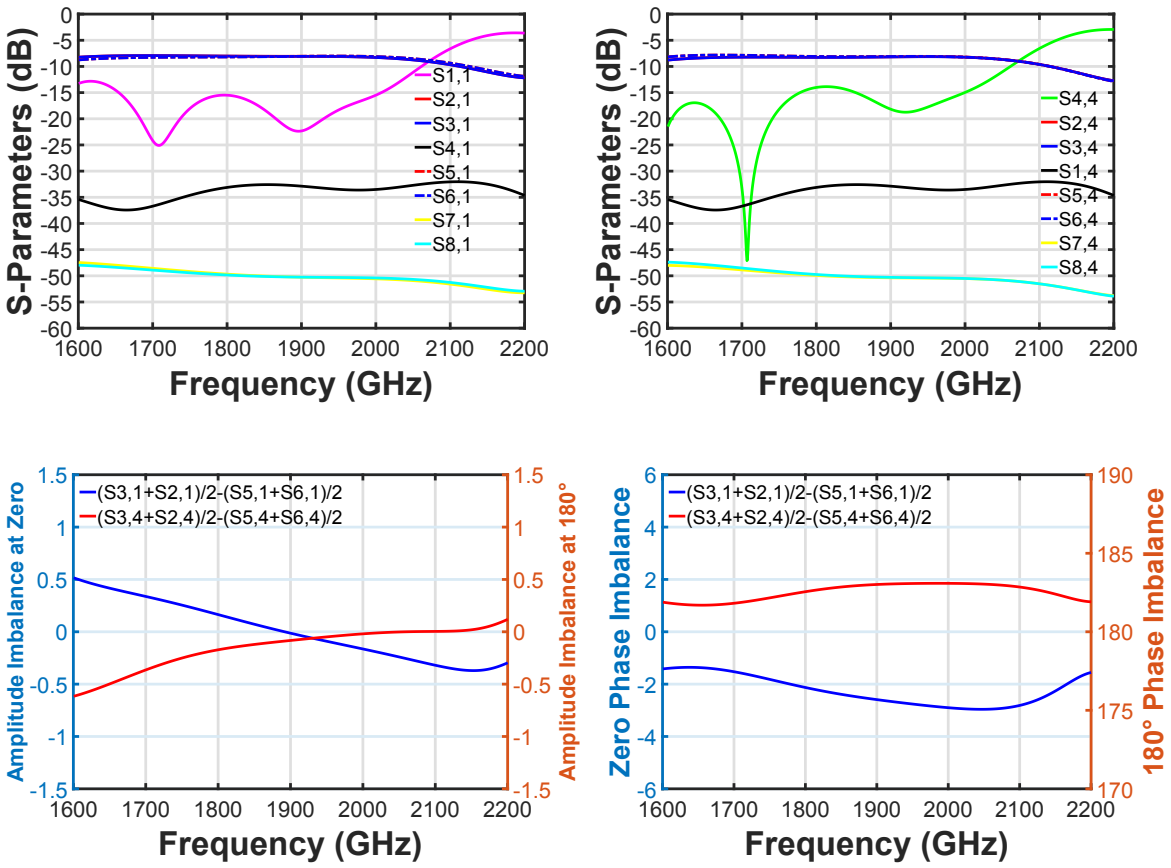


Figure 3.29: S-parameters of the complete on-chip non-crossover 1.9 THz integrated 180° balanced HEB mixer with 2 HEB bridges per substrate channel, Top-Left: When port 1 at the 0° side of the hybrid-ring coupler is excited, Top-Right: When port 4 at the 180° side of the hybrid-ring coupler in excited, Bottom-Left: Amplitude imbalances between ports 2, 3 and 5, 6 when the RF signal is excited at port 1 ((S3,1+2,1)/2-(S5,1+S6,1)/2)) and at port 4 ((S3,4+2,4)/2-(S5,4+S6,4)/2)), Bottom-Right: Phase imbalances between ports 2 ,3 and 5, 6 when the RF signal is excited at ports 1 and 4.

## 3.6 Crossover integrated 1.9 THz balanced HEBs

Up to now, I have reported the design of balanced HEB mixers with two separated IF outputs. However, there is a big interest to design an integrated 180° balanced HEB mixers with two IF outputs at one side of the substrate to reduce the complexity in building focal plane arrays. The crossover type simplifies the combining of the two IF outputs with the integrated IF 180° hybrid or IF Wilkinson immediately after the mixers, so only one amplifier per balanced pixel is necessary. Compared to the previous designs, one needs to bend one of the IF outputs and extend it in parallel to the side of

other IF output. That means this CPW line carrying the IF signal crosses the CPW line with the launched RF signal (from the waveguide side) feeding the hybrid-ring coupler. For this purpose, the first step is to design a CPW-CPW crossover with the lowest coupling between two lines. [68] reported two types of CPW-CPW crossover junctions with air bridges on 410 $\mu$m silicon substrates with low coupling about -0.6 dB at the mid of the 2-40 GHz frequency range where both CPWs carry the signals at the same frequency. Here the crossover junction has been designed for the two lines, one transporting IF, and the other transporting RF frequencies. The micro-bridges are not bond wires but have an SiO2 support layer beneath the bridge. In addition, I have designed a 3-micro-bridges CPW-CPW crossover to reduce the coupling between two lines at the RF frequency. The designs of CPW-CPW crossovers with one and three micro-bridges are depicted in figures 3.30 and 3.31. For the case in figure 3.30, the RF signal on the CPW line transmits over the CPW line with the IF signal with helping of a 400 nm SiO2 isolation. There are two micro-bridges on the IF line (keeping the CPW mode to propagate). These also take care of ground plane continuity for the RF propagation. The simulated S-parameters of this crossover junction are plotted in IF and RF frequencies, see figure 3.30. At the IF frequency the transmission from port 1 to 2 (S2,1) when port 1 is excited is about 0 dB (totally transmitted). The reflection (S1,1) at the port 1 stays lower than -40 dB and coupling to the RF path (S4,1 & S3,1) is about -60 dB at frequency range of 0.5-3 GHz (IF noise bandwidth of a NbN HEB mixer). At the RF frequency the transmission from port 3 to 4 (S4,3) is about -0.73 at 1.9 THz and coupling to the IF path (S1,3 & S2,3) is about -13 dB. The reflection at the port 3 (S3,3) is about -23 dB in the frequency range of 1600-2200 GHz.
The coupling between the IF and RF paths is further reduced in the second design, see figure 3.31, by adding more capacitance (3 micro-bridges structure) in the IF path and two micro-bridges in the RF path before and after crossing of the lines for shorting out the any unwanted generated slotline mode. The simulation results of this new type of CPW-CPW crossover show reduction of the coupling to -80 dB at the IF frequency. At the RF frequency the transmission improves to -0.68 dB at 1.9 THz. The coupling of the RF signal to the IF path is reduced from -13 dB to about -18 dB. At the IF frequency also coupling is reduced to about -80 dB instead of -65 dB at 0.5 GHz. The final design of the crossover 1.9 THz integrated balanced HEB with one HEB per substrate channel is shown in figure 3.32. One of the HEB arms at the port 2 side is extended and 90° bent on the 3 $\mu$m silicon. The substrate is 47 $\mu$m wide in comparison to 34 $\mu$m in Subsection 3.5.4. This width has been chosen to be as narrow as possible to avoid any unwanted coupling wave from waveguide to

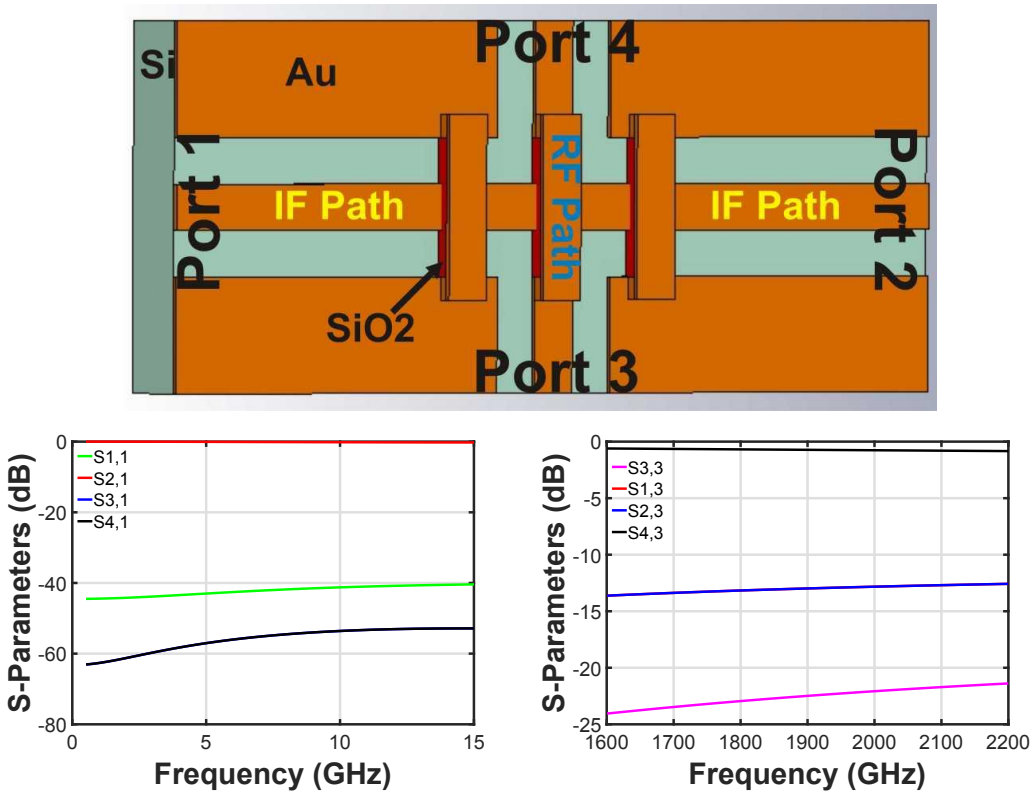


Figure 3.30: RF-IF crossover with one bridge in the IF path.

the substrate channels (transverse resonance). This parallel CPW line carrying IF signal generated at HEB mixer 2 (port 2) crosses the waveguide to the opposite side reaching to port 6 (at the same side of port 5). The 3 micro-bridges crossover junction is integrated at the 0° side of the hybrid-ring coupler (at the side of port 1) in figure 3.25 which is easier to match due to the less complex circuitry (no 180° out-of-phase T-junction). Subsequently, several matching methods are introduced for this new circuit structure. By integrating the crossover, the end of the CPW-slotline transition at the side of port 1 sees a different impedance than in the non crossover structure of figure 3.25. This new circuitry consists of the crossover, the hybrid-ring coupler and the crossing IF line. Therefore an optimum matching-structure with two Pi-networks of series inductors and parallel capacitors is added to the CPW line. Figure 3.33 shows the zoom into the crossover 1.9 THz balanced HEB circuit at the side of port 3. All the following reported optimum distances are achieved by studying many simulation iterations from the S-parameters to the E-field monitoring (figures 3.35 and 3.36). The L1 and L2 with 29 $\mu$m and 6 $\mu$m length are used as series inductors. The two additional micro-bridges (one added between L1 and L2 and the second to the crossover) act as capacitors with a 6 $\mu m^2$ area and a 400 nm SiO2 dielectric layer (capacitance of 0.5

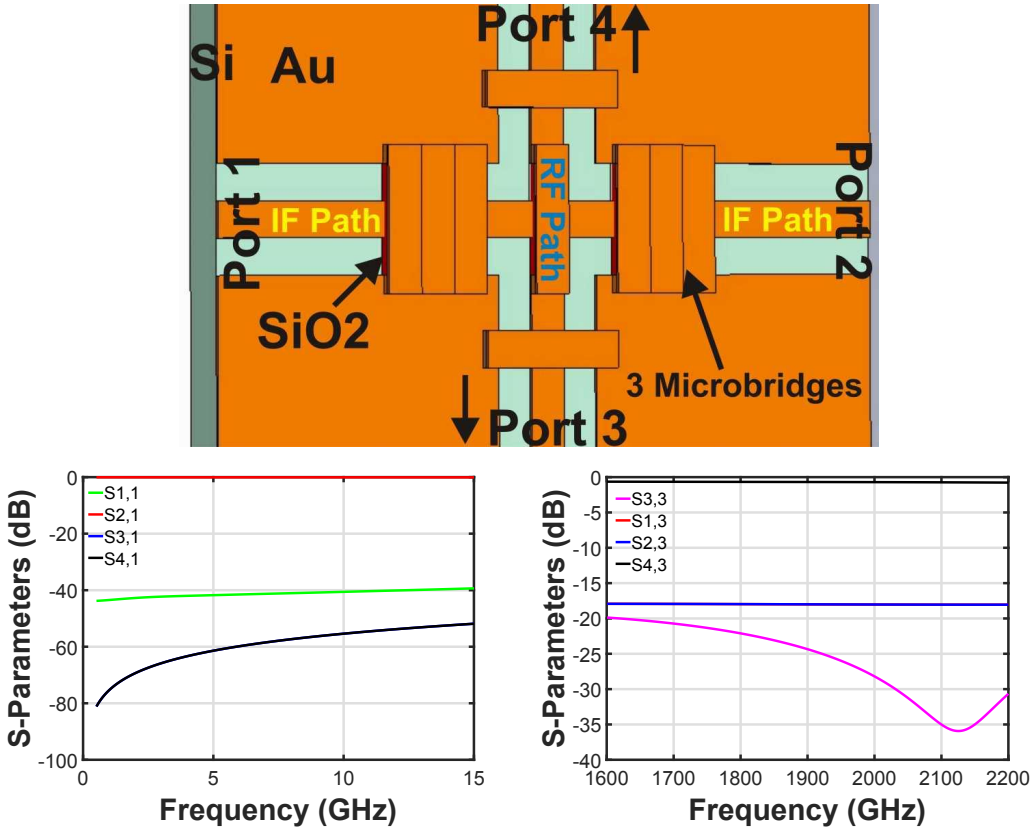


Figure 3.31: RF-IF crossover with three bridges in the IF path.

fF. Because the new bent CPW IF line is in parallel to the main CPW line, there are chances of coupling of signals at IF and RF frequencies directly between them. The RF coupled to the new line can be filtered out with adding an extra LPF on the extended IF line preferably same as the existing LPFs. However, there is a need of constructive interference of the reflected coupled RF by this additional LPF in the new line and transmitted RF in the original line. For this purpose, the additional LPF is shifted closer to the crossover with the optimum distance of $L4 = 19$ $\mu$m. That means by choosing the correct distance $(2 \times L4 + 2 \times L8)$, the RF signal coupled to the new CPW line and reflected back from the new LPF will have a delay such that when it is coupling back to the original line it has the same phase as the incident RF signal, see figure 3.35-bottom. The length of L8 is 12.5 $\mu$m which is a distance between the new and the original CPW lines.

The same principle of the constructive transmission and reflection of the RF signal is introduced when maximizing the transmission to the HEB. Some of the RF signal not directly absorbed by the HEB, reflects back from the LPF on the original line and unfortunately couples to the new line. It seems to reflect back from the last

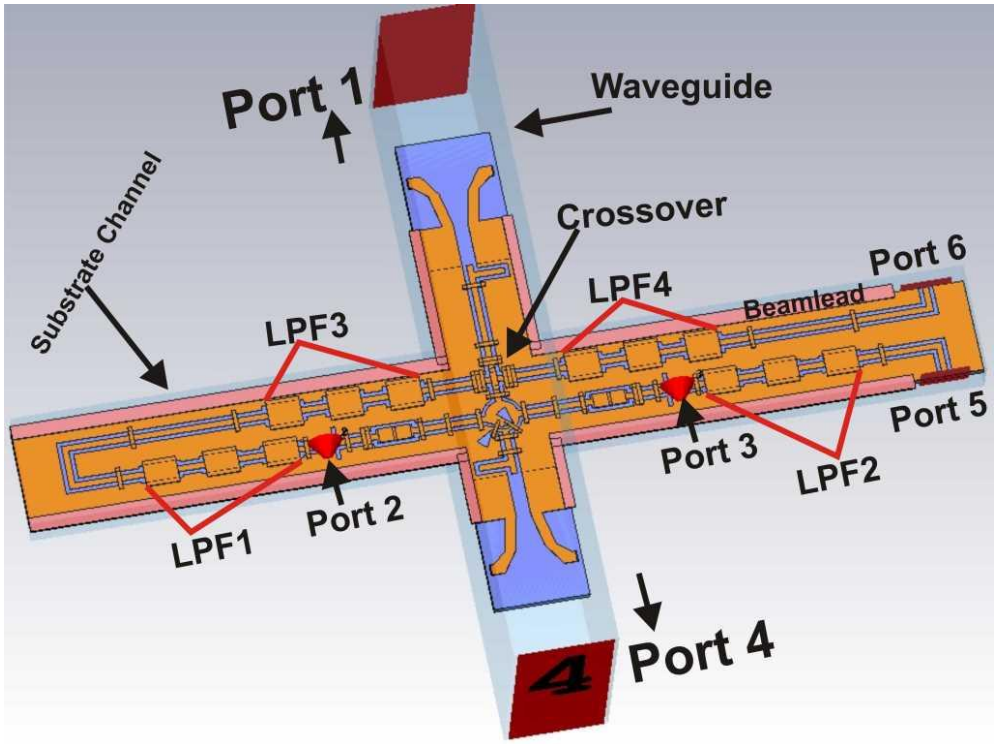


Figure 3.32: The complete view of a crossover 1.9 THz balanced HEB with one HEB per substrate channel.

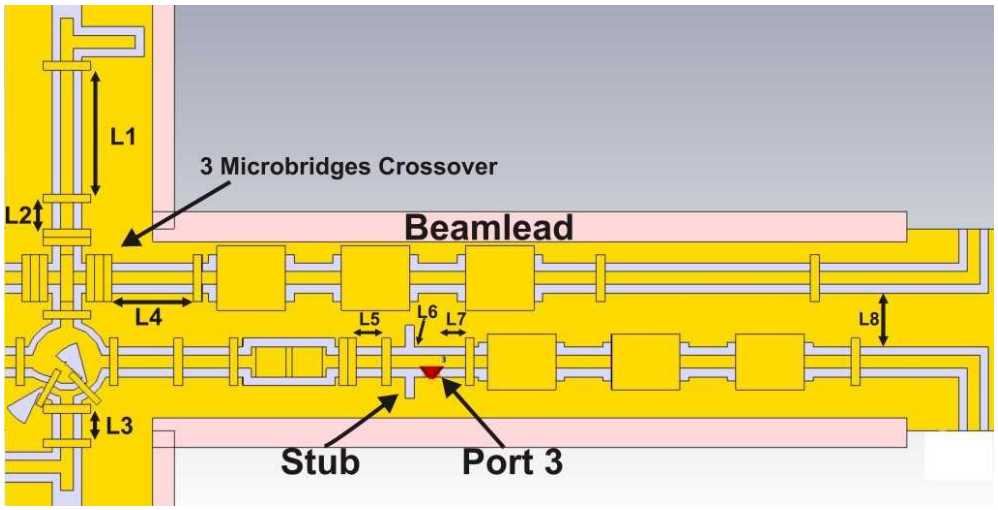


Figure 3.33: Zoom in to the crossover 1.9 THz balanced HEB mixer.

two capacitors of the new LPF to the main line by traveling approximately $2 \times L8$. However, monitoring the E-field at 1.9 THz shows that this double reflection does not interfere constructively with the RF signal incident on the original line. Therefore, a slot stub is introduced to the original line before the HEB. This stub works as a

delay to the incident signal for phase matching to the reflected RF signals from the LPFs. The length of the stub is 5 $\mu$m. So, the combination of the two LPFs in parallel integrated on the main and new lines with the optimum location of the new LPF and added the phase delay stub makes the operation of this design possible, see figure 3.36. The optimum values of $L5 = 6$ $\mu$m, $L6 = 2$ $\mu$m and $L7 = 6$ $\mu$m are obtained for the best matching between the main HEB arms and the hybrid-ring coupler with the crossover implemented at the arm of the hybrid towards port 1. The 2.5 $\mu$m thick Au beamleads are added for the GND connection to the PEC background.

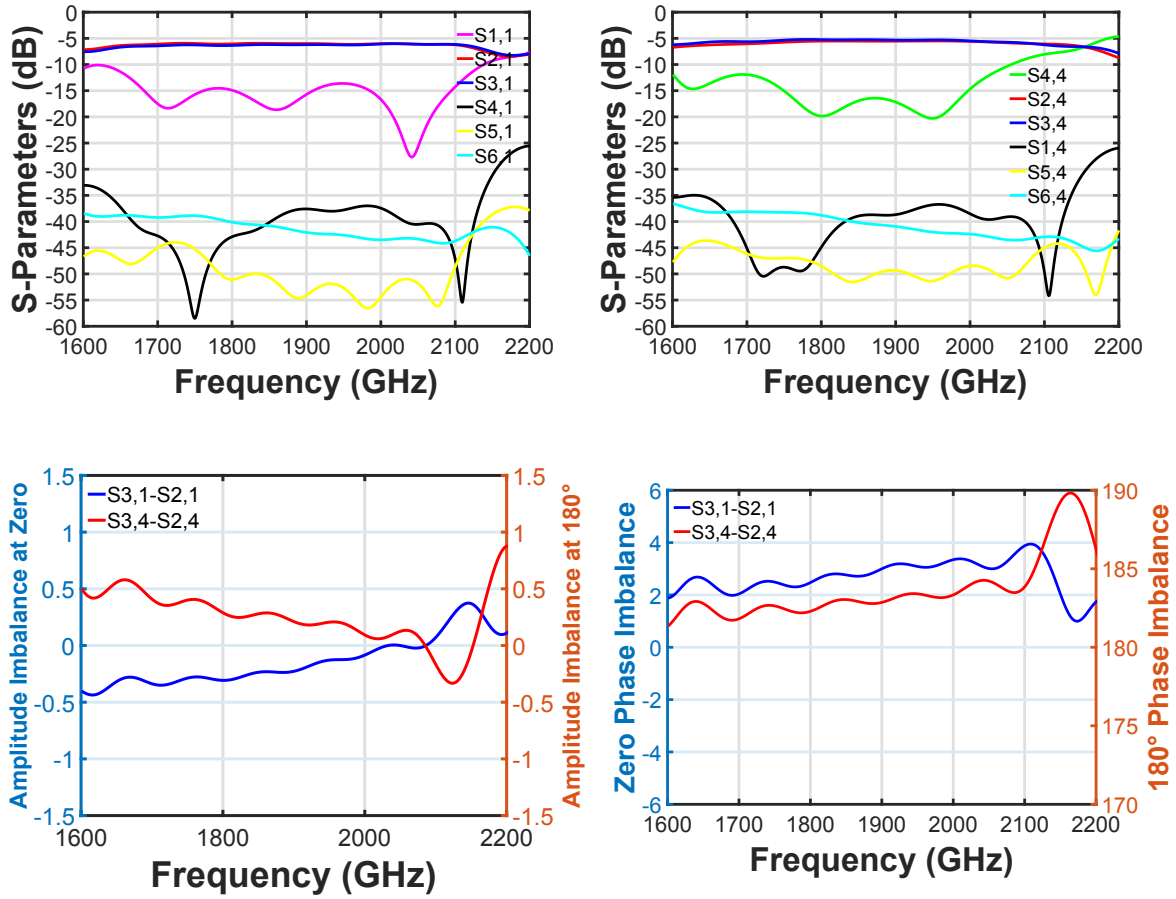


Figure 3.34: S-parameters of the complete on-chip crossover 1.9 THz balanced HEB mixer with one HEB bridge per substrate channel, Top-Left: When port 1 at the 0 ° side of the hybrid-ring coupler is excited, Top-Right: When port 4 at the 180° side of the hybrid-ring coupler in excited, Bottom-Left: Amplitude imbalances between ports 2 and 3 when a signal is excited at port 1 (S3,1-S2,1) and at port 4 (S3,4-S2,4), Bottom-Right: Phase imbalances between ports 2 and 3 when a signal is excited at ports 1 and 4.

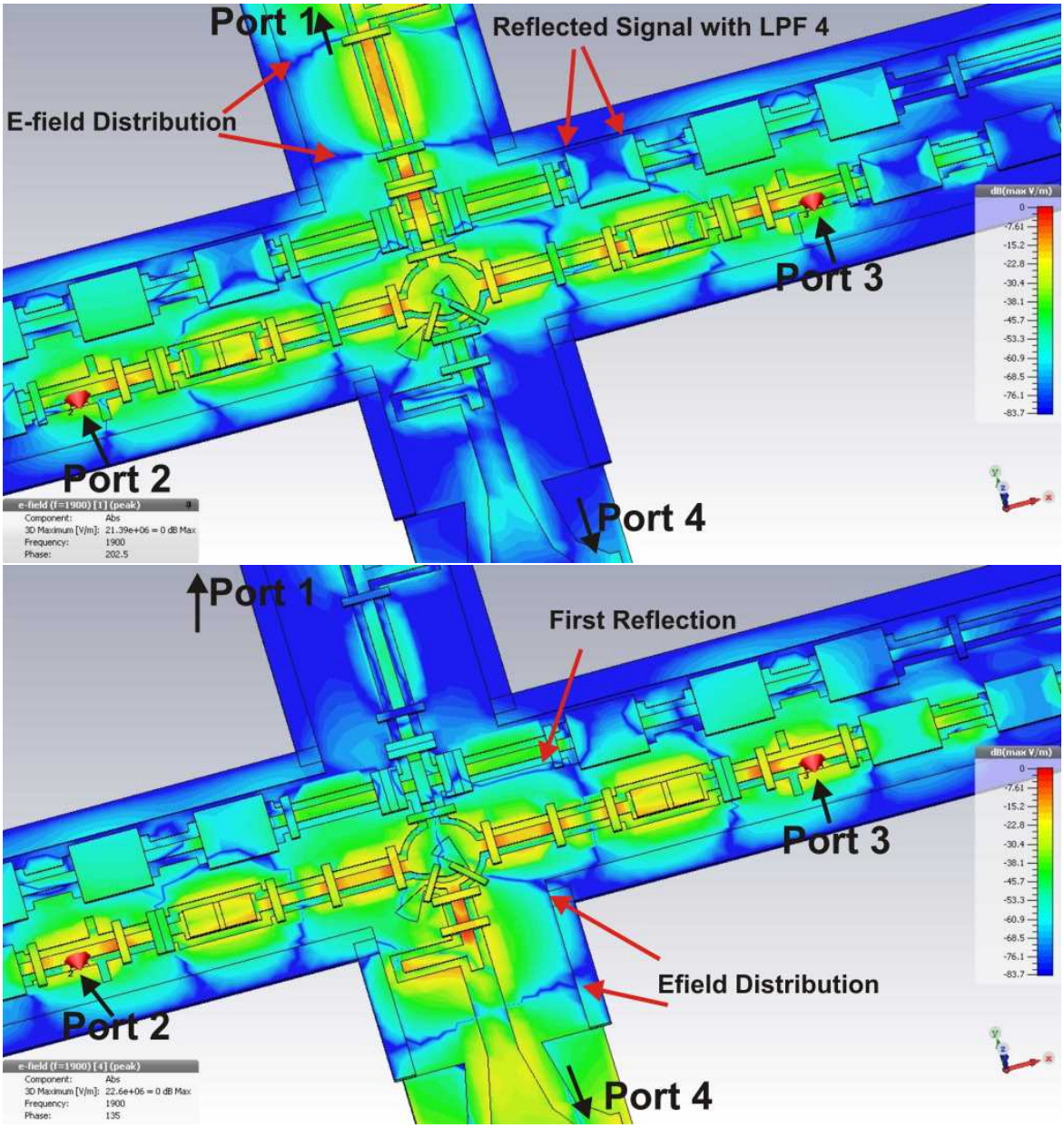


Figure 3.35: The monitoring of the E-field distribution at 1.9 THz of the crossover 1.9 THz integrated balanced HEB mixer with one HEB per arm, Top: When port 1 is excited. The monitoring shows the moment when the maximum E-field amplitude is delivered to the arms of port 2 and 3 at the hybrid. At the side of port 3 it can be seen that some signals (<-20 dB to -45 dB, please see the scale in the figure) is coupled to the new CPW line through the crossover and coupling from the main line. Some of the signal on the new line is reflected back from the first stage of the LPF 4. Bottom: When the port 4 is excited. The monitoring also shows the moment when the maximum E-field amplitude is present at the device output arms of the hybrid. At the side of port 3 the moment is captured when the first reflection of the coupled signal from main CPW line to the new line (<-30 dB to -45 dB), mostly green color) happens on the first stage of LPF 4.

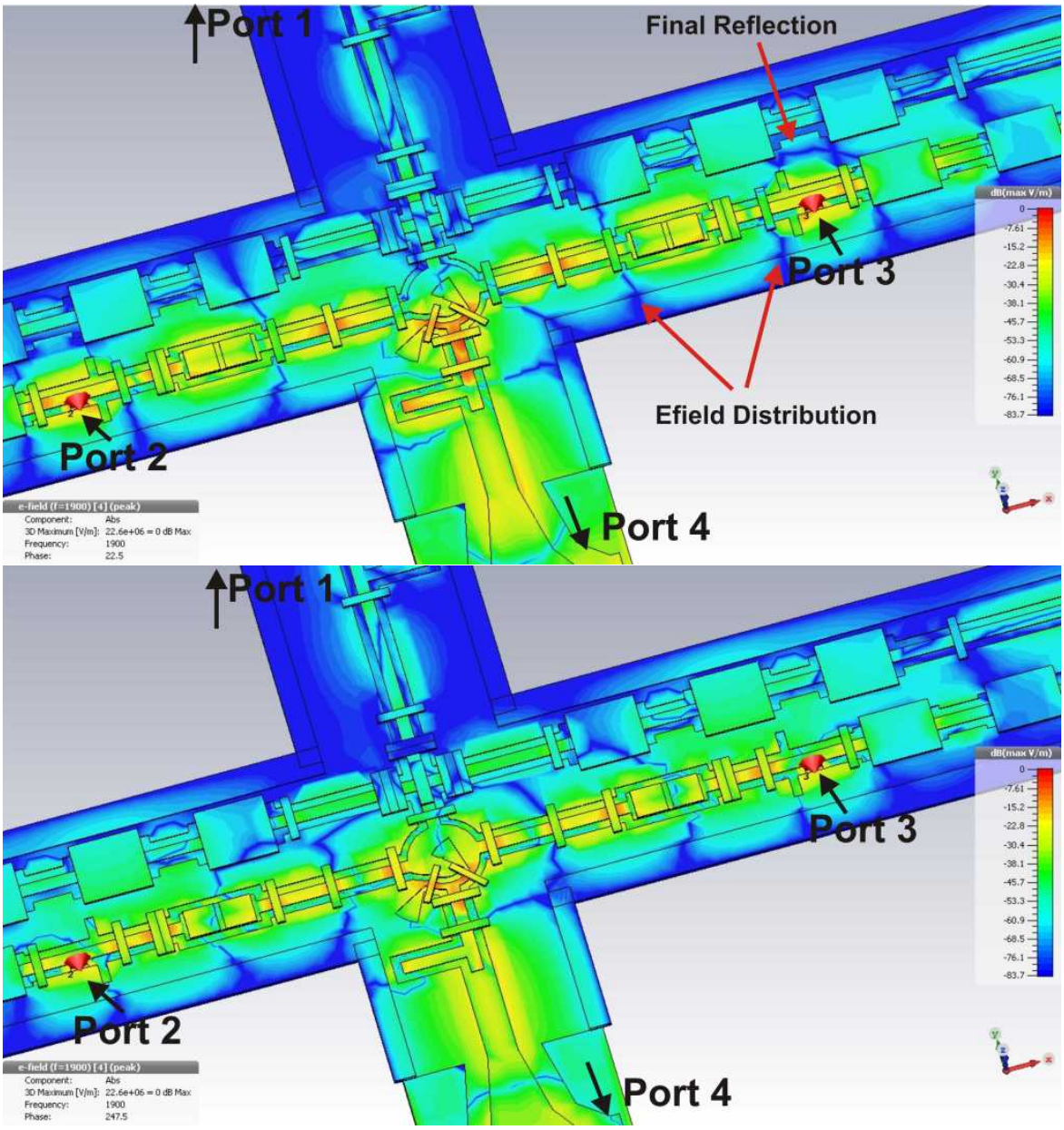


Figure 3.36: The monitoring of the E-field distribution at 1.9 THz of the crossover 1.9 THz integrated balanced HEB mixer with one HEB per arm, Top: When port 4 is excited. At the side of port 3 the moment when the coupled signal (from reflection of LPF2) on the new line is reflected back by the two last stages of the LPF4 and meets the delayed new incoming signal on the slot stub at the right phase. Bottom: When the port 4 is excited. The moment when the reflected and coupled signals are absorbed by port 3 (and port 2).

## 3.7 IF circuitry

In order to combine the down-converted IF signal from the two mixers at the output of the balanced mixer device, the IF circuitry is introduced. The ideal case is to bond the mixer device outputs directly to the SMA or GPO connectors. However, for such a tiny membrane THz device is impossible to directly wire bonded, because the slightest movement in the connector inner conductor will break the membrane. Therefore, an intermediate IF board is necessary to be designed and glued into a pocket in the mixer block. Two types of the IF circuity are studied because of existing two types of IF outputs for the non-crossover (2 and 4 HEB bridges) and the crossover 1.9 THz 180° balanced HEB mixers. Simulation of the complete RF chip with the IF circuitry at the same time in 3D exceeds our resources (memory) of the microwave CST suite and if it fits, it takes really long time. This is because the dimensions of the mesh cells for the simulation are determined by the tiny RF part of the circuit. For the IF the mesh cells are then about a factor of $10^9$ too many. Considering this, The IF- and the RF-part of the circuit are simulated separately. After the 3D simulations the resulting S-parameters are introduced as blocks and are combined in CST design studio for the total IF frequency response.

### 3.7.1 IF Circuitry for the non-crossover RF circuit

The transition of one IF output signal from the non-crossover balanced mixer to a SMA connector is designed and simulated. This is done in three steps, the transition from the CPW line at the end of the LPF of the RF-chip to the IF intermediate board, the transition from the IF board to the SMA connector and the combination of the simulated S-parameters of the complete non-crossover balanced mixer in the IF with the simulated S-parameters of the two IF transitions. In figure 3.37, the design and frequency response of the transition from the 50 Ω CPW line to the 50 Ω microstrip line is depicted. The microstrip is 400 $\mu$m wide on a 500 $\mu$m thick silicon+metal which at one side is connected to about 50 Ω waveguide port and in another side to the tapered shape CPW with the IF output beamlead (250 $\mu$m length, 2.5 $\mu$m thick, 50 $\mu$m wide). The IF board functions as a large bond pad because its electrical length is too small. Simulation is necessary to verify that the CPW mode is properly launched onto the SMA coaxial transmission line. The CPW line is on a 3 $\mu$m silicon is placed in the substrate channel (stamped waveguide) with the same dimensions as the substrate channel (20×40 $\mu m^2$). The CPW-microstrip transition is placed in the pocket shape waveguide (milled waveguide, 40 $\mu$m height and radius 104 $\mu$m). The IF

board is placed on the bottom of the waveguide (milled waveguide) with dimensions 1069 $\times$1630 $\mu$m$^2$. For more detail about stamping and milling the balanced waveguide block see Section 4.3. The IF frequency response of the transition is shown in figure 3.37 where has about 0 dB transition from port 1 to the port 2 (S2,1) and lower than -25 dB reflection at port 1 (S1,1) up to 6 GHz.

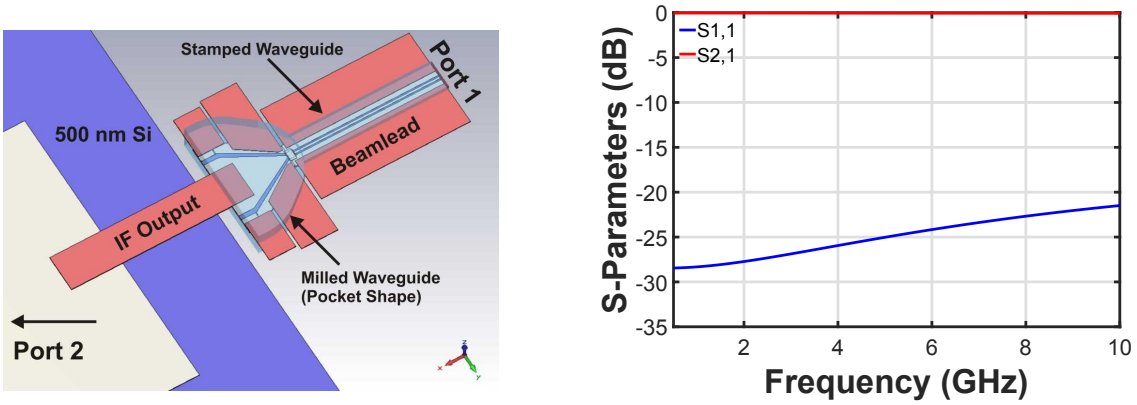


Figure 3.37: CPW IF-output to the intermediate microstrip line board, Left: design, Right: S-parameters with S1,1 (red curve) and S2,1 (blue curve).

The next step is to simulate the transmission of the IF signal from the intermediate board to a SMA connector. The SMA connector has the outer radius of 2100 $\mu$m (filled by dielectric) and inner-connector (filled by PEC) radius of 655 $\mu$m. It is cut to half for easier electrically bonding to the IF board. The bond wire is simulated as a continuation of the strip from the IF board, see figure 3.38. In reality there will be at least two 25 $\mu$m diameter bond wires in parallel. The simulated results when the port 1 is attached to the IF board and port 2 to the 50 $\Omega$ SMA connector are depicted in figure 3.38. There is a full transmission from port 1 to port 2 (S2,1) and lower than -20 dB reflection up to 6 GHz with about -32 dB at 0.5 GHz.
After simulating the IF sections separately, now is the time to see the IF frequency response of the 1.9 THz balanced HEB chip together with them. This is done in CST design studio as shown in figure 3.37. Prior to that, the non-crossover balanced 1.9 THz with one HEB per substrate channel from Subsection 3.5.4 is simulated at the IF frequencies for all 6 ports which takes about one week of simulation time. When the S-parameters of all blocks are ready, the final IF frequency response is simulated. The result is depicted in figure 3.39. Ports 5 and 6 are the two IF output ports towards the SMA cables and from there to the two low noise amplifiers (LNAs) out side of the mixer block. The reflections at ports 5 (S5,5) and 6 (S6,6) are about -9 dB at 0.5-3

GHz. There is about 0.5 dB loss in transmission between ports 2 and 5 (S2,5), 3 and 6 (S3,6). This response can be explained as the mismatch between the 120 Ω HEB and the 50 Ω load. The IF circuitry in between does not have much influence, except for a small inductivity. However the IF output impedance of the HEB mixer is unknown. Some references like [69] argue that it is lower than the normal state resistance, as the HEB is biased approximately in the center of the superconducting transition where the resistance is about half the normal state resistance (see figure 2.4). This means the reflection and transmission will be improved.

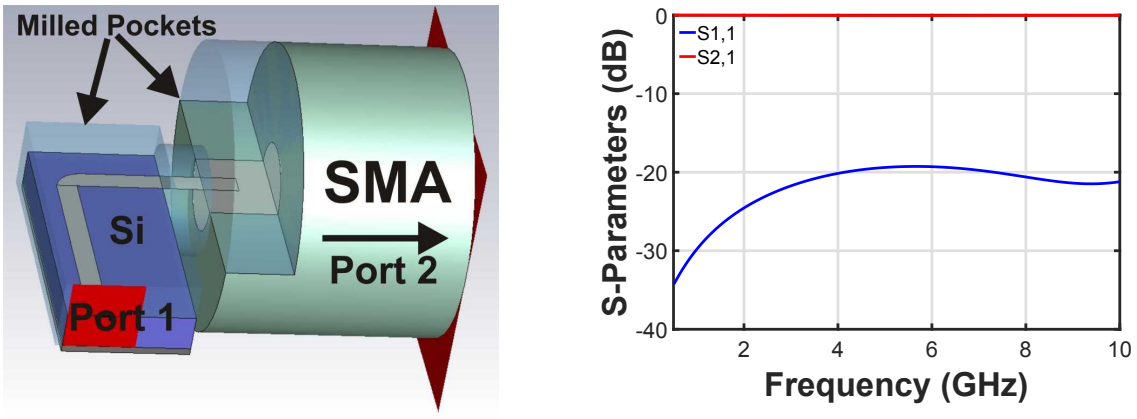


Figure 3.38: Intermediate microstrip line board to the half SMA connector, Left: design, Right: S-parameters with S1,1 in red curve and S2,1 in blue curve.

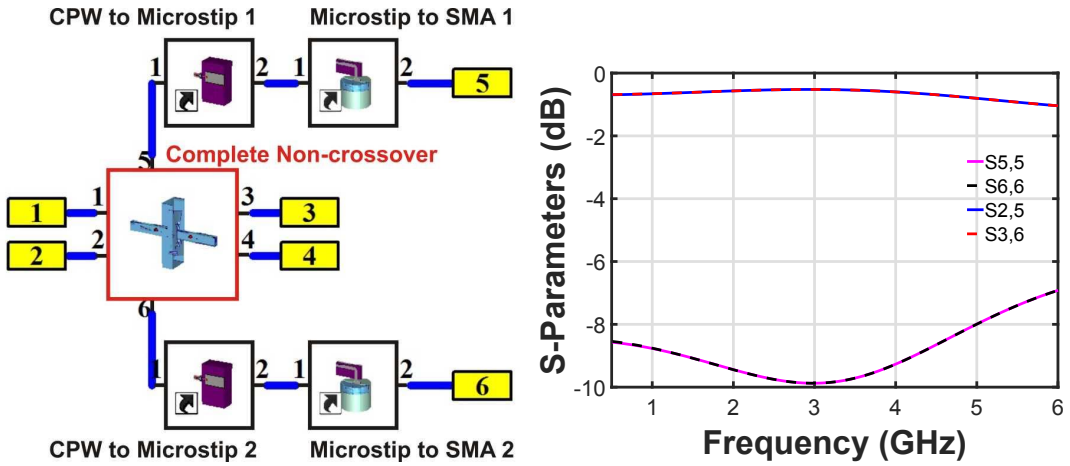


Figure 3.39: S-parameter checking of the IF output in CST design studio to predict possible matching between separate circuit blocks.

### 3.7.2 IF circuitry for the crossover RF circuit

IF circuitry for the crossover 1.9 THz balanced HEB in Section 3.6 is different with the one mentioned in Subsection 3.7.1. This is because of existing two IF outputs on one side of the silicon substrate instead of two IFs at the opposite sides. The design of this circuitry is done in three steps, transition from the two IF outputs on the balanced device after the LPFs to the first intermediate board (IF-board no.1), transition from the IF-board no.1 to the IF-board no.2 and combining the simulated S-parameters of the complete crossover balanced mixer in the IF with the simulated S-parameters of the two IF transitions. Because the two IF signal outputs of the crossover balanced mixer device are about 12.5 $\mu$m away from each other, there is a need of two IF boards to widen this distance for possible wire bonding to two SMA connectors. Despite the design of CPW-microstrip line transition with one IF mentioned in Subsection 3.7.1, here the transition is re-designed for the two IF outputs. The new transition is depicted in figure 3.40. As discussed in Subsection 3.7.1, at this step only the transitions from the two IF outputs based on CPW lines after the two LPFs are considered. The center line of the two CPW lines are connected to two L-shape beamleads with distance of 80 $\mu$m. The 3 $\mu$m substrate is shaped to the new width of about 230 $\mu$m. The transition is placed in the center of the rectangular pocket waveguide with the lateral dimensions of 120×250 $\mu$m$^2$. There are added also two 101 $\mu$m wide micro-bridges over the two 3 CPW lines for keeping the first mode of CPW to propagate. The two 50 $\mu$m wide beamleads are in a maximum distance of 647 $\mu$m ended up on the IF board no.1. This intermediate board is on a 200 $\mu$m silicon and the strips are 150 $\mu$m wide ($Z$ = 50 $\Omega$). It is placed in the bottom of the waveguide with dimensions of 835× 3000 $\mu$m$^2$. The two strips are gradually separated from each other until to the optimum distance of 920 $\mu$m. This distance is achieved for better isolation between two microstrip lines (lower coupling). The simulated results are shown in figure 3.41. The transmissions from port 1 to 4 (S4,1) and from port 2 to 3 (S3,2) are about 0 dB up to 10 GHz. The reflections at ports 1 (S1,1) and 2 (S2,2) are lower than -10 dB up to 10 GHz. The coupling between ports 1 and 2 (S1,2) and ports 3 and 4 (S3,4) is lower than -45 dB between 0.5-3 GHz.

Next, it is necessary to increase the distance between the two microstrip lines for possible connection to two SMAs sitting close to each other with their center lines connected to the strips. This is done with the help of the IF-board no.2 which is shown in figure 3.42. The substrate is a 635 $\mu$m thick TMM10 the dielectric constant of about 9.2. These two new microstrip lines have a width of 400 $\mu$m ($Z$ = 50 $\Omega$).

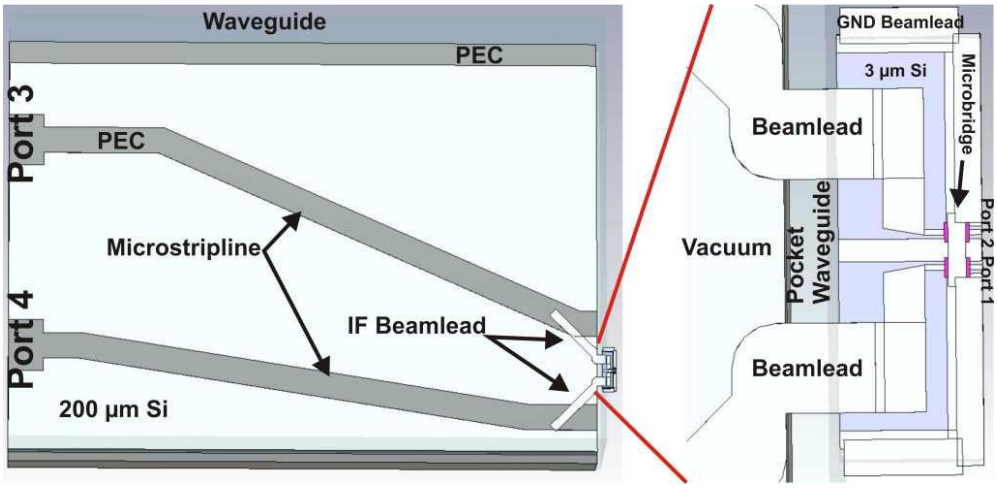


Figure 3.40: A first intermediate IF board for crossover 1.9 THz balanced HEB.

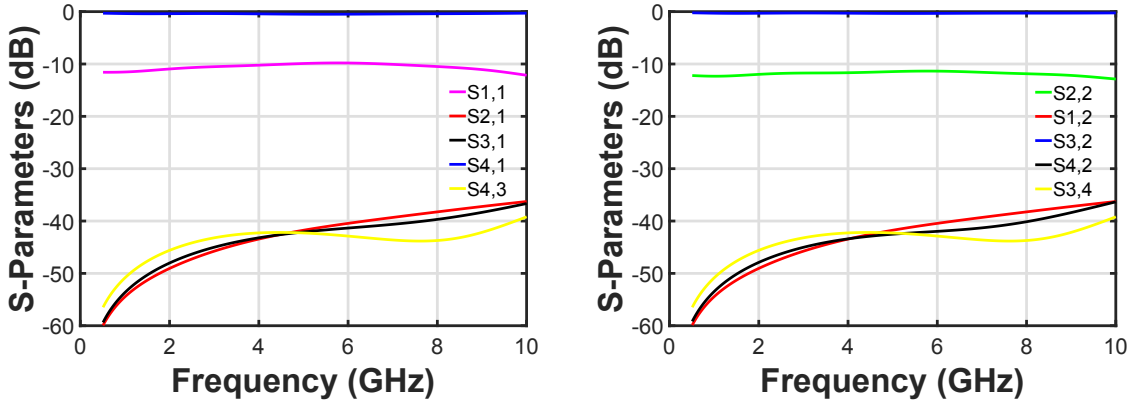


Figure 3.41: S-parameters of a first intermediate IF board for crossover 1.9 THz balanced HEB.

They are separated at the end of the TMM10 board with a distance of about 5400 $\mu$m. The IF-board no.2 is placed on the bottom of pocket milled into the mixer block with dimensions of 1270×8800 $\mu m^2$. In addition, one should notice that the length of microstrip lines from port 1 to port 4 and from port 2 to port 3 remains the same to avoid any extra phase difference between them. The simulated S-parameters of the total IF circuitry (two IF-lines CPW-microstrip transition, IF-board no.1 and IF-board no.2) for the crossover type of 180° balanced mixer is shown in figure 3.43.
The transmissions from the port 1 and 2 on the 3 $\mu$m silicon to the ports 4 and 3 on the TMM10 stay about 0 dB up to 10 GHz. The reflections at ports 1 and 2 are about -20 dB at 2 GHz (mid frequency of the IF noise bandwidth of the NbN HEB mixers). The coupling between ports 1 and 2 (S1,2) and ports 3 and 4 (S3,4) is about -35 dB

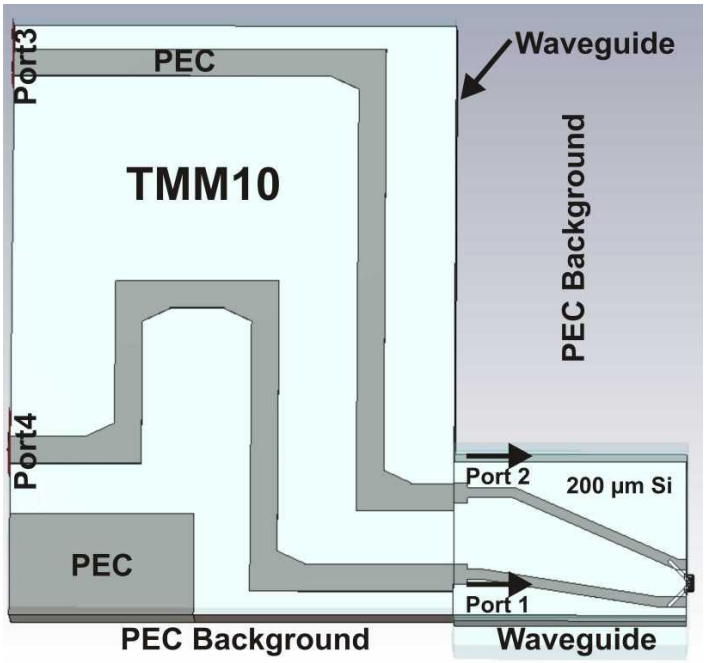


Figure 3.42: The complete IF circuitry for a crossover 1.9 THz balanced HEB mixer.

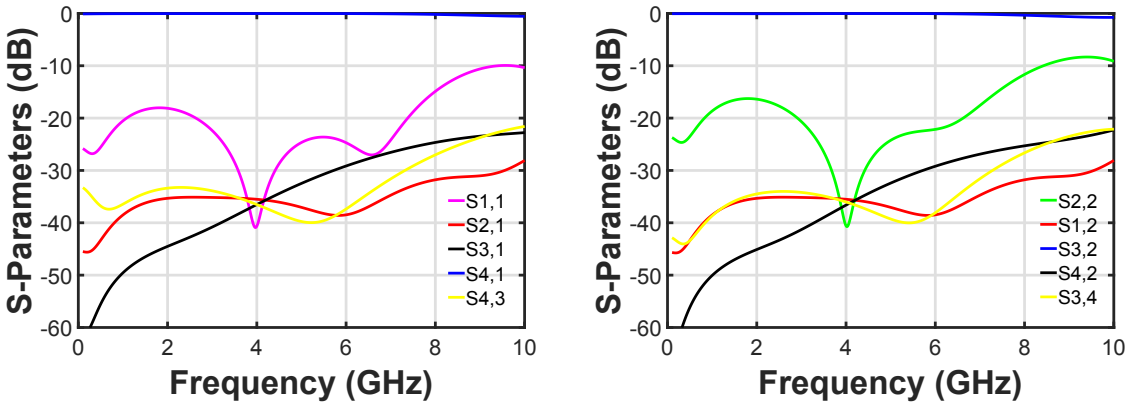


Figure 3.43: S-parameters of the complete IF circuitry for a crossover 1.9 THz balanced HEB mixer.

up to 6 GHz. The coupling between port 1 and 3 (S3,1) and ports 2 and 4 (S4,2) is about -45 dB at 2 GHz.

The last step is to simulate the crossover circuit in Section 3.6 at the IF frequencies for all ports and put together with the calculated S-parameters of the total crossover IF circuitry. The schematic in CST design studio is depicted in figure 3.44. The simulated S-parameters show the transmission of about -2 dB between ports 3 and 5 (S3,5), 2 and 6 (S2,6). There is about 1.5 dB more loss in transmission compared to the design

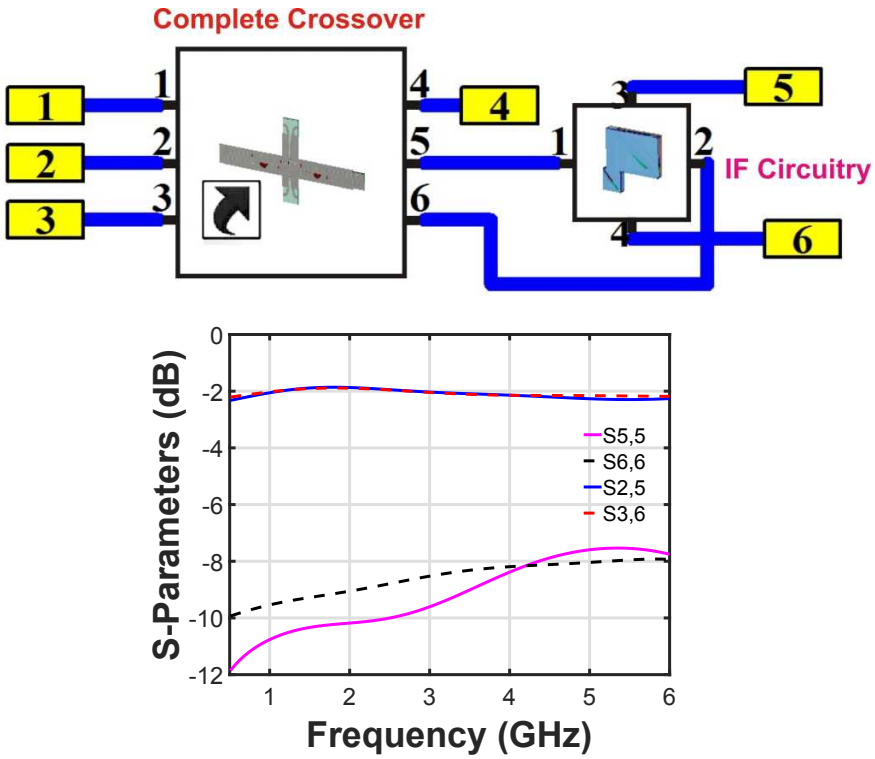


Figure 3.44: S-parameter checking of the IF output in CST design studio to predict a possible matching between the separate circuit blocks.

for one IF output, see figure 3.39. This can be explained as the cross coupling between the two IF output parallel lines at the same side of the substrate.

# Chapter 4

# Fabrication of the 1.9 THz 180° integrated balanced HEB mixers

This chapter presents the lithography mask and fabrication processes from a blank SOI wafer to final 1.9 THz balance HEB mixer devices.

## 4.1 Design of a lithography mask

Prior to the device fabrication, there is a need of a lithography mask which is drawn in AutoCAD mechanical software [70]. After the devices are designed, the fabrication mask implements this design into the proper amount of fabrication layers and alignment marks. For the E-beam lithography also writing fields, and possible stitching of writing fields have to be taken into account. In addition, the fabrication mask has to supply the DC and RF connections with adapted to the later block and IF connection. It also induces conducting lines to DC test devices on the handle wafer, prior to separation into single devices. Because the wafer is not DC tested as a whole but is separated into sectors, these connections ( e.g. GND) have to be repeated such that they exist per sector. In addition of course obvious things like device numbers have to be implemented. In figure 4.1, the complete lithographic mask is depicted. It has the size of 3×3 $cm^2$ and contains 18 dies with 8 mixer devices per each. The Van der Pauw structures and meander shape strips are added to characterize the sputtered and electroplated Au thin films.
The mask consists of three types of devices following as two, four HEB bridges non-crossovers and two HEBs crossover as mentioned in sections 3.5, 3.5.5 and 3.6 respectively. Therefore, three different types of DC connections are drawn for the later R-T

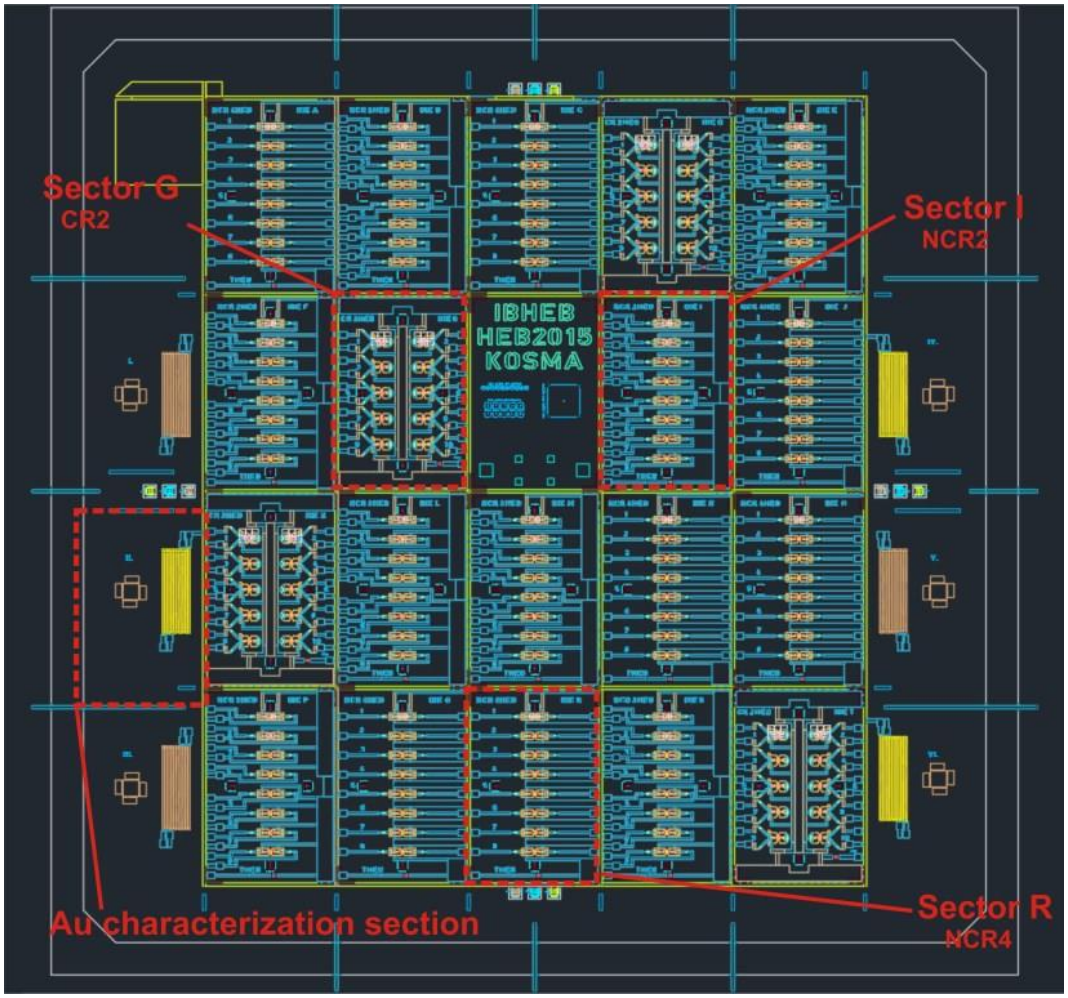


Figure 4.1: The complete 3×3 $cm^2$ CAD designed lithography mask for fabricating the 1.9 THz balanced HEB mixers. This mask contains of 18 dies with non-crossover 2 HEBs (NCR2), non-crossover 4 HEBs (NCR4) and crossover 2 HEBs (CR2) mixer devices, E-beam and photo lithography alignment marks, wiring for DC characterizations, connections for electroplating of Au and additional sections to characterize the sputtered and electroplated Au.

and DC I-V characterizations. These variations in DC connection are shown in figure 4.2.

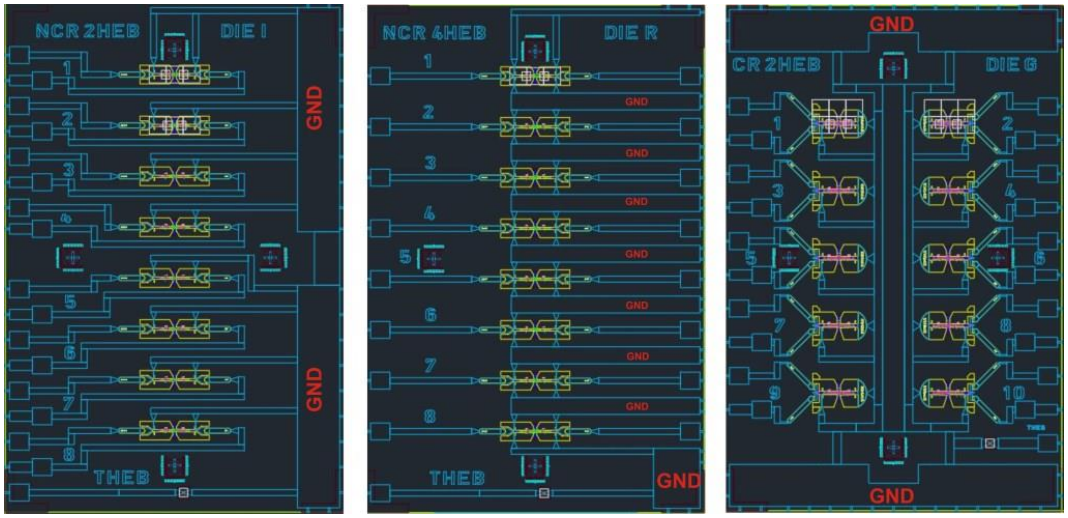


Figure 4.2: Three sample dies which each presents different designs of the 180° 1.9 THz balance HEB mixers. Left: die-I with NCR2 mixers , GND pad on the right side and DC pads on the left, Center: die-R with NCR4 mixers , several GND pads and DC pads on the both sides, Right: die-G with CR2 mixers, GND pad on the bottom and top connected to circuits and DC pads on the both sides.

## 4.2 Device micro-nanofabrication

The fabrication starts with choosing a proper substrate which based on our design is a 3 $\mu$m thick silicon membrane, see Section 3.5. As there can not be processed directly on such a thin substrate, 300 $\mu$m thick SOI wafer is chosen in which contains of a handle wafer, a thin SiO2 layer and high resistivity 3 $\mu$m Si on top. About 4.5 nm superconducting NbN (thickness of the HEB bridges) is sputtered on the blank SOI wafer in a $800^{\circ c}$ condition. For this wafer, the thin NbN layer development was done by our former PhD student Dr. Stefan Selig. About 10.5 K critical temperature of the sputtered thin film is measured by dipstick in liquid helium (L-He). The rest of the fabrication was done by Dr. Karl Jacobs. The next step is to define a length of HEB bridges by spinning bi-layer PMMA photoresist for high resolution lift-off (undercut control), writing the contacts of bolometers by the E-beam, cleaning the contact area of the NbN by Ar sputter etch and then a thin layer of superconducting NbTiN, immediately (in situ) followed by a 45 nm sputtered Au. This additional superconducting layer enhances the contact between Au layer and the thin NbN layer. Later on, these contacts are connected to a 200 nm thick Au bottom layer including the CPW and slot lines, the 180° ring coupler, planar antennas and transitions, bottom layer of capacitors for LPFs and DC-blocks, all defined by the E-beam lithography. After that, the width of HEB bridges is defined by spinning a negative photoresist and E-beam

lithography. The uncovered NbN areas are etched down to the surface of SOI by a deep reactive ion etching (DRIE) tool.
Next, a layer of 400 nm SiO2 is sputtered on the defined E-beam opened areas as a dielectric layer for micro-bridges and capacitors (LPFs and DC blocks). A 300 nm Au as a top layer of micro-bridges and capacitors is sputtered after one more E-beam lithography step. The existing of micro-bridges is important to connect the two ground sides of the CPW lines therefore with choosing a thick SiO2, we could also obtain a quite good step-coverage of the sputtered Au over the dielectric.
Later on, a 150 nm seed layer Au is sputtered on the opened areas which are defined by photo - lithography technique. This thin Au layer is applied to make DC connections for electroplating of about 2.5-3 $\mu$m thick Au as beam-leads. These BLs are for GND contact of a membrane mixer device to a waveguide block and output connections from the device to the IF intermediate boards (see Chapter 3). The fabricated crossover 1.9 THz balanced HEB, CR2-G06 (die G, device-number 6) mixer device after electroplating of Au is shown in figure 4.3. Consequently, the fabricated wafer is diced into different dies by a dicing saw. Before device separation, we are in need of DC characterizing of the fabricated circuits on dies, for more details see Section 6.1.
After DC characterization with sufficient good results, the handle wafer is backside etched with a DRIE technique up to the thin SiO2 layer of the SOI substrate. Subsequently, the SiO2 of SOI is removed by the wet etching technique using a buffered hydrofluoric (BHF) acid. The 3 $\mu$m Si substrate of the individual device is defined by the photolithography. Finally, the mixer devices on each die are separated by etching the uncovered 3 $\mu$m Si using the DRIE Bosch process [71]. The fabricated non-crossover 1.9 THz balanced HEB, NCR2-M07 (die M, device-number 7) mixer device with BLs after separation is depicted in figure 4.4. The measured distance between two Au contacts (length of HEB) on the scanning electron microscopy (SEM) image shows a desired gap of 200 nm.

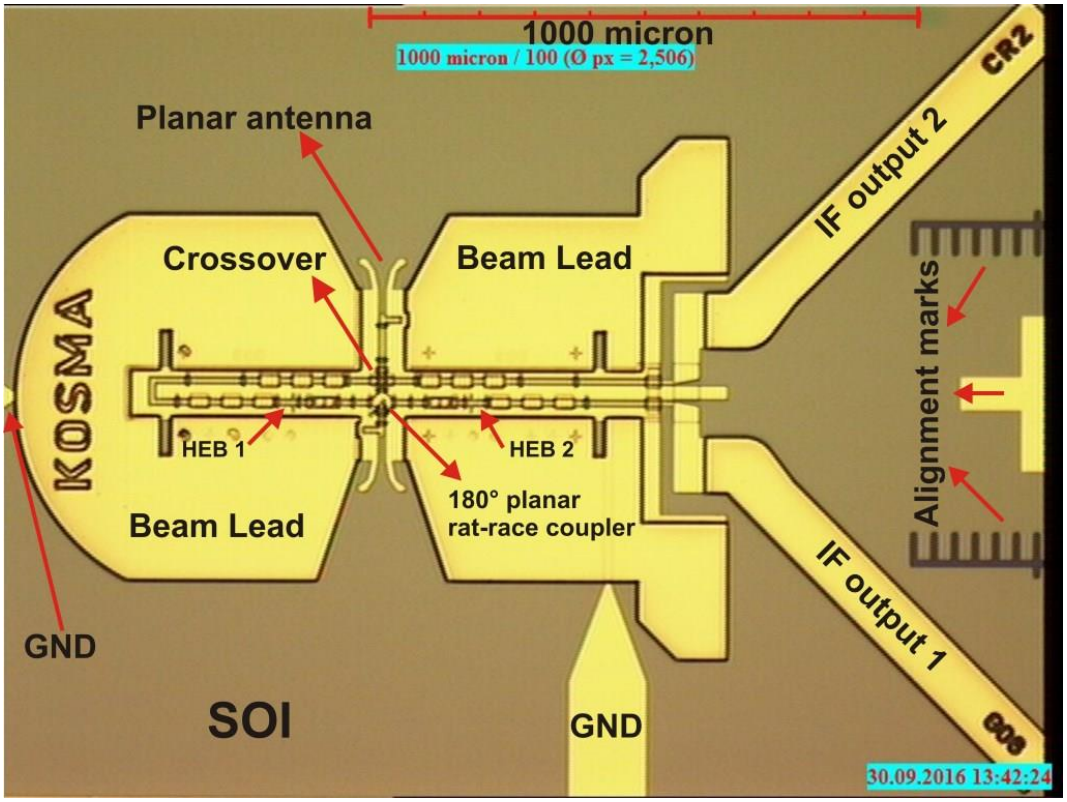


Figure 4.3: The image of the crossover 2 HEB bridges G06 (die-G, number 6) on wafer after electroplating 2.5-3 $\mu$m thick Au. After dicing the wafer into different dies, this device will be ready for DC measurements.

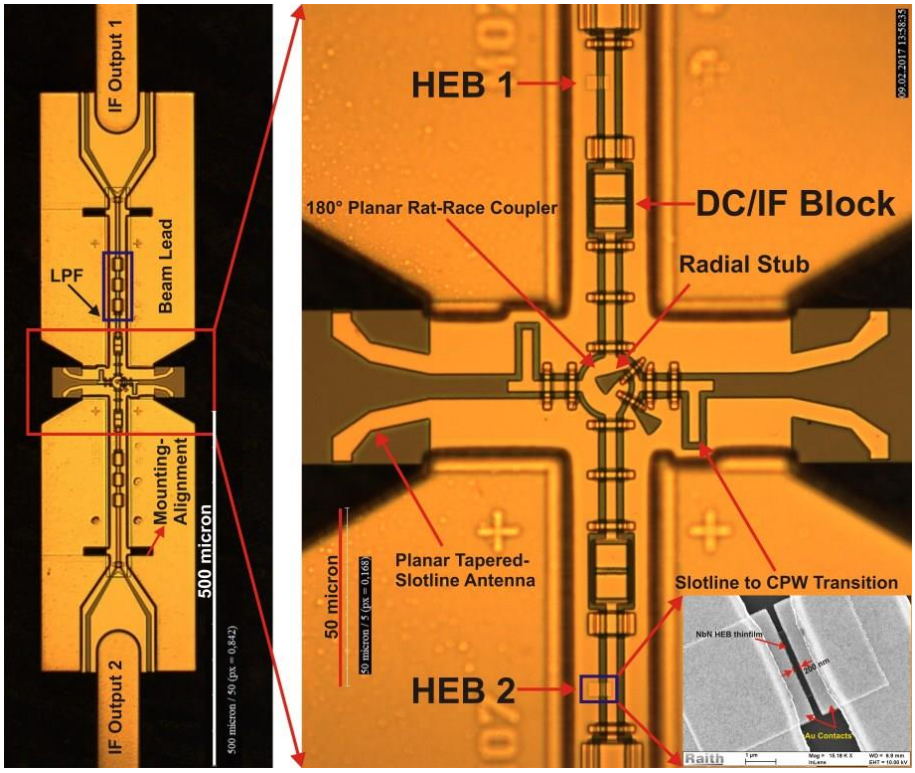


Figure 4.4: Left: The image of the non-crossover 2 HEBs device M07 (die-M, number 7) after separation with showing beamleads, LPFs, two IF outputs, etc. Right: Zoom in image of two HEB bridges, 180° hybrid ring coupler with two radial stubs, two DC/IF blocks, two planar antennas, two transitions and several micro-bridges. There is also a SEM image of the left HEB bridge with showing the Au contacts, about 200 nm measured gap between the contacts with NbN under it and Si on the rest.

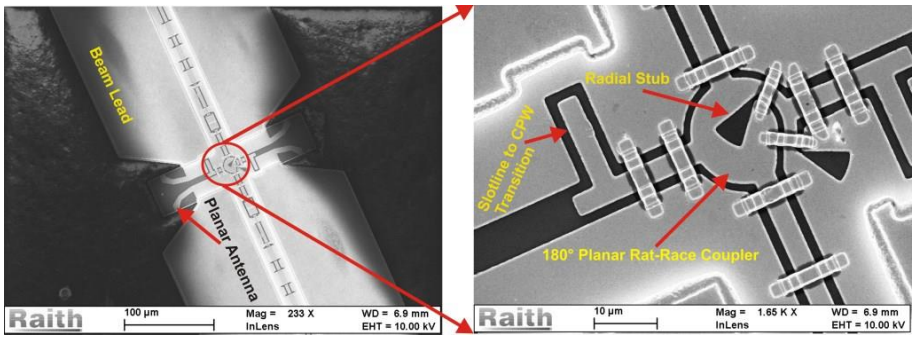


Figure 4.5: The SEM image of the complete 1.9 THz balanced HEB has been shown with the zoom into the area of 180° hybrid-ring coupler area of a sample device, M07.

## 4.3 1.9 THz waveguide balanced mixer blocks

In order to measure the performance of the fabricated 1.9 THz balanced mixer devices, there is a need of manufacturing waveguide blocks. The blocks must be in the same dimensions with acceptable tolerances as the simulated structures, see Section 3.5.
The blocks have been manufactured in our machining workshop with the experience of delivering the LFA and HFA mixer blocks [10]. The main differe between the 1.9 THz balanced waveguide blocks to the single ended type [10] is the cross shape at the junction between two waveguides and the exist of two substrate channels. Additionally, because our design has the E-field antenna type, it requires two exactly similar half blocks which they will be fit on top each other by screws and pins. However, this is only good enough for some guidance and not sufficient for aligning. The real alignment has been done under the microscope. The oxygen free copper tellurium alloy (CuTe )is chosen for manufacturing the blocks. This type of copper is favorable for its superior machinability and high thermal-electrical conductivity because of existence of tellurium and almost free oxygen, respectively. The waveguide and substrate channels are stamped and the rest is milled, all by the CNC machine [72] in house. The mechanical workshop tried several test blocks iterations due to the existing of burrs left inside of the waveguides or substrate channels, dimensions out of the desired tolerances, etc.
The desired waveguide blocks consist of one rectangular waveguide ($50 \times 100$ $\mu m^2$) crossed at approximately 1/4 of its length by a substrate channel ($40 \times 20$ $\mu m^2$). The length of the waveguide from one horn (the spline horn that has to be assembled on the block) to the substrate channel crossing is approximately 500 $\mu$m. The waveguide at the other side, up to the integrated diagonal horn is about 1300 $\mu$m long. The divergent beam of the diagonal horn is focused by a mirror that is integrated in the upper half of the block, to prevent issues with the critical alignment between horn and mirror. At each side of the substrate channel, an intermediate pocket to the IF output and a gap for the IF intermediate board are milled, see figures 4.6 and 4.7. The ideal case is to avoid any extra waveguides between two horn antennas and our mixer, like the case in LFA or HFA where a spline horn is located on top of the probe antenna of the circuit [10], [73]. Nevertheless, it is almost impossible to have two spline horns locating on our balanced mixer due to the integration of the planar RF hybrid coupler instead of waveguide types. This brings unavoidable extra waveguides between two input horns and the balanced mixer. Additionally, the gaps for mounting SMAs, screws and fitting pins (keeping two halves together with sufficient pressure) prohibit

the use of two spline horns. We chose to use the spline horn, that has been verified in the LFA mixers used in upGREAT for the coupling of the sky signal, implementing the shortest length of waveguide between the horn and the chip at that side. We have added an integrated diagonal horn in place of a spline horn for guiding the local oscillator signal to the circuit [74]. Taking into account all of the limitations and concerns, we have reached the final 1.9 THz balanced block design which is shown in figure 4.6. In this design, we aimed for the shortest possible waveguide between signal horn and chip due to unknown loss per length of our machined waveguides at 1.9 THz. There is a reported loss of machined silicon waveguides by JPL [75] which is about 2 dB per millimeter length. This would mean about 1 dB loss (∼21% of signal loss) between the spline horn and the chip antenna. In general, we made the block manufacturing as simple as possible for the machine shop. We used as much as possible previously established techniques.

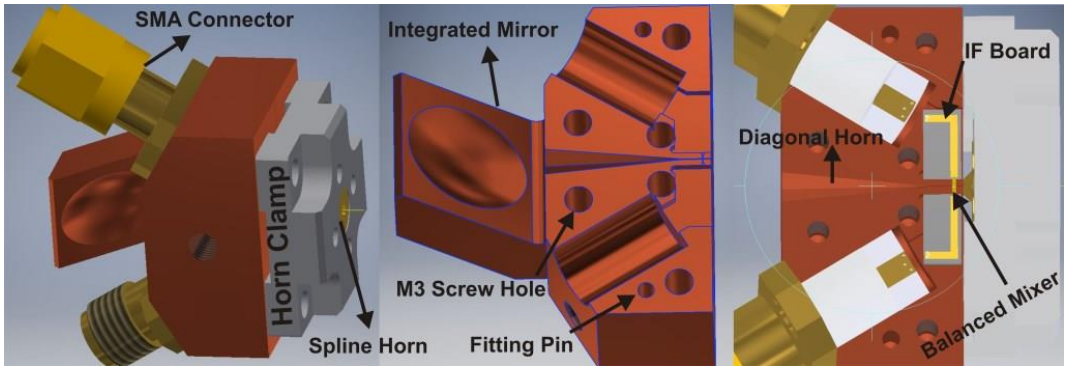


Figure 4.6: An Inventor Autodesk 3D drawing of a 1.9 THz balanced HEB mixer, Left: complete block with an integrated mirror, horn clamp, spline horn and two SMAs for the IF outputs, Center: top half of the waveguide block, Right: bottom half of the block with showing two IF microstrip boards, implemented mixer chip, two half SMAs.

The balanced mixer with a 3 $\mu$m thick substrate is mounted in the machined block as depicted in figure 4.8. First, the bottom half of the block is warmed up to 90 degrees and four drops of the crystal bond are used in the edge of pockets. Later on, when the block is cooled, a balanced device is located and aligned on the crystal bond and warmed up the block again to 90 degrees. After final aligning, BLs are cold bonded with ultra sonic bonding technique on the block for GND and to the two output boards for IF and DC contacts. Later on, the two IF intermediate boards are wire bonded to the half SMAs. The top half is screwed on the bottom piece and checked under the microscope to cross check for alignment and any probable gap between two halves. Finally, the spline horn with clamp is aligned and mounted on the block.

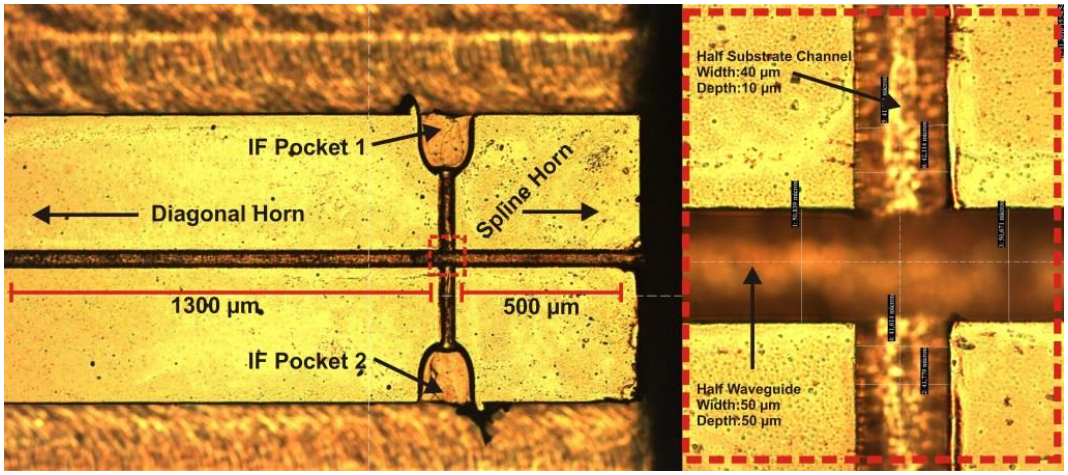


Figure 4.7: The machined 1.9 THz balanced block number 1 with 100 nm sputtered Au, Left: Two waevguides, two substrate channels and two IF pockets, Right: zoom in to the cross with measured values of about $\pm 2$ $\mu$m for height and width which is quite well in the tolerance range.

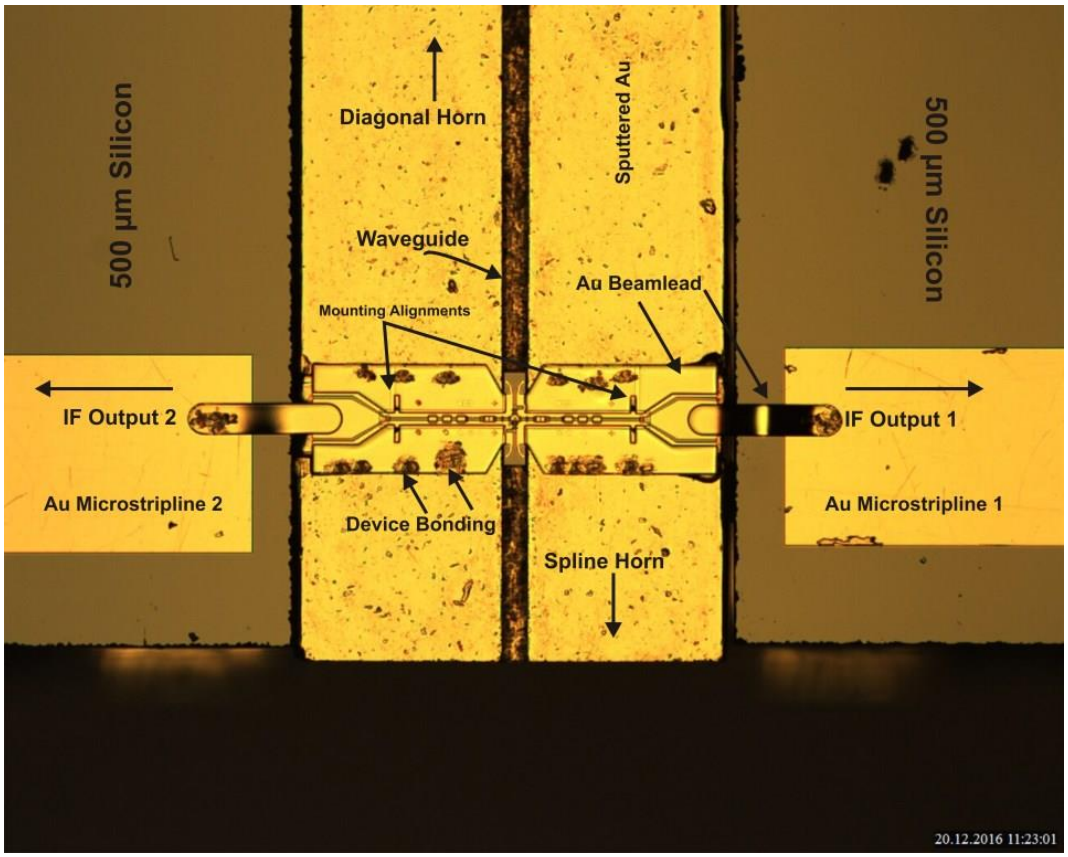


Figure 4.8: Mounted M02 device in the bottom-half of the 1.9 THz balanced block. The BLs of the device are ultrasonic cold bonded on the surface of block and to the two IF intermediate boards.

# Chapter 5

# Terahertz Time Domain Spectroscopy (TTDS) to study machined waveguide blocks

I report in this chapter, measurements with the terahertz time domain spectroscopy (TTDS). It is a fast and reliable technique for characterizing machined waveguide blocks in the THz frequency regime. It has been done by studying a transmission of the generated THz signal through the machined waveguide blocks. Once the system runs smoothly, it would be possible to exchange easily the under test waveguide blocks. But of course, the distance of lenses should be updated due to the different waist of the waveguide horns. This characterization will lead us towards a possible more clear understanding about our balance mixer block with almost blind LO port and losses due to the existing long waveguides, for more details see Chapter 6.

## 5.1 Introduction

There exist different kinds of spectroscopy techniques at THz frequencies. For debugging purposes, the THz time-domain spectroscopy due to its broad bandwidth, almost real time responses and high signal to noise ratio is a practical technique. Unlike the single frequency spectroscopy, the generated pulsed radiation from TTDS probes the sample over the wide frequency range from the IF up to 5 THz in one measurement run with being less sensitive at higher frequencies. The TTDS generates phase information of the measured sample in addition to the amplitude which applies for measuring like the refractive index, thickness of sample under test, etc. The schematic of our set up of

the TTDS system [76] is shown in figure 5.1. The femtosecond pulsed laser signal gets divided to two paths which each feeds the emitter and detector with an erbium-doped fiber optic (1560 nm wavelength). An additional optical delay (mirror based) is implemented in the path of a detector. Therefore, different points in time, can be measured by changing the delay. The THz antennas using in the emitter and the detector are photo-conductive switches based on semiconductor substrate with a structured metal electrode on top of it. The coupled laser signal through the gap between the antenna electrodes, gets absorbed by the semiconductor material and generates electron-hole pairs. At the emitter, the electrode is connected to the bias supply where can accelerate the charge carriers and consequently emits a THz electrical filed. This field is proportional to the time-derivation of the photo-current. At the detector, the generated charge carriers get accelerated by detecting the THz field towards its electrodes. There is an amplifier connected to the detector in order to amplify the weak generated photo-current. In addition, the silicon lenses have been mounted on the substrate of the emitter and the detector to generate a more or less Gaussian beam. At the end, the received time-domain signal is transformed to its frequency-domain by the fourier transformation.

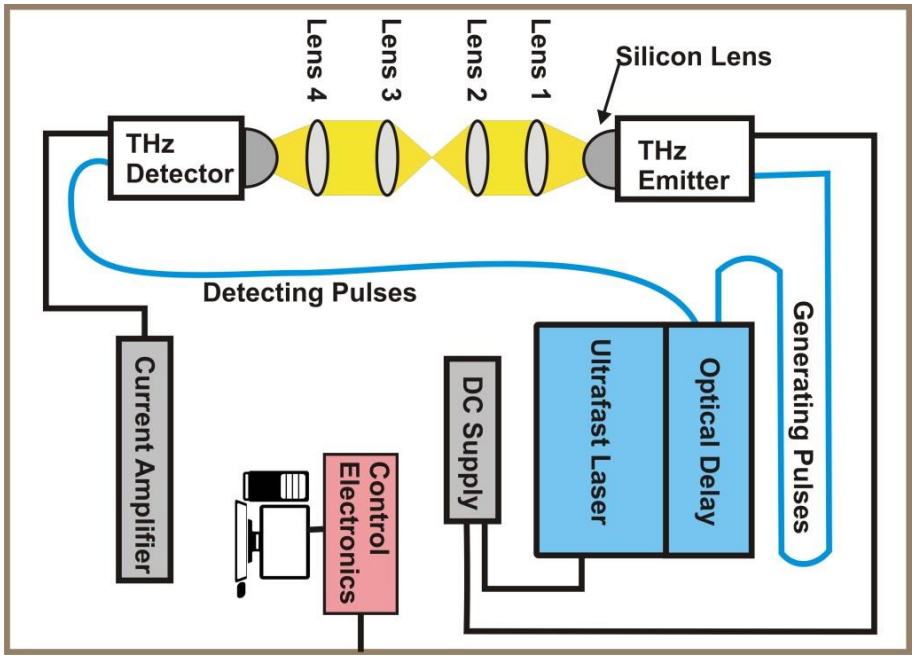


Figure 5.1: Schematic of the THz Time Domain Spectroscopy (TTDS) system set-up.

## 5.2 Direct TTDS measurements

An optical path of our direct TTDS set-up consists of a transmitter with a THz cone shape silicon lens, four intermediate TPX 50 THz lenses for focusing the beam and a detector. A waveguide block under test (WBUT) stands between the two most centered lenses where the waist of the horns should be at the focus for the best optical coupling. Two wire grids as polarizers (THz wire grids) are used to suppress any unwanted polarization of the generated signal. A 3 axis stable holder to adjust the position of a WBUT is also applied. Prior to measuring the detected field transmitting

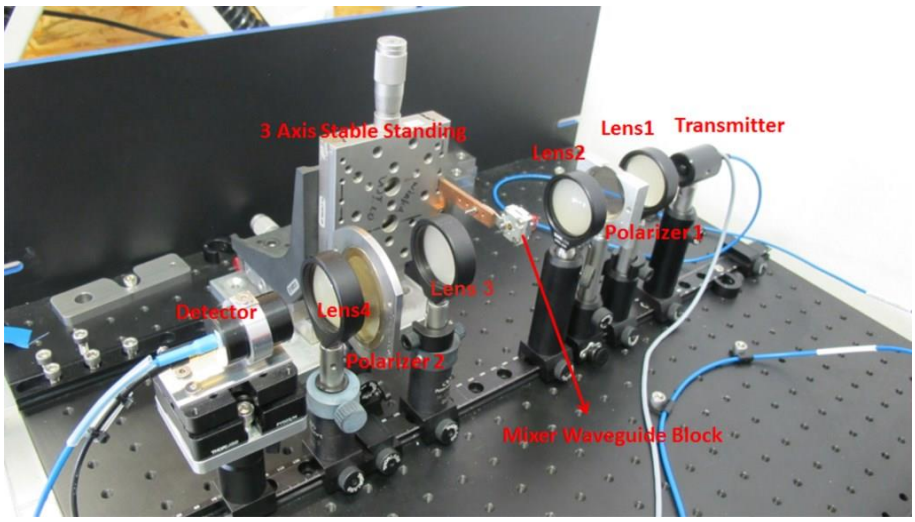


Figure 5.2: Direct TTDS set-up with the 1.9 THz back to back LFA horn antennas as an under test waveguide block

through any WBUT, the set-up must be operated in its optimum situation. This can be achieved by adjusting the correct distance, height and rotation of the optical elements with respect to each other. In figures 5.2 and 5.3, the optimum direct system set-up and its THz fourier response are depicted, respectively. The Fourier transform is averaged in total time of 500 s measurements. One should notice that the measured blue curve is achieved with a tiny hole of about 2 mm diameter standing diaphragm to confirm the functionality of the set-up. As can be seen, the amplitude of the detected field drops drastically at 0.5 THz, with another drop at 1.5 THz, but still is sufficiently large enough to measure our frequency range of interest. Because the system is not in vacuum, there are water absorption lines in the response.

As a first step, we have replaced the aperture diaphragm with two connected back to back 1.9 THz spline horns [77], see figure 5.3. The reason for choosing this configuration is that we wanted to establish the optimum distance between the 2 center lenses ( lens

2 and 3 in figure 5.2) and the horns for maximum signal transmission. We need to know this distance for later measurements. The result of the measurements is also shown in figure 5.3. The 2 horns connected back to back are effectively connected by a very short piece of waveguide (integrated in both of the horns), which adds a negligible transmission loss. The functionality of the horns has been confirmed during the measurement of the LFA array channel of the GREAT receiver for the SOFIA observatory [73]. As it is depicted in figure 5.3, the detected field response versus frequency shows a well measurable transmission with the expected 1.5 THz waveguide cut off frequency. Well above the cut-off frequency the transmission of the back to back horns is almost identical to the transmission of a 2 mm aperture diaphragm.

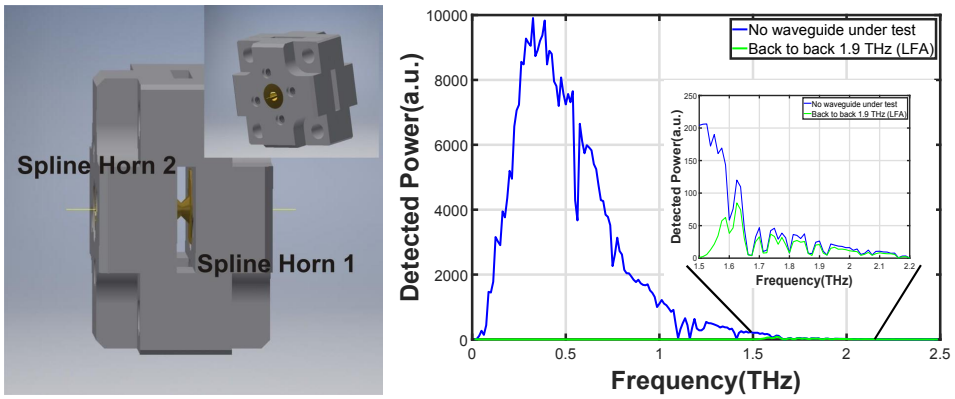


Figure 5.3: Left: The 1.9 THz back to back horns sketch in Autodesk Inventor, Right: Detected field versus frequency response of the aperture diaphragm hole and response of the back to back 1.9 THz horns in the direct TTDS set-up, 500 s integration time.

We noticed during the measurements that the positioning of the horns with respect to the 2 lenses is very critical and takes quite some time to reproduce. Therefore, we applied the same method inside the cryostat using in our cryogenic measurement with replacing one lens by an elliptical mirror. A precision mounting flange is integrated with this mirror for the horn. This has the advantage that the horn is attached to the flange is always in the right position with respect to the mirror. The mirror stays in place, well adjusted to the detector and lens 4, see figure 5.4. Now if the second horn is replaced by e.g. a waveguide + horn or by the balanced mixer block, only lens 2, lens 1 and the emitter have to be shifted, along the rails over a well defined and reproducible distance. This makes the measurement and its reference more reliable and reproducible compared to the previous measurements in the same set-up.

## 5.3 90° angle TTDS measurements

The main change compared to section 5.2 is the replacement of the lens 3 with an elliptical mirror + integrated horn mounting flange that is also used inside the dewar. The mirror is mounted on a 5 axis pitch, yaw and translation stage [78], see figure 5.4.

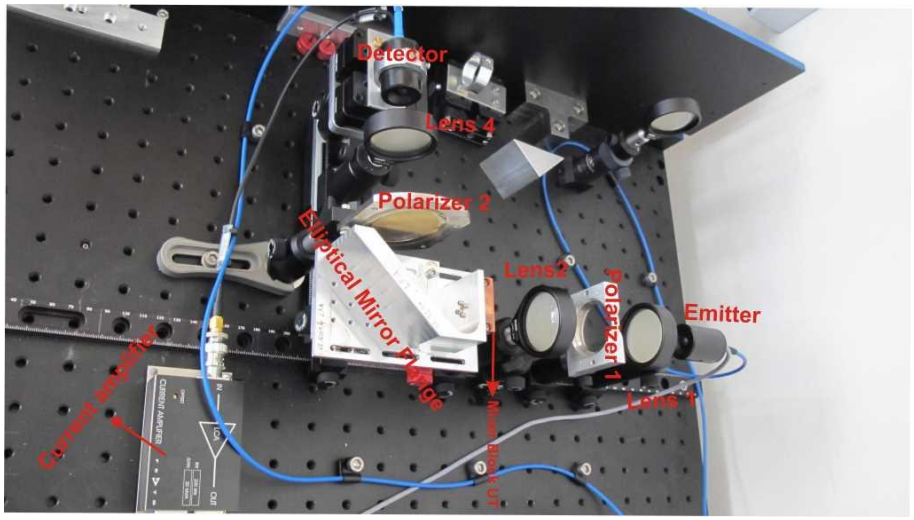


Figure 5.4: TTDS 90 degrees angle set-up using an elliptical mirror + flange instead of focusing lens 3.

As it was mentioned in Section 5.2, the 1.9 THz back to back spline horns is used as the reference transmission to which the next measurements are compared. Consequently, the first measurement in the 90 degrees angle set-up has been done with the 2 LFA spline horns back to back. All following measurements are done in the same set-up to avoid changes in the calibration by a change in the alignment. The TTDS is highly sensitive to the alignment of the optical path including the waveguide blocks. Because, the other WBUTs use the same LFA spline horn (figure 5.5 towards the detector, the distances between mirror flange-lens 4 (D4=103 mm) and lens 4-detector (D5=17 mm) are kept constant. Additionally, the distance between emitter-lens 1 (D1=28 mm) is also constant. These optimum values have been achieved after many measurements of changing distances, heights and rotations using the back to back LFA horns to get the highest transmission through the block (detected power). The best obtained distances between L1-L2 and L2-to the middle point of the parabolic mirror are D2=61 mm and D3=94 mm, respectively.

The back to back LFA horns are then replaced by the rectangular waveguide block with a length of 1.8 mm between the two spline horns, see figure 5.5-left. The reason

of this measurement is to find out the waveguide loss per length at our THz frequency range of interest. This 1.8 mm value is chosen equal to the sum of the length of the two waveguide pieces in the balanced mixer block from the spline rectangular output to the end tip of the diagonal horn in the balance waveguide block, see figure 5.5-right. The two substrate channel arms with 40 $\mu$m at their longer sides have a cut off frequency ($f = \frac{C}{2d}$) of about 3.7 THz which is beyond the frequency band of the waveguide channels. In the equation, C and d stand for the speed of light and longer side of rectangle, respectively. Consequently, almost no signal transmits in the waveguide of substrate channels. This has been also proven by simulating the balance block without the mixer circuit in CST microwave studio. The detected power (field squared) versus frequency is shown in figure 5.6. This optimum response has been achieved by changing D2 and D3 to 95 mm and 60 mm, respectively. These changes have occurred because of adding longer waveguide which has shifted the position of waist of the spline horn in the optical path towards the emitter.
Thereafter, the long waveguide and the second LFA horn are replaced by the balance waveguide block. In order to have a direct comparison to the measurements before, the mechanical workshop has cut the integrated mirror at the diagonal side on the block. As a result, the new block configuration has similarity to the back to back long waveguide LFA with replacement of spline horn towards emitter by the machined diagonal horn in the balance block, see figure 5.5-right. The D3 value is changed to 98 mm due to the different waist of the diagonal than spline horn. The D2 is also 61 mm. The optimum result of measuring the transmission through the balance block with no integrated mirror as a detected power (squared detected field) is depicted in figure 5.6.

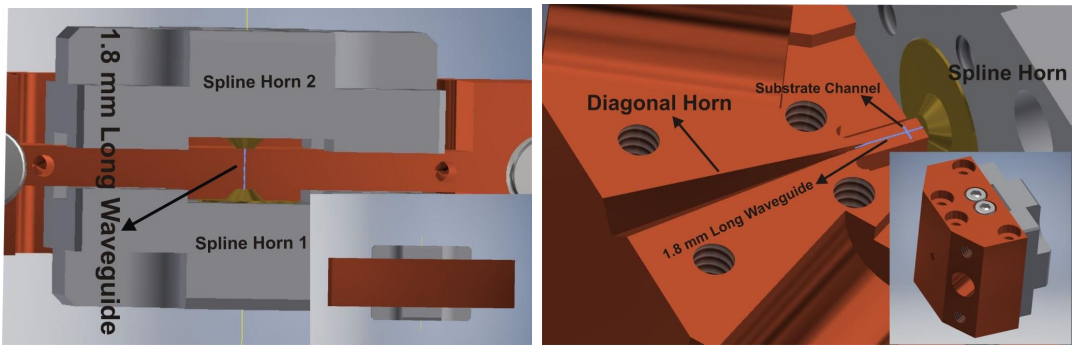


Figure 5.5: Inventor sketches Left: A 1.8 mm rectangular long waveguide between the two 1.9 THz spline horns manufactured by the RPG GmbH. Right: A balance waveguide block consisting of a 1.8 mm rectangular waveguide between a milled diagonal and a spline horn antennas without an integrated mirror.

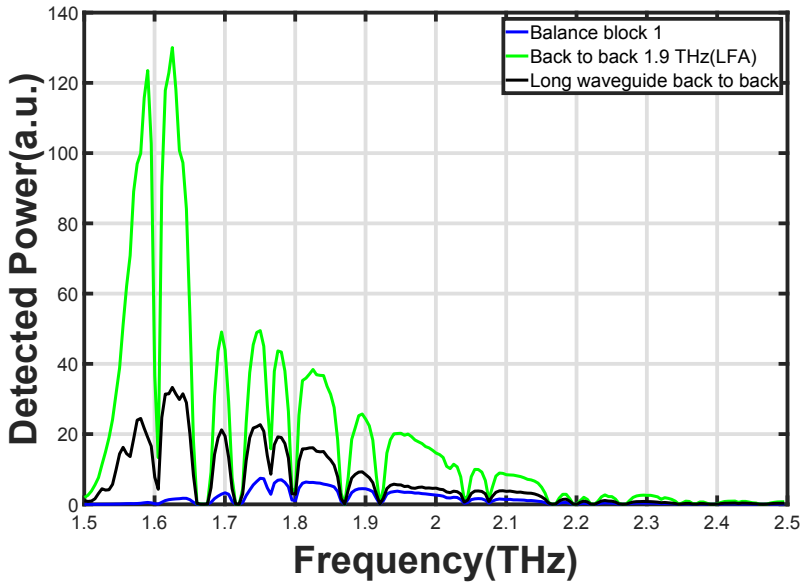


Figure 5.6: TTDS Measurement results of LFA spline horns connected back to back (green curve), LFA spline horns back to back with a 1.8 mm rectangular waveguide between them (black curve) and balance block number 1 with sputtered gold (blue curve) are obtained in the 90°angle set-up with 200 s integration time. The curves include water lines absorption.

Figure 5.6 shows the transmission through the balanced block and the back-to-back LFA horns with a 1.8 mm long waveguide between. By comparing them to the transmission through back-to-back LFA horns, we can calculate the loss due to the 1.8 mm long stamped waveguide and milled diagonal horn. The detected power in the back-to-back LFA horns with the 1.8 mm long stamped waveguide between and the balanced waveguide block with the milled diagonal horn are about 2.7 and 6 times lower than the detected power in the back-to-back LFA horns. Consequently, there is about 2.4 dB loss per millimeter length of the stamped waveguide and about 3.5 dB loss because of the milled diagonal horn. The higher cut off frequency in the balanced waveguide block could also be caused by milled diagonal horn. As discussed earlier, the sky signal for the heterodyne measurement couples through the spline horn side of the balance waveguide block that sees a 500 $\mu$m long waveguide which causes, according to the TDS measurements, equal to 1.2 dB loss.
The mechanical workshop also manufactured a second balance waveguide split block. The TTDS measurement for the block number 2, where contrary to block number 1 no Au was sputtered on the waveguide walls, was also done in 90 degrees angle set-up. As it is shown in figure 5.7, the detected power is much lower in comparison to the

response of the measurement of the block number 1. After some significant burrs in the throat of the diagonal horn were removed by an electro-chemical polishing process, the block was measured again. The improved transmission is also shown in figure 5.7.

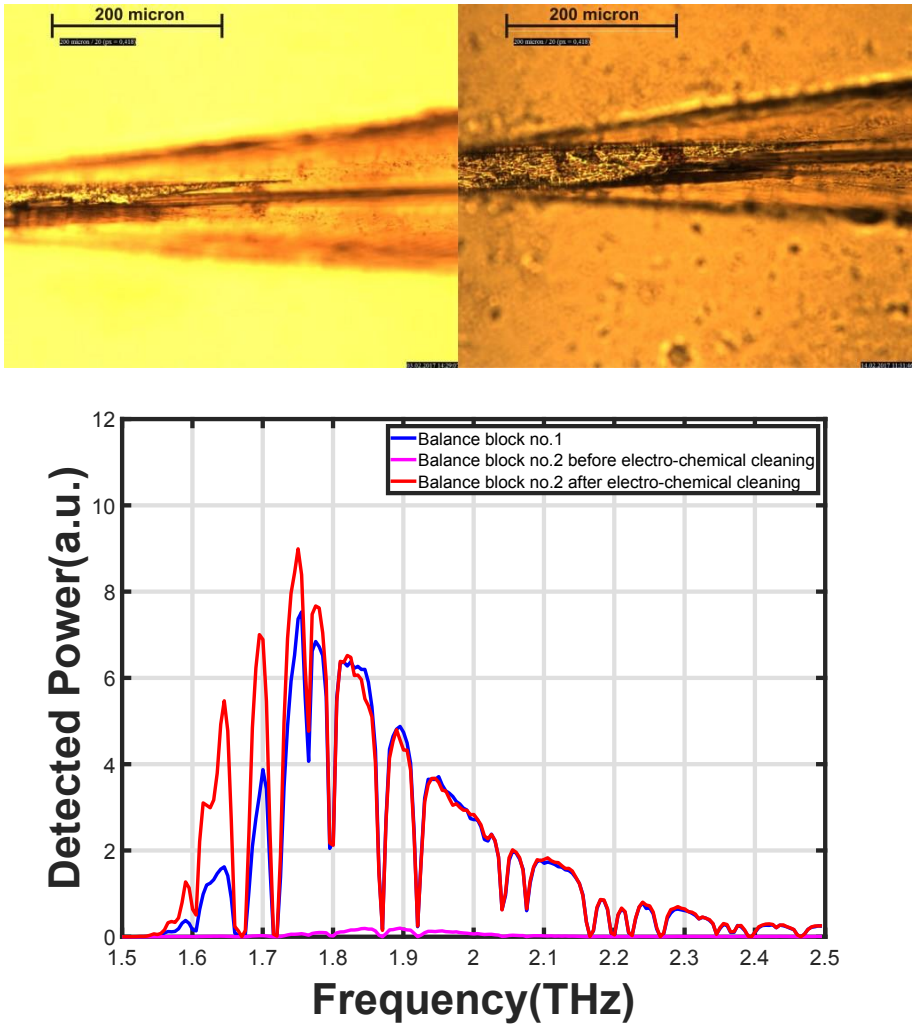


Figure 5.7: Top: Images taken by an optical microscope of the balance waveguide block number 2, left: before electro-chemical cleaning process, right: after the cleaning process. Bottom: Comparing of the TTDS measurement detected fields versus frequency of the balance blocks 1 (after cleaning process) and 2 (before and after of cleaning process).

# Chapter 6

# Measurements of the fabricated 1.9 THz balanced HEB mixers

In this chapter, first the DC characterization of the fabricated 1.9 THz balanced HEB mixers is reported. After that, the cryogenic-high frequency heterodyne measurements of the selected and mounted devices in the balanced waveguides blocks are presented.

## 6.1 DC characterizations

The DC behavior of the superconducting 1.9 THz balanced HEB mixers is verified by the resistance versus temperature (RT) and current versus voltage (IV) dependency. Generally, the DC characterization is done at three different stages being before device separation (on wafer sectors), after device separation (individual device mounted inside the waveguide block with horns) and mounted inside the dewar. The first two measurements are done with a dipstick in liquid helium and the last one in the vacuum LHe dewar. However, because our balanced blocks with two SMAs are too large to fit in the available dipsticks, here only results from before device separation and inside of the vacuum dewar are reported.
The importance of measuring after and before device separation is related to the fact that there are extra steps for etching the SOI wafer from backside (see Section 4.2) to seperate the membrane mixers which can influence the RT and IV curves. In addition, when mounting inside of the waveguide block and mounting the spline horn there is also a chance to degrade devices, e.g. by ESD or strain. In my balanced design, it is easier to mount the spline horn as it clamped to the waveguide block compared to the LFA and HFA single ended HEB mixers where the spline horn is mounted directly on

the probe antenna of the device [10]. So, I expect less influence of mounting the horns. On the other hand the device is clamped between the 2 halves of the split balanced block, a process of which we cannot very well observe the result. The more so because if we open the block again (remove one half ) the device is usually broken.
After dicing the fabricated 1.9 THz balanced HEB wafer into different sectors, I have selected a sector more to the center of the wafer, hoping to have less inhomogeneity in the NbN thin film, glued it with a wax (APiezon-N) on a carrier and wire bonded each balanced HEB mixers to the DC pads. After that, the carrier is placed inside of a dipstick and immersed in liquid helium. The RT measurements are done by using a calibrated sensor diode to monitor the temperature and applying a small current modulation of about 10 $\mu$A to the each device for recording the resistance by use of a lock-in amplifier. Therefore, the change of the resistance while reducing the temperature from 20 K to 4.2 K is recorded, see figure 6.1 for the measured RT curves of the sectors I, M and R. There are (at least) two important parameters to obtain from the RT curves, one is the resistance at 20 K $R_N$ and the other one is the transition temperature $T_C$. As can be seen from figure 6.1, the mean value of the $R_N$ varies for the sectors I , M and R of about 110 $\Omega$, 100 $\Omega$ and 75 $\Omega$, respectively. The design value for the one HEB per arm is 120 $\Omega$ and for the two HEBs on one arm is about 90 $\Omega$, which shows a difference from the design value of about 17% in both cases. The measured $T_C$ is about 7.9 K, 7.8 K and 8.1 K for the sectors I, M and R, respectively. This value of $T_C$ is about 2.5 K lower than the $T_C$ (10.5 K) of the sputtered NbN thin film on the blank (not-processed) SOI wafer. In addition, sector M shows significantly less spread in $R_N$ and $T_C$ than the sectors I and R.
For the balanced HEB mixers, it is important to achieve as similar as possible RT curves with equal $R_N$ and $T_C$ for the two HEB bridges (left and right) on one device. This is to avoid as much as possible imbalanced responses introduced by the HEB bridges on one device. As an example, the RT curve for the right and left HEB bridges of the device R04 (two HEB bridges parallel in one arm, $R_N$ design value is 90 $\Omega$ is shown in figure 6.2 and with a zoom into the response at temperatures lower than the $T_C$.
Additionally, the RT of the individual balanced HEB device I01 mounted in the waveguide block, Section 4.3, is measured inside of the dewar and plotted in figure 6.3 and compared to its RT response of the device on wafer with dipstick in liquid helium on the same plot. The same curves are also shown for the M07 device in figure 6.3. For the purpose of RT measurements inside of the dewar, a resistor heater is used to heat up the mixer block. Because it is not possible to mount the heater directly

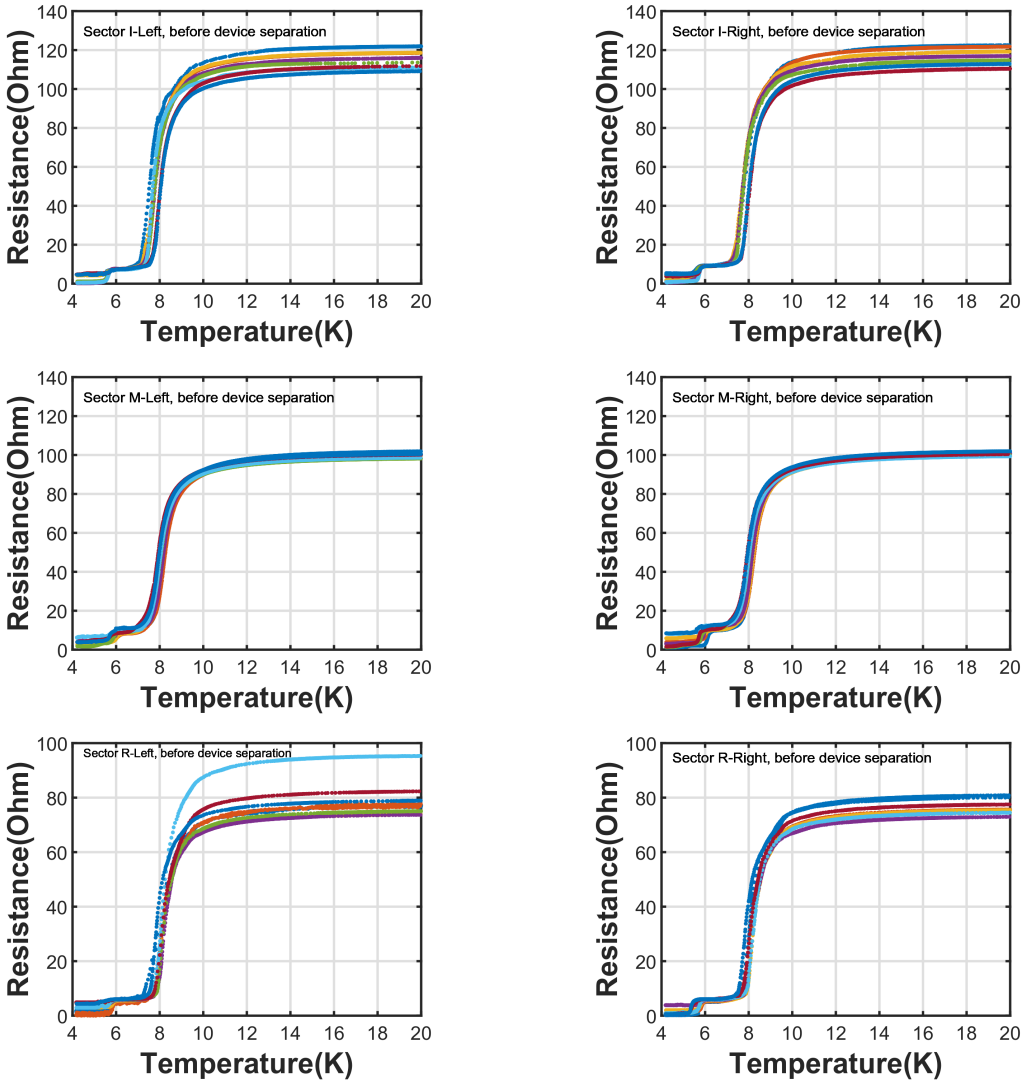


Figure 6.1: Measured RT curves of the sample diced sectors chosen from the fabricated wafer before device separation. The color indicates the mixer device. The HEB bridges at the left and right sides of the hybrid-ring coupler are called as left-HEB and right-HEB, respectively.

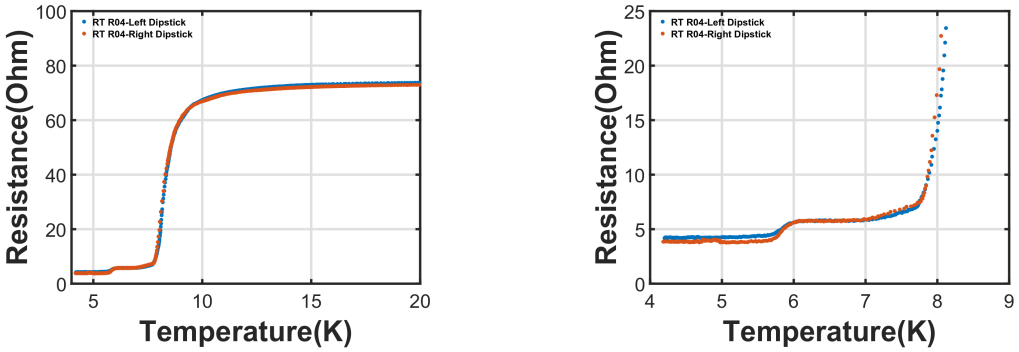


Figure 6.2: Left: Measured RT for the left and right HEB bridges of the device R04 with the dipstick in liquid helium, Right: Zoom into the part of the RT at the superconducting region.

on the existing balanced block, it is placed on the cold plate of the dewar in a some distance. This is the reason for not recording the RT curves inside of the dewar at the high temperatures. The RT curves measured inside the dewar show a $R_N$ that is lower about 10 Ω compared to the value measured in the dipstick on the wafer. The measured value for the $T_C$ is almost identical for the both measurements. While these measurements were done as an additional health check for the devices in the mixer block, the shape of the RT curves at temperature lower than $T_C$ comes as a surprise because the curves inside the dewar do not show the additional step compared to the measured RT curves on the wafer before separating the membrane devices. For an overview about the fabricated balanced HEB mixers in DC, the RT measured curves with the dipstick and inside of the dewar for the M07-right HEB bridge are compared with the R07-LFA and H18-HFA pixels, see figure 6.4. In addition, the RT curve of the device J08-LFA is also plotted and compared where it is a newly fabricated single-ended mixer on a similar set of sputtered NbN thin film on SOI wafers by Dr. Stefan Selig. It is clear that also for the previous devices, the step below $T_C$ looks different inside the dewar than it does in the dipstick. For the fabricated balanced mixer device it can be seen that the $R_N$ and $T_C$ are lower than for the other devices. In addition, the step in the RT curve at the superconducting region lower than $T_C$ measured in the dipstick is much more dominant for the balanced devices.

The DC-IV measurements are done at 4.2 K either with a dipstick kept in the liquid helium or inside of the vacuumed-cooled dewar when the LO is off (not-pumped curves). With sweeping the voltage over the device from -30 to 30 or -50 to 50, the response current is recorded. The slope of the linear parts of the IV curve indicates the normal state resistance that is the same as measured in the RT curve. The slope

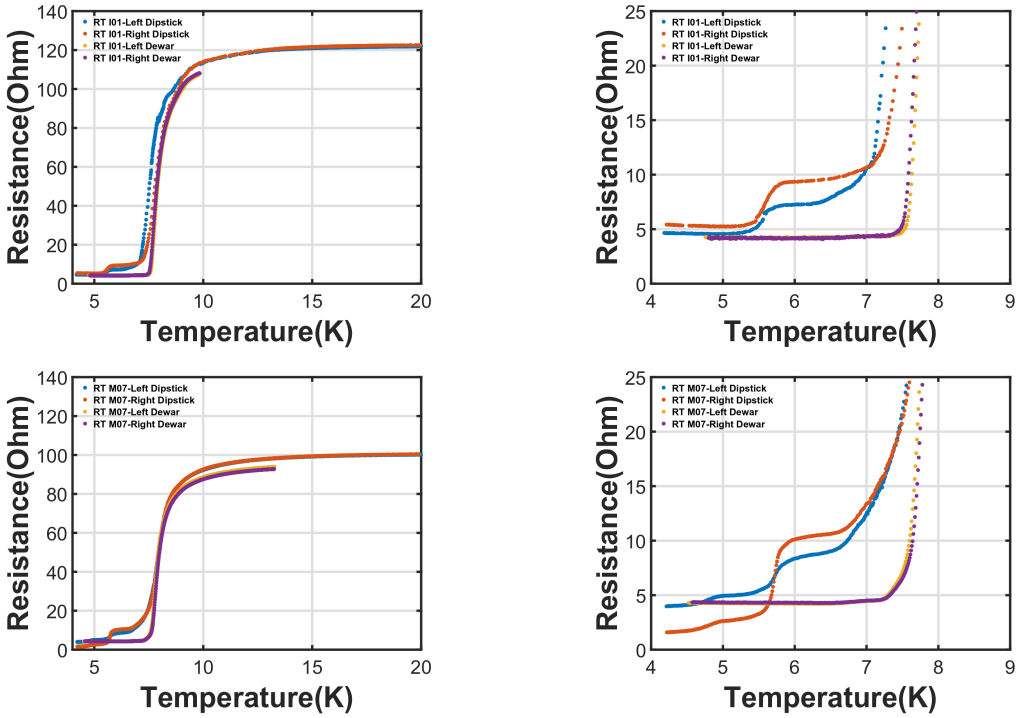


Figure 6.3: Measured RT curves with a dipstick in liquid helium and compared to the RT's measured inside of the dewar, Top-Left: Device I01, Top-Right: Device I01 zoom in, Bottom-Left: Device M07, Bottom-Right: Device M07 zoom in.

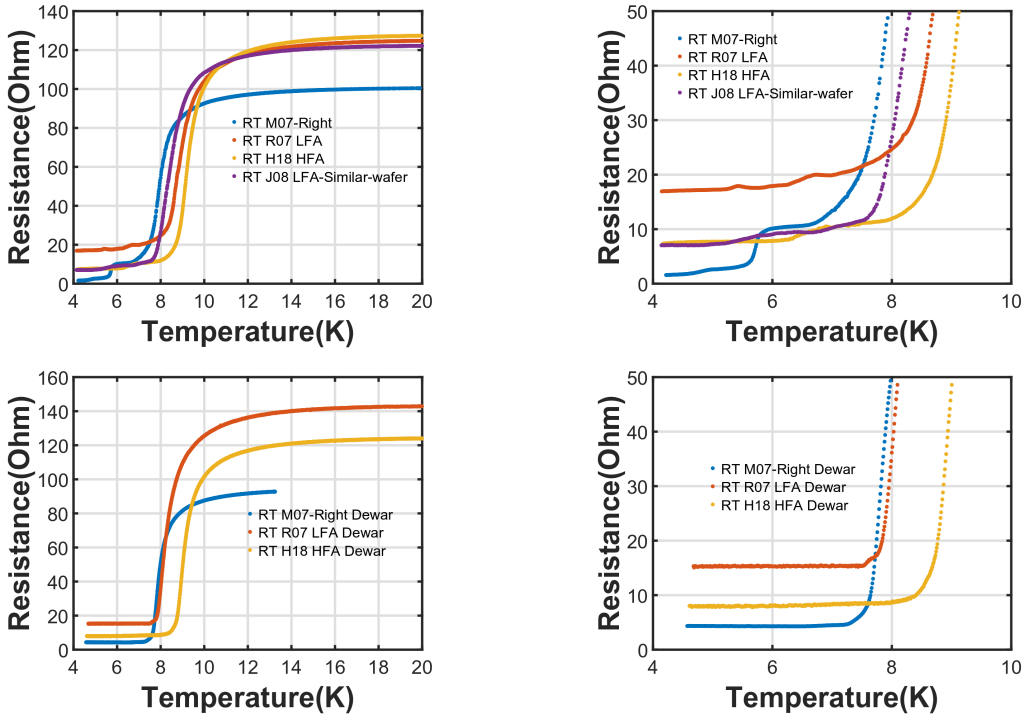


Figure 6.4: Comparison of the measured RT's between the right-HEB bridge of device M07 and devices R07-LFA, H18-HFA, measured and newly reported J08-LFA, Top: On the wafer with dipstick in liquid helium, Bottom: After device separation and inside of the block (no available dewar result from the device J08-LFA.

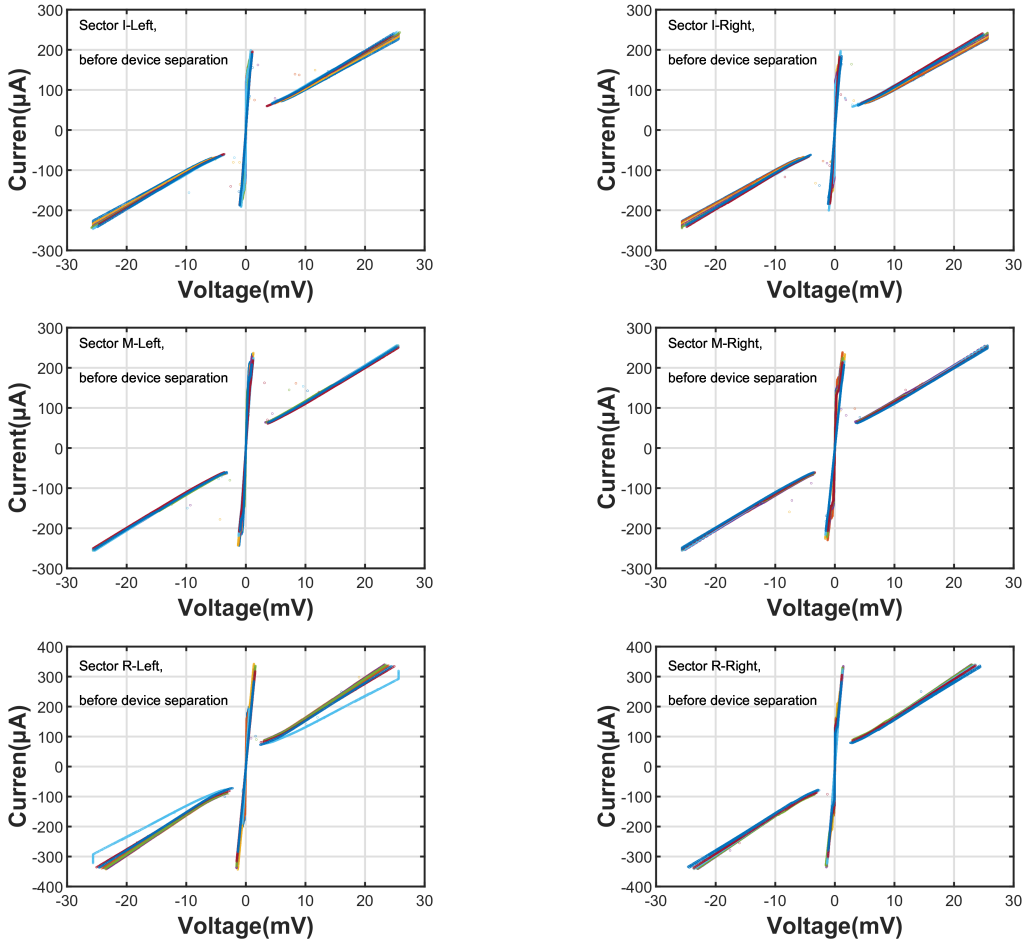


Figure 6.5: Measured DC-IV curves of the sample diced sectors chosen from the fabricated wafer before device separation

of the superconducting region is related to the resistance lower than $T_C$ as observed in the the RT curve. One of the important characteristics of the DC-IV curve is the current at the critical voltage [26], $I_C$, which plays an important role in estimating the amount of the LO power necessary for an optimum pump of the device. In [10], it is shown that HEB mixers from one fabricated batch with lower $I_C$'s need less LO pumping power. In figure 6.5, the DC-IV curves of the sectors I, M and R measured with the dipstick are depicted where the mean value of the $I_C$'s are about 185 $\mu$A, 215 $\mu$A and 320 $\mu$A, respectively. From figure 6.5, it can be seen that there are changes in the slope of the curve at the superconducting region. This behavior is related to the existing strong resistance steps in the region below $T_C$ in the RT curves in some of the devices as shown in figure 6.1.

For the balanced HEB mixers, another important DC characteristic to preselect a device from a sector for further RF measurements, is that the HEB bridges on one device

having as similar as possible DC-IV curves with especially also equal $I_C$'s, to make sure that the 2 mixers have a very similar LO power requirement. As an example, in figure 6.6, the measured DC-IV in the dipstick is shown for the device R04. It shows two similar curves with almost equal $I_C$'s for left and right HEB bridges where there are two HEB bridges in parallel at each balanced arm. Additionally, the DC-IV characteristics measured in the dipstick are compared with the measurements inside of the dewar for devices I01 and M07 as depicted in figure 6.7. The difference in the $I_C$'s is quite small, but one noticeable change has happened especially in a case of device M07, where the IV of the right HEB does not show anymore the structure in the superconducting region that it did in the dipstick. This change in the shape of the IV is in correspondence with the non-existing strong step in the RT curve lower than $T_C$ measured in the dewar compared to the dipstick, see figure 6.3.

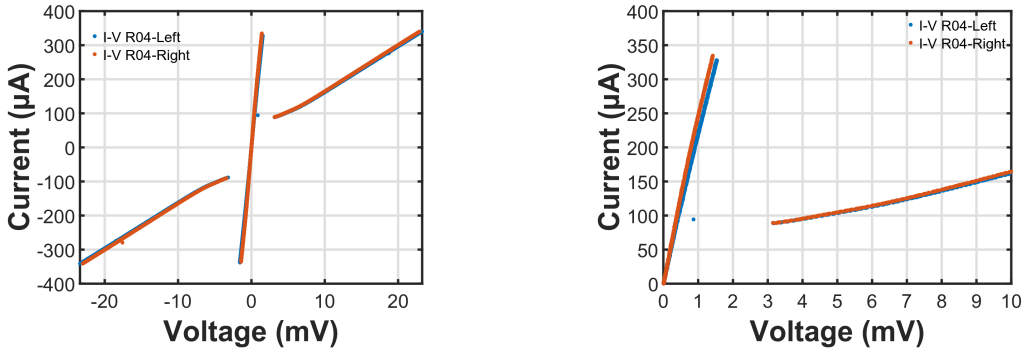


Figure 6.6: Left: Measured DC-IV of the left and right HEB bridges of the device R04 with the dipstick in liquid helium, Right: Zoom into the IV curves for more detail.

Similar to the case of RT characterization, the DC-IV of the balanced device M07 for the right HEB is compared to the pixels from LFA and HFA, see figure 6.8. The reported measured noise temperatures for these single-ended devices are in the range of 800-1000 K at the IF frequency of 1 GHz, and therefore it would be expected that the balanced mixers with similar RT's and IV's would show noise temperatures in a similar range. Also, in table 6.1, some of the selected devices with their DC characteristics for further RF measurements are listed.

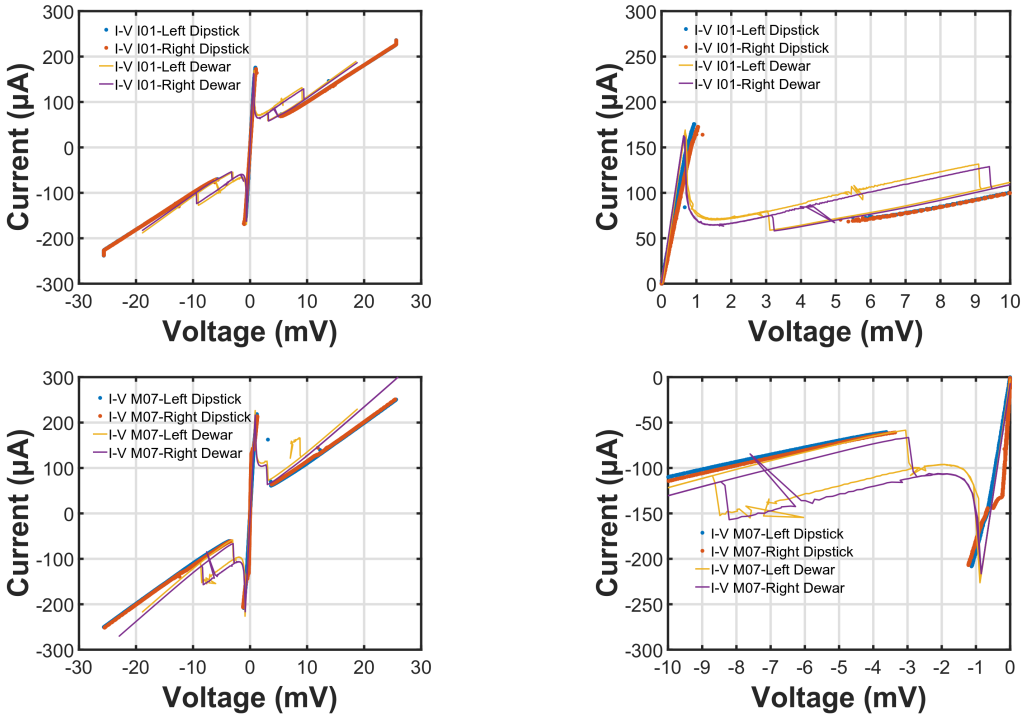


Figure 6.7: Measured DC-IV curves with dipstick in liquid helium and compared to the IV's measured inside of the dewar, Top-Left: Device I01, Top-Right: Device I01 zoom into the $+V_{bias}$ region, Bottom-Left: device M07, Bottom-Right: Device M07 zoom into the $-V_{bias}$ region.

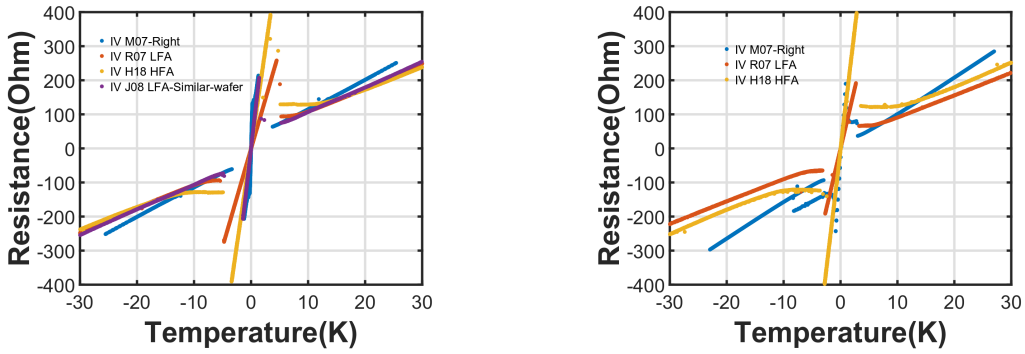


Figure 6.8: Comparison of the measured IV's between the right HEB bridge of device M07 and devices R07-LFA, H18-HFA, measured and newly reported J08-LFA, Left:On the wafer with dipstick in liquid helium, Bottom: After device separation and inside of the dewar for M07-Right and inside of the mixer block and mounted horn dipped in liquid helium with dip stick for R07-LFA and H18-HFA, no available data for newly reported J08-LFA inside of the mixer block and mounted horn, dipped in liquid helium.

| Device | RN | Tc | Ic |
|---|---|---|---|
| $M_{07}$-L | 100.2 Ω | 7.95 K | 219 $\mu$A |
| $M_{07}$-R | 100.4 Ω | 7.97 K | 214.8 $\mu$A |
| $I_{02}$-L | 118.5 Ω | 7.82 K | 158.1 $\mu$A |
| $I_{02}$-R | 121.8 Ω | 7.89 K | 157.7 $\mu$A |
| $I_{07}$-L | 111.8 Ω | 8.11 K | 193.4 $\mu$A |
| $I_{07}$-R | 110.4 Ω | 8.12 K | 185.8 $\mu$A |
| $R_{04}$-L | 73.7 Ω | 8.34 K | 328.7 $\mu$A |
| $R_{04}$-R | 72.9 Ω | 8.25 K | 335.2 $\mu$A |

Table 6.1: Some DC characteristics of the selected devices for further RF measurements where L stands for Left and R for Right.

## 6.2 Heterodyne measurements

To perform RF heterodyne measurements, the balanced device is mounted inside the waveguide block where the integrated mirror is at the diagonal horn side and the 1.9 THz horn clamp is assembled at the spline horn side, see Section 4.3. After that, the balanced block is mounted on the cold plate of the dewar attached to an elliptical mirror flange to certain the alignment of its spline horn which is directed towards the window 1 (signal path). The diagonal side (LO path) is aligned to the window 2, see figure 6.9. There are two 0.5-5 GHz LNAs with about 10 K noise temperature to amplify the generated IF signals. Additionally, two bias tees are attached to the LNAs and electrically connected to bias the HEB bridges over the same coaxial cables as is used to connect the mixer to the LNAs. In order to avoid any additional imbalances in amplitude and more dominantly in phase which can be introduced by the length difference between the two coaxial cables (from the SMA output connectors of the balanced block to the inputs of LNA 1 and 2, and from outputs of the two LNAs to the two IF outputs of the dewar), the total length of the two coaxial are chosen to be the same.

For the purpose of recording the approximate temperature of the mixer, a sensor diode is screwed to the balanced block. Additionally, for heating up the block (RT measurement in the dewar, "pumping" the device with heat), there is a heater is connected to the back of the mirror flange instead of placing on the block due to the lack of space. Because it is placed with some distance from the block, therefore it was not possible to heat up the mixer for the RT measurements inside of the dewar at higher temperatures, see Section 6.1. By pumping the dewar over-night the pressure of about $10^{-5}$ mbar was reached for the isolation vacuum. When the dewar, after

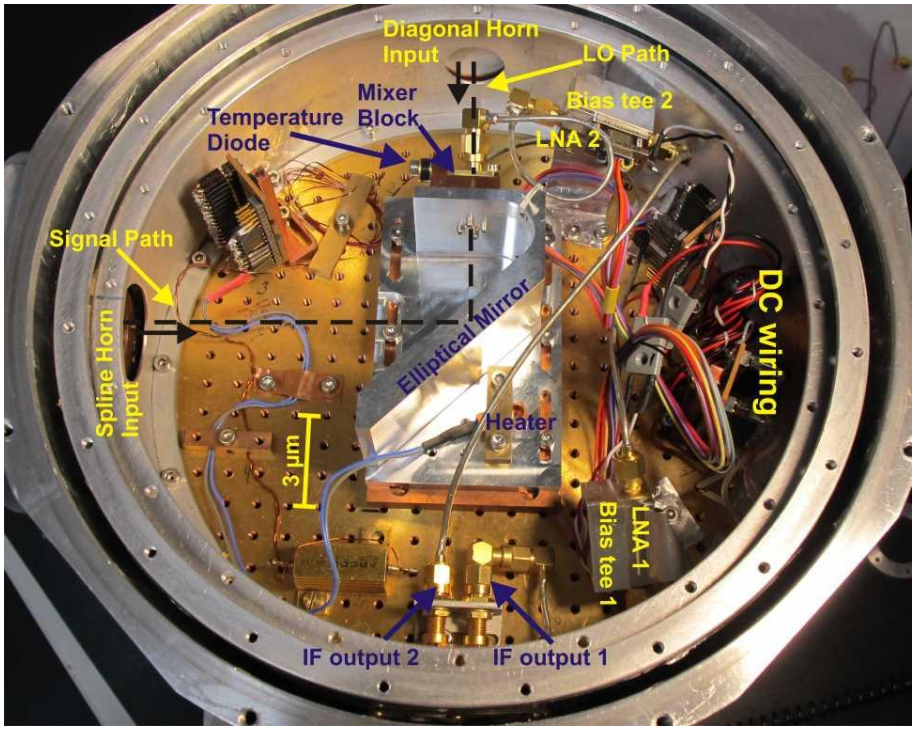


Figure 6.9: Inside look of the balanced dewar consisting of a balanced block, an elliptical mirror, two LNAs, two bias tees, a heater, a sensor diode and DC wiring.

pre-cooling with LN2, is filled with LHe, it reaches a temperature of 4.3 K measured on the temperature sensor on the cold plate. The dewar temperature rises to about 4.9 K after switching on and biasing the two LNAs.

In figure 6.10, the schematic of the heterodyne RF measurement set-up is depicted. One should notice that the indicated set-up has no focusing lens in the optics at the diagonal side for the case of the waveguide balanced block with the integrated mirror. For pumping a balanced HEB mixer, the existing in house built 1.9 THz QCL [74] is applied at the diagonal side. To use this LO at its high output power, it is mounted inside of a vacuum dewar. In addition, there is an absorber to use as a 295 K load and when filling it by liquid nitrogen as a 77 K load for doing the Y-factor measurements at the spline horn side of the balanced block. A warm commercial 0.698-2.2 GHz 180° IF hybrid [79] is used at the output of the dewar for the balance measurements. Based on the applied bias polarity on the HEB bridges, one can choose the $\Delta$ or $\Sigma$ output port of this IF hybrid. There is also a MITEQ warm LNA after the 180° IF hybrid to amplify the combined IF signal for the further IF processing. Subsequently, there are two electronic paths inside of the IF processor [10] to define two outputs, one for the 1-5 GHz spectrometer and the other one after passing a 1-2 GHz band pass filter,

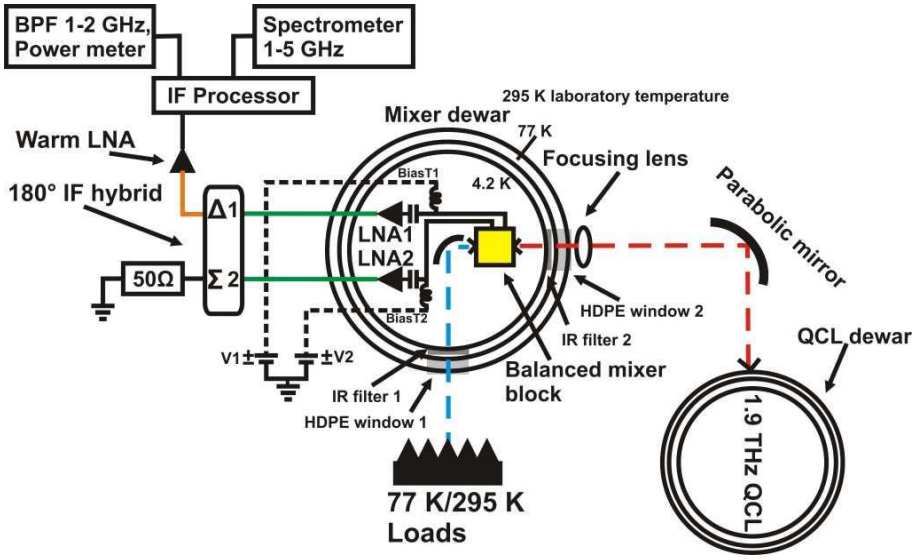


Figure 6.10: Schematic image of one LO 1.9 THz balanced HEB mixer. Two 370 $\mu$m thick HDPE foils have high transmissions at 1.9 THz [10]. Two IR filters are used as shields to the unwanted infrared external radiation.

is connected to a power meter. The spectrometer is used to record the combined IF signal as a function of frequency, and the power sensor to record the integrated power in the 1-2 GHz bandwidth and measure it with a calibrated power meter.

Device M04 is selected as the first balanced HEB device for the RF measurements based on its measured DC characteristics see Section 6.1. After mounting it inside the balanced block (block number 1, where 200 nm Au is sputtered on top of the half of the block that contains the device for better contact), its 180° port towards the spline horn side and 0° port towards the diagonal side, it is placed inside the dewar. The QCL dewar is placed also in the heterodyne set-up after doing initial aligning with an optical laser. After that, all required cabling are connected and both LNAs are DC biased at $V_{drain} = 5$ mV and $I_{drain} = 5$ mA. Next, the HEB bridges (left and right) of the M04 device are separately biased and their IVs with no pumping LO are inspected. The QCL LO is biased to operate in its first mode (1.885 THz, 69 $\mu$W) for pumping the HEB bridges from the side of the diagonal horn. After several aligning attempts, the HEB bridges were barely pumped. The alignment attempts were severely limited by the short holding time of liquid helium in the QCL dewar ($\sim$20 minutes) when the LO was continuously on.

Cooling down an extra time the mixer dewar, one of the HEB bridges of the M04 device went open and I was not able to investigate further on this device.

M07 is selected as the next HEB balanced device for the RF measurements. This time

the device is rotated 180° inside the block compared to the M04 device, to investigate if the device itself is the reason of being not possible to pump the mixer at the side of the diagonal horn. In addition to that, the block is also electro-chemical polished by our machining laboratory to improve the signal transmission at the diagonal side, see Section 5.3. First, the QCL LO is placed in the optics path of the spline horn side and similar to the device M04, the HEB bridges are fully pumped. After that, the QCL LO is placed back to the LO optics path to pump the mixer at the diagonal side of the balanced block. After several alignment approaches, there was a bit of improvement in the amplitude of the pumped IV curves, but not enough to fully pump the devices from the side of the diagonal horn.

One critical element of the balanced split block at the diagonal side is the integrated mirror because it is not possible to mechanically inspect the curvature of the machined mirror. Additionally, at that time there was no measured data about the loss per length of our machined waveguides at the THz frequencies which this almost blind response might be caused by the 1.3 mm long waveguide at the diagonal side compared to the 500 $\mu$m at the spline horn side to the mixer. Therefore, because of the two mentioned above reasons, the TTDS measurements described in Chapter 5 are done to characterize the machined balanced blocks. As a result, 2.4 dB loss per millimeter length, the longer waveguide at the diagonal side cannot be the reason behind the almost blocking the incoming LO signal. After several more unsuccessful alignment attempts, it was decided to use the balanced blocks without the integrated mirror (cut the mirror) and add a borrowed lens from the TTDS set-up to focus the LO signal to the mixer block at the diagonal side. To improve the coupling, the location of the mirror flange inside the dewar is shifted to be perpendicular and closer to the window at the diagonal side.

For the further measurement, I07 balanced device is selected from the sector-I which is mounted inside the block number 1. In this orientation, the 0° and 180° ports of the device are towards the spline and diagonal horn sides, respectively. First, the QCL LO is placed at the side of the signal path where with a combination of the hot/cold signals and a mylar beam splitter, I have tried to measure the noise temperature of the balanced HEB mixer as two single ended mixers. This is important step to estimate the noise temperature of a HEB balanced mixer with the assumptions that the IF gain introduced by the two cold LNAs are the same and the hybrid-ring coupler has a zero phase imbalance. In the ideal case, the balanced noise temperature is 0.5 times the measured noise temperature of each HEB bridge separately.

For this measurement purpose, the Voltage Sweep (VS) technique is used in which

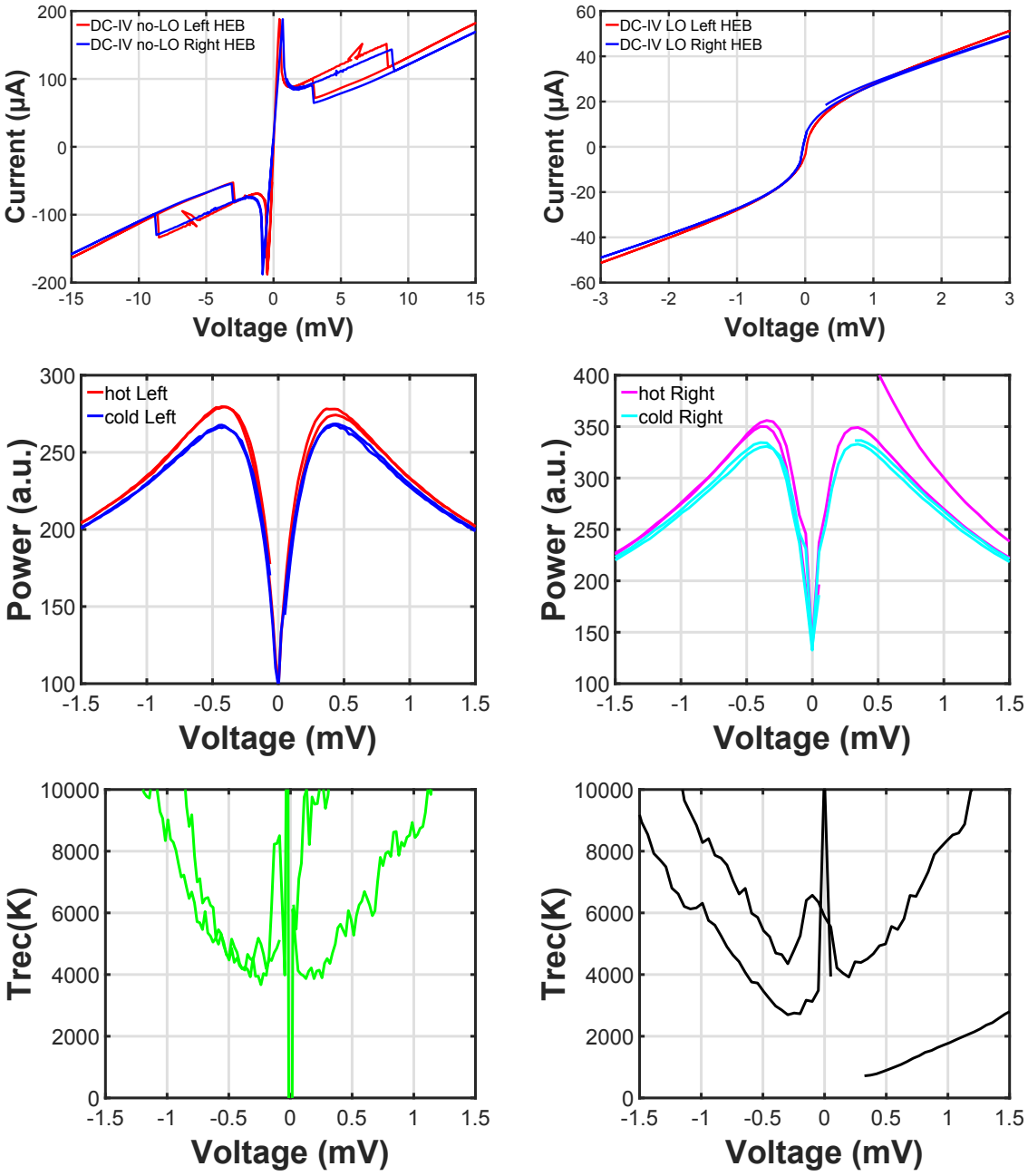


Figure 6.11: I07 plots contain unpumped, pumped, IF output power and noise temperature.

| Device | Balanced block | LO | Spline | daigonal |
|---|---|---|---|---|
| $M_{04}$ | 1-IM | QCL | Yes | Blind |
| $M_{07}$ | 1-IM | QCL | Yes | Blind |
| $I_{07}$ | 1 | QCL | Yes | Yes |
| $I_{02}$ | 1 | QCL | No | Yes |
| $I_{01}$ | 2 | VDI-QCL | Yes | Yes |
| $M_{03}$ | 2 | VDI-QCL | yes | No |
| $R_{04}$ | 2 | VDI-QCL | Yes | Yes |
| $M_{06}$ | 1 | VDI-QCL | Yes | No |

Table 6.2: An overview of the heterodyne measurements of the mounted 1.9 THz balanced devices inside of the block. In the second column the waveguide block that is used is noted. IM stands for the Integrated Mirror. The 3rd column gives the LO source that is used and the 4th and the 5th columns indicate if a measurement is done from that side of the block.

the pump power of the LO is fixed at the optimum level and the generated IF output power is measured by the power meter while the DC voltage is swept over the HEB bridge in a range of -50 mV to +50 mV. As here, the first approach is to measure a single ended noise temperature in a balanced configuration, therefore, one of the HEB bridges is biased in the normal region (no mixing) and the DC voltage is swept over the other HEB bridge. The DC-IV curves for the left and right HEBs of the balanced device I07 with no pumping LO signal are depicted in figure 6.11. A 12 $\mu$m thick Mylar is applied as a beamsplitter which reflects 10% of the LO power and transmits 90% hot/cold signal to the dewar window at the spline horn side. The QCL LO is used in its second mode which shines radiation at 1.98 THz with an estimated power of about 360 $\mu$W [74]. In figure 6.11, the DC-IV curves with pumping LO for the left and right HEB bridges of device I07 are depicted. There are also IF output power for the hot and cold loads in a case of left and right HEBs are plotted. The measured noise temperature of the receiver $T_{rec}$ for the two HEBs derived from these measurements are shown. The best noise temperature for the left HEB mixer at 1-2 GHz IF frequency is about 4000 K at +0.2 mV and about 5000 K at +0.5 mV. The measured noise temperature for the right HEB mixer is approximately equal to the left one. One should notice that here the voltage range for a good noise temperature is narrow 0.2-0.5 mV compared to the LFA or HFA mixers with about 0.5-1.5 mV bias voltage range [10].

After characterizing the balanced HEB mixer I07 as the two single-ended mixers, the QCL LO is replaced in the optics path at the diagonal horn side. This time with the help of a focusing lens, see figure 6.10, as close as possible to the dewar window, and

no integrated mirror on the balanced block, the HEB bridges from the diagonal side are pumped. The VS technique to measure the noise temperature of the balanced HEB mixers is as follows, first biasing one of the HEB bridges in the mixing region which for the I07 device can be about $\pm 0.5mV$ and sweep the voltage in a range of -50 to +50 mV over the other HEB bridge. Depending on the output of the IF 180° hybrid and biase polarity over the two HEBs, the combined IF output power can be maximized or canceling out. However, the measurements were postponed to the next day due to unstable QCL LO power (the second mode did not seem to be stable anymore) causing another thermal cycle also for the mixer dewar which unfortunately degraded the device I07. Therefore it was not possible to do a balanced measurement and also the single-ended response of device I07 could not be repeated. This time, it was possible to remove other half of the split block to look into the I07 balanced device. There was a clear crack on the IF path of the right HEB. As indicated in Table 6.2, I measured a few more devices, but in no device, I could measure a balanced noise temperature.

### 6.2.1 IF LNA noise measurements

In order to investigate the power linearity response of the IF chain consisting of one of the cold LNAs, the warm MITECH LNA and IF amplifiers inside the IF processor, each of the cold LNAs is connected to a 50 Ω load. The load is connected to the cold plate of the dewar with a piece of low conducting material and additionally a heater and a sensor diode are screwed to the housing of the load. This type of measurement for the both cold LNAs, also provides important information about the difference between their gain. A substantial difference in gain would make a balanced measurement as tried in Section 6.2 impossible. The 50 Ω load works as a noise source of which the power can be adjusted via its physical temperature. The output power at the end of the IF chain is measured by the power meter for different set of temperatures applied by the heater to the load. In figure 6.12, the linearity power response to the temperature of the IF chain for the two cold LNAs is shown. As it is seen the slope of the fitted lines for the two LNAs is different which in a case of the balanced measurements should be similar to avoid IF power difference introduced by the IF chains. Changing the DC bias of one of the cold LNAs, this gain difference can be fixed. Therefore, the bias of the cold LNA (named as number 196) is adjusted to be $V_{drain} = 1.43$ V and $I_{drain} = 5.5$ mA instead of the old value $V_{drain} = 1.39$ V, $I_{drain} = 5$ mA to equal the gains of the 2 IF systems. The bias of the other cold LNA (named as number 58)

remains $V_{drain} = 1.39$ V and $I_{drain} = 5$ mA.
The average IF gain in the 1-2 GHz band pass filter can be calculated from the slope in figure 6.12

$$G_{IF}(1-2GHz) = \frac{Slope.10^{att/10}}{k_B B}, \tag{6.1}$$

where att is the attenuation introduced by the IF processor in 0-10 dB range, $k_B$ is the Boltzmann constant, $B$ is the 1 GHz filter bandwidth of the IF processor.

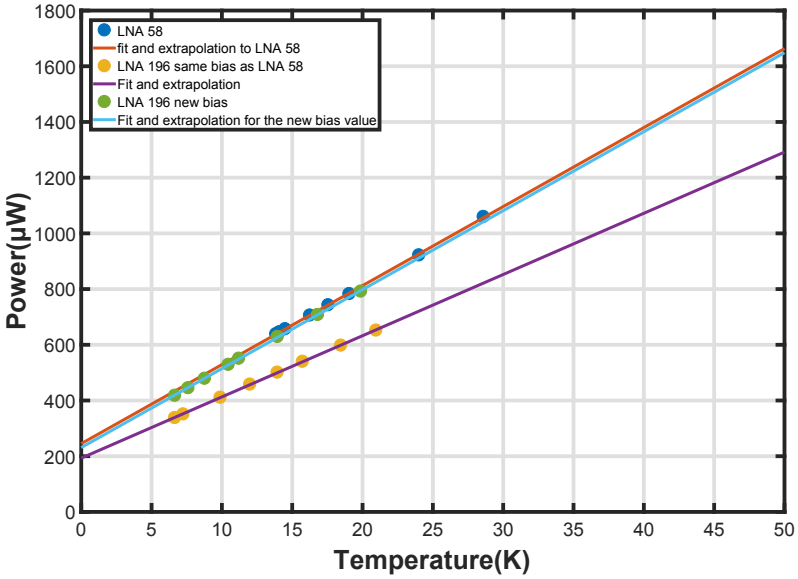


Figure 6.12: Power versus temperature response of two cold LNAs inside the dewar with similar and corrected bias polarities.

## 6.3 Balanced response characterization

In this section, the phase behavior of a 1.9 THz HEB mixer is investigated. Additionally, the RF bandwidth response of one of the balanced devices is studied. As the measured 1.9 THz balanced HEBs are not sensitive enough to study the phase response with a hot (295 K)/cold (77 K) load as input, it is replaced by a stronger source. A 1.9 THz VDI multiplier chain is used in this measurement as a second LO at the spline horn input port and its power can be attenuated by a rotatable grid in front of the LO. The change in the angle of the rotatable grid is controlled by software. Based on the polarization of the VDI LO, the grid can be fully transmitting or by 90° rotation fully reflecting. This new RF measurement set-up is shown in figure 6.13. For the purpose of this measurement, the balanced device I01 is mounted inside the

balanced block number 2 in an orientation that the 180° port of the mixer is directed towards the spline horn side and the 0° port towards the diagonal horn side. The DC-IV curves for the left and right HEBs of the device I01 with no LO and inside the dewar are already shown in Section 6.1.

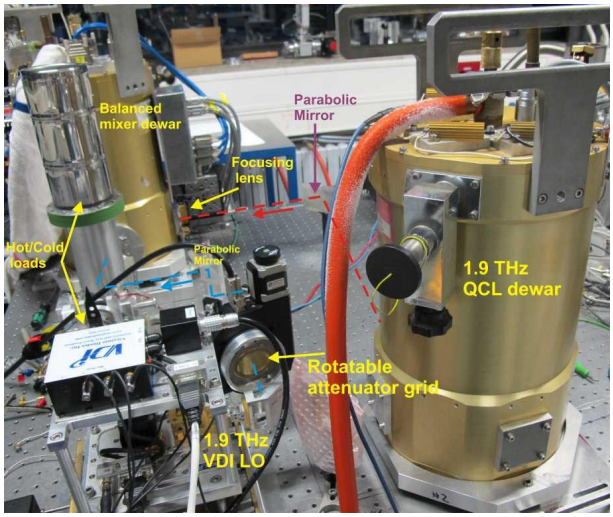


Figure 6.13: Image of the two LO's heterodyne measurement set-up to characterize the balanced phase response of a mounted 1.9 THz balanced HEB mixer device.

Beforehand, I checked the power balance between the two HEB bridges when pumping them from the spline horn side with the VDI LO and after that from the diagonal side with the QCL LO. The optimum pumped IV curves of the left and right HEBs, measured simultaneously, of the I01 balanced device with applying either VDI LO or QCL LO are shown in figure 6.14. The figure shows that the IV's pumped from the diagonal side show less power balance.
Subsequently, the VDI LO is significantly attenuated, down to a level where it is not visible as a pump anymore on the DC-IV curve. A spectrum analyzer is employed for measuring the power of the generated IF signal versus frequency. Similar to the balanced measurement set-up, here also the warm commercial 180° IF hybrid, a phase shifter and some lengths of coaxial cables are used between the dewar IF out-puts and the spectrum analyzer to achieve the phase balance. The balanced IF of the mixer is measured at either the $\Delta$ or the $\Sigma$ ports of the 180° IF hybrid and bias polarities over the HEB bridges are varied.
In figure 6.15, the maximum achievable summation or cancellation of the two generated IF outputs by the balanced I01 device by choosing $\Sigma$ or $\Delta$ and biasing HEB bridges are plotted. First, the $\Sigma$ port of the IF hybrid is connected to the spectrum analyzer. The phase shifter is set to its maximum additional phase of about $14^{\circ}$ and

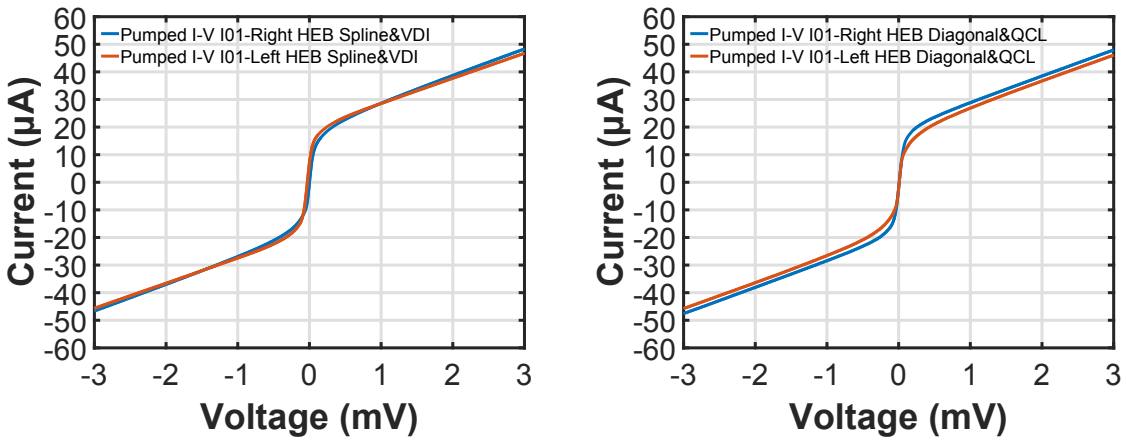


Figure 6.14: Optimum pumped IV curves of the right and left HEB bridges of the balanced device I01, Left: pumping with the VDI LO at the spline horn side of the balanced block, Right: pumping with the QCL LO at the diagonal horn side of the balanced block.

connected to the IF output 2 (HEB-left) where the IF output 1 (HEB-right) is connected via a SMA male to female connector. To achieve the highest peak from the in-phase summation of the two IF outputs, the HEB-right is biased at $V_r = -0.72$ mV and HEB-left at $V_l = 0.87$ mV. If the bias voltage polarity at HEB-left is reversed and set to a value of -0.22 mV the maximum suppression of the signal is achieved. By choosing the $\Delta$ port, and taking the exact same set-up as in the measurements at the $\Sigma$ port, the suppression is measured at the bias polarities for HEB-right $V_r = -0.72$ mV and for HEB-left $V_r = 0.27$ mV. The highest peak occurs at the bias for HEB-right, $V_r = -0.72$ mV, and for HEB-left, $V_r = -0.46$ mV. In both $\Sigma$ and $\Delta$ cases, the suppression of the two IF signals is about 38 dB.

Next, the phase balance response of the device I01 at the diagonal side is measured. This time, the QCL LO is heavily attenuated with the rotatable grid and the VDI LO is used to pump the HEB bridges, while keeping the rest of the set-up identical to that of the previous measurements. As expected the relative polarities of the bias voltage are the same as in the previous measurements. For the $\Sigma$ port of the IF hybrid the highest suppression of about 30 dB is obtained when the HEB bridges are biased for HEB-right at $V_r = -0.72$ mV and HEB-left at $V_l = -0.1$ mV and the highest summation is obtained for HEB-right at $V_r = -0.72$ mV and HEB-left at $V_l = 0.5$ mV. When the $\Delta$ port is connected, the highest suppression about 28 dB is achieved at bias voltages which for HEB-right is $V_r = -0.72$ mV and for HEB-left is at $V_l = 0.1$ mV (good range of 0.1-0.77 mV). The highest summation of the two IF outputs is

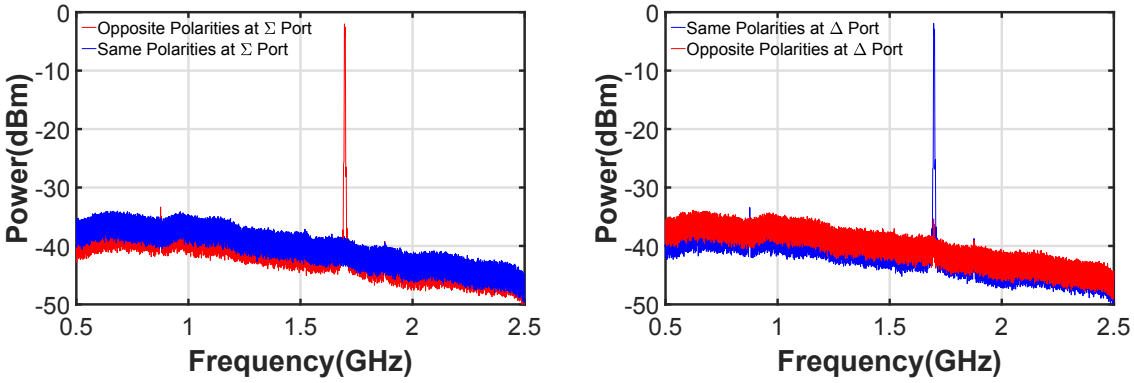


Figure 6.15: Measured Power versus frequency with the spectrum analyzer at when the weak signal is incident on the spline horn side, Left: With opposite and same polarities of the right and left HEB bridges using the $\Sigma$ port of the 180° IF hybrid, Right: With opposite and same polarities of the right and left HEB bridges using the $\Delta$ port of the 180° IF hybrid.

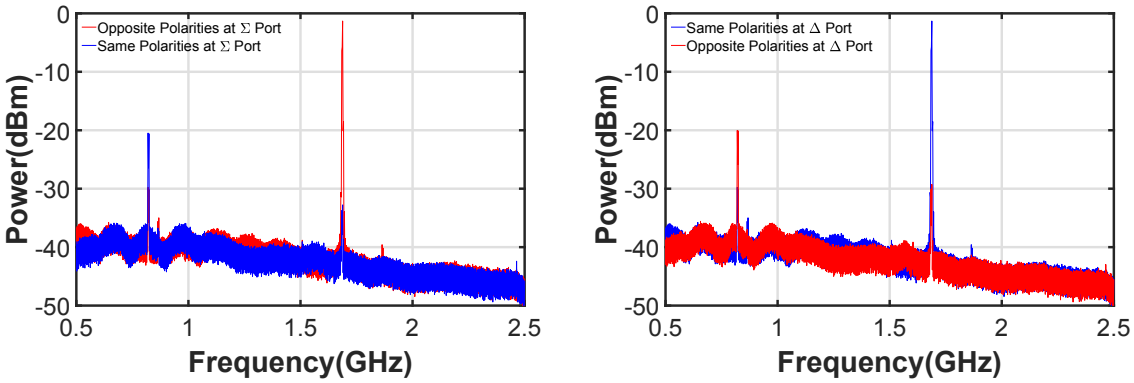


Figure 6.16: Measured Power versus frequency with the spectrum analyzer when the weak signal is incident on the diagonal horn side, Left: With opposite and same polarities of the right and left HEB bridges using the $\Sigma$ port of the 180° IF hybrid, Right: With opposite and same polarities of the right and left HEB bridges using the $\Delta$ port of the 180° IF hybrid.

measured when HEB-right is biased at $V_r = -0.72$ mV and HEB-left at $V_r = -0.46$ mV.

Due to the unavailability at that time, of the FTS instrument for RF bandwidth characterization of the balanced HEB device and to compare with the simulations, here, I have used the (limited) tunability of the VDI LO (1.75-2 THz) to scan at least part of the RF-band. The $I_c$ current of the two vastly under pumped HEB bridges are measured at different frequencies using the attenuated VDI LO. Prior to this mea-

surement, it is important to characterize the linearity of the dependence of $I_c$ to an incident power on the mixer. This is verified by changing the VDI LO power employing different angles of the rotatable attenuation-grid in front of the LO. This will allow to define a linear limit for the pumped $I_c$'s. In this limit, the current at critical voltage $I_c$ of the each HEB bridge is linearly proportional to the incident power. The incident power at the window of the dewar (P) is related to a power of the VDI LO ($P_0$) and cosine of the grid angle ($\theta$) [10]

$$P = P_0 cos^2\theta. \tag{6.2}$$

In figure 6.17, the $I_c$'s values of the two HEB bridges of the device I01 versus the different angle of the grid are depicted. It can be seen that both HEB bridges have similar linearly response to the incident power which up to an $I_c$ of about 50 $\mu$A where the current starts to saturate. Consequently, this enables to choose the $I_c$'s that are not in the saturation level for the further measurements. The result of these measurements is compared to the simulated S-parameters of the final design for the non-crossover 1.9 THz balanced HEB mixer, see Section 3.5, with the difference of the measured $I_c$'s at different VDI LO frequencies. First the mixer is pumped at the spline horn side with the VDI LO in a frequency range of 1.75-2 THz with using a rotatable grid to attenuate the LO power that does not bring the $I_c$ values to the saturation level. In figure 6.18-left, the difference between right and left HEB bridges at different frequencies is compared with the simulation result when the 180° port is at the spline horn side. The design S-parameters for comparison are, first converted to linear values, squared and then subtracted from each other ($(S34^2\text{-}S24^2)$ in linear). The dewar is rotated and the diagonal side is placed front of the VDI LO and different IV curves for left and right HEB bridges at different frequencies are measured. In figure 6.18-right, the difference between $I_c$'s at the diagonal side is compared to the 0° side of the balanced circuit towards the diagonal side ($(S31^2\text{-}S21^2)$ in linear).

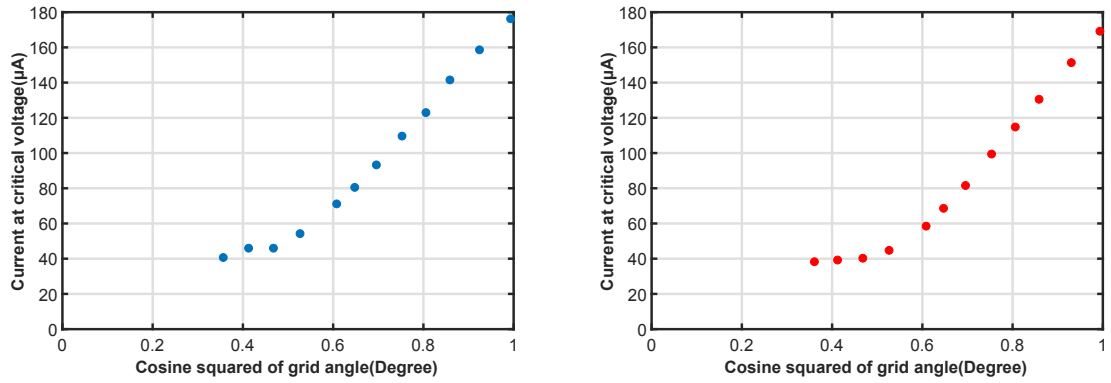


Figure 6.17: The measured currents at the critical voltages ($I_c$'s) when pumping the I01 device with the VDI LO while changing the grid angle in front of the LO at the spline horn side. Left: Response for the right HEB bridge, Right: Response for the left HEB bridge.

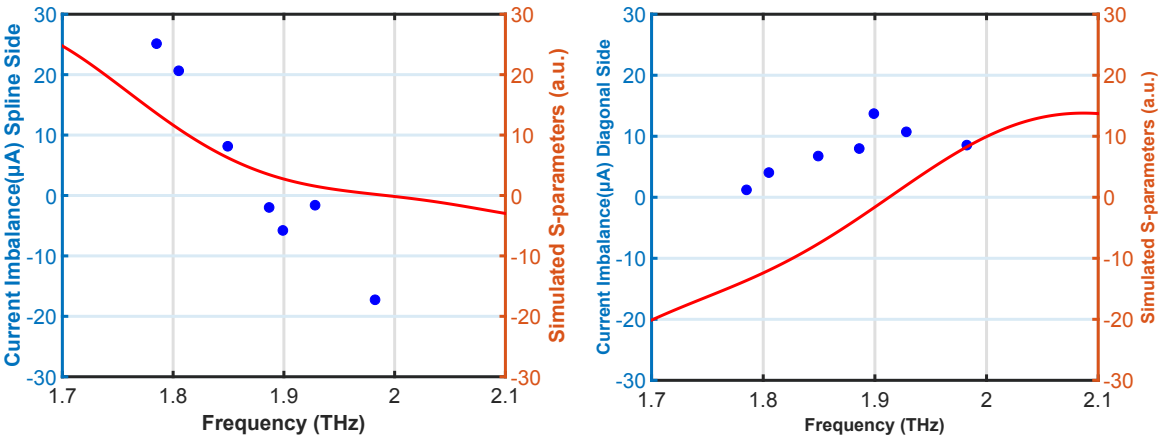


Figure 6.18: Comparison the measured difference of $I_c$'s when pumping the I01 device with the VDI LO with the simulation S-parameters, Left: At the spline horn side, Right: At the diagonal horn side.

# Chapter 7

# Integrated superconducting IF circuitry for THz mixers

The two IF signals generated by a superconducting balanced mixer need to be combined to obtain the final balanced response (receiver noise). This can be achieved by two different methods, either using a LNA directly at the each of the IF outputs and combine the amplified signals with a room temperature IF Wilkinson combiner or 180° IF hybrid, or first combine the two IF outputs with an integrated superconducting IF Wilkinson combiner or 180° IF hybrid and amplify the combined signal with only one LNA. The latter has the advantage of reducing cooling power budget, which is especially important in a case of many pixel focal plane array (e.g. CHAI receiver for the CCAT-p observatory). By using only one LNA per balanced mixer pixel, one needs half amount of the DC bias wiring and generates only half the power dissipation. Additionally, the superconducting integrated IF hybrid circuits are almost without loss and by the use of lumped element transmission lines their sizes can be miniaturized, which is necessary for the integration with superconducting balanced mixers in a many pixel focal plane array.
This chapter covers the development of a 4-12 GHz integrated IF 180° hybrid. It consists of design, fabrication and cryogenic measurement results. It was the part of the project to integrate the superconducting IF hybrid with the existing 490 GHz [5] and future 800 GHz SIS balanced mixers for the focal plane array CHAI receiver of the future CCAT observatory, see Chapter 1. The 4-12 GHz is the typical down converted frequency band of operating SIS mixers. The transmission lines are based on superconducting Nb technology which is fully compatible with the fabrication process of the RF devices.

## 7.1 A 180° lumped element IF hybrids

The conventional 180° ring couplers based on transmission lines are the most common used hybrids, see figure 7.1. They have four arms, three with an electrical length of $\lambda/4$ introducing a 90° phase difference and a $3\lambda/4$ arm with a 270° or -90° phase difference. Ideally, when the outputs of mixers 1 and 2 of a balanced configuration are matched to the inputs 1 and 2 of the ring coupler, half of the generated IF power of mixer 1 and half of the generated IF power of mixer 2 are incident on the $\Sigma$ port with an additional 0° phase difference. The other half of the IF powers of both mixers are incident on the $\Delta$ port with a 180° phase difference.

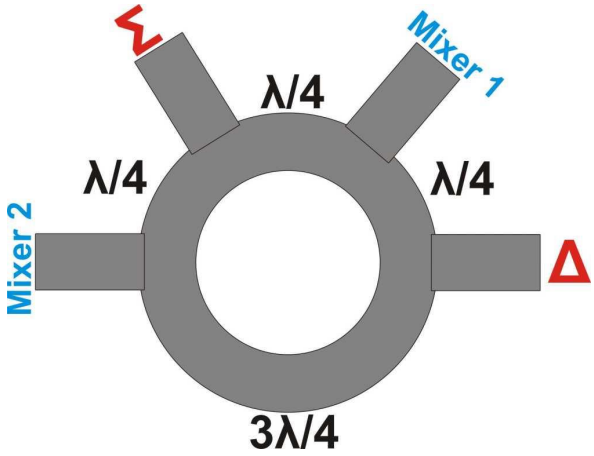


Figure 7.1: Conventional transmission line based hybrid-ring coupler.

However, the transmission line type of hybrid coupler at IF frequencies is too large to integrate with a tiny THz balanced mixer. As an example, the size of a microstripline ring with an electrical length of $3\lambda/2$ on a 500 $\mu$m silicon at 6 GHz (center frequency of 4-8 GHz) is about 1.1 cm compared to the size of the 490 GHz balanced SIS mixer in [52] of 2.2 mm in its largest dimension, see figure 7.2. The size of the transmission line hybrids can be reduced with about a factor of 20 using the designed hybrid in figure 7.2. It is based on planar lumped elements (planar inductors (L), capacitors (C)).

Parisi [80] has reported the design method to reduce the size of transmission line based hybrids with employing the LC lumped elements. This is achieved by equating the ABCD matrix elements for the transmission line segment with a length $l$, characteristic impedance $Z_0$ and propagation constant $\beta$ to ABCD matrix elements for the lumped element networks at the center designed frequency. The ABCD matrix for a

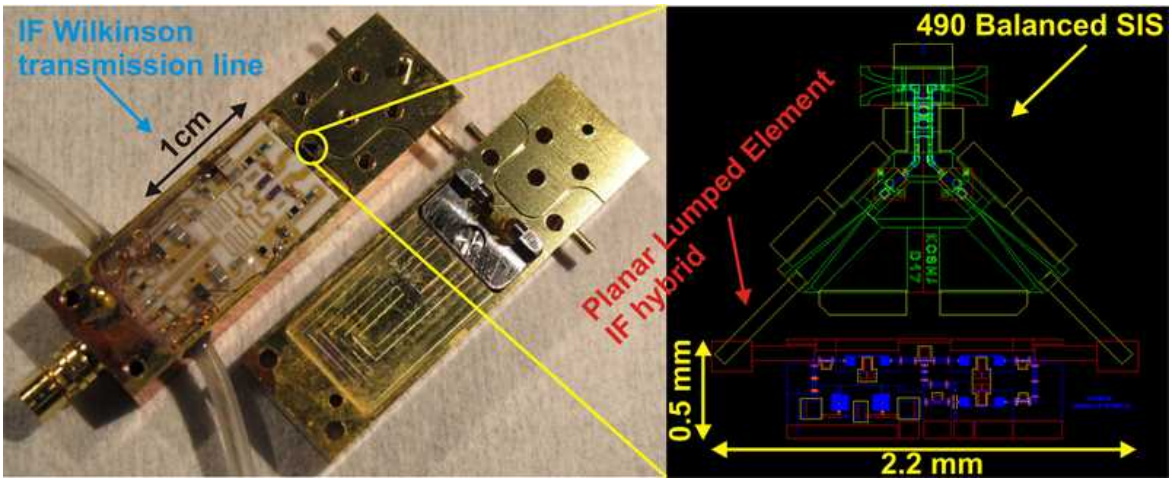


Figure 7.2: The 460 GHz balanced SIS mixer with a folded transmission line IF Wilkinson combiner in comparison to the designed 4-12 GHz 180° IF hybrid integrated with the mixer. The size difference is also noted.

transmission line with $\beta l = 90°$ is

$$\begin{bmatrix} A & B \\ C & D \end{bmatrix}_{TL(f_0)} = \begin{bmatrix} cos\beta l & jZ_0 sin\beta l \\ jY_0 sin\beta l & cos\beta l \end{bmatrix} = \begin{bmatrix} 0 & jZ_0 \\ jY_0 & 0 \end{bmatrix}. \tag{7.1}$$

This transmission line segment can be modeled as a low pass Pi network of series element impedances and shunt element admittances shown in figure 7.3. The ABCD matrix for this Pi-network is

$$\begin{aligned} \begin{bmatrix} A & B \\ C & D \end{bmatrix}_{Pi-Network} &= \begin{bmatrix} 1 & 0 \\ jB_C & 1 \end{bmatrix} \begin{bmatrix} 1 & jX_L \\ 0 & 1 \end{bmatrix} \begin{bmatrix} 1 & 0 \\ jB_C & 1 \end{bmatrix} \\ &= \begin{bmatrix} 1 - X_L B_C & jX_L \\ jB_C(2 - X_L B_C) & 1 - X_L B_C \end{bmatrix}. \end{aligned} \tag{7.2}$$

Equating the matrix in Eq.7.1 to the matrix in Eq.7.2 gives

$$X_L B_C = 1, X_L = Z_0 \rightarrow B_C = Y_0. \tag{7.3}$$

Cascading the two Pi-networks introduces higher bandwidth at the expense of slightly higher loss (two inductors instead of one) which is however not the case for the superconducting based IF hybrids. The ABCD matrix of the cascade two Pi networks

is

$$\begin{bmatrix} A & B \\ C & D \end{bmatrix}_{cascade} = \begin{bmatrix} 1 - 4X_L B_C + 2X_L^2 B_C^2 & 2jX_L(1 - X_L B_C) \\ 2jB_C(1 - X_L B_C)(2 - X_L B_C) & 1 - 4X_L B_C + 2X_L^2 B_C^2 \end{bmatrix}. \quad (7.4)$$

With equating this matrix to the ABCD matrix in Eq.7.1 gives

$$X_L = \frac{Z_0}{\sqrt{2}}, B_C = (\sqrt{2} - 1)Y_0. \quad (7.5)$$

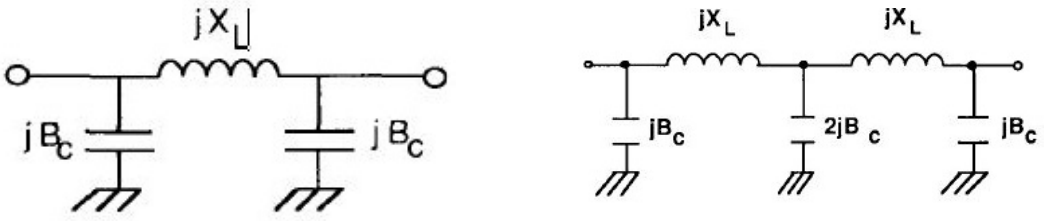


Figure 7.3: Pi network, Left: Less boradband, Right: Broadband.

Consequently, the initial values for the lumped inductors and capacitors of the cascade Pi networks are

$$Z_L = j\omega L \rightarrow L = \frac{Z_L}{j\omega} = \frac{jX_L}{j\omega}, \quad (7.6)$$

$$Z_C = \frac{1}{j\omega_C} \rightarrow C = \frac{1}{j\omega Z_C} = \frac{1}{j\omega(\frac{1}{jB_C})}. \quad (7.7)$$

Substituting $X_L$ and $B_C$ from Eq.7.5 into Eq.7.6 and Eq.7.7, and calculating for a $Z_0 = 70.7\ \Omega$ at 6 GHz center frequency, obtains the values for the $C_1$ and $L_1$, 0.14 pF and 1.32 nH, respectively.

To achieve a wide band -90° arm, the two high pass tee networks are cascaded as shown in figure 7.4. In this case the ABCD matrix is

$$\begin{bmatrix} A & B \\ C & D \end{bmatrix} = \begin{bmatrix} 2B_L^2 X_C^2 - 4B_L X_C + 1 & -j2X_C(2 - B_L X_C)(1 - B_L X_C) \\ -2jB_L(1 - B_L X_C) & 2B_L^2 X_C^2 - 4B_L X_C + 1 \end{bmatrix}. \quad (7.8)$$

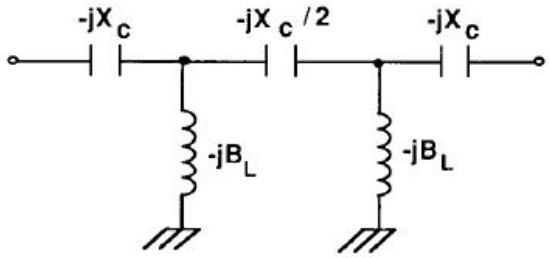


Figure 7.4: Tee-high pass -90° network of lumped elements.

The ABCD matrix for a transmission line with $\beta l = -90°$ or 270° is

$$\begin{bmatrix} A & B \\ C & D \end{bmatrix} = \begin{bmatrix} 0 & -jZ_0 \\ -jY_0 & 0 \end{bmatrix}. \tag{7.9}$$

Equating the matrix of Eq.7.8 to the elements of the matrix in Eq.7.9 results in

$$B_L = \frac{Y_0}{\sqrt{2}}, X_C = (\sqrt{2} - 1)Z_0. \tag{7.10}$$

Subsequently, the initial values of the inductor and capacitor of the cascade high pass tee networks at 6 GHz are as follows $C_2 = 0.9$ pF, $L_2 = 2.65$ nH.

### 7.1.1 Design of an integrated superconducting 4-12 GHz 180° IF hybrid

As emphasized by Kerr in [81], the parasitic capacitance of the planar lumped inductor and the parasitic inductance of the lumped capacitance cannot be neglected in the design. The design therefore takes several iterations starting with the analytical lumped values calculated above. I have listed the different steps which have been done by me to come to the design of a planar superconducting 4-8 GHz integrated 180° IF hybrid in the flowchart depicted in figure 7.5. First, the calculated Parisi's lumped elements from the subsection 7.1 are employed to the Parisi's complete 180° IF hybrid circuit model which is verified in the AWR Microwave Office software [82], see figure 7.6. This design translates the transmission line hybrid of figure 7.1 into a lumped element circuit, using a -90° line for the 270° section of the hybrid [81]. Subsequently, I have achieved the optimum values for the lumped inductors and capacitors by optimizing this complete circuit with the following optimization goals: the reflection at ports 1 (S1,1) and 2 (S2,2) lower than -15 dB, the transmission from ports 1 (S4,1) and 2

(S4,2) to the port 4 equal to -3 dB and the phase difference between them equal to -180°in a frequency range of 4-8 GHz. The extracted optimum values are $C_1 = 0.13$ pF, $C_2 = 0.8$ pF, $L_1 = 0.86$ nH, $L_2 = 2.2$ nH.

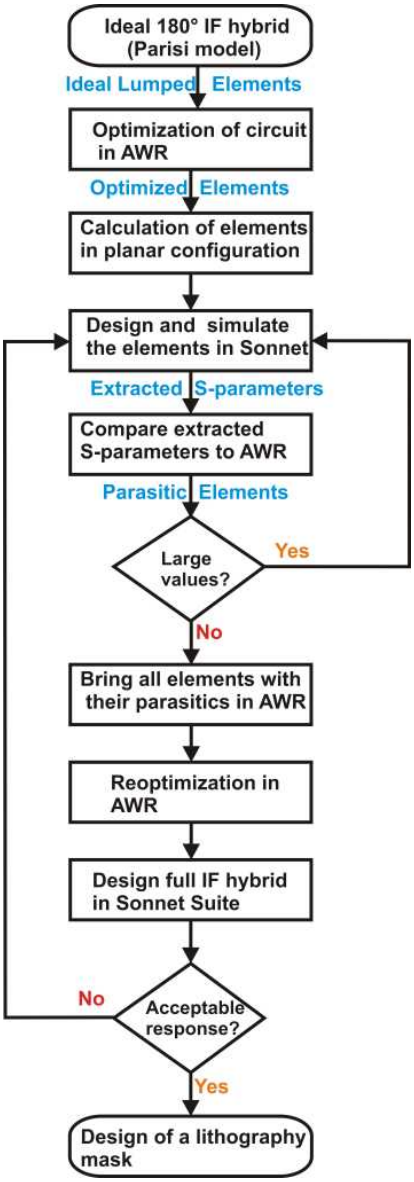


Figure 7.5: Flowchart showing the different steps for designing a planar 180° IF hybrid.

The simulated frequency response of the optimized 4-12 GHz lumped element 180° hybrid is shown in figure 7.7. The reflections at ports 1 (S1,1) and 2 (S2,2) are lower than -20 dB in the middle of the 4-12 GHz band. The transmitted signals from mixers 1 and 2 to the port 3 (S3,1 and S3,2 to the $\Sigma$ port) at 7 GHz are about -3.2 dB and -2.9 dB, respectively. The values for the S4,1 and S4,2 to the $\Delta$ port are about -2.9 dB and -3.18 dB, respectively. The maximum amplitude imbalance between the

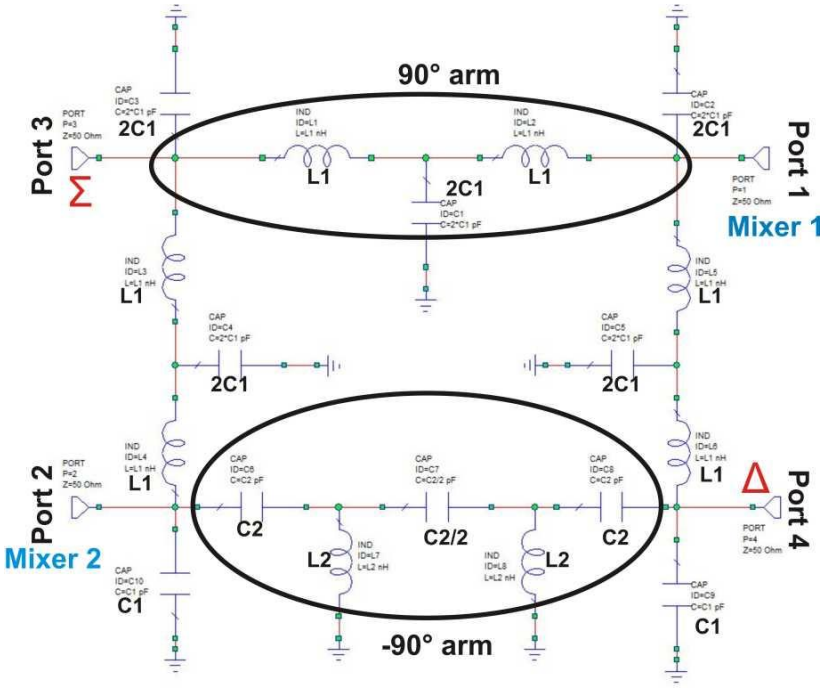


Figure 7.6: Complete 4-12 GHz lumped element 180° IF hybrid circuit model in the AWR Microwave Office.

transmitted signals from ports 1 and 2 to the both port 3 and port 4 is about ±0.5 dB at 5 GHz. The phase imbalances for both Σ port and Δ ports are at a maximum about 5° at 7 GHz. Additionally, the reflections at ports 1 and 2 of the Parisi's circuit model before optimization are also plotted. The improvement in the bandwidth of the optimized Parisi's model compared to the not optimized type can be clearly observed. As a result, the optimized lumped element IF hybrid in figure 7.6 has about a 2.5 octave of a bandwidth with good amplitude and phase imbalances.

The next step is to design the (analytical) optimized lumped elements in planar lumped elements in the available technology on a 9 $\mu$m silicon substrate with Nb superconducting lines and a SiO2 dielectric to separate the Nb layers. The 9 $\mu$m thick Si membrane substrate is chosen to be compatible with the RF balanced mixer substrate. The planar elements are spiral inductors and parallel plate capacitors. I began the calculations by finding the initial length of the line based inductors analytically as a starting value. After that, the planar inductors are drawn in the 2.5D Sonnet suite software where one of their inputs are matched to the 50 Ω port and the other port is shorted. This will give the total reflection of the planar structure to be able to compare to the ideal lumped elements. The dimensions of the planar lumped elements must be much smaller than the wavelength. For an effective permittivity $\varepsilon_{eff}$ the wavelength is given

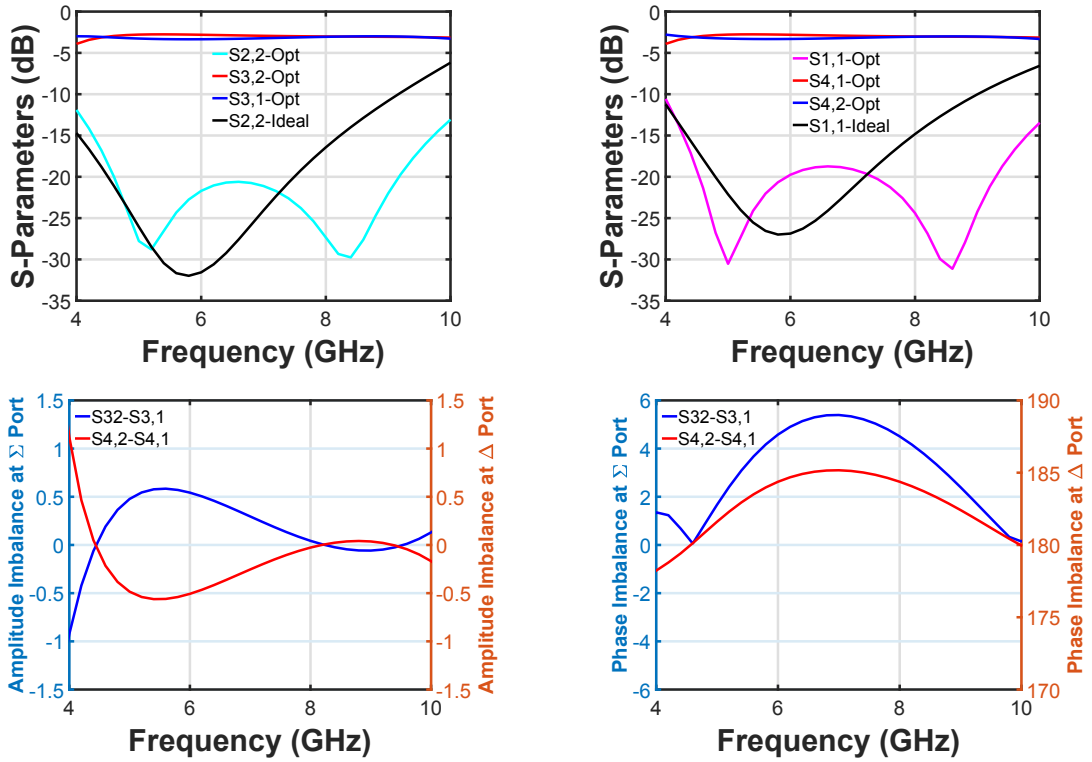


Figure 7.7: S-parameters of the simulated IF hybrid optimized Parisi model in AWR suite. Its reflections at ports 1 and 2 are compared to the ideal type.

by

$$\lambda = \frac{\lambda_0}{\varepsilon_{eff}}. \tag{7.11}$$

For 6 GHz taking an $\varepsilon_{eff}$ of 6.5, $\lambda$ is 2 cm, which is an order of magnitude larger than the size of the largest inductor. The initial line length of the inductor is determined from the Smith chart, by simulating just a 3 $\mu$m wide straight line. With the determined length of the line, one can shape the planar inductors to the rectangular spirals with dividing them by four (number of bends) and number of turns. The length of the line forming the rectangular spiral is then adapted until the desired value of the inductance is reached. As an example, the designed planar 0.86 nH $L_1$ inductor in Sonnet suite environment is shown in figure 7.8. At one side, a 50 $\Omega$ input port is placed and other side is connected to ground. Its center line is connected to the input line with a micro-bridge over the turns of the inductor. For the simulation purpose, the bridge is connected at its ends to the inductor with two via holes through the isolating SiO2 layer. Its simulated S-parameters (S1,1 versus frequency) are extracted and imported to the AWR Microwave Office as a block (SUBckt). Now, it is possible to check the planar structure with the ideal optimized inductor by comparing their

reflections (S-parameter responses) on the same Smith chart and adapt the value of the parasitic capacitor until the two responses are the same. This comparison introduces any reducing or increasing the initial designed length of the planar inductor. The parasitic parallel capacitor is due to the possible coupling between lines of the planar inductor and also to the coupling between the micro-bridge and the inductor's turns passing under it.

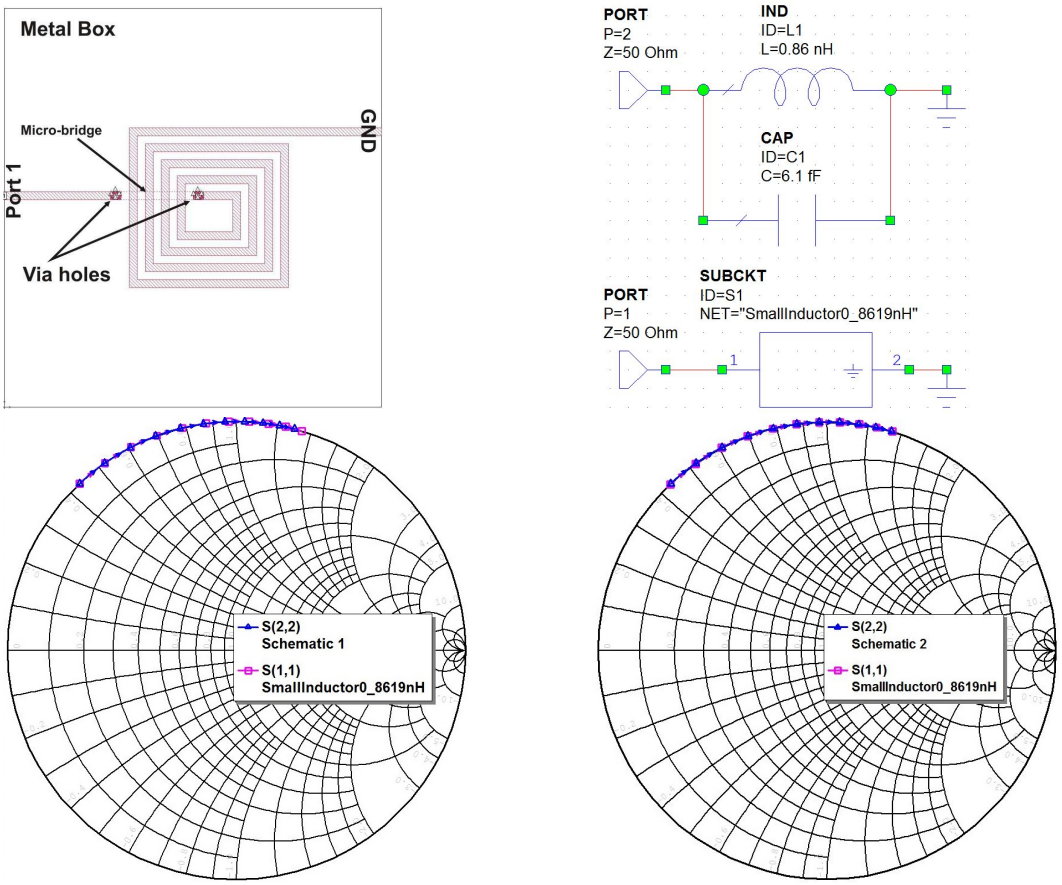


Figure 7.8: Top-Left: A planar 0.86 nH inductor in Sonnet suite, Top-Right: Comparing the ideal optimized inductor with the generated S-parameters of the planar inductor and extracting the parasitic parallel capacitor, Bottom-Left: Plotting the S-parameters at 4-12 GHz of the ideal (pink color) and planar (blue color) on top of each other on one smith chart without parasitic parallel capacitor, Bottom-Right: With adding a 6.1 fF parallel parasitic capacitor on one smith chart.

The initial value of the parasitic parallel capacitor is calculated by

$$Y_{L-Ideal} + Y_{C-Parasitic} = Y_{L-Planar}, \tag{7.12}$$

where $Y_{L-Ideal}$, $Y_{C-Parasitic}$ and $Y_{L-Planar}$ are the admittance of the ideal lumped inductor, the parasitic capacitor and the planar inductor.
The design continues with obtaining the initial size of the planar capacitors. this is achieved by using the parallel plate capacitor formula

$$A = \frac{Cd}{\varepsilon_0 \varepsilon_r}, \tag{7.13}$$

where d is the thickness of the SiO2 dielectric (300 nm), C is the capacitance of the optimized $C_1$ or $C_2$, $\varepsilon_0$ is the vacuum permittivity $8.85 \times 10^{-12} F/m$ and $\varepsilon_r$ the relative permittivity of the SiO2 which is 3.9. After getting the initial size of the area of the capacitors, I have drawn them in the Sonnet suite. One example of the $C_2/2$ is shown in figure 7.9. The area calculated from Eq.7.13 is adapted, if needed, until the desired capacitance value is reached at the center frequency. Subsequently the capacitors are imported into AWR Microwave Studio and compared with the ideal capacitor, as is shown in figure 7.9. If needed, the value of the parasitic inductor in series (figure 7.9) is adapted until the 2 responses are equal. A possible parasitic inductor in series is needed to account for the size of the capacitor, especially if it is large. The initial value of the parasitic inductor is calculated by

$$Z_{C-Ideal} + Z_{L-Parasitic} = Z_{C-Planar}. \tag{7.14}$$

In figure 7.9, it is shown that the initial value of the planar capacitor is in very good agreement with the ideal capacitor in the frequency range of 4-12 GHz. Consequently the value of the parasitic inductor is extremely small about 0.0019 nH.
After designing each lumped element of the 180°IF hybrid in a planar configuration, I have integrated all of them on a 9 $\mu$m silicon substrate. The final integrated circuit is depicted in figure 7.10. This integration defines also the CPW- and microstrip- lines to electrically connect the planar elements. The CPW lines have a $W_{CPW} = 12$ $\mu$m and $G_{CPW} = 4$ $\mu$m equal to about 50 $\Omega$. The width of the lines in the -90° arm are about 12 $\mu$m, 135 $\Omega$. There are also 3 $\mu$m wide lines to connect the spiral inductors and $2C1$ to the rest of the circuit. Because the operation wavelength is very large in comparison to the length of these lines, their influence on the frequency response of the complete IF hybrid is almost negligible.

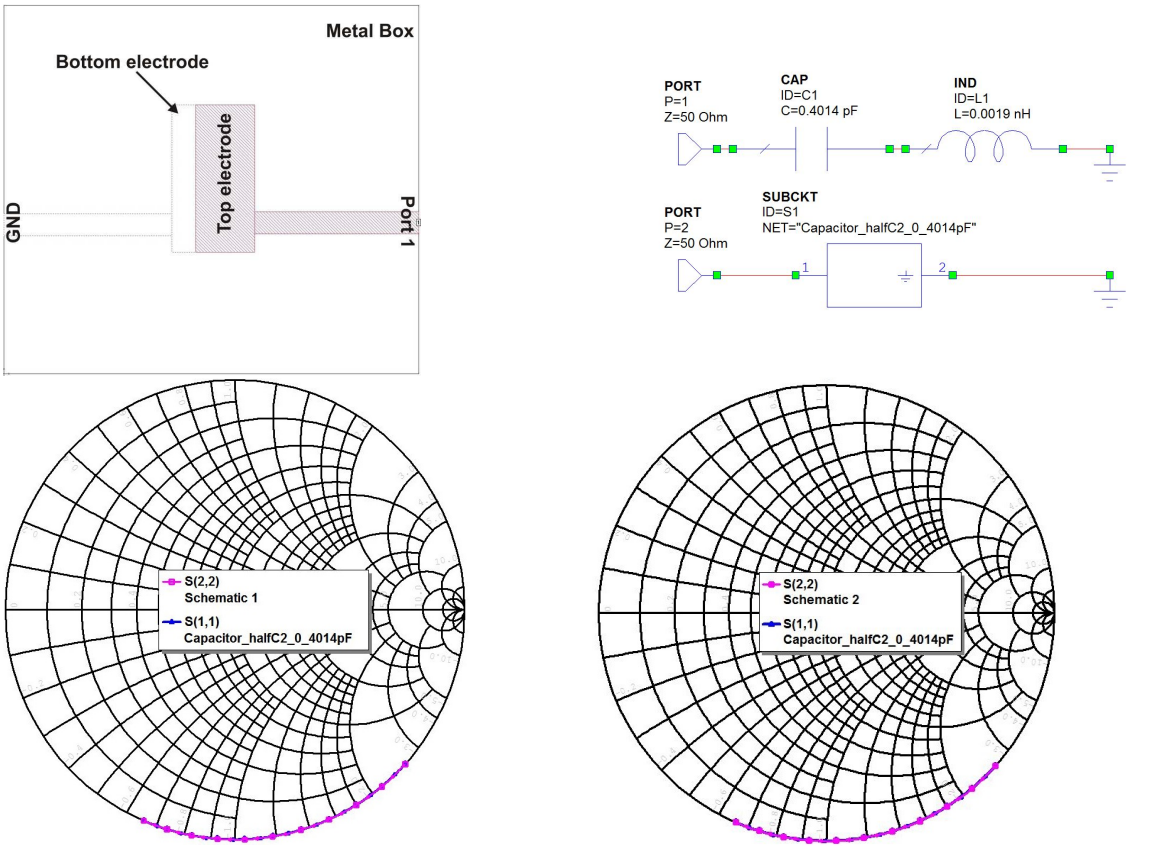


Figure 7.9: Top-Left: The planar 0.4 pF parallel plate capacitor in Sonnet suite where the bottom electrode is extended a bit further than top electrode to avoid any short contact between due to the possible micro-fabrication tolerances, Top-Right: Comparing the ideal lumped capacitor with the generated S-parameters of the planar capacitor and extracting the parasitic series inductor, Bottom-Left: Plotting the S-parameters at 4-12 GHz of the ideal (pink color) and planar (blue color) on top of each other on one Smith chart without parasitic series inductor, Bottom-Right: With adding a 0.0019 nH series inductor on one Smith chart.

An additional step is to bring all the planar elements as lumped elements with their parasitics, and models of the connecting CPW- and microstrip- lines in one equivalent circuit in the AWR Microwave Office. This is important to check if an optimization of the parameters is needed, once they are connected to the complete circuit. If there is any new optimized value, one should go back to the step of evaluating this component in the SONNET suite and follow the rest of the iteration steps to implement the new dimensions.

The complete equivalent circuit model of the 4-12 GHz 180° IF hybrid is depicted in figure 7.11. The new optimum value of $L_1$ e.g. is about 0.7 nH instead of 0.86 nH and the rest of the other lumped elements stay the same. Nevertheless, this change in

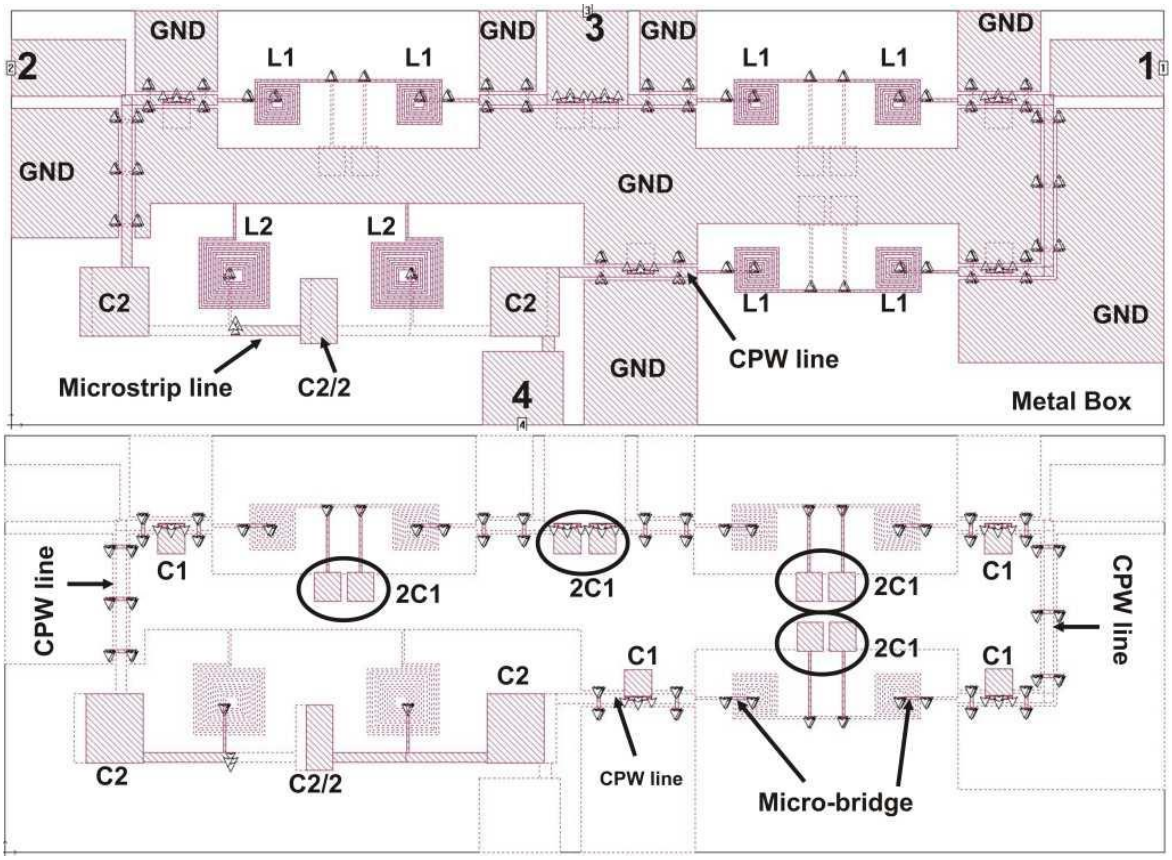


Figure 7.10: The complete 4-12 GHz integrated planar IF hybrid with PEC material employing micro-bridges with via holes, Top: The bottom metal layer Bottom: The top metal layer. The total size of the hybrid is about 0.5×1.4 mm$^2$.

the value of the $L_1$ has a quite minor effect (wins about 0.5 GHz at the higher side of the band to the 12 GHz). The values and sizes of the lumped elements with their parasitic are shown in table 7.1.

The simulated frequency responses of the equivalent circuit model is shown in figure 7.12. They are also compared with the simulated results for the complete 4-12 GHz integrated IF hybrid on a 9 $\mu$m silicon using PEC as a metal. For the complete planar IF hybrid, the transmission form ports 1 and 2 to the port 3 is about -3.8 dB and -2.8 dB at 7 GHz. This is for port 4 is about -2.6 dB and -3.4 dB. The reflections at ports 1 and 2 at 8 GHz are about -15 dB and -18 dB, respectively. The amplitude imbalance at ports $\Sigma$ (port 3) and $\Delta$ (port 4) are about 1 dB and -0.8 dB when ports 1 and 2 are excited at 7 GHz. The phase imbalance is about 3° and -4° at 7 GHz, this value is about 2° for both ports at 6 GHz. Additionally, The comparison between the simulated S-parameters of the equivalent and planar 180° IF hybrids, shows that they are in good agreement. The only noticeable difference is that the equivalent circuit is

few more broadband than the planar IF hybrid.

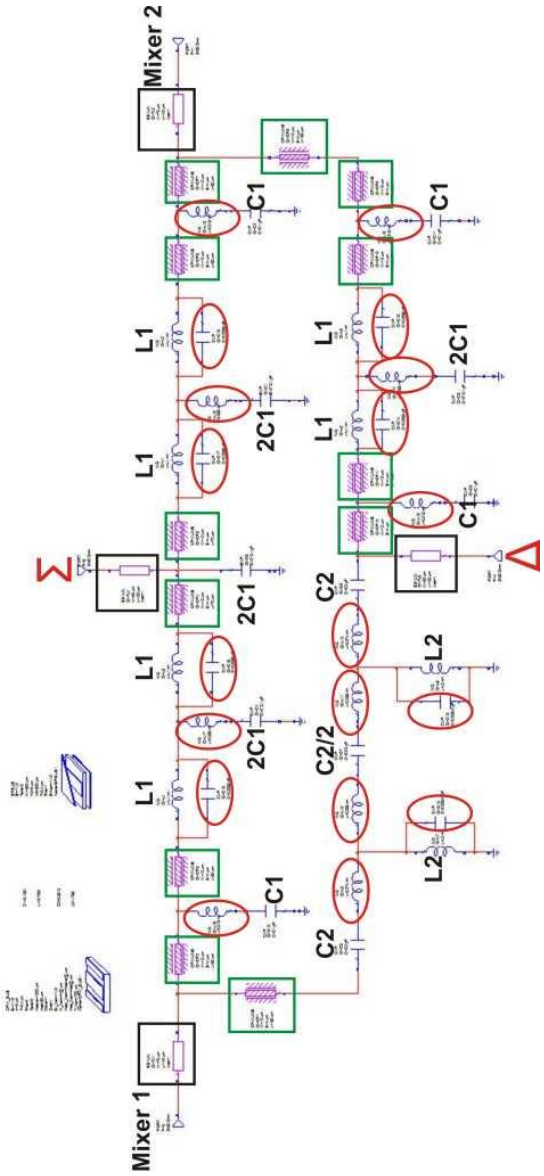


Figure 7.11: Equivalent circuit of the complete IF hybrid with parasitic elements in the AWR suite. The elements inside of the black squares , green squares and red elliptical shapes are for the microstrip lines, CPW lines and parasitic of the main elements (parasitic capacitors parallel to the $L_1, L_2$ and parasitic indcutors series to the $C_1, C_2$), respectively.

In addition, I had taken over a designed configuration (folded-port 3) of the IF hybrid done by Dr. Karl Jacobs which enables to easier access the $\Sigma$ and $\Delta$ ports at one side of the substrate. I have re-designed to employ all planar elements similar to the original planar IF hybrid, see figure 7.13. The only differences are added an extra folded CPW line and a microstrip-microstrip crossover. The new CPW line with few micro-bridges

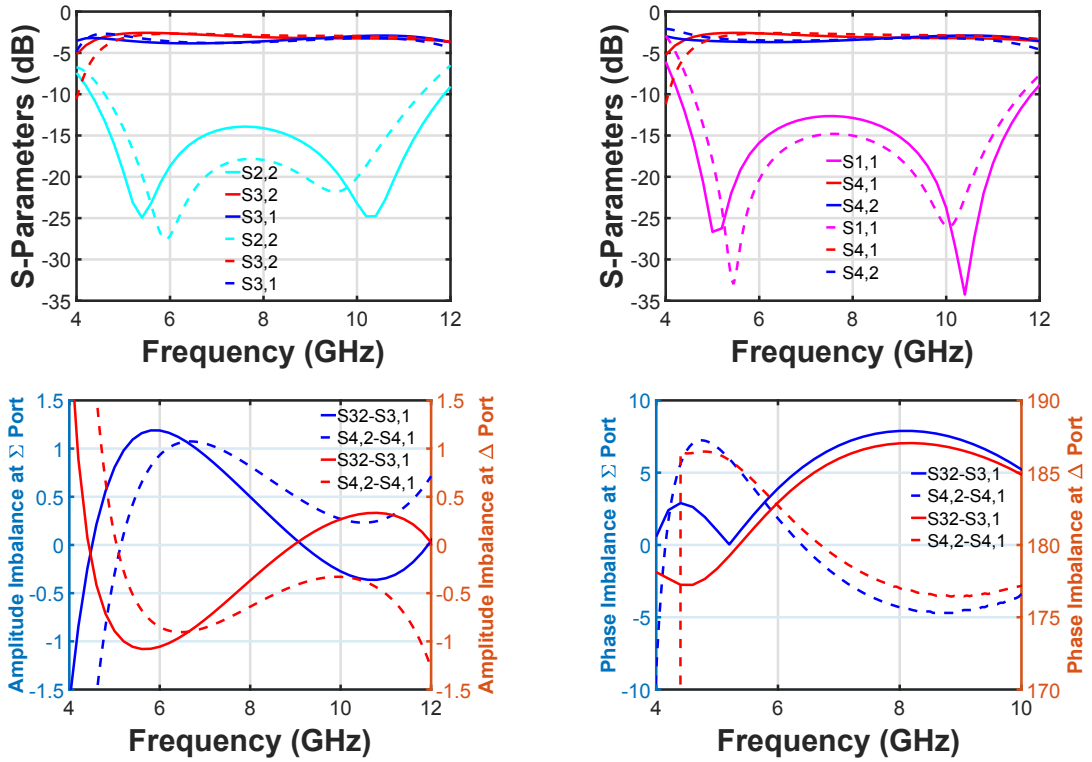


Figure 7.12: Comparison of the simulated S-parameters of the complete equivalent 4-12 GHz IF hybrid circuit (solid line) and of the complete 4-12 GHz integrated planar IF hybrid on a 9 $\mu$m silicon substrate (dashed line).

has the similar width and gap to the original CPW lines on the IF hybrid circuit. Its center line is extended to the substrate side where the Port 4 is located. This extended line which in principle is a microstrip line crosses over the microstrip line connected between $L_1$ and $C_1$. The simulated frequency responses of the folded-port 3 IF hybrid is shown in figure 7.14. It shows comparable results to the original integrated 180° IF hybrid.

As this IF hybrid is based on superconducting Nb, therefore I have imported the impedance of the Nb cryogenic-frequency dependence, into the Sonnet suite instead of

| Element | Parisi | Optimized Parisi | Planar | Parasitic |
|---|---|---|---|---|
| $C_1$ | 0.14 pF | 0.13 pF | $32\times32\mu m^2$ | 0.013 nH |
| $C_2$ | 0.9 pF | 0.8 pF | $70\times85\mu m^2$ | 0.07 nH |
| $L_1$ | 1.32 nH | 0.86 nH | 544 $\mu$m | 6.1 fF |
| $L_2$ | 2.65 nH | 2.2 nH | 1300 $\mu$m | 3.4 fF |

Table 7.1: Values of the calculated and optimized lumped and planar sizes of the inductors and capacitors of the integrated 4-12 GHz 180°IF hybrid.

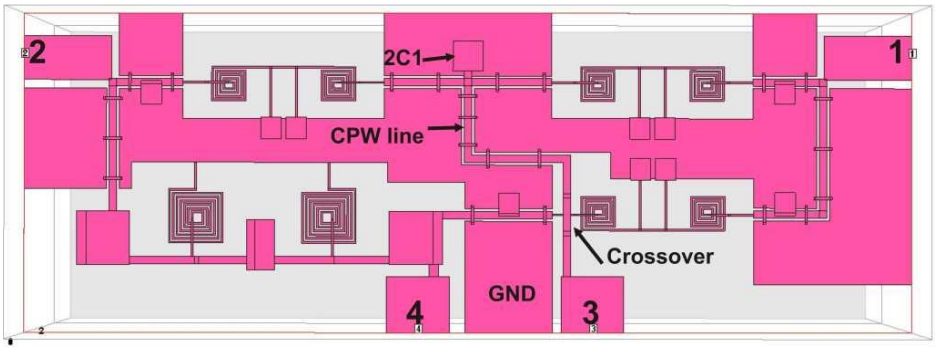


Figure 7.13: 3D view of a complete 4-12 GHz integrated 180° planar IF hybrid with the folded port 3.

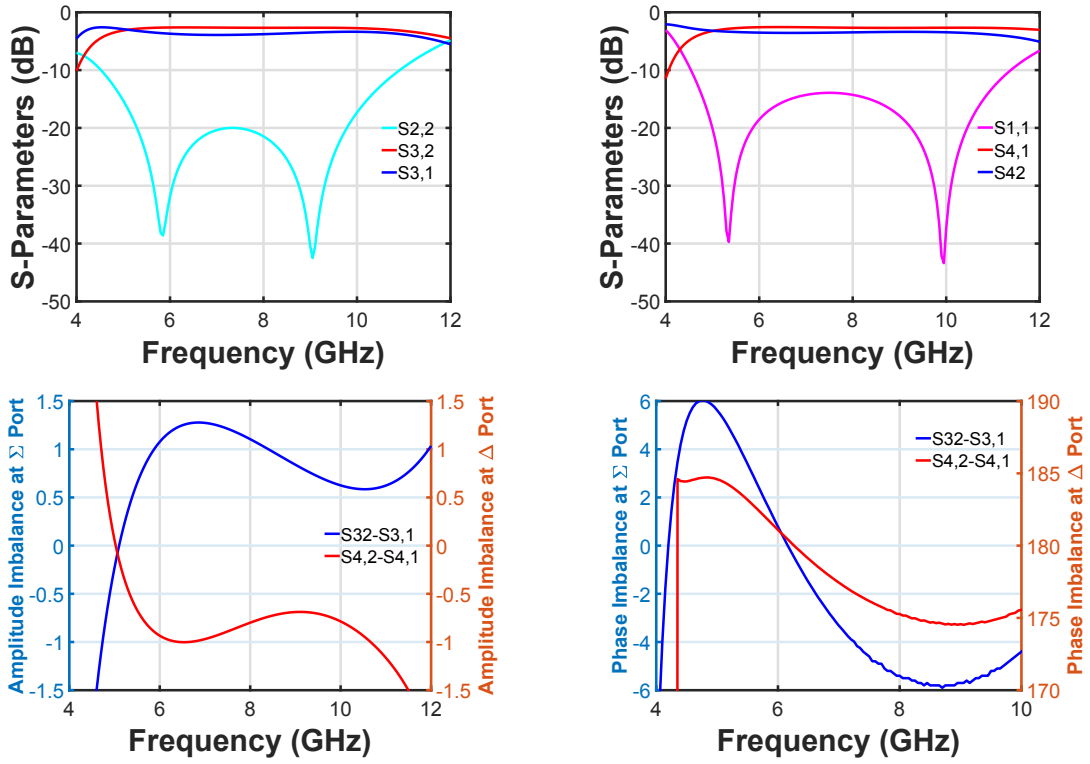


Figure 7.14: S-parameters of the simulated 4-12 GHz IF hybrid folded model in Sonnet suite.

PEC, to obtain frequency responses as similar as possible to the reality. Up to now, I have had the design on the 9 $\mu$m silicon substrate. How ever for simplicity I have also simulated the IF hybrid with 500 nm silicon thick. The results of the IF hybrid with Nb on a 500 nm silicon thick is compared to the measurements in Section 7.2.1.

### 7.1.2 Fabrication of the 180° IF hybrid device

In order to fabricate the designed 4-12 GHz 180° planar IF hybrids, I have drawn a lithography mask as shown in figure 7.15. It is divided to four sectors. The sectors 1 and 2 consist of the IF hybrids with the folded port 3 type of the design and the calibration circuits both on 500 $\mu$m silicon substrate. The sectors 3 and 4 have devices with and without the folded port 3 with beam-leads on a 9 $\mu$m silicon substrate and some calibration circuits. There are alignment marks on the lithography mask to do different fabrication steps with the photo-lithography technique. Additionally, there are alignment marks for doing back side etching of the SOI wafer for the membrane devices with beam leads. The mentioned different types of the IF 180° hybrids on the mask are shown in figure 7.16.

The fabrication of the IF hybrids are done by Dr. Karl Jacobs in house. All fabrication steps for defining inductors and capacitors are done by a photo-lithography technique for a 9 $\mu$m SOI or a bulk silicon wafers. First the areas for the bottom electrodes of the capacitors and traces of the planar inductors are defined by liftoff-photolithography. After that, a 200 nm Nb film is sputtered as a bottom electrode. A 300 nm SiO2 film is sputtered in the defined areas to introduce the dielectric layer for the capacitors and micro-bridges over the inductors and the CPW lines. The next step is to sputter a 400 nm Nb film on the defined areas for the top electrodes of the capacitors and the micro-bridges over the CPW lines (4$\mu$m wide) and over the inductors's turns (3$\mu$m wide). For the devices on 500 $\mu$m thick bulk silicon, the last step is to dice the wafer into the individual sectors and also dice out and separate the devices from the sectors A and B. However, the fabrication in a case of the devices on the sectors C and D on a 9 $\mu$m SOI wafer continues with fabricating beamleads. This is done first with sputtering a 25 nm Nb adhesion layer and a 100 nm Au as a seed layer on the defined areas. Later on, a 3 $\mu$m Au is electroplated on the defined areas with photolithography to make the beam leads. The handle wafer of the SOI is etched from the backside and IF hybrid devices with beam leads are separated with the same fabrication recipe as the 1.9 THz balanced HEB mixers in 4.2. In figure 7.17, the final fabricated 4-12 GHz integrated 180° IF hybrid with no beam leads on a 500 $\mu$m thick silicon is depicted.

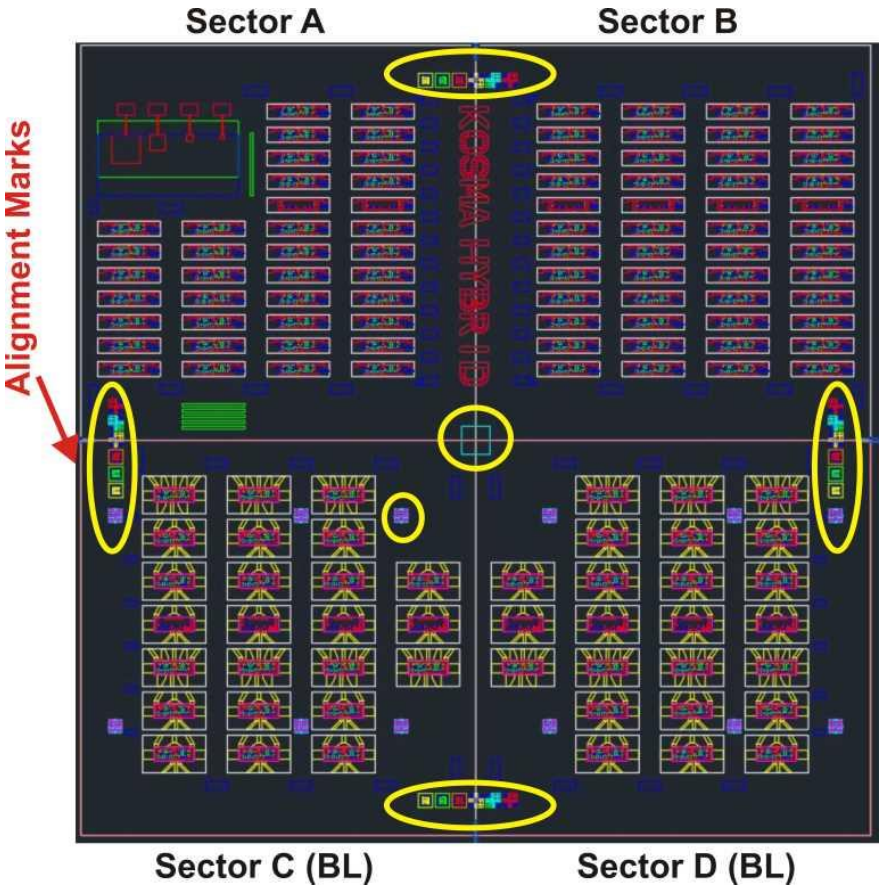


Figure 7.15: Lithography mask to enable to fabricate the designed IF hybrids.

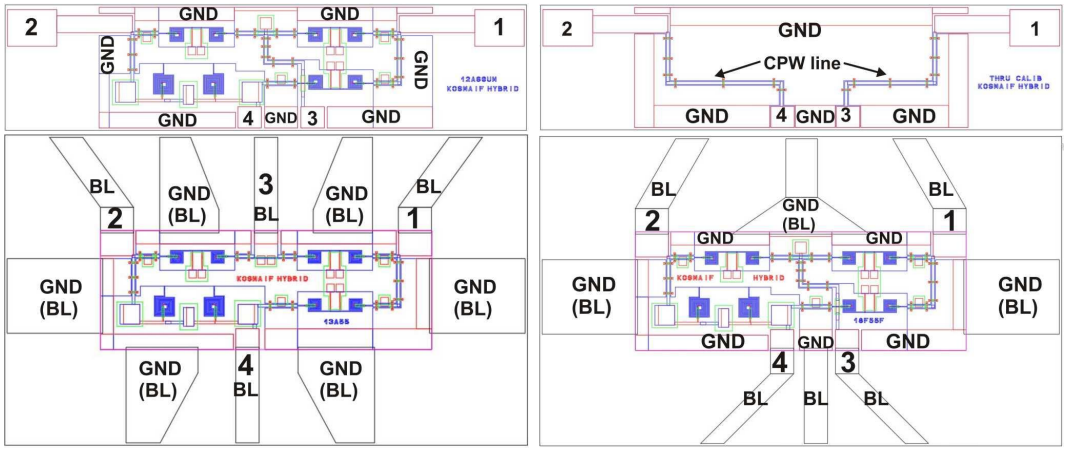


Figure 7.16: Designs on the lithography mask, Top-Left: 4-12 GHz IF Hybrid on 500 $\mu$m silicon substrate with the folded port 3, Top-Right: A calibration circuit on a 500 $\mu$m thick silicon substrate consisting of two CPW lines connecting port 1 to port 3 and port 2 to port 4, Bottom-Left: A 4-12 GHz hybrid without folded port 3 with beam leads on a 9 $\mu$m silicon substrate, Bottom-Right: The same, but with a folded port 3 and beam leads on a 9 $\mu$m silicon substrate.

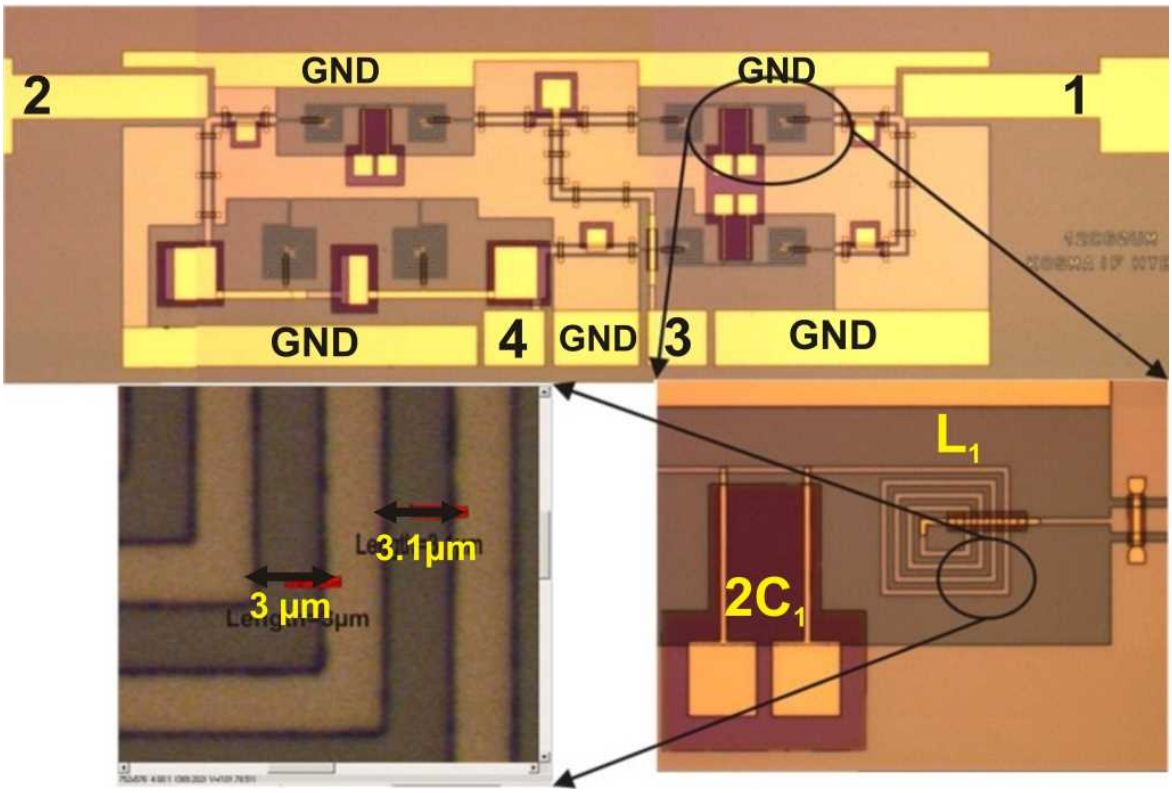


Figure 7.17: Fabricated IF hybrid circuit with zoom into the inductor $L_1$ at the 90° arm. The distance measured under the microscope showed about 3 $\mu$m desired gap between the turns of the inductor.

## 7.2 Test fixture block

I have designed a test fixture using the CST suite software to enable to measure the fabricated devices on the thick 500 $\mu$m Si substrate that have a folded port 3. The final designed fixture is shown in figure 7.18. It consists of four TMM10 ($\varepsilon_r = 9.2$) boards. There are four microstrip lines with a width of 500 $\mu$m (50 $\Omega$) to electrically connect the device under test to the four GPO output connectors. The GPO connectors [83] are also modeled, using a PEC center connector surrounded with a cylinder shape dielectric ($\varepsilon_r = 4.1$) producing a (50 $\Omega$) port in CST suite. Four contact areas are defined to electrically connect the GND areas of the device under test to the surrounding test fixture block. In addition, the GND areas are made between ports 1 and 2, 3 and 4 for reducing any possible coupling between these ports.
For checking the functionality of this test fixture in the simulations, the calibration circuit (two separated CPW lines to connect ports 1 to 3 and ports 2 to 4) is simulated inside of the block and connected with wire bonds to the desired ports and GNDs. A surrounding vacuum is also introduced for the simulations where the background is PEC. The simulated frequency response of the calibration circuit inside of the test fixture is plotted in figure 7.19, when the port 1 is exited. It shows about 0 dB transmission from port 1 to port 3 up to 9 GHz. The port 1 is isolated from ports 2 and 4 with about -30 dB at 6 GHz.

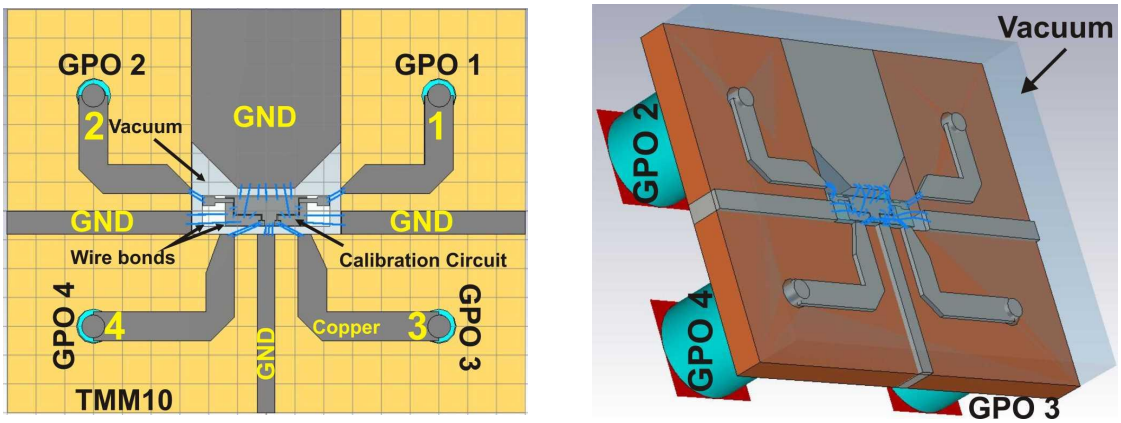


Figure 7.18: Test fixture on TMM10 board, Left: Top view showing the four microstri lines connected to four output GPOs from one side and wire bonded to the four ports of the calibration circuit on the other side, Right: Side-view showing the cylinder shape of the dielectric belongs to the GPOs and surrounding vacuum.

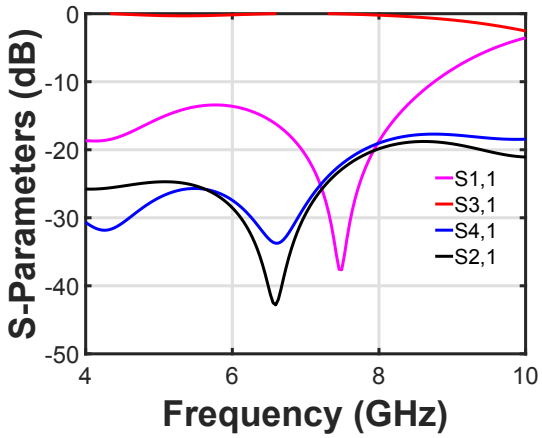


Figure 7.19: Simulated S-parameters of the calibration circuit inside the test fixture.

### 7.2.1 Measurement of the 180° IF hybrid device

In order to do DC and high frequency characterization of a 4-12 GHz integrated 180° IF hybrid, the fabricated and separated device with a 500 $\mu$m silicon substrate is mounted inside of the test fixture with a crystal bond. After that, its four ports and GNDs are wire bonded to the four separate TMM10 boards and the copper block. The DC measurement is done by a multimeter to check the electrically connections between ports and to see how inductors conducting and capacitors (open) respond. Measurements at room temperature show a resistance of about 440 Ω for the three arms with 90° phase and about 1.2 kΩ for the arm with -90° phase. Because the three similar 90° arms have Nb based spiral inductors in series and capacitors in parallel to the transmission line between two ports, therefore all of the three arms should show almost the same amount of resistance at room temperature. One would expect an open circuit in DC at the -90° arm because of existing series capacitors. However the measured 1.2 kΩ can be due to the DC current passes through mounted silicon substrate on the isolated crystal bond. The DC measurements are done to check the connection in the three 90° sections. Two previously fabricated batches of the devices were not possible to use because of open circuits of the series inductors due to problems with step coverage. This is solved in the fabricated batch number three by increasing the width of the micro-bridges over the turns of the inductors (improved step coverage).
To characterize the superconducting IF hybrids at the desired 4-12 GHz frequencies in liquid helium, a measurement set-up is prepared as shown in figure 7.20. It consists of a vector network analyzer (VNA), two SMA-SMA cables from VNA to a dipstick, a dipstick with two long steel coaxial cables, two SMA-GPO cables, two 50 Ω load-GPOs

and the test fixture described previously.

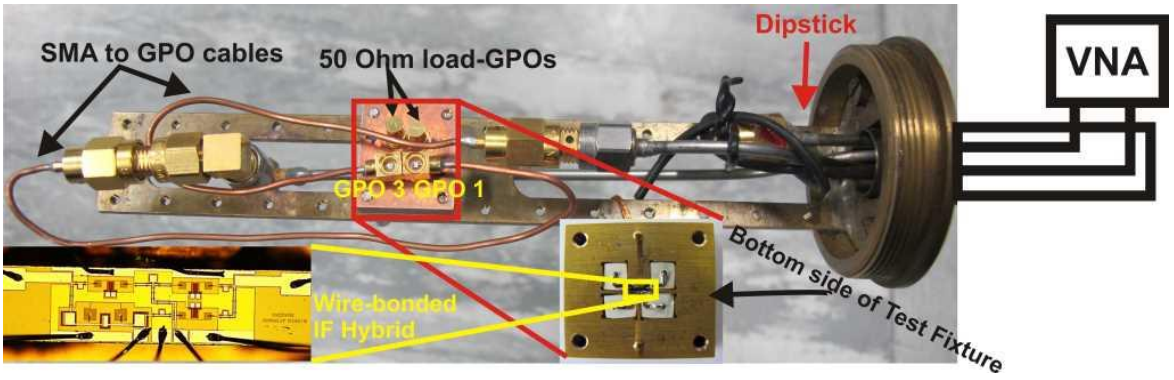


Figure 7.20: Measurement set-up for characterizing the transmission between ports of the 180° IF hybrid.

First a measurement is done without the test fixture, simply connecting the two GPO connectors together and measure the transmission with the dipstick immersed in liquid helium. Then the calibration circuit on a 500 $\mu$m silicon is mounted inside the test fixture block number 2 similar to the machined test fixture number 1 with the mounted and wire bonded IF hybrid. This is important to de-embed the complete measurement set-up including the test fixture block. The transmission of the calibration circuit with the test fixture placed inside of the dipstick in liquid helium, after de-embedding the rest of the set-up, is read on the VNA. This transmission is depicted in figure 7.21. It shows about 0 dB up to 6 GHz and mean value of about 0.5 dB from 6 GHz to the 9 GHz.

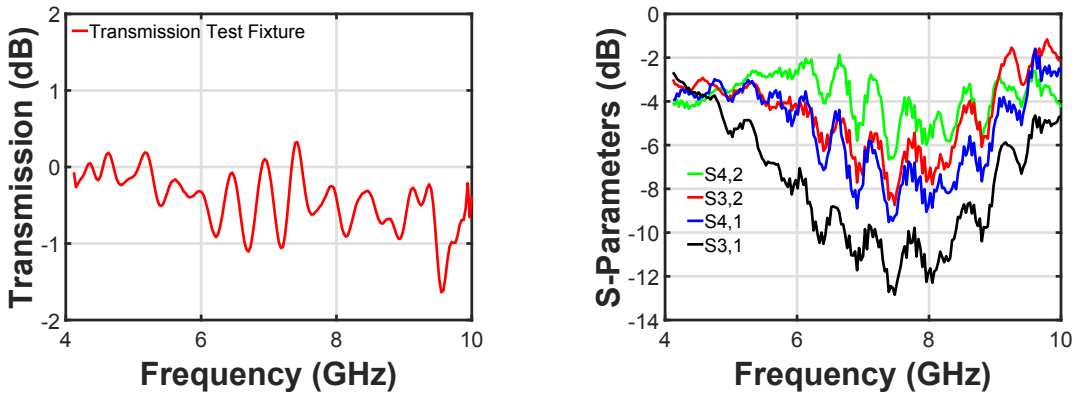


Figure 7.21: Left: Transmission through the calibration circuit inside the test fixture. Right: Measured transmissions of the 180° IF hybrid taken from the fabricated batch 3.

According to the simulation in 7.2, this transmission (S3,1) is about 0 dB in the 4-9

GHz band. Now is possible to measure the high frequency response of the IF hybrid. The amplitude and phase of the transmissions after de-embedding the complete set-up including the test fixture are measured for all 4 ports at 4-10 GHz. The amplitude transmission from ports 1 and 2 to ports 3 and 4 are depicted in figure 7.21. According to the simulations, these transmissions should be in average about -3 dB for all 4 traces however here are different. The amplitude and phase imbalances at port 3 and port 4 when the port 1 and 2 are excited are plotted in figure 7.22. They are compared to the simulated S-aparmeters of the complete 4-12 GHz 180° IF hybrid with an implemented superconducting Nb on a 500 $\mu$m silicon substrate.

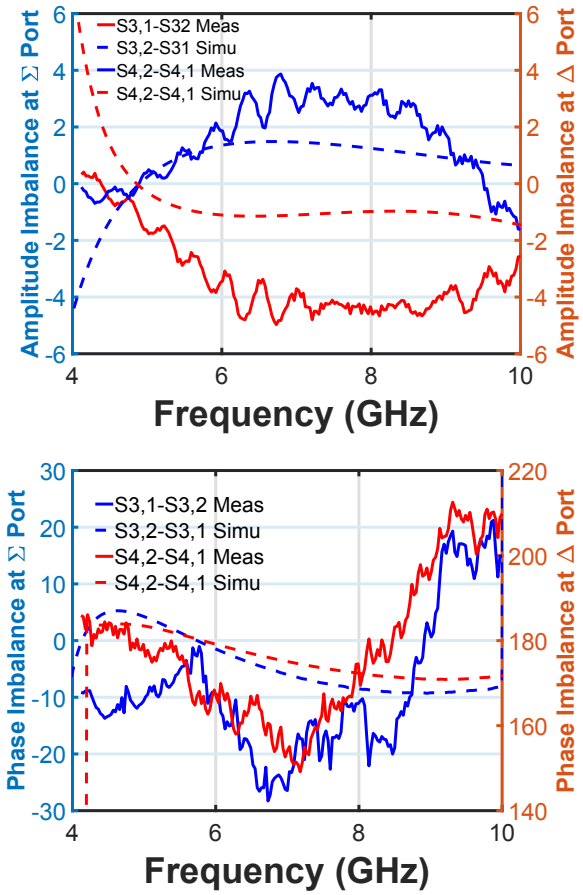


Figure 7.22: Comparison between the simulation and measurement, Top: Amplitude imbalances in dB, Bottom: Phase imbalances in degrees.

As there are some discrepancy between simulation and measurement frequency responses, therefore there is a need to analyze it in the simulation. I have tried to tune the different values of the optimized lumped elements (inductors and capacitors) from open to short circuit in the optimized lumped model of figure 7.6 to obtain the possible

similar transmissions as the high frequency measurements. The only parameter which influences the -3 dB simulated transmissions similar to the measurements is to have the value of $C_1$ and $C_2$ about 2 times lower e.g. SiO2 thickness being 600 nm instead of 300 nm thick designed value, see figure 7.23.

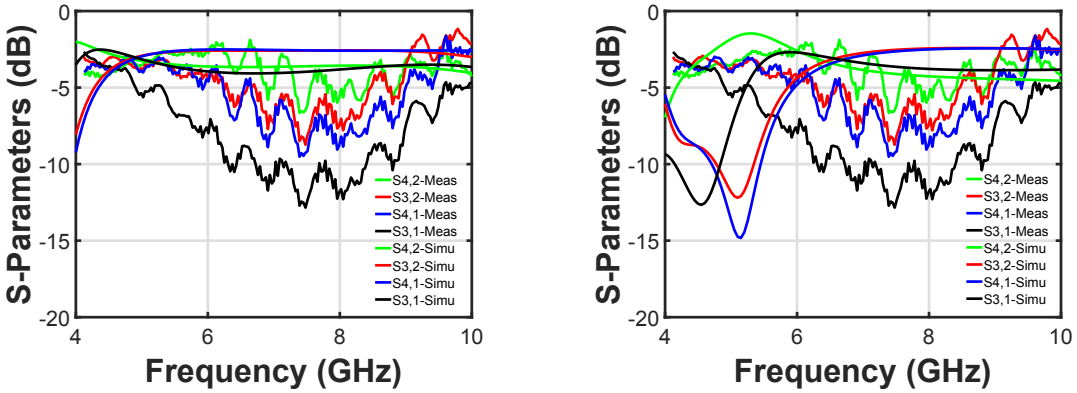


Figure 7.23: Measured transmission of the IF hybrid and simulation of the planar design of a Nb based IF hybrid on a 500 $\mu$m silicon, Left: With a 300 nm thick SiO2, Right: With a 600 nm thick SiO2.

# Chapter 8

# Summary and conclusion

A one octave (700-1500 GHz) planar 180° hybrid-ring coupler was successfully designed using the combination of CPW and slotline transitions on a 6 $\mu$m thick silicon substrate. The calculated complex surface impedance versus frequency of a superconducting NbTiN was implemented in the simulations instead of a perfect conductor. It has been shown that the transmission drops drastically at the gap frequency about 1080 GHz at which the resistance of the superconductor increases with frequency. The reactance of the complex surface impedance, especially around the gap frequency, was taken into account in the design. A modified CPW-slotline transition was designed which achieves a $\lambda/2$ phase delay without shortening the center line of the CPW to ground, this is important especially in a case of designing balanced HEB mixers. The two stage planar slotline tapered waveguide antenna was adapted to various substrate thicknesses for the waveguide.

Employing some additional matching methods, I have successfully designed the RF part of balanced mixers all on one chip to cover the 800-1100 GHz frequency band and the 1.6-2.1 THz band.

The latter design was made for a 3 $\mu$m thick silicon substrate because of the high frequency. In addition, instead of a superconductor, Au was used as the thin film material for the transmission lines. Simulations with implementing 200 nm Au surface impedance show very good phase and amplitude balances at 1.9 THz of about 2° and 0 dB between the split signals at both inputs to the two HEB bridges. A high isolation between two input ports of about -35 dB has been achieved. Additionally, to enable two IF output ports at one side of the substrate, a CPW-CPW crossover was designed. The high frequency design was taken into production. A batch of integrated 1.9 THz balanced HEB mixers with 180° hybrid-ring couplers was for the first time fabricated

in house on a 3 $\mu$m silicon membrane. The device fabrication procedures were based on the heritage of the HEB mixer development for the SOFIA observatory, and 2.5-3 $\mu$m thick electroplated Au beam leads were added for assembly and contacting.
For the purpose of measurements, two balanced 1.9 THz waveguide split blocks were fabricated in our machine shop. The blocks contain a feed-through waveguide crossed by a substrate channel for the two HEB mixers and the IF output. At one side of the waveguide is a flange to mount a separate spline waveguide horn with a 500 $\mu$m length of waveguide towards the mixer device. At the other side of the waveguide, designated to be the side where the local oscillator would be coupled, a diaganol horn was milled into the block integrated with the waveguide. From that side there is a 1.3 mm of waveguide length towards the mixer device. Optical inspections of the dimensions of blocks are within the range of simulated tolerances.
I have successfully characterized the machined 1.9 THz balanced waveguide blocks by using the THz Time Domain Spectrometer (TTDS). The measurements of the balanced block show about 2.4 dB loss per millimeter length for the waveguides. The transmission through two spline horns mounted back-to-back was measured and used as the reference measurement for the characterization of the balanced blocks. Excessive losses especially at the transition of the integrated diagonal horn and the waveguide have been found in these measurements. They could for some part be repaired by the electro-chemical polishing of the block in our in house workshop. Nevertheless this excess loss has severely limited the choice of a THz LO, forcing me to use more powerful QCL, with the short holding time. In addition, it made it impossible to use the diagonal horn side to couple the hot/cold radiation on the mixer device, as was the original plan. Except for a diagonal horn, also a mirror was integrated in that side of the block. After several investigations, it was also clear that the machined integrated mirror is not functioning as designed and we were forced to cut the mirror and introduce new external optic path to the RF measurement set-up. Because of all these difficulties with the blocks, the blocks for the other designs that were also on the fabrication mask have never been fabricated.
The fabricated balanced HEB mixer devices of the design that fitted to the fabricated blocks were DC characterized on the wafer in a dipstick and after separation inside a vacuum cold dewar. The measured results show in average about 17% difference in the value of $R_N$ compared to the design 120$\Omega$ HEB impedance. The average measured $T_c$ of the devices is about 7.9 K compared to 8.5 K for the other reported single ended HEB mixers fabricated in our laboratory with almost the same thickness of the sputtered NbN thin film. It is not yet clear how the lower $T_C$ influences the measured noise

temperature of the HEB mixers. However, it is known that a better superconducting thin film has a higher $T_C$. In addition, there is a much more dominant step lower than $T_c$ in the RT curves for the all of the DC measured balanced devices in the dipstick compared to the RT curves of the mixers for LFA and HFA [10]. This effect can be also observed in the measured DC-IV curves as some additional steps. Surprisingly, these effects were vanished in the RT and DC-IV measurements in the dewar. The origin of the step in the RT curve is according to the newest insights of a device intrinsic nature due to the charge conversion that originates if normal conducting electrons are converted into Cooper pairs [26]. So I had expected to measure about the same curve shape in the dipstick and the dewar. The further investigation of the RT curves and the DC IV-curves was deferred to future PhD-students. My work has concentrated on the RF performance of the balanced mixers.

The RF measurements of the 1.9 THz balanced HEB mixers were done in a set-up with a QCL LO and hot/cold load at the spline horn side. Optimistically we immediately started the RF-measurements for the two first balanced devices of the M-sector from the wafer. After a promising non balanced noise temperature of 4000 K, using a 12 $\mu$m mylar beamsplitter, measured from the spline horn port, it was discovered that the diagonal horn port was blind. Since the first device broke due to the thermal cycling, a second device was mounted with a 180° flipped orientation to check if the blindness of the diagonal horn port might be due to the mixer device itself. After this was excluded, a TTDS investigation of the waveguide block lead to the electro-chemical polishing of the diagonal horn side and cutting off of the integrated mirror to improve the coupling at that side of the block. A second waveguide block was also treated in the same way. Several more balanced devices were measured. Administering the LO power from both input ports showed a good symmetric division of the LO-power over the 2 HEB bridges. Unfortunately no promising noise temperatures were measured anymore, either single ended or balanced. A further investigation into the balance of the IF output circuits showed that a slight adjustment was necessary, but balanced mixer measurements afterwards still did not show a satisfying response. I have been able to show though the proper balanced behavior of the mixer-chip using a stronger input source than a hot/cold load, in the form of a heavily attenuated synthesizer driven THz source. The combined or suppressed power of the two generated IF outputs was measured using a spectrum analyzer. By choosing the $\Sigma$ or $\Delta$ port of the warm 180° IF hybrid and, the same or opposite polarity of the optimum DC-bias for the two HEB bridges, a best suppression value about 38 dB of the combined two IF outputs was measured. The difference in phase behavior measuring from the spline

horn input port and the diagonal one in relation to the bias polarity of the left and right HEB bridges was in accordance with what is theoretically expected. The fact that the signal suppression when pumping from the diagonal port (and thus the signal from the spline horn port) was about 8 dB worse than in the reversed situation is attributed to the fact that the pump power division is less symmetric from the diagonal horn port. These phase measurement results prove the balanced response of the measured 180° balanced device.

The linearity of the dependence of $I_c$ of the two HEB bridges on a balanced device to a varying low input power was verified. It was shown that the two HEBs on one device have similar response to the incoming power. To estimate the RF-bandwidth of the mixer the $I_c$'s of the two HEB bridges on the balanced device were measured pumping from the spline horn side respectively the diagonal horn side with low power at different frequencies. The difference of the measured $I_c$'s was calculated and compared to the simulation results. The results show that the measured RF bandwidth of the balanced device is in a good agreement with the design for both input ports however, it is shifted to lower frequencies for about 100 GHz.

I conclude that the verification of crucial performance characteristics of the balanced mixer, the equal division of pump power and the 180° phase shift behavior confirm the quality of the design and the fabrication. Also, the single ended noise temperature measured at the start is compliant with measurements of previous mixers. This noise temperature in a voltage bias range of 0.2-07 mV was measured to be about 4000 K compared to the reported 1000 K for the state-of-the-art single-ended mixers (mounted horn on the device) at the 1-2 GHz IF bandwidth. This value should be divided by two because of measuring the balanced mixer as two single-ended ones where the hot/cold signal split to two almost equal signals before incident on the mixer. There is also about 1.2 dB loss due to the 500 $\mu$m long waveguide at the spline horn (the path for the hot/cold signal to the mixer). Additional 1 dB loss is introduced by the sputtered Au as a metal in the balanced circuit compared to the LFA or HFA mixers for the upGREAT receiver for SOFIA where the horn is mounted directly on the probe antenna of the device.

It remains unsatisfying that I have not been able to find a single device showing a comparable sensitivity after the various improvements of the mixer block and the measurement set-up, and to directly measure a balanced hot/cold noise temperature. One honest mistake with serious consequences has been that the devices, were equipped with 3 $\mu$m thick beamleads for contact, similar to previous devices. Contrary to those devices that were mounted over a waveguide cavity, my devices were meant for split

block assembly and should have had thin (500 nm) beamleads to clamp them easily between the two halves of the E-plane split block. The consequences were that there was a lot of strain on the devices, causing problems with assembly and thermal cycling. In addition the waveguide blocks were visibly damaged, a bit more with every new device assembly. Furthermore, due to the fabrication problems with the integrated diagonal horn and the malfunctioning of the integrated coupling mirror, the coupling at the LO port of the mixer was severely reduced. This required the use of the powerful QCL LO in a dewar with a hold time, prohibiting a thorough investigation and optimization of each device. So my conclusion is that the design has potential but that various technical difficulties need to be overcome first to create a more reliable and stable test environment for a thorough evaluation of the devices. The main improvements are an LO port with a better transmission, and a batch of devices with much thinner beamleads.

Concerning my work at the intermediate frequency devices, superconducting integrated 4-12 GHz 180° IF hybrids were developed. It is clear the bandwidth does not fit to the HEB mixers. The devices where originally meant for the SIS mixers 800-1100 GHz. The design was done for the 9 $\mu$m and the 500 $\mu$m thick silicon substrates. The two designs show only tiny differences since the performance of the lumped elements is hardly dependent on the substrate thickness. The design shows about 5° phase imbalance and 0.5 dB amplitude imbalance. The final size of the miniaturized planar 180° hybrid device is about $2.2 \times 0.5\ mm^2$. The micro-fabrication of the IF hybrids on a 500 $\mu$m silicon substrate was done with using photolithography technique. The measurements with the dipstick immersed in liquid helium show that the transmissions between ports does not follow the simulation results for a device with a folded arm which two outputs are on one side of the substrate. The analysis shows that the fabricated capacitors of the IF hybrid seem to have a much higher values than the design numbers. It seems to be a mistake to assume that the development of the IF circuits would be not so critical. For future devices there is a need of more test devices on the fabrication wafer, like separate test lumped elements and test ports. For HEB balanced mixers the development of 0.5-3 GHz Wilkinson power combiners is needed using the same techniques.

# Bibliography


[1] Y. Okada, R. Güsten, M. A. Requena-Torres, M. Röllig, J. Stutzki, U. U. Graf, and A. Hughes, "Velocity profiles of [CII],[CI], CO, and [OI] and physical conditions in four star-forming regions in the Large Magellanic Cloud," *arXiv preprint arXiv:1808.08826*, 2018.

[2] S. W. Stahler and F. Palla, *The formation of stars*. John Wiley & Sons, 2008.

[3] E. F. van Dishoeck and F. P. Helmich, "Scientific drivers for future high-resolution far-infrared spectroscopy in space," in *Submillimetre and Far-Infrared Space Instrumentation*, vol. 388, 1996, p. 3.

[4] M. Röllig, N. P. Abel, T. Bell, F. Bensch, J. Black, G. J. Ferland, B. Jonkheid, I. Kamp, M. Kaufman, J. Le Bourlot *et al.*, "A photon dominated region code comparison study," *Astronomy & Astrophysics*, vol. 467, no. 1, pp. 187–206, 2007.

[5] M. P. Westig, "Quantum limited balanced superconducting 380-520 GHz mixer on a silicon membrane and mesoscopic tunnel devices for terahertz frequencies," 2013.

[6] B. T. Draine, *Physics of the interstellar and intergalactic medium*. Princeton University Press, 2010, vol. 19.

[7] T. De Graauw, F. Helmich, T. Phillips, J. Stutzki, E. Caux, N. Whyborn, P. Dieleman, P. Roelfsema, H. Aarts, R. Assendorp *et al.*, "The Herschel-heterodyne instrument for the far-infrared (HIFI)," *Astronomy & Astrophysics*, vol. 518, p. L6, 2010.

[8] "Ronan higgins," Private communication and simulated data set for atmospheric transitions.

[9] C. Risacher, R. Güsten, J. Stutzki, H.-W. Hübers, D. Büchel, U. U. Graf, S. Heyminck, C. E. Honingh, K. Jacobs, B. Klein *et al.*, "First supra-THz heterodyne array receivers for astronomy with the SOFIA observatory," *IEEE Transactions on Terahertz Science and Technology*, vol. 6, no. 2, pp. 199–211, 2016.

[10] D. Büchel, "Hot Electron Bolometer Mixers for THz Arrays," 2017.

[11] B. Klein, S. Hochgürtel, I. Krämer, A. Bell, K. Meyer, and R. Güsten, "High-resolution wide-band fast fourier transform spectrometers," *Astronomy & Astrophysics*, vol. 542, p. L3, 2012.

[12] J. M. Payna, "Focal plane arrays," *Single-Dish Astronomy: Techniques and Applications ASP Conference Series*, vol. 278, 2002.

[13] C. Risacher, R. Güsten, J. Stutzki, H.-W. Hübers, A. Bell, C. Buchbender, D. Büchel, T. Csengeri, U. Graf, S. Heyminck *et al.*, "The upGREAT 1.9 thz multi-pixel high resolution spectrometer for the SOFIA Observatory," *Astronomy & Astrophysics*, vol. 595, p. A34, 2016.

[14] J. Zmuidzinas, A. Karpov, D. Miller, F. Rice, H. G. Leduc, J. Pearson, and J. A. Stern, "Coherent detection and SIS mixers," in *Far-IR, Sub-mm and MM Detector Technology Workshop*, 2002.

[15] A. Karpov, J. Blondel, B. Lazareff, and K. Gundlach, "Millimeter and Submillimeter SIS Mixers with the Noise Temperature Close to the Quantum Limit," in *Fifth International Symposium on Space Terahertz Technology*, 1994, p. 73.

[16] M. Tinkham, *Introduction to superconductivity*. Courier Corporation, 2004.

[17] J. Bardeen, L. N. Cooper, and J. R. Schrieffer, "Theory of superconductivity," *Physical Review*, vol. 108, no. 5, p. 1175, 1957.

[18] K. Rohlfs and T. L. Wilson, *Tools of radio astronomy*. Springer Science & Business Media, 2013.

[19] S. Selig, M. P. Westig, K. Jacobs, M. Schultz, and N. Honingh, "Heat transfer coefficient saturation in superconducting Nb tunnel junctions contacted to a NbTiN circuit and an Au energy relaxation layer," *IEEE Transactions on Applied Superconductivity*, vol. 25, no. 3, pp. 1–5, 2015.

[20] A. Shurakov, Y. Lobanov, and G. Goltsman, "Superconducting hot-electron bolometer: from the discovery of hot-electron phenomena to practical applications," *Superconductor Science and Technology*, vol. 29, no. 2, p. 023001, 2015.

[21] K. Gundlach and M. Schicke, "SIS and bolometer mixers for terahertz frequencies," *Superconductor Science and Technology*, vol. 13, no. 12, p. R171, 2000.

[22] S. Krause, D. Meledin, V. Desmaris, A. Pavolotsky, H. Rashid, and V. Belitsky, "Noise and IF gain bandwidth of a Balanced Waveguide NbN/GaN Hot Electron Bolometer Mixer Operating at 1.3 THz," *IEEE Transactions on Terahertz Science and Technology*, vol. 8, no. 3, pp. 365–371, 2018.

[23] E. Novoselov and S. Cherednichenko, "Low noise terahertz MgB2 hot-electron bolometer mixers with an 11 GHz bandwidth," *Applied Physics Letters*, vol. 110, no. 3, p. 032601, 2017.

[24] P. Richards, "Bolometers for infrared and millimeter waves," *Journal of Applied Physics*, vol. 76, no. 1, pp. 1–24, 1994.

[25] D. Morozov, P. D. Mauskopf, P. Ade, D. M. Glowacka, D. Goldie, S. Withington, M. Bruijn, P. A. De Korte, H. Hoevers, M. Ridder *et al.*, "Ultasensitive tes detectors for fir space astronomy." in *Infrared, Millimeter and Terahertz Waves, 2008. IRMMW-THz 2008. 33rd International Conference on.* IEEE, 2008, pp. 1–2.

[26] T. M. Klapwijk and A. Semenov, "Engineering physics of superconducting hot-electron bolometer mixers," *IEEE Transactions on Terahertz Science and Technology*, vol. 7, no. 6, pp. 627–648, 2017.

[27] A. D. Semenov, G. N. Gol'tsman, and R. Sobolewski, "Hot-electron effect in superconductors and its applications for radiation sensors," *Superconductor Science and Technology*, vol. 15, no. 4, p. R1, 2002.

[28] S. Cherednichenko, P. Khosropanah, E. Kollberg, M. Kroug, and H. Merkel, "Terahertz superconducting hot-electron bolometer mixers," *Physica C: Superconductivity*, vol. 372, pp. 407–415, 2002.

[29] J. J. Baselmans, M. Hajenius, J. Gao, T. Klapwijk, P. De Korte, B. Voronov, and G. Goltsman, "Doubling of sensitivity and bandwidth in phonon cooled hot electron bolometer mixers," *Applied physics letters*, vol. 84, no. 11, pp. 1958–1960, 2004.

[30] S. Cherednichenko, P. Yagoubov, K. Ilin, G. Goltsman, and E. Gershenzon, "Large bandwidth of nbn phonon-cooled hot-electron bolometer mixers on sapphire substrates," in *Proc. 8th Int. Symp. on Space Terahertz Technology*, vol. 245, 1997.

[31] E. Gershenzon, G. Goltsman, I. Gogidze, Y. Gusev, A. Elantev, B. Karasik, and A. Semenov, "Millimeter and submillimeter range mixer based on electronic heating of superconducting films in the resistive state," *Sov. Phys. Superconductivity*, vol. 3, p. 1582, 1990.

[32] K. Yngvesson and E. Kollberg, "Optimum receiver noise temperature for nbn heb mixers according to the standard model," in *Tenth International Symposium on Space Terahertz Technology*, 1999, p. 563.

[33] B. Karasik and A. Elantiev, "Noise temperature limit of a superconducting hot-electron bolometer mixer," *Applied physics letters*, vol. 68, no. 6, pp. 853–855, 1996.

[34] D. W. Floet, E. Miedema, T. Klapwijk, and J. Gao, "Hotspot mixing: A framework for heterodyne mixing in superconducting hot-electron bolometers," *Applied physics letters*, vol. 74, no. 3, pp. 433–435, 1999.

[35] H. Merkel, P. Khosropanah, P. Yagoubov, and E. Kollberg, "A hot-spot mixer model for phonon-cooled nbn hot electron bolometric mixers," *IEEE Transactions on applied superconductivity*, vol. 9, no. 2, pp. 4201–4204, 1999.

[36] J. W. Kooi, *Advanced receivers for submillimeter and far infrared astronomy.* Rijkuniversiteit Groningen, 2008.

[37] C. M. Caves, "Quantum limits on noise in linear amplifiers," *Physical Review D*, vol. 26, no. 8, p. 1817, 1982.

[38] D. M. Pozar, *Microwave engineering.* John Wiley & Sons, 2009.

[39] A. R. Thompson, J. M. Moran, G. W. Swenson *et al.*, *Interferometry and synthesis in radio astronomy.* Springer, 1986.

[40] H. B. Callen and T. A. Welton, "Irreversibility and generalized noise," *Physical Review*, vol. 83, no. 1, p. 34, 1951.

[41] "Computer Simulation Technology: Microwave Studio," https://www.cst.com.

[42] R. L. Kautz, "Miniaturization of normal-state and superconducting striplines," *Journal of Research*, vol. 84, pp. 247–259, 1979.

[43] A. Pippard, "Metallic conduction at high frequencies and low temperatures," in *Advances in Electronics and Electron Physics*. Elsevier, 1954, vol. 6, pp. 1–45.

[44] G. Reuter and E. Sondheimer, "The theory of the anomalous skin effect in metals," *Proc. R. Soc. Lond. A*, vol. 195, no. 1042, pp. 336–364, 1948.

[45] N. W. Ashcroft and N. D. Mermin, "Solid state physics (holt, rinehart and winston, new york, 1976)," *Google Scholar*, vol. 403, 2005.

[46] D. Hottgenroth, "Superconductor-insulator-superconductor heterodyne mixers on niobium basis above the gap frequency of niobium and their use in an astronomical receiver," 1997.

[47] D. Mattis and J. Bardeen, "Theory of the anomalous skin effect in normal and superconducting metals," *Physical Review*, vol. 111, no. 2, p. 412, 1958.

[48] R. L. Kautz, "Picosecond pulses on superconducting striplines," *Journal of Applied Physics*, vol. 49, no. 1, pp. 308–314, 1978.

[49] E. Driessen, P. Coumou, R. Tromp, P. De Visser, and T. Klapwijk, "Strongly disordered TiN and NbTiN s-wave superconductors probed by microwave electrodynamics," *Physical review letters*, vol. 109, no. 10, p. 107003, 2012.

[50] R. Barends, "Photon-detecting superconducting resonators," Ph.D. dissertation, TU Delft, Delft University of Technology, 2009.

[51] S. A. Maas, "Microwave mixers," *Norwood, MA, Artech House, Inc., 1993, 368 p.*, 1993.

[52] M. Peter Westig, M. Justen, K. Jacobs, J. Stutzki, M. Schultz, F. Schomacker, and N. Honingh, "A 490 GHz planar circuit balanced Nb-Al2O3-Nb quasiparticle mixer for radio astronomy: Application to quantitative local oscillator noise determination," *Journal of Applied Physics*, vol. 112, no. 9, p. 093919, 2012.

[53] F. Boussaha, J. Kawamura, J. Stern, and C. Jung-Kubiak, "2.7 THz balanced waveguide HEB mixer," *IEEE Transactions on Terahertz Science and Technology*, vol. 4, no. 5, pp. 545–551, 2014.

[54] S. M. Krause, V. D., Desmaris, and V. Belitsky, "Noise performance of a balanced waveguide NbN HEB mixer utilizing a GaN buffer-layer at 1.3 THz," in *International Symposium on Space Terahertz Technology*, 2018.

[55] K. Gupta, R. Garg, I. Bahl, and P. Bhartia, "Microstrip lines and Slotlines (Artech House, Boston, 1996)," *Google Scholar*, p. 113.

[56] E. Jones, "Wide-band strip-line magic-T," *IRE Transactions on Microwave Theory and Techniques*, vol. 8, no. 2, pp. 160–168, 1960.

[57] L. Chua, "New broadband matched hybrids for microwave integrated circuits," in *1971 2nd European Microwave Conference*, no. 2, 1971, pp. 1–4.

[58] C.-H. Ho, L. Fan, and K. Chang, "Broad-band uniplanar hybrid-ring and branch-line couplers," *IEEE transactions on microwave theory and techniques*, vol. 41, no. 12, pp. 2116–2125, 1993.

[59] C.-H. Ho, L. Fan, and k. Chang, "New uniplanar coplanar waveguide hybrid-ring couplers and magic-T's," *IEEE Transactions on Microwave Theory and Techniques*, vol. 42, no. 12, pp. 2440–2448, 1994.

[60] H.-R. Ahn, *Asymmetric passive components in microwave integrated circuits*. John Wiley & Sons, 2006, vol. 182.

[61] L. Fan, S. Kanamaluru, and K. Chang, "A new wide-band and reduced-size uniplanar magic-T," in *IEEE MTT S INTERNATIONAL MICROWAVE SYMPOSIUM DIGEST*, vol. 2. INSTITUTE OF ELECTRICAL ENGINEERS INC (IEEE), 1995, pp. 667–667.

[62] K. S. Yngvesson, "Integrated Tapered Slot Antenna Arrays and Devices," in *Intern. Symp. Space Terahertz Technol*, 1990, pp. 176–186.

[63] P. R. Acharya, H. Ekstrom, S. S. Gearhart, S. Jacobsson, J. F. Johansson, E. L. Kollberg, and G. M. Rebeiz, "Tapered slotline antennas at 802 GHz," *IEEE Transactions on Microwave Theory and Techniques*, vol. 41, no. 10, pp. 1715–1719, 1993.

[64] T.-H. Lin and R.-B. Wu, "Cpw to waveguide transition with tapered slotline probe," *IEEE Microwave and Wireless components letters*, vol. 11, no. 7, pp. 314–316, 2001.

[65] V. S. Mottonen, "Wideband coplanar waveguide-to-rectangular waveguide transition using fin-line taper," *IEEE Microwave and Wireless Components Letters*, vol. 15, no. 2, pp. 119–121, 2005.

[66] K.-P. Ma, Y. Qian, and T. Itoh, "Analysis and applications of a new CPW-slotline transition," *IEEE Transactions on Microwave theory and Techniques*, vol. 47, no. 4, pp. 426–432, 1999.

[67] J. Lee, H. Lee, W. Kim, J. Lee, and J. Kim, "Suppression of coupled-slotline mode on CPW using air-bridges measured by picosecond photoconductive sampling," *IEEE microwave and guided wave letters*, vol. 9, no. 7, pp. 265–267, 1999.

[68] G. E. Ponchak and E. Tentzeris, "Development of finite ground coplanar (FGC) waveguide 90 degree crossover junctions with low coupling," in *Microwave Symposium Digest. 2000 IEEE MTT-S International*, vol. 3. IEEE, 2000, pp. 1891–1894.

[69] D. Loudkov, C.-Y. Tong, R. Blundell, N. Kaurova, E. Grishina, B. Voronov, and G. Gol'Tsman, "An investigation of the performance of the superconducting HEB mixer as a function of its RF embedding impedance," *IEEE transactions on applied superconductivity*, vol. 15, no. 2, pp. 472–475, 2005.

[70] "AutoCAD Mechanical," https://www.autodesk.de.

[71] "DRIE Bosch process, Robert Bosch GmbH."

[72] "Kern microtechnik," https://www.kern-microtechnik.com.

[73] D. Büchel, P. Pütz, K. Jacobs, M. Schultz, U. U. Graf, C. Risacher, H. Richter, O. Ricken, H.-W. Hübers, R. Güsten *et al.*, "4.7-THz superconducting hot electron bolometer waveguide mixer," *IEEE Transactions on Terahertz Science and Technology*, vol. 5, no. 2, pp. 207–214, 2015.

[74] M. Justen, K. Otani, D. Turcikova, F. Castellano, M. Beck, U. Graf, D. Büchel, M. Schultz, and J. Faist, "Waveguide Embedding of a Double-Metal 1.9-thz Quantum Cascade Laser: Design, Manufacturing, and Results," *IEEE Transactions on Terahertz Science and Technology*, vol. 7, no. 5, pp. 609–613, 2017.

[75] F. Boussaha, J. Kawamura, J. Stern, and C. Jung-Kubiak, "2.7 THz balanced waveguide HEB mixer," *IEEE Transactions on Terahertz Science and Technology*, vol. 4, no. 5, pp. 545–551, 2014.

[76] "Menlo TERA K15," https://www.menlosystems.com.

[77] "radiometer Physics GmbH," https://www.radiometer-physics.de.

[78] "PY005 Thor Labs," https://www.thorlabs.com.

[79] "Clear Microwave, howpublished = https://www.clearmicrowave.com,."

[80] S. J. Parisi, "180 degrees lumped element hybrid," in *Microwave Symposium Digest, 1989., IEEE MTT-S International*. IEEE, 1989, pp. 1243–1246.

[81] A. Kerr, A. Lichtenberger, C. Lyons, E. Lauria, L. Ziurys, and M. Lambeth, "A superconducting 180Â° IF hybrid for balanced SIS mixers," in *17th International Symposium on Space and Terahertz Technology*, vol. 36, 2006, pp. 37–56.

[82] "AWR," https://www.awrcorp.com.

[83] "GPO 7070 Corning Gilbert," https://www.corning.com.

# Acknowledgement

I am grateful to Prof. Dr. Jürgen Stutzki for giving me such opportunity to do my PhD studies and research in his workgroup at the I.Physikalisches Institut, Universität zu Köln.
Dr. Netty Honingh suprvised my PhD work and I am grateful to her for all her supervision through all these challenging research years.
I am thankful Dr. Karl Jacobs for the fabrication of my 1.9 THz integrated balanced HEB mixers and superconducting 4-12 GHz IF hybrids.
Thanks to Michael Schultz For the mounting the fabricated super tiny THz devices in the machined waveguides.
Thanks to Bettina Lindhorst for her appreciable help during the TTDS measurements which without that I could not succeed.
Thanks to my former colleagues, Sina, Denis, Florian, Johanna, Stefan, Marc, Patrick, Stephan Ignacio for providing the nice research and friendly working atmosphere.
Thanks to Dr. Ronan Higgins and Dr. Alvaro Sanchez-Monge for their help and scientific conversations.
Last but not least, I am grateful to my parents, Soulmaz, Radvin and Naser for supporting me during the PhD time, I simply love you.
My research work was supported within the Collaborative Research Council 956 (SFB 956, funded by the Deutsche Forschungsgemeinschaft (DFG).

# Eidesamtlich Erklärung

Ich versichere, dass ich die von mir vorgelegte Dissertation selbständig angefertigt, die benutzten Quellen und Hilfsmittel vollständig angegeben und die Stellen der Arbeit einschließlich Tabellen, Karten und Abbildungen, die anderen Werken im Wortlaut oder dem Sinn nach entnommen sind, in jedem Einzelfall als Entlehnung kenntlich gemacht habe; dass diese Dissertation noch keiner anderen Fakultät oder Universität zur Prüfung vorgelegen hat; dass sie abgesehen von unten angegebenen Teilpublikationen noch nicht veröffentlicht worden ist, sowie, dass ich eine solche Veröffentlichung vor Abschluss des Promotionsverfahrens nicht vornehmen werde. Die Bestimmungen der Promotionsordnung sind mir bekannt. Die von mir vorgelegte Dissertation ist von Prof. Dr. Jürgen Stutzki betreut worden.

Köln, den 22.04.2019

# Lebenslauf

**Sina Fathi**
Zülpicher str.58E
50674 Köln

| | |
|---|---|
| Geburtstag: | 28. May 1984 |
| Geburtsort: | Teheran, Iran |

| Promotion | |
|---|---|
| Februar 2019: | Abschluss der Promotion mit dem Thema "Development of Integrated Superconducting Balanced Mixers for THz Focal Plane Arrays" |
| October 2012: | Beginn der Promotion in Experimentalphysik am I. Physikalischen Institut der Universität zu Köln. |

| Studium | |
|---|---|
| August 2012: | Abschluss zum M.Sc. Radio-Weltraumwissenschaft-Ingenieurphysik am Chalmers Technische Universität, Göteborg, Schweden mit der Masterarbeit: Development of a Ferroelectric MMIC multiplier-Design, Fabrication and Characterization of a Ferroelectric Frequency Tripler at 100 GHz |
| May 2008: | Abschluss zum Bc.Sc.Elektroingenieur: Real-time face detection and recognition am Babol Technische Universität, Babol, Iran |

| Schulbildung | |
|---|---|
| 1995-2002: | Seraj Gesamtschule, Teheran, Iran |
| 1990-1995: | Shahid Bagheri Grundschule, Teheran, Iran |

| Anstellungsverhältnis | |
|---|---|
| Okt. 2012 bis Sept.2018: | Wissenschaftlicher Mitarbeiter am I. Physikalischen Institut der Universität zu Köln. |